UCGE Reports
Number 20206

Department of Geomatics Engineering

The Influence of Target Acceleration on Dual-Channel SAR-GMTI (Synthetic Aperture Radar Ground Moving Target Indication) Data

(URL: http://www.geomatics.ucalgary.ca/links/GradTheses.html)

by

Jayanti Sharma

October 2004

THE UNIVERSITY OF CALGARY

The influence of target acceleration on dual-channel SAR-GMTI (synthetic aperture radar ground moving target indication) data

by

Jayanti Sharma

A THESIS
SUBMITTED TO THE FACULTY OF GRADUATE STUDIES
IN PARTIAL FULFILLMENT OF THE REQUIREMENTS FOR THE
DEGREE OF MASTER OF SCIENCE

DEPARTMENT OF GEOMATICS ENGINEERING

CALGARY, ALBERTA
OCTOBER, 2004

Abstract

This thesis investigates the effects of acceleration on the detection and estimation of the velocity of ground moving targets in airborne dual-channel synthetic aperture radar (SAR) data. The airborne results give an indication of the performance we may expect in an upcoming spaceborne system, the GMTI (ground moving target indication) mode of RADARSAT-2.

Acceleration has (i) an insignificant impact on the detection of moving targets using the displaced phase centre antenna (DPCA) algorithm; (ii) only minor affects on the estimation of across-track velocity (the component perpendicular to the line of flight) using along-track interferometric (ATI) phase and (iii) may significantly bias the estimate of along-track velocity. Estimation of both acceleration and velocity components is not uniquely determined using only two receive channels.

Acceleration also has severe effects on focusing. Time-frequency analysis is used to improve target focusing and to detect the presence of significant target acceleration.

Acknowledgements

I would like to thank Dr. Chuck Livingstone and my supervisor Dr. Michael Collins for providing me the unique opportunity of combining work experience at a defence research facility with a Master's degree. Chuck has done an amazing job directing the GMTI group and focusing our collective energy towards the RADARSAT-2 launch date. I thank Dr. Collins for allowing me considerable flexibility in conducting my research, and for providing long distance supervision from Calgary to Ottawa.

I would like to especially thank Dr. Christoph Gierull for his invaluable guidance and advice at all stages of the research, and Mr. Ishuwa Sikaneta for his help and depth of knowledge of mathematics, radar, linux, and LaTeX. I am grateful to the entire GMTI team at DRDC Ottawa including Shen Chiu, Sean Gong, Marielle Quinton and Pete Beaulne for their help and patience, and for providing an enjoyable and stimulating environment in which to work. Finally I thank my parents for their support, encouragement, and for fostering in me a love of learning.

This work has been financed by Defence Research and Development Canada - Ottawa, and I have been supported by the National Science and Engineering Research Council, the University of Calgary, and Alberta Learning. Their financial support is greatly appreciated.

Table of Contents

Abstract ii

Acknowledgements iii

Table of Contents iv

List of Tables vi

List of Tables vii

List of Figures vii

List of Figures viii

List of Symbols xiii

List of Abbreviations xvi

1 Introduction 1
- 1.1 Background . . . 1
- 1.2 Research objectives . . . 5
- 1.3 Thesis organization . . . 5

2 SAR-GMTI background and theory 8
- 2.1 SAR fundamentals . . . 8
- 2.2 Classic MTI . . . 13
- 2.3 Multi-aperture GMTI . . . 15
  - 2.3.1 Range compressed signal . . . 16
  - 2.3.2 Multi-aperture GMTI techniques . . . 24
- 2.4 Time-frequency analysis . . . 30
  - 2.4.1 Introduction . . . 30
  - 2.4.2 Utility of TF analysis . . . 31
  - 2.4.3 Time-frequency transformations . . . 33

3 Detection 40
- 3.1 Theory . . . 40
  - 3.1.1 DPCA mathematical representation . . . 41
  - 3.1.2 Analysis of the DPCA expression . . . 43

3.2 Simulations . . . 44
3.2.1 DPCA magnitude with v_{y0} . . . 45
3.2.2 DPCA magnitude with v_{x0} . . . 47
3.2.3 DPCA magnitude with a_{y0} . . . 49
3.2.4 DPCA magnitude with along-track acceleration a_{x0} . . . 51
3.2.5 DPCA magnitude with $\dot{a}_{y0}$ . . . 53
3.2.6 DPCA magnitude for spaceborne geometries . . . 53
3.2.7 Analysis of DPCA magnitude simulations on target detection 57
3.3 Experimental results . . . 59
3.3.1 Detection and tracking algorithm . . . 59
3.3.2 Analysis and results of experimental detections . . . 63

4 Focusing **68**
4.1 Theory and simulations . . . 68
4.1.1 Focusing a stationary target . . . 69
4.1.2 Focusing a moving target with a SWMF . . . 70
4.1.3 Focusing a moving target with a matched reference filter . . . 96
4.2 Experimental Results . . . 102
4.2.1 Focusing a stationary target . . . 103
4.2.2 Focusing a moving target with a SWMF . . . 104
4.2.3 Focusing a moving target with a matched reference filter . . . 107

5 Estimation of along-track velocity v_{x0} **111**
5.1 Theory and Simulations . . . 112
5.1.1 Estimating v_{x0} for a target with only along-track velocity . . . 112
5.1.2 Estimating v_{x0} in the presence of v_{y0} . . . 114
5.1.3 Estimating v_{x0} in the presence of a_{y0} . . . 118
5.1.4 Estimating v_{x0} in the presence of a_{x0} . . . 120
5.1.5 Estimating v_{x0} in the presence of $\dot{a}_{y0}$ . . . 124
5.1.6 Estimating v_{x0} in a spaceborne geometry . . . 124
5.2 Experimental Results . . . 127

6 Estimation of across-track velocity v_{y0} **133**
6.1 Theory . . . 133
6.2 Simulations . . . 134
6.2.1 Variation in ATI with v_{y0} . . . 135
6.2.2 Variation in ATI with v_{x0} . . . 138
6.2.3 Variation in ATI with a_{y0} . . . 140
6.2.4 Variation in ATI with a_{x0} and $\dot{a}_{y0}$ . . . 143
6.2.5 Variation in ATI phase for spaceborne scenarios . . . 143

6.2.6 ATI simulation summary . . . 144
6.3 Experimental Results . . . 146
6.3.1 Across-track velocity estimation algorithm . . . 146
6.3.2 Analysis of estimated velocities . . . 148

7 Acceleration detection and focusing improvements 152
7.1 Theory . . . 153
7.1.1 Tracking the instantaneous frequency . . . 153
7.1.2 Detecting acceleration using TF analysis . . . 155
7.1.3 Focusing using TF Analysis . . . 157
7.2 Simulations . . . 158
7.2.1 Tracking the instantaneous frequency . . . 158
7.2.2 Detecting acceleration using TF analysis . . . 160
7.2.3 Focusing using TF Analysis . . . 173
7.3 Experimental Results . . . 176
7.3.1 TF transform . . . 176
7.3.2 Tracking the instantaneous frequency . . . 177
7.3.3 Detecting acceleration using TF analysis . . . 179
7.3.4 Focusing using TF Analysis . . . 182

8 Conclusions and extensions 186
8.1 Conclusions . . . 186
8.2 Extensions . . . 189

References 198

A Experimental data 199
A.1 Experimental set up . . . 199
A.2 Data pre-processing . . . 202
A.3 Motion parameter estimation accuracies . . . 204
A.3.1 GPS accuracies . . . 207

B ATI ambiguities and performance analysis 211
B.1 ATI ambiguities . . . 211
B.1.1 Directional ambiguities . . . 211
B.1.2 Blind-speed ambiguities . . . 213
B.1.3 Doppler ambiguities . . . 213
B.2 Performance analysis . . . 217
B.2.1 Coherence . . . 221

List of Tables

3.1 Radar and geometry parameters for airborne SAR simulations. 45
3.2 Radar and geometry parameters for RADARSAT-2 simulations. . . . 54

A.1 Radar and geometry parameters for CV 580 Petawawa data collection in November 2000. 199
A.2 A comparison of along-track velocities estimated using the filter-bank method from dual-channel SAR data and GPS. 205
A.3 A comparison of across-track velocities estimated using along-track interferometric phase from dual-channel SAR data and GPS. 206
A.4 A comparison of the absolute differences in along- and across-track velocities estimated using SAR data and velocities estimated from GPS. 207
A.5 Transforming GPS speed and heading into along-track and across-track velocities. 208

List of Figures

1.1 Artist's rendition of the RADARSAT-2 sensor ©CSA. 3

2.1 Doppler frequency of a moving target shifted out of the clutter bandwidth, enabling its detection. 14
2.2 Top-down view of antenna and accelerating target geometry for an airborne scenario. 17
2.3 Top-down view of antenna and target geometry for two-channel data collection. 20
2.4 Classical DPCA geometry. 26

3.1 Range compressed DPCA magnitude through time for a simulated target with constant velocity v_{y0} varied from -25 to 25 m/s and $v_{x0} = 0$. 46
3.2 Range compressed DPCA magnitude through time for a simulated target with constant velocity v_{x0} varied from -25 to 25 m/s and $v_{y0} = 0$. 47
3.3 Range compressed DPCA magnitude through time for a simulated target with constant velocity $v_{x0} = -25$ m/s and v_{y0} varied from -25 to 25 m/s. 48
3.4 Range compressed DPCA magnitude through time for a simulated target with constant velocities $v_{x0} = -25$ m/s and $v_{y0} = 1$ m/s. 49
3.5 Range compressed DPCA magnitude through time for a simulated target with constant across-track acceleration a_{y0} varied from -1 to 1 m/s^2. 50
3.6 Range compressed DPCA magnitude through time for a simulated target with constant along-track acceleration a_{x0} varied from -1 to 1 m/s^2. 52
3.7 Range compressed DPCA magnitude through time for a simulated target with time-varying across-track acceleration with rate of change $\dot{a}_{y0}$ varied from -0.1 to 0.1 m/s^3. 53
3.8 Range compressed DPCA magnitude through time for a simulated target observed in a spaceborne geometry with across-track velocity v_{y0} varied from -25 to 25 m/s. 55
3.9 Range compressed DPCA magnitude through time for a simulated target observed in a spaceborne geometry with constant across-track acceleration a_{y0} varied from -1 to 1 m/s^2. 56
3.10 Four stages of the target detection and tracking process operating in the range compressed domain. 61
3.11 Variation of target velocity (obtained from GPS) through time in the vicinity of broadside time t=0 for a single pass. 65
3.12 Range compressed DPCA magnitude through time for one pass of the Juliet target. 67

4.1 Magnitude response (after azimuth compression) of simulated non-accelerating point targets focused using a SWMF versus azimuthal distance. 73
4.2 Example TF representation of a SWMF and a target moving in the across-track direction with $v_y > 0$ m/s. 74
4.3 Example TF representation of a SWMF and a target moving in the across-track direction with sufficient $v_y > 0$ m/s such that the Doppler frequency wraps across the $\pm$PRF/2 boundary. 76
4.4 Example TF representation of a SWMF and a target moving in the across-track direction with $v_x > 0$ m/s. 77
4.5 Magnitude response (after azimuth compression) of simulated point targets with constant acceleration focused using a SWMF. 79
4.6 Across-track acceleration $a_y(t)$ (with constant $\dot{a}_{y0}$) and corresponding across-track velocity $v_y(t)$ for a point target through time. The target's azimuth response is given in Figure 4.7. 82
4.7 Magnitude response (after azimuth compression) of a simulated point target (with constant $\dot{a}_{y0}$ and an $a_y(t)$ given in Figure 4.6) focused using a SWMF. 83
4.8 Across-track acceleration $a_y(t)$ (a rectangular window centred at broadside) and corresponding across-track velocity $v_y(t)$ for a point target through time whose azimuth response to a SWMF is given in Figure 4.9. 85
4.9 Magnitude response (after azimuth compression) of a simulated point target (with time-varying across-track acceleration given in Figure 4.8) focused using a SWMF. 86
4.10 Across-track acceleration $a_y(t)$ (a rectangular window centred at 1.3 s past broadside) for a simulated point target, corresponding across-track velocity $v_y(t)$, and its magnitude response (after azimuth compression) when focused using a SWMF. 88
4.11 Across-track acceleration $a_y(t)$ (a unit step function with height 0.1 m/s^2) and corresponding across-track velocity $v_y(t)$ for a point target through time whose azimuth response to a SWMF is given in Figure 4.13. 89
4.12 Across-track acceleration $a_y(t)$ (which is ramped until broadside) and corresponding across-track velocity $v_y(t)$ for a point target through time whose azimuth response to a SWMF is given in Figure 4.13. . . 90
4.13 Magnitude response (after azimuth compression) of simulated point targets (with time-varying across-track accelerations given in Figures 4.11 and 4.12) focused using a SWMF. 91

4.14 Magnitude response (after azimuth compression) of simulated non-accelerating point targets focused using a SWMF for a spaceborne geometry. 93
4.15 Magnitude response (after azimuth compression) of simulated point targets with constant acceleration focused using a SWMF for a spaceborne geometry. 95
4.16 Impulse responses of simulated point targets focused using perfectly matched filters. 99
4.17 Magnitude response after azimuth compression of a stationary corner reflector from the Ottawa 2001 data set. 105
4.18 Magnitude response (after clutter suppression using DPCA) for a moving target (l1p9 Convoy) focused using a SWMF. 106
4.19 DPCA magnitude after azimuth compression of one pass of the Convoy target using a SWMF and a MTMF. 108
4.20 DPCA magnitude after azimuth compression of one pass of the Juliet target using a SWMF and a MTMF. 109

5.1 Magnitude responses of a simulated point target with constant $v_{x0} = 10$ m/s after compression with a bank of reference filters initialized with various v_{x0} velocities. 115
5.2 DPCA magnitude responses of a simulated point target with $v_{y0} = 30$ m/s after compression with a bank of reference filters initialized with various v_{x0} velocities. 117
5.3 Magnitude responses of a simulated point target with $a_{y0} = 0.1$ m/s^2 after compression with a bank of reference filters initialized with various v_{x0}. 119
5.4 Magnitude responses of a simulated point target with $a_{x0} = 0.5$ m/s^2 after compression with a bank of reference filters initialized with varying v_{x0}. 121
5.5 Example TF history for a target accelerating in the along-track direction. 123
5.6 Magnitude responses of a simulated point target with $\dot{a}_{y0} = 0.04$ m/s^3 after compression with a bank of reference filters initialized with various v_{x0} velocities. 125
5.7 Magnitude responses of a simulated point target for a spaceborne geometry with $v_{x0} = 10$ m/s after compression with a bank of reference filters initialized with various v_{x0} velocities. 126
5.8 DPCA filter-bank magnitude map from one pass of the Convoy target (line 1, pass 5). 129
5.9 DPCA filter-bank magnitude map from one pass of the Juliet target (line 2, pass 2). 130

5.10 DPCA filter-bank magnitude map from one pass of the Juliet target (line 3, pass 3). 131

6.1 ATI signal for varying across-track velocities v_{y0}. 136
6.2 ATI signal for varying across-track velocities v_{y0} and constant $v_{x0} = -30$ m/s compared with the expected ATI phase when the v_{x0} dependence is neglected. 139
6.3 Compressed target response from a SWMF and ATI signal for a point target with $v_{x0} = 10$ m/s. 141
6.4 ATI signal for varying across-track broadside velocities v_{y0} and constant across-track acceleration $a_{y0} = 1$ m/s^2 compared with the expected ATI phase when the a_{y0} dependence is neglected. 142
6.5 ATI signal (with normalized magnitude) for various experimental target tracks. 150

7.1 Instantaneous frequency of a simulated target with constant velocity ($v_{x0} = 10$ m/s, $v_{y0} = 15$ m/s, SCR = 0 dB) tracked through azimuthal slow-time. 158
7.2 Enlarged portion of Figure 7.1. 159
7.3 Instantaneous frequency of a simulated target in a spaceborne geometry with slow constant velocity ($v_{y0} = 3$ m/s and SCR = 0 dB) tracked through azimuthal slow-time. 161
7.4 Absolute error in the mean value of the cubic coefficient (of a polynomial fit to the DPCA phase) for a simulated target moving with constant velocity as a function of SCR. 166
7.5 Inverse variance of the cubic coefficient (of a polynomial fit to the DPCA phase) for a simulated target moving with constant velocity as a function of SCR. 167
7.6 Absolute error in the mean value of the cubic coefficient (of a polynomial fit to the DPCA phase) for a simulated accelerating target as a function of SCR. 168
7.7 Inverse variance of the cubic coefficient (of a polynomial fit to the DPCA phase) for a simulated accelerating target as a function of SCR. 169
7.8 Unwrapped DPCA phase through azimuthal slow-time for a target with an SCR of 0 dB moving with constant velocity. 171
7.9 Normalized DPCA magnitude of a simulated accelerating target focused using instantaneous phase from IF integration. 174
7.10 Normalized DPCA magnitude of a simulated accelerating target focused using conventional SAR processing. 175
7.11 DPCA magnitude of a target track (l1p9 Convoy) in the TF domain after application of the PWVD. 177

7.12 Instantaneous frequency of a vehicle target (l1p9 Convoy) through azimuth time. 178
7.13 Antenna gain pattern of the receiving fore antenna for the CV 580 system. 180
7.14 Differences between a target's TF track $f(t)$ and its linear, quadratic, and cubic fits over time. 181
7.15 DPCA magnitudes of a vehicle target (l1p9 Convoy) focused using matched filters derived from various TF histories. 183
7.16 DPCA magnitude of a vehicle target (l1p9 Convoy) focused using a reference filter initialized with $\hat{v}_{x0}$ and $\hat{v}_{y0}$ computed from a matched filter-bank and from the ATI phase, respectively. 185

A.1 Delta control target from the Petawawa 2000 data collection. 201
A.2 Sketch of Juliet and Delta moving target rail systems with their surrounding structure and environment. 201
A.3 Four vehicle convoy from the Petawawa 2000 data collection. 202
A.4 Aerial photograph mosaic of CFB Petawawa training area, site of the 2000 GMTI experiment. 203

B.1 Example TF representation of a SWMF and a target moving in the across-track direction with sufficient $v_{y0} > 0$ m/s such that there is zero spectral overlap between the target and reference signals. 216
B.2 Illustration of the across-track interferometric (ATI) signal in the complex plane for a moving target with accompanying clutter. 220

List of Symbols

A : signal amplitude 10

a_{x0} : target along-track acceleration at broadside time $t = 0$ 18

a_{y0} : target across-track acceleration at broadside time $t = 0$ 18

B_ν : pulse bandwidth 10

c : speed of light 10

d : physical antenna separation distance 19

f_{nyq} : Nyquist frequency 213

f_{PRF} : pulse repetition frequency 18

$f_{\text{sta lims}}$: frequency limits of stationary world reference filter 215

$g(t)$: difference in the two-way path length to the fore and registered aft apertures 23

H : altitude of radar platform 18

$I(t)$: azimuth compressed target image 68

j : imaginary unit 9

$k = \frac{2\pi}{\lambda}$: wave number 21

λ : wavelength 10

ν_0 : carrier frequency 9

ρ : correlation coefficient (coherence) 159

$r(t)$: reference signal for matched filtering 69

$\Re\{\cdot\}$: retains the real component of the argument 37

R_0 : range to target at broadside time $t = 0$ 18

$R(t)$: range to the target as a function of time 18

$R_1(t)$: range from fore antenna to the target as a function of time ... 19

$R_2(t)$: range from aft antenna to the target as a function of time 19

$R^n(0)$: nth derivative of range function evaluated at $t = 0$ 18

rect(x/L) : Rectangular function of length L 11

sinc$(x) = \frac{sin(x)}{x}$: 11

σ_x : standard deviation of x 210

$S(\omega) = \mathcal{F}\{s(t)\} = \int_{-\infty}^{\infty} s(t)e^{-j\omega t}dt$: Fourier transform 10

$s(t)$: range compressed target signal 12

t : time variable (azimuthal or slow-time) 11

t_{img} : azimuthal time at which azimuth compressed target signal is focused 80

t_0 : azimuthal broadside time $t = 0$ 178

τ : time variable (for one pulse or fast-time) 9

T : synthetic aperture time 12

$\theta(t)$: phase history function 27

$\vec{v}$: vector 24

$\vec{v}^T$: transpose 23

$\vec{v}^*$: complex conjugation 27

v_a : aircraft velocity 16

v_{x0} : target along-track velocity at broadside time $t = 0$ 18

v_{y0} : target across-track velocity at broadside time $t = 0$ 18

y_0 : target across-track position at broadside time $t = 0$ 18

$\langle x \rangle$: expectation 219

$|x|$: absolute value 11

$\overline{x}$: mean value 60

$\dot{x} = \frac{dx(t)}{dt}$: first-order time derivative 18

$\ddot{x} = \frac{d^2x(t)}{dt^2}$: second-order time derivative 184

List of Abbreviations

A/D: Analog to Digital conversion 10

ATI: Along-Track Interferometry 5

CFAR: Constant False Alarm Rate 42

CNR: Clutter-to-Noise Ratio 219

CRLB: Cramer-Rao Lower Bound 163

CV: Convair 2

DPCA: Displaced Phase Centre Antenna 5

FFT: Fast Fourier Transform 30

GMTI: Ground Moving Target Indication 1

GPS: Global Positioning System 6

ICM: Internal Clutter Motion 26

IF: Instantaneous Frequency 153

LFM: Linear Frequency Modulation 11

MODEX: Moving Object Detection Experiment 2

MTI: Moving Target Indication 13

MTMF: Moving Target Matched Filter 107

PRI: Pulse Repetition Interval 24

PRF: Pulse Repetition Frequency 14

PWVD: Pseudo Wigner-Ville Distribution 5

RF: Radio Frequency 9

RCS: Radar Cross Section 9

SAR: Synthetic Aperture Radar 1

SCR: Signal-to-Clutter Ratio 96

SNR: Signal-to-Noise Ratio 10

STAP: Space Time Adaptive Processing 26

SWMF: Stationary World Matched Filter 69

TF: Time-Frequency 30

WVD: Wigner-Ville Distribution 36

Chapter 1

Introduction

1.1 Background

Synthetic aperture radar (SAR) systems have been used extensively in the past two decades for fine resolution mapping and other remote sensing applications [72]. Since the SAR principle for developing high resolution radar images was first suggested by Carl Wiley in 1954 [63], many airborne and spaceborne SAR systems have been used operationally. SAR is an active, coherent, all-weather, day-night imaging system which operates in the microwave region of the electromagnetic spectrum [90]. It has been used in such diverse applications as land use and topographic mapping, polar ice research, studies of ocean dynamics, and military surveillance and reconnaissance [30, 53, 72, 82].

With the advancement of sophisticated SAR signal processing and imaging methods, more specialized radar problems are being studied including the detection, parameter estimation, and imaging of ground moving targets in a SAR scene [82]. In many civilian and military applications of airborne and spaceborne SAR imaging, it is desirable to simultaneously monitor ground traffic [37, 79].

In the past, detection and tracking of moving targets was primarily a military concern and was performed by specialized airborne sensors. Extensive investment by the military resulted in the development of operational airborne platforms (such as Joint-STARS, developed by the United States in the late 1980's) which were able to detect and map vehicles moving on the Earth's surface [35]. In addition to military ground moving target indication (GMTI) systems, today there exist several experimental airborne SAR-GMTI radars including Environment Canada's Convair (CV)

580 [49], the German AER-II and PAMIR sensors [25, 28], and a C-band Andover system developed by the Defence Evaluation Research Agency in the UK [55].

However, with the rapid evolution of radar technology, it is now economically feasible to also create spaceborne sensors to perform moving target detection and measurement [35]. From a military perspective, such spaceborne systems have the potential to significantly augment existing operational capabilities by offering increased coverage and the ability to monitor unfriendly territories. For civilian applications, spaceborne GMTI can provide land and sea traffic monitoring capabilities which may be valuable in designing, monitoring, and controlling transportation infrastructure [35]. Additional applications of both spaceborne and airborne GMTI have been envisioned to include intelligence collection, counter-terrorism operations, customs, immigration and law enforcement, search and rescue, and remote exploration, as well as support for conventional military roles [23].

Due to the large capital costs associated with the development and operation of airborne GMTI sensors, these systems are expensive even by military standards, and have not been used for transportation system monitoring or other civilian applications to date [35]. Spaceborne sensors, on the other hand, are unmanned, are able to function 24 hours a day, and support large coverage areas, which increases their attractiveness for commercial applications.

Presently no spaceborne radar system has GMTI capability, although several SAR systems with GMTI modes will be launched in the near future [35]. The Canadian RADARSAT-2 sensor (scheduled for launch in the spring of 2005 [51]) will offer an experimental moving object detection mode (abbreviated MODEX), and will provide the first opportunity to routinely measure and monitor vehicles moving on the Earth's surface from space. An artist's rendition of the RADARSAT-2 sensor is shown in Figure 1.1. RADARSAT-2 was designed primarily as an imaging radar, thus imposing limitations on its ability to perform GMTI. However, MODEX will be a valuable tool in evaluating assumptions made in modelling spaceborne GMTI, developing im-

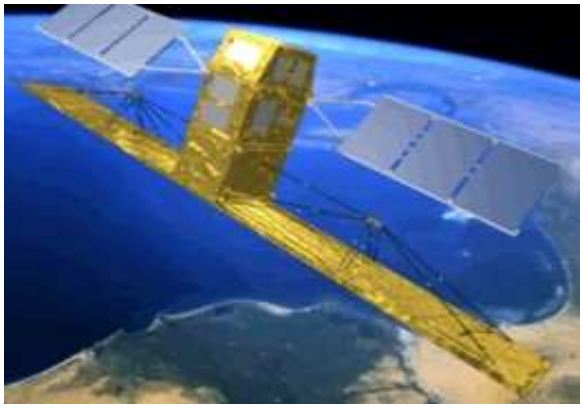

Figure 1.1: Artist's rendition of the RADARSAT-2 sensor ©CSA [51].

proved processing algorithms for the spaceborne case, identifying the strengths and weaknesses of single-pass spaceborne SAR-GMTI, and demonstrating potential applications to interested parties [35]. A second commercial spaceborne SAR with GMTI capability is the German TerraSAR-X, scheduled for a launch date of spring 2006 [91]; it is hoped that together these sensors will provide further understanding of spaceborne GMTI.

Despite the numerous applications of SAR-GMTI, there are significant challenges in detecting and measuring target motion from airborne and spaceborne platforms. SAR forms high resolution images using phase information in the received echoes. The instantaneous phase is determined by the relative motion between the radar sensor and the scene, and the resulting image focusing and quality is dependent (among other things) upon the ability to reconstruct this phase [20, 89] . SAR imaging from both spaceborne and airborne radars of stationary scenes is well understood [83]. However, in the presence of unknown target motion, the target will appear defocused and spatially displaced from its true location in the image. Numerous papers (e.g. [17, 20, 35, 41, 67, 80, 90, 93]) have examined the response of a SAR to moving targets and have suggested methods for estimating the target motion and achieving a focused image. However, in the majority of GMTI literature, it is assumed

that targets travel with constant velocity (e.g. [5, 11, 36, 41, 49, 56, 80, 82]). This assumption is often violated in real world applications such as monitoring vehicle traffic on roads and highways, where target acceleration is commonplace and must be considered.

There has been little published research examining the impacts of target acceleration on GMTI directly. Although some papers include one component of acceleration in the standard range equations for completeness (e.g. [62, 68]), there are no papers (to this author's knowledge) which examine the effects of target acceleration in experimental data. Yadin [93] notes in passing that target acceleration during the integration time results in a varying apparent angular position of the target and thus a smearing in azimuth, although this variation in position is not quantified. Soumekh [82] observes in the analysis of his experimental data (consisting of military vehicles) that the focused peaks of some targets seem 'chaotic' and 'not localized' which he attributes to target maneuvering and/or target acceleration or deceleration.

Carrara [12] has examined the effects of uncompensated motion of an airborne platform on focusing. In the preivous paragraphs, it was described how a SAR signal's instantaneous phase is determined by the relative radar-target motion. Uncompensated *platform* motion (possibly due to errors in motion compensation routines) introduces errors in this phase, which may be equivalent to errors due to uncompensated *target* motion. Carrara noted that higher-order phase errors from residual platform motion can cause defocusing effects in the processed imagery.

These observations suggest that acceleration has an impact upon target focusing, providing the rationale for a more systematic examination of acceleration, and its potential effects on focusing as well as on the closely-related tasks of detection and parameter estimation.

1.2 Research objectives

The primary objective of this research is to examine the influence of acceleration on detection, velocity estimation, and focusing of moving targets in dual-channel SAR data. Theory, simulations, and the analysis of experimental data will be used to determine acceleration's effects on detection, and to describe the detrimental effects of both constant and time-varying accelerations on estimating target motion and on target focusing if left uncompensated.

The secondary objective is to determine a method of detecting target acceleration and to compensate for its effects to obtain a focused target image. Although the acceleration parameters themselves cannot be uniquely determined using only two channels of SAR data, possibilities lie in detecting certain acceleration components and obtaining a focused image irrespective of the target motion.

1.3 Thesis organization

Chapter 2 provides the necessary background and theory regarding SAR and GMTI. The SAR response to a stationary point target is reviewed, followed by an overview of both classical and multi-aperture GMTI techniques with an emphasis on the displaced phase centre antenna (DPCA) method and along-track interferometry (ATI). Other detection and estimation techniques are also reviewed. In addition to analysis of the SAR time-series signal, further insight may be gained by transforming the data into a two-dimensional time-frequency space. The utility of time-frequency analysis is described, and a review of various transformation methods including the Pseudo Wigner-Ville Distribution (PWVD) is provided.

Chapter 3 examines the impact of acceleration on target detection when using the DPCA technique. The theoretical DPCA response for a range compressed accelerating point target is derived, and its repercussions on detection are examined through simulations of an airborne geometry. The DPCA technique is then used to detect

moving targets in experimental data collected using the CV 580 airborne SAR, and comparisons are made with the theoretical and simulated results.

Chapter 4 describes effects of acceleration on focusing a moving point target in dual-channel SAR data. The response of a SAR to a stationary target and its response to moving (possibly accelerating) targets when using conventional azimuth processing are compared, and the influence of different reference filters on target focusing are examined. Following the theoretical analysis, stationary and moving targets from experimental data are compressed in the azimuth dimension using various reference filters, and their responses are examined in context to the previous results.

Chapters 5 and 6 examine the influence of target acceleration on estimation of the along-track and across-track target velocity components, respectively. The estimation methods and the effects of acceleration on each velocity component are very different, which is why they are separated. Each chapter begins with a description of the estimation algorithm, where along-track velocity estimation makes use of a bank of matched filters and across-track velocity estimation employs along-track interferometric phase. The effects of each motion component (along- and across-track velocities and accelerations) on estimation of the velocity vector are examined separately using simulations. Lastly, the accuracy in estimating the velocity of targets in experimental data are determined using comparisons with GPS (Global Positioning System) data.

Having examined the effects of target acceleration on detection, focusing and parameter estimation, chapter 7 investigates methods of detecting certain components of acceleration (specifically along-track acceleration and time-varying across-track acceleration) and focusing a target irrespective of its motion. The suggested algorithms make use of the instantaneous frequency of the target SAR signal, which is extracted from the time-frequency domain. An acceleration detection algorithm is proposed based on polynomial fits to the range and/or frequency history of the target, and a focusing algorithm is suggested involving reconstruction of the target phase history

through integration of the instantaneous frequency. Simulations are used to assess these algorithms, after which they are applied to experimental data.

A summary of the research and recommendations for future work are presented in the closing chapter.

Chapter 2

SAR-GMTI background and theory

The challenge of SAR-GMTI is to detect moving targets, estimate their motion parameters, and then focus and insert them into the imaged scene [49]. Generally there is no *a priori* knowledge of the targets and we thus start from a stationary-scene assumption. There exist many different techniques to perform SAR-GMTI, although all require fundamental understanding of the SAR image formation process.

In this chapter, certain basics of synthetic aperture radar are reviewed, followed by a brief history of GMTI including classical techniques using a single channel. Presently, the development of more sophisticated radar systems collecting multi-channel SAR data has increased the robustness and accuracy of GMTI within various clutter environments. Experimental airborne systems in use today and future spaceborne systems are reviewed, and a description of multi-channel techniques and time-frequency techniques for detection and parameter estimation of moving targets is provided. The advantages of joint time-frequency analysis over strictly time-domain methods is investigated, and the properties of various time-frequency transforms are described.

2.1 SAR fundamentals

The basic purpose of SAR is to derive an image, which is a map of the microwave reflectivity of a scene [64]. In every monostatic SAR system an antenna transmits a series of radar pulses, and receives the reflected energy from scatterers. Scatterers may include moving targets (of primary interest in GMTI) and clutter such as buildings, fields, and trees, where clutter refers to any unwanted returns that may interfere with the detection of the desired targets [16]. Time delays between the transmission and

reception of each pulse provide information on the range to the targets [90].

SARs are generally coherent, meaning that they retain information regarding both the amplitude and phase of the received signal [74]. The amplitude is related to the radar cross section (RCS) of the target, where RCS is a measure of the target's ability to reflect electromagnetic waves [16]. The phase is related to the range history of the target, i.e. the changing distance between the radar platform and the scatterer over time as the radar sweeps by. To form a SAR image, an accurate model of the imaging system, the transmitted signal, the imaging geometry, and its evolution through time is necessary [49]. If any of these are unknown (such as in GMTI), the task of detecting and focusing a target will be made more complex.

Let the azimuth direction (or along-track) be the dimension parallel to the radar's line of flight, and let the range direction (also called across-track) be perpendicular to the line of flight. When imaging a stationary scene, a SAR achieves fine range resolution through pulse (or range) compression and high azimuth resolution through cross-correlating a theoretical stationary target's phase response with the collected data (also called azimuth compression) [45]. Imaging stationary targets is a special case of the general GMTI scenario, and many of processing steps are shared in common including range compression. The following description of range compression follows that of [13] and [73].

Assume that the radar transmits a single RF (radio frequency) pulse of the form $n(\tau)$ with complex envelope $g(\tau)$ and carrier frequency ν_0 :

$$n(\tau) = g(\tau)\exp(j2\pi\nu_0\tau), \tag{2.1}$$

where j is the imaginary unit, and τ represents the time scale over one pulse in the range direction (also known as fast-time). Imagine a scenario in which the radar pulse reflects off a point target on the ground located at distance R from the radar, and returns to the antenna. It is assumed that the radar does not move between pulse transmission and reception (i.e. that R is constant during that time). For typical airborne and spaceborne SAR systems, this motion can be considered negligible [81].

The received signal (from any target, moving or stationary) is analog and must be digitized, requiring an A/D converter (analog-to-digital) operating at a sampling rate above the signal bandwidth and with a sufficient number of bits to maintain image fidelity [63]. In this treatment the signals are presented in their continuous forms to simplify notation and mathematical manipulation, although in reality all signals will be sampled and digitized prior to further processing.

The received pulse $r(\tau)$ is a delayed and scaled version of the transmitted signal $n(\tau)$,

$$r(\tau) = A(\theta, \beta) g\left(\tau - \frac{2R}{c}\right) \exp\left(j2\pi\nu_0\left(\tau - \frac{2R}{c}\right)\right), \tag{2.2}$$

where c represents the speed of light, and a round-trip time delay of $2R/c$ has been introduced. The received signal is multiplied by a positive amplitude factor A, determined by the target's reflectivity as well as the elevation angle θ and azimuth angle β to the target, which in turn dictates the antenna gain applied. Next, the signal is processed by a typical chain of RF downconversion and intermediate frequency bandpass filtering in order to strip off the carrier frequency [41] and obtain the target echo signal $e(t)$:

$$e(\tau) = A(\theta, \beta) g\left(\tau - \frac{2R}{c}\right) \exp\left(-j\frac{4\pi R}{\lambda}\right), \tag{2.3}$$

where λ is the carrier wavelength of the signal, related to the carrier frequency by $\lambda = c/\nu_0$. The shape of pulse envelope $g(\tau)$ determines the range resolution of the radar, where resolution is defined as the ability to separate two scatterers located at slightly different ranges [73]. Ideally, $g(\tau)$ should approach an impulse function, but practical limits on the bandwidth of the radar will limit the resolution. For improved signal-to-noise ratios (SNRs) it is desirable to use the radar bandwidth B_ν uniformly such that

$$|G(\nu)| \propto \text{rect}(\nu/B_\nu), \tag{2.4}$$

where $G(\nu)$ is the Fourier transform of $g(\tau)$, $|G(\nu)|$ is its absolute value, and the

rectangular function is defined as:

$$\text{rect}(x) = \begin{cases} 1 & \text{for } |x| \leq 1/2 \\ 0 & \text{for } |x| > 1/2. \end{cases}$$

The time-domain function fulfilling the requirement of equation 2.4 is $g(\tau) = \text{sinc}(\tau B_\nu)$. If range resolution is defined as the half-power (-3 dB) width of $g(\tau)$, then the resolution in metres ρ_{res} is approximately

$$\rho_{\text{res}} = 0.886 \frac{c}{2B_\nu}. \tag{2.5}$$

However, in order to avoid the practical difficulties in transmitting pulses with a high peak power, usually longer pulses are generated instead of narrow sinc-functions. The most common pulse coding is the chirp function with envelope:

$$g(\tau) = \exp(j\pi a\tau^2)\text{rect}\left(\frac{\tau a}{B_\nu}\right), \tag{2.6}$$

where a is the frequency rate. The instantaneous phase of the chirp is $a\pi\tau^2$, and thus the phase rate of change or frequency is $2a\pi\tau$, which is linear in τ, such that the chirp is also known as a linear frequency modulated (LFM) pulse. The chirp can be compressed into a sinc-function through cross-correlation with a chirp of the same frequency rate a, leading to a range resolution given in equation 2.5 [73]. This cross-correlation operation is also termed matched filtering or range compression.

A single radar LFM pulse after range compression can thus be represented by a simplified version of equation 2.3:

$$e(\tau) = A(\theta, \beta)\text{sinc}(\tau B_\nu) \exp\left(-j\frac{4\pi R}{\lambda}\right), \tag{2.7}$$

where the pulse bandwidth B_ν is determined by multiplying the frequency rate a (in units of Hz/s) by the duration of the pulse. A series of such pulses form the signal received from a point target through azimuthal slow-time (represented by the variable t). The amplitude of the response will change through t as the sensor advances in the along-track direction, changing the direction of arrival of the target signal (where this

direction is typically represented by the so-called directional cosine $u(t)$). The range to the target will also be dependent upon azimuthal slow-time as the radar sweeps by.

The target energy for each pulse in the range dimension is concentrated along the peak of the sinc function from equation 2.7. Extracting the target signal along these peaks for each pulse, and assuming that the target is in the beam of the antenna for duration T seconds gives the following target signal $s(t)$ after pulse compression:

$$s(t) = A(u(t)) \ \exp\left(-j\frac{4\pi R(t)}{\lambda}\right) \ \text{rect}\left(\frac{t}{T}\right). \tag{2.8}$$

Following range compression, the signal is corrected for range migration, which - to a first approximation - consists of a linear term (known as range walk) and a quadratic term (known as range curvature). Range walk occurs if the antenna beam centre is oriented off-broadside (i.e. squinted) [63]. Range walk may also occur in the presence of target motion, although this portion of range walk is not corrected at this time. Range curvature occurs if the range to a stationary target changes by more than one range resolution cell over the observation interval, and is of greatest concern for long-range systems such as spaceborne SARs [63]. Further information on the correction of range migration is available in [73, 87].

Next the signal is compressed in azimuth to form the SAR image. It is azimuth compression which separates real aperture radar from synthetic aperture radar. A real aperture radar has an azimuthal resolution proportional to the beamwidth, and thus an impractically large antenna is required to create a narrow beam for fine azimuth resolution [16, 63]. Synthetic aperture radar uses a wide beam to collect the returns from multiple pulses, and then synthesizes a narrow beam by filtering the array of pulses after data collection [78]. Moving targets require a slightly different filter function than stationary targets in order to obtain a properly focused image, although the matched filtering principle is the same. Further details on all steps of the SAR image formation process and algorithms for focusing stationary targets are provided in [9, 13, 29, 73, 87].

2.2 Classic MTI

SAR processing was originally developed to image the stationary world [37]. When conventional processing (as described in section 2.1) is applied to SAR data containing moving target returns, the targets inevitably appear smeared and defocused in the image. However, it has been only relatively recently that researchers have combined both SAR and GMTI capabilities to simultaneously form images of the terrain and to detect, estimate motion parameters, and focus ground moving targets.

Prior to SAR-GMTI were MTI (moving-target indication) ground systems, which did not form images, but were used only to detect moving targets. The purpose of these surface systems was to reject any signals from fixed or slow-moving scatterers such as buildings, hills, trees, sea and rain, and retain, for detection or display, any signals from moving targets such as aircraft [76]. Consecutive radar pulses were compared, and if the reflection times to a scatterer changed between pulses, it was a potential moving target.

The basic principle behind both MTI and GMTI is to utilize the Doppler shift imparted on a reflected radar signal in order to distinguish moving targets from fixed ones [76]. The Doppler shift is related to the velocity of the target in the across-track (or range) direction. The first airborne MTI systems grew out of airborne early-warning radars developed by the U.S. Navy to detect low-flying aircraft approaching forces below. Moving the radars from the ground to an airborne platform greatly increased the available coverage area, although the high platform altitude, mobility, and speed, as well as restrictions on size, weight, and power consumption of the radar presented new challenges to the designers of MTI systems [84]. Additional complications arose in the airborne scenario (compared to the ground scenario) since the clutter collected by the radar changes over time, thus hindering the ability to detect moving targets.

Classical airborne MTI assumes that the Doppler shift of a moving target may be observable directly in each return signal [62]. While the range bandwidth of a SAR

is generally too large to observe the Doppler shift, the azimuthal bandwidth may be small enough such that the shift due to target motion displaces the signal's Doppler outside the clutter bandwidth, and the presence of the target becomes evident (see Figure 2.1). Whether or not one can detect moving targets using a single-channel MTI

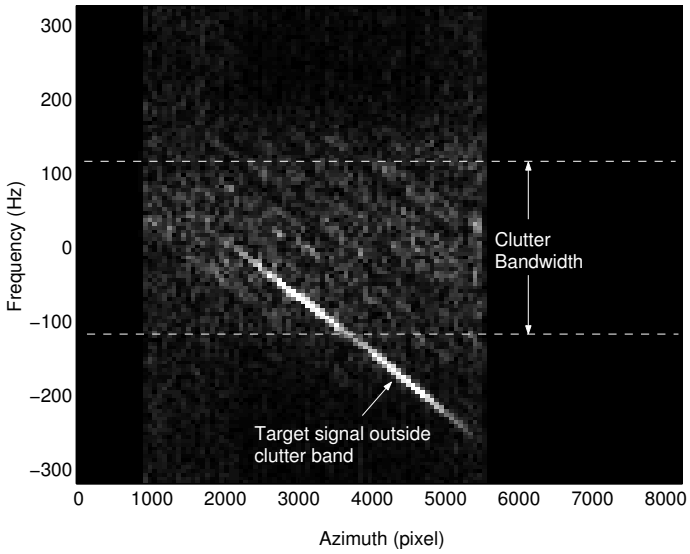

Figure 2.1: Doppler frequency of a moving target shifted out of the clutter bandwidth, enabling its detection. These data were collected using an airborne platform with a pulse repetition frequency of 600 Hz (corresponding to a frequency band of ± 300 Hz) and a clutter bandwidth of ± 116 Hz. Courtesy of Shen Chiu, DRDC Ottawa [19].

system depends on the pulse repetition frequency (PRF), the antenna beamwidth (which in turn determines the clutter spectral width), and the target velocities of interest.

The basic limitation of single-channel MTI is that the moving target Doppler shift must be greater than the clutter Doppler spectrum width [62], such that a portion of the target signal falls outside of the clutter background and may be detected. This is achieved using a high PRF and a narrow azimuth antenna beamwidth [54]. However, this method has several shortcomings, including difficulties in detecting targets with small across-track velocity components (and therefore small Doppler shifts) since the

target spectra will be superimposed upon the clutter spectra [4]. The small azimuth bandwidth precludes the formation of an image with satisfactory resolution. As well, there is an uncertainty in the azimuth position of the target, since a measure of the Doppler shift alone is insufficient to evaluate the target azimuth position with respect to the fixed ground [6]. Additionally, the high PRF reduces the unambiguous swath width and increases the required data recording rates. In the spaceborne case, the clutter bandwidth is usually larger than in airborne scenarios, such that even higher PRFs provide only a small clutter-free spectral region and clutter cancellation becomes essential.

With only one antenna available, the problem is that Doppler filtering must be used to remove undesired contributions from the clutter [6]. Traditional MTI may be used for applications in which targets move sufficiently fast such that their Doppler spectra are distinct from that of the clutter [60]. However, in modern-day GMTI, we wish to detect slowly moving ground targets in which the Doppler shift is not necessarily separated from the clutter. This is particularly important in spaceborne systems and airborne systems with wide beams, where nearly all moving targets are obscured by the clutter. With traditional MTI systems giving unsatisfactory performance, array techniques using multiple antennae were developed [60].

2.3 Multi-aperture GMTI

It is difficult to detect, focus, and estimate the motion parameters of moving targets using conventional SAR systems operating with a single antenna [67]. A significant body of research (e.g. [54, 55, 66, 79, 93]) advocates the use of a radar system with two or more antennae displaced in the along-track direction for performing GMTI.

Multiple apertures provide an additional degree of freedom with which unwanted clutter may be suppressed [57]. In single-channel SAR data, there is an ambiguity in the Doppler signature of a scatterer since the Doppler shift could be due to the object's position in the radar beam, or to its across-track velocity component. To

resolve this ambiguity, multiple channels are required [92].

Of particular interest is the dual-antenna case, since most operational and near-future airborne and spaceborne GMTI systems are limited to two channels for financial and practical reasons. Examples of existing and future dual-channel systems include Environment Canada's CV 580 SAR, the Canadian RADARSAT-2 satellite (to be launched in spring 2005 [51]), and the German TerraSAR-X satellite (with a launch date of April 2006 [91]). The use of additional phase centres (such as three or four antenna elements and phased array systems) can eliminate velocity and azimuth-location ambiguities [20, 22]. However, due to limited resources, most existing and near-future SAR systems are restricted to two apertures [36].

In subsequent sections the theoretical range compressed signals for a dual-channel airborne SAR are derived, and GMTI detection and estimation techniques employing multiple antennae are described.

2.3.1 Range compressed signal

This section proposes a deterministic model for the echoes backscattered from a moving point target and received by an antenna array with two elements. This model provides the basis for deriving a processing scheme to detect and focus SAR data containing moving targets, and more specifically for determining the effects of acceleration on the received and processed signal data.

The range compressed signals are derived for a SAR on an airborne platform only. The spaceborne expressions are similar, but additional factors such as earth curvature and earth rotation must be taken into account [65]. A conventional range and azimuth co-ordinate system is assumed in which the azimuth direction is taken to be parallel to the motion of the radar, and range is perpendicular to the motion of the radar. An illustration of the radar-target geometry is given in Figure 2.2. It is assumed that the radar transmitter on board the aircraft moves with constant velocity v_a along the x-axis (the azimuth axis, which crosses the range or y-axis at broadside time t=0).

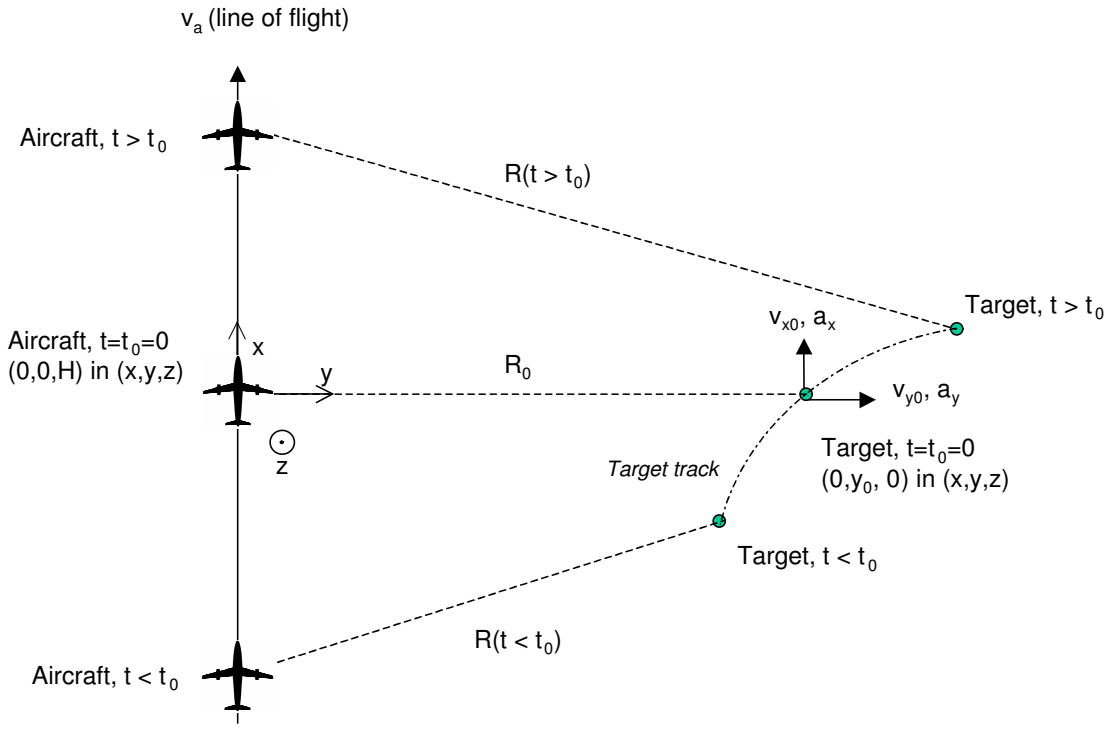

Figure 2.2: Top-down view of antenna and accelerating target geometry for an airborne scenario. Along-track and across-track (ground) dimensions are given by the x and y axes, respectively. Elevation is given by the z axis (out of the page, origin at the Earth's surface). A point-target moves with velocities v_{x0} and v_{y0} at broadside time t=0 and accelerations a_x and a_y in the along-track and across-track directions. R_0 is the slant range at broadside, and $R(t)$ represents the range from the radar to the target at any time t.

The z-axis is normal to the flat Earth's surface and represents the height above the ground. The radar is side-looking with a fixed pointing angle orthogonal to the flight path (i.e. no squint) and fixed altitude H. Radar pulses are transmitted at regular intervals given by the PRF, represented as f_{PRF} in mathematical formulae. A point target is assumed to be at the (x, y, z) position $(0, y_0, 0)$ at t=0 and to move with velocity components v_{x0} and v_{y0} at broadside and acceleration components a_x and a_y (which may or may not be time-varying) along the x- and y-axes, respectively. The target's height is assumed to be zero over the entire observation period, and the target is assumed to be non-rotating. $R_0 = \sqrt{y_0^2 + H^2}$ is the slant range at t=0 and $R(t)$ represents the range from the radar to the target at any time t.

General range equation

The equation for the range to an accelerating point target from the radar platform (through slow-time t) is given as:

$$R(t) = \sqrt{\left(v_{x0}t + \frac{a_{x0}}{2}t^2 + \frac{\dot{a}_{x0}}{6}t^3 - v_a t\right)^2 + \left(y_0 + v_{y0}t + \frac{a_{y0}}{2}t^2 + \frac{\dot{a}_{y0}}{6}t^3\right)^2 + H^2}, \tag{2.9}$$

where a_{x0} and a_{y0} are the across-track and along-track accelerations at broadside, and the dots indicate time derivatives of the target acceleration (higher-order acceleration terms are assumed to be negligible).

Because of the square root, this equation is difficult to work with analytically. Equation 2.9 may be written as a Taylor series expansion about broadside time t=0:

$$R(t) \simeq R(0) \; + \; \frac{1}{1!}R'(t)\bigg|_{t=0} t \; + \; \frac{1}{2!}R''(t)\bigg|_{t=0} t^2 \; + \; \frac{1}{3!}R'''(t)\bigg|_{t=0} t^3 + O(t^4), \tag{2.10}$$

where $R^n(t)$ is the nth derivative of the range function evaluated at time t and $O(t^4)$ represents all terms of fourth-order and above. Evaluating equation 2.10, we have:

$$\begin{aligned} R(t) \;\; \simeq \;\; & R_0 + \frac{y_0 v_{y0}}{R_0}t + \frac{1}{2R_0}\left[(v_{x0} - v_a)^2 + v_{y0}^2\left(1 - \frac{y_0^2}{R_0^2}\right) + y_0 a_{y0}\right]t^2 \\ & + \frac{1}{2R_0}\left[v_{y0}a_{y0}\left(1 - \frac{y_0^2}{R_0^2}\right) + a_{x0}(v_{x0} - v_a) + \frac{y_0\;\dot{a}_{y0}}{3}\right]t^3, \end{aligned} \tag{2.11}$$

where cubic terms on the order of $1/R_0^2$ and fourth and higher-order terms have been dropped.

Radar-target geometry

A dual-channel system is equipped with two antennae (labelled as the fore and aft antennae, respectively) which are separated by distance d (see Figure 2.3). The distance from the radar platform to the target is assumed to be large enough such that the far-field approximation may apply (i.e. such that the reflected signal or wavefront received at antenna 1 (fore) is parallel to that received at antenna 2 (aft)). At any time t, the range from the fore antenna to the target $R_1(t)$ will be shorter or longer than the range from the aft antenna to the target $R_2(t)$ (except at broadside, at which time the ranges are the same under the far-field approximation). In order to process multi-aperture data, one must determine the relation between these ranges through time.

Channel-specific range equation

It is assumed that at each $(1/f_{\mathrm{PRF}})$ second interval, a radar pulse is transmitted from the fore antenna, backscattered from a single ground point scatterer, received by each antenna, and processed by a typical chain of RF downconversion, intermediate frequency bandpass filtering, range compression, range migration compensation, and digital sampling above the Nyquist rate [41].

Slightly modifying equation 2.8 from section 2.1, the range-compressed target signal $s_i(t)$ for the i^{th} receiving channel can be expressed in terms of the range history through time using the following model [35]:

$$s_i(t) = A_i(u_i(t))\ \exp\left(-jkR_i^{2-\mathrm{way}}(t)\right)\ \mathrm{rect}\left(\frac{t}{T}\right), \tag{2.12}$$

where $A_i(u)$ is the magnitude of the i^{th} channel, $u_i(t)$ is the directional cosine from the i^{th} antenna to the moving target on the ground, $R_i^{2-\mathrm{way}}(t)$ is the range from the transmitting antenna to the moving target and back to the i^{th} antenna, k is

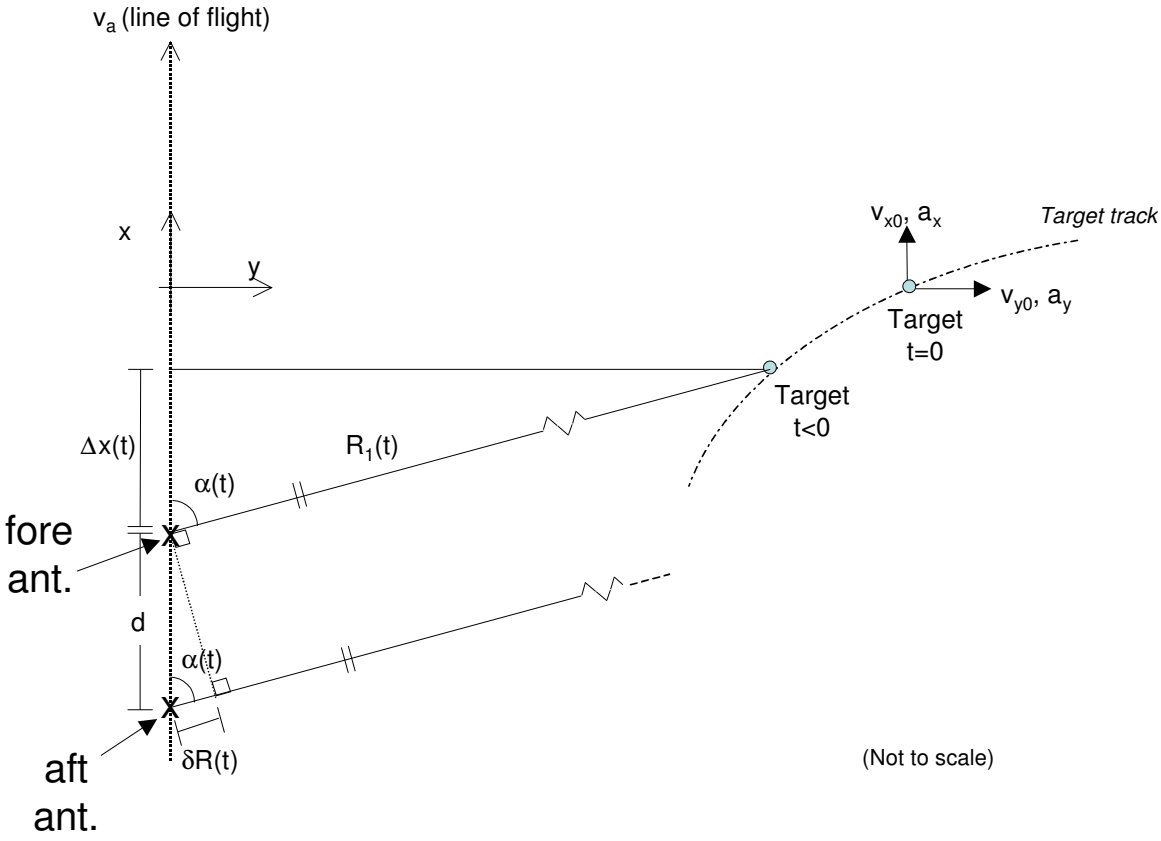

Figure 2.3: Top-down view of antenna and target geometry for two-channel data collection. Along-track and across-track (ground) dimensions are given by the x and y axes, respectively. A point-target moves with velocities v_{x0} and v_{y0} at broadside and accelerations a_x and a_y in the along-track and across-track directions. The fore and aft antenna locations are denoted by 'x's, and are separated by distance d. $R_1(t)$ represents the range from the fore antenna to the target at any time t. The distance along the x-direction from the fore antenna to the target is given by $\Delta x(t)$. Note that for airborne geometries, d is typically less than a metre whereas $\Delta x(t)$ may be hundreds of metres, and thus the image is not to scale. The difference between the range from the fore antenna to the target and the aft antenna to the target is represented by $\delta R(t)$, and the angle between the antenna-target line of sight and the radar line of flight is given by $\alpha(t)$.

the wave number ($2\pi/\lambda$), and T is the synthetic aperture length in units of time. The magnitude variable $A_i(u)$ includes the two-way antenna gain pattern, target reflectivity, and spherical propagation losses. It is assumed that the RCS (radar cross section) of the point target remains constant with viewing angle over the course of the synthetic aperture. Here the signals have been represented in continuous time, although for a discrete representation, t must simply be replaced with samples taken at every pulse repetition interval (n/f_{PRF}) for integer n.

Let the difference between the range from the target to the fore antenna and the range from the target to the aft antenna be $\delta R(t)$, which varies with time. Thus, let:

$$R_2(t) = R_1(t) + \delta R(t), \tag{2.13}$$

where from trigonometry and Figure 2.3,

$$\delta R(t) = d\cos(\alpha(t)), \tag{2.14}$$

where $\alpha(t)$ is the angle between the antenna-target line of sight and the flight direction (i.e. the x-axis). The term $\cos(\alpha(t))$ is often referred to as the directional cosine $u(t)$. This term may be written as a function of the range $R_1(t)$ and the separation in the x-direction between the target and fore antenna of the radar platform $\Delta x(t)$. Thus the range difference becomes

$$\begin{aligned} \delta R(t) &= d\frac{\Delta x(t)}{R_1(t)} \\ &= d\frac{(v_{x0} - v_a)t + \frac{1}{2}a_{x0}t^2 + \frac{1}{6}\dot{a}_{x0}t^3}{R_1(t)}. \end{aligned} \tag{2.15}$$

Performing a Taylor expansion of $\delta R(t)$ about t=0 to the first-order (the second-order term is several thousand times smaller than the first-order term for typical airborne parameters, and a hundred thousand times smaller for spaceborne parameters) simplifies the expression to the following:

$$\delta R(t) \simeq d\frac{(v_{x0} - v_a)t}{R_0}, \tag{2.16}$$

where $R_1(0) = R_2(0) = R_0$. Radar parameters typical of the airborne CV 580 system and anticipated parameters for the spaceborne RADARSAT-2 system are provided in section 3.2 for reference.

Equations 2.13 and 2.16 express the aft antenna to target distance $R_2(t)$ as a function of $R_1(t)$. However, several of the multi-aperture GMTI techniques used for detection and parameter estimation (including DPCA and ATI) require channel registration prior to further processing. Registration aligns the channels such that the two antenna phase centres are at the same spatial location at different times. One can select a PRF in accordance with the radar platform speed and physical separation distance of the antennae such that the antenna phase centres for consecutive pulses coincide. However, as will be discussed in section 2.3.2, such restrictions on the PRF are unnecessary, and channel registration may be performed by interpolating the aft samples at non-sampled times.

The effective antenna phase centre is determined by the two-way range to the target. Since the fore antenna both transmits and receives, the two-way range $R_{\text{fore}}^{2-\text{way}}(t)$ is simply twice the range equation previously derived:

$$R_{\text{fore}}^{2-\text{way}}(t) = 2R_1(t). \tag{2.17}$$

However, the aft aperture, which is receive-only, receives radar pulses transmitted from the fore aperture, such that the two-way range is:

$$\begin{aligned} R_{\text{aft}}^{2-\text{way}}(t) &= R_1(t) + R_2(t) \\ &= 2R_1(t) + \delta R(t). \end{aligned} \tag{2.18}$$

For any sampled time t' available in the fore channel, the range to the target at time $t' + d/(2v_a)$ must be determined for the aft data in order to line up the channels. Thus, the registered aft channel can be expressed as the following:

$$R_{\text{aft reg.}}^{2-\text{way}}(t) = 2R_1\left(t + \frac{d}{2v_a}\right) + \delta R\left(t + \frac{d}{2v_a}\right). \tag{2.19}$$

Using the third-order Taylor expansion for $R_1(t)$ (equation 2.11) and the Taylor expansion for $\delta R(t)$ (equation 2.16) this may be rewritten as:

$$\begin{aligned} R^{2-\text{way}}_{\text{aft reg.}}(t) \;\simeq\; & 2\Bigg[R_0 + \frac{y_0 v_{y0}}{R_0}\left(t + \frac{d}{2v_a}\right) \\ & + \frac{1}{2R_0}\left[(v_{x0}-v_a)^2 + v_{y0}^2\left(1 - \frac{y_0^2}{R_0^2}\right) + y_0 a_{y0}\right]\left(t + \frac{d}{2v_a}\right)^2 \\ & + \frac{1}{2R_0}\left[v_{y0}a_{y0}\left(1 - \frac{y_0^2}{R_0^2}\right) + a_{x0}(v_{x0}-v_a) + \frac{y_0\ \dot{a}_{y0}}{3}\right]\left(t + \frac{d}{2v_a}\right)^3\Bigg] \\ & + d\frac{(v_{x0}-v_a)\left(t + \frac{d}{2v_a}\right)}{R_0}. \end{aligned} \tag{2.20}$$

Rearranging equation 2.20, we can express $R^{2-\text{way}}_{\text{aft reg.}}(t)$ as a function of $R_1(t)$, with leftover terms represented by $g(t)$:

$$R^{2-\text{way}}_{\text{aft reg.}}(t) \simeq 2R_1(t) + g(t), \tag{2.21}$$

where

$$\begin{aligned} R_1(t) = R_0 + \frac{y_0 v_{y0}}{R_0}t + \frac{1}{2R_0}\left[(v_{x0}-v_a)^2 + v_{y0}^2\left(1 - \frac{y_0^2}{R_0^2}\right) + y_0 a_{y0}\right]t^2 \\ + \frac{1}{2R_0}\left[v_{y0}a_{y0}\left(1 - \frac{y_0^2}{R_0^2}\right) + a_{x0}(v_{x0}-v_a) + \frac{y_0\ \dot{a}_{y0}}{3}\right]t^3, \end{aligned} \tag{2.22}$$

and

$$\begin{aligned} g(t) = & \frac{y_0 v_{y0}}{R_0}\frac{d}{v_a} \\ & + \frac{1}{R_0}\left[(v_{x0}-v_a)^2 + v_{y0}^2\left(1 - \frac{y_0^2}{R_0^2}\right) + y_0 a_{y0}\right]\left(\frac{d}{v_a}t + \frac{d^2}{4v_a^2}\right) \\ & + \frac{1}{R_0}\left[v_{y0}a_{y0}\left(1 - \frac{y_0^2}{R_0^2}\right) + a_{x0}(v_{x0}-v_a) + \frac{y_0\ \dot{a}_{y0}}{3}\right]\left(\frac{3d}{2v_a}t^2 + \frac{3d^2}{4v_a^2}t + \frac{d^3}{8v_a^3}\right) \\ & + d\frac{(v_{x0}-v_a)}{R_0}\left(t + \frac{d}{2v_a}\right). \end{aligned} \tag{2.23}$$

It can be verified that equation 2.21 behaves as expected for a stationary target, i.e. for a target with $[v_{x0}\ v_{y0}\ a_{x0}\ a_{y0}\ \dot{a}_{y0}]^T = \vec{0}$, where ^{T} denotes the transpose operator,

and the overhead arrow denotes a vector. If a target is stationary, the two-way range from the target to the aft antenna should be identical to that measured using the fore antenna $d/(2v_a)$ seconds earlier (i.e. $R^{2-\text{way}}_{\text{aft reg.}}(t) = R^{2-\text{way}}_{\text{fore}}(t)$) since nothing has moved. Substituting $[v_{x0}\ v_{y0}\ a_{x0}\ a_{y0}\ \dot{a}_{y0}]^T = \vec{0}$ into equation 2.21, $R^{2-\text{way}}_{\text{aft reg.}}(t) = 2R_1(t) - \frac{d^2}{2R_0}$ for stationary targets, where $\frac{d^2}{2R_0}$ is on the order of 1×10^{-5} m for both the RADARSAT-2 spaceborne and CV 580 airborne geometries (and is thus negligible at less than 0.01% of a wavelength). This residual is due to the assumption of the far-field condition.

Assuming that at each PRI (pulse repetition interval, every $1/f_{\text{PRF}}$ seconds) the radar transmits a pulse with the fore antenna and receives on both channels, the signals are given as:

$$\begin{aligned} s_1(t) &= A_1(t) \exp\left(-jk[R^{2-\text{way}}_{\text{fore}}(t)]\right) \text{rect}\left(\frac{t}{T}\right) \qquad (2.24) \\ &= A_1(t) \exp\left(-2jkR_1(t)\right) \text{rect}\left(\frac{t}{T}\right) \\ s_2(t) &= A_2(t) \exp\left(-jk[R^{2-\text{way}}_{\text{aft reg.}}(t)]\right) \text{rect}\left(\frac{t}{T}\right) \qquad (2.25) \\ &= A_2(t) \exp\left(-jk[2R_1(t) + g(t)]\right) \text{rect}\left(\frac{t}{T}\right). \end{aligned}$$

2.3.2 Multi-aperture GMTI techniques

Starting from a stationary-scene assumption, the challenge in SAR-GMTI is to detect moving targets, estimate their velocities, and obtain a focused image of the targets and the surrounding terrain [49]. Many approaches exist to identify and measure moving targets using multi-aperture SAR data including the DPCA method for detection, and ATI for across-track velocity estimation. The history and methodology for each technique is briefly described in subsequent sections. Additional techniques for detection and estimation are also discussed, including methods making use of the time-frequency domain.

Displaced Phase Centre Antenna (DPCA)

A common method of clutter suppression for GMTI is the displaced phase centre antenna technique. Essentially, DPCA is the difference of the complex SAR data from two (co-registered) channels [35]:

$$\mathrm{DPCA}(t) = s_1(t) - s_2(t). \tag{2.26}$$

In ground-based radars, stationary interference produces identical responses in successive received pulses since neither the antenna nor the clutter moves between measurements [39]. Thus, clutter can be rejected by subtracting consecutive measurements, and any energy remaining after subtraction will be due to noise or to moving targets. The DPCA technique is an attempt to apply this method of clutter suppression to a radar on a moving platform.

DPCA requires the use of multiple antennae displaced along the radar platform's direction of travel. In classical DPCA, the speed of the radar and the physical separation distance between antennae determines the allowable PRF such that the antenna phase centres for consecutive pulses are at the same spatial location [39]. Classical DPCA for two antennae is demonstrated in Figure 2.4, where the radar parameters are selected such that for two consecutive sampling times, the antennae provide identical views of the illuminated field [66]. A difference image of the two channels isolates moving targets since stationary objects will appear at the same position in each image, whereas moving targets will have displaced in the time interval between observations, allowing for the detection of slow moving targets that are otherwise masked by the clutter [93].

The requirement that the antennae spatially coincide at subsequent sampling times sets severe limitations on the PRF [21]. The PRF has a large influence on radar performance since high PRFs allow a greater degree of oversampling and make available a region in the Doppler domain not occupied by clutter. However, the maximum unambiguous swath width is inversely proportional to the PRF, and thus an increase in the PRF reduces the available swath and increases data rates [4]. It would

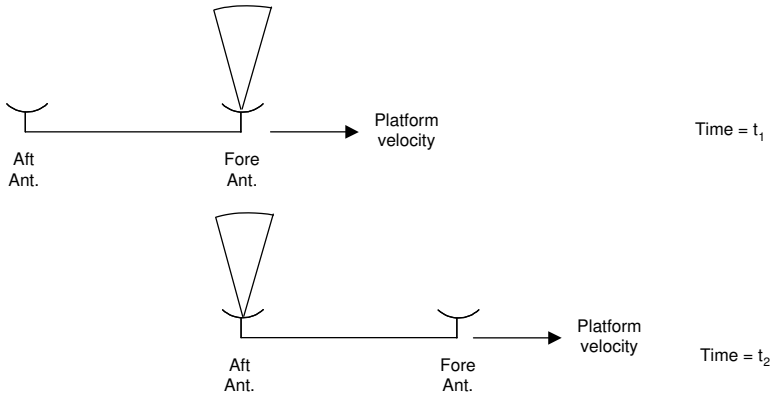

Figure 2.4: Classical DPCA geometry, in which the phase centres of the fore and aft antennae coincide for subsequent epochs t_1 and t_2. Adapted from [55].

be convenient to be able to choose a PRF suitable to the speed of the targets being imaged and to the desired swath widths of the application.

Numerous papers (e.g. [22, 60, 92]) have shown that such restrictions on the PRF are unnecessary, as the data may be resampled in the along-track direction to synthesize the arrangement of Figure 2.4 as long as the PRF is at or above the Nyquist limit. This resampling process is commonly referred to as 'channel registration'.

DPCA with two antennae can be regarded as an approximation of the optimal clutter suppression achieved using STAP (space-time adaptive processing) [35]. Unlike STAP, DPCA does not require estimation of the clutter plus noise covariance matrix at every sample, and is thus considerably simpler and less computationally intensive to implement. However, significant performance improvements may be achieved with STAP including more robust clutter suppression and a mechanism for dealing with jammers [39]. Further discussions on optimum processing using STAP may be found in [24, 26, 35, 37, 74].

With an ideal noise-free radar and no internal clutter motion (ICM), stationary targets and ground clutter are completely removed after DPCA [50]. However, for real systems, clutter suppression is limited by the noise floor of the radar, ICM (from

time decorrelation of the clutter), fine registration errors between channels, and phase and amplitude differences in the two receiver chains. In the complex plane, stationary scene elements after DPCA map to a circular cluster symmetrically distributed about the origin, i.e. with a uniform phase distribution [49]. The magnitude of these elements determines the minimum detectable velocity of scene targets, below which the DPCA magnitude of moving targets will be indistinguishable from the noise. Moving target detection using DPCA is further discussed in Chapter 4.

Along-track interferometry (ATI)

Along-track interferometry is another multi-aperture technique used in GMTI to detect and measure target motion. Like DPCA, ATI requires multiple antennae displaced in the along-track direction (i.e. the radar's direction of travel) such that the channels observe the same scene at different times. For a two-channel SAR system, the ATI signal may be computed by multiplying the signal from one channel by the complex conjugate of the second (registered) channel:

$$\mathrm{ATI}(t) = s_1(t)s_2^*(t) = |s_1(t)||s_2(t)| \ \exp\left(j[\varphi_1(t) - \varphi_2(t)]\right) \tag{2.27}$$

where * denotes complex conjugation, and $\varphi_1(t)$ and $\varphi_2(t)$ are the phases of the first and second channel, respectively [49]. The phase of the ATI signal is related to the target motion parameters (although dominated by the across-track velocity v_{y0}) and may thus be used to estimate v_{y0}. For stationary terrain, the fore and aft channel signals are identical and the ATI phase is zero.

Early advances in SAR interferometry including the history of ATI are described in [72]. The first application of along-track interferometry was reported by Goldstein and Zebker who used ATI to measure tidal currents by imaging the ocean surface at multiple times [38]. An airborne system with 0.1 s between fore and aft observations was able to measure tidal motion in the San Francisco bay area with an accuracy of several cm/s. The technique was named 'along-track interferometry' due to the arrangement of the two antennae along the flight track on a single platform. Although

primarily used for measuring sea surface currents in the past ([71, 72]), SAR-ATI is also applicable for ground moving target detection and estimation [33, 49, 59].

In the interferometric SAR system concept, radar pulses are transmitted from one antenna, and echoes are received by two antennae [72]. The phase of a single SAR image is random, such that one cannot extract any useful information from the phase alone [20]. However, by coherently combining the signals from two channels, interferometric phase differences (the interferogram) may be formed. These phase differences are related to a change in the geometric path length to the target between observations. With knowledge of the interferometer geometry (including the antenna separation and local incidence angle to the target), phase differences can be converted into target/surface velocities if the antennae are separated in the along-track direction, or converted into surface elevations if the antennae are separated in the across-track direction (such as in traditional SAR interferometry) [72].

ATI phase is subject to several ambiguities which affect velocity estimation. The various types of ambiguities and methods of resolving them are further discussed in Appendix B.1. There are also several potential error sources in the ATI phase including clutter contamination, systematic errors in the differential phase, and phase noise. These influences on ATI are investigated in Appendix B.2.

Detection and parameter estimation

There is a wide variation in detection and estimation techniques available for GMTI in addition to DPCA and ATI methods. A number of detection and estimation algorithms have been proposed in the last decade, some of which are described below. However, DPCA and ATI are established and relatively simple techniques, which is why these methods were selected with which to evaluate the effects of target acceleration.

Detecting a moving target requires the ability to distinguish between targets and stationary clutter. This may be achieved by searching for targets in clutter-free regions after some transformation of the signal data, or by enhancing the signal-

to-clutter ratio by suppressing the clutter [78]. As previously mentioned, STAP techniques are available for the combined spatial-temporal filtering of data, giving improved signal-to-clutter ratios. DPCA is the optimal linear filter for detecting a target in homogeneous clutter [43], although an increasing amount of research is examining target detection in extremely heterogeneous clutter environments of interest such as urban areas. Sikaneta et al. [78, 79] have proposed several target detectors based on an eigen-decomposition of the multi-channel covariance matrix. Comparisons with DPCA and ATI detectors indicate improved performance with these new eigen-based methods (including the so-called hyperbolic detector) in heterogeneous terrain.

Estimation of the velocity vector can be performed incoherently with a single channel or coherently (with increased reliability) using two or more apertures [79]. In both cases, range walk, azimuth displacement, azimuth smear, and defocusing effects may provide non-coherent evidence of target motion [35]. Several multi-channel algorithms make use of defocusing effects for estimation of along-track velocity (e.g. [36, 82]); this method is further described in section 5.1.

Sub-aperture techniques may also be used for both single and multi-aperture velocity estimation (e.g. [42, 47]). This involves the filtering of the SAR signal spectrum into overlapping sub-bands in the azimuth direction, where each sub-band corresponds to a portion of the radar's azimuth illumination beam [49]. A sequence of images may be generated, one from each sub-beam, and moving targets (whose locations shift from one sub-beam to the next) may be identified and their velocities estimated from the magnitude of the shift. Single aperture techniques can be used to provide a coarse estimation of target velocity, but generally only for sufficiently bright (i.e. high RCS), and sufficiently fast targets.

The majority of these detection and estimation techniques are applied to SAR signals which have been range compressed. Some methods (such as certain variations of STAP or the sub-aperture techniques) make use of range compressed SAR

data transformed into the Doppler frequency domain using a fast Fourier transform (FFT). However, in addition to the one-dimensional analyzes of time series or Fourier transformed data, one can also examine the two-dimensional time-frequency (TF) space, which may give additional insight for moving target detection and parameter estimation. Barbarossa [5] was one of the first to propose the use of the Wigner-Ville distribution (a TF transform) for detecting and focusing moving objects. The advantages of joint time-frequency analysis are described in section 2.4.2, and additional uses of TF analysis for investigating target acceleration are described in Chapter 7.

Various focusing algorithms for GMTI have not been described here, since generally they all involve the creation of a reference filter which is cross-correlated with the received signal to obtain the azimuth compressed target response. The available algorithms vary according to the approximations and assumptions made, processing speed, and shortcuts [90]. Details on focusing targets with various motion parameters is described in Chapter 4.

It is extremely difficult to quantify the expected accuracy in detection, parameter estimation and focusing available using each technique. Accurate statistical models of the clutter and target are required, although it is challenging to emulate realistic heterogeneous clutter scenarios. Elaborate statistical modelling was beyond the scope of this research, which is why expected accuracies of the detection, parameter estimation and focusing algorithms are not provided.

2.4 Time-frequency analysis

2.4.1 Introduction

A time series representation is usually the first and most natural description of a signal [2]. However, in order to extract the information present and use it to its full potential, one may analyze the signal using various data representations. The Fourier transform is the basis of a wide range of signal processing techniques used in radar

data analysis [85] and is given by the following:

$$S(f) = \int_{-\infty}^{\infty} s(t) \exp(-j2\pi ft)dt, \tag{2.28}$$

where $s(t)$ is the input signal, $S(f)$ is the Fourier transformed signal, and f is frequency. Throughout, capital letters indicate the Fourier transforms of the corresponding time-domain functions. The Fourier transform indicates which frequency components are contained in the signal, but does not reveal how frequencies change with time [16].

In many engineering applications such as radar, sonar, and telecommunications, the signals under consideration are known to be non-stationary, that is, their spectral contents vary with time [8]. In order to derive information regarding the *time localization* of spectral components, a representation of the signal data in terms of both time and frequency is needed. To this end, the field of time-frequency analysis was developed. In recent decades, numerous time-frequency distributions have been put forth mapping a one-dimensional time series into a two-dimensional time and frequency space.

2.4.2 Utility of TF analysis

Time-frequency analysis is a powerful tool which may be used in signal detection, characterization, and processing [85]. Understanding the Doppler frequency shift induced in SAR signal returns is essential in appreciating the utility of TF analysis for GMTI applications.

Due to radar platform motion, each scatterer on the ground reflects an echo with a Doppler shift proportional to the projection of the platform velocity along the line-of-sight (the line passing through the radar and the scattering element) [6]. At broadside, this line-of-sight velocity is zero, and thus all stationary scatterers have a zero Doppler centroid (when observed by a side-looking radar). If a scatterer is moving however, an additional Doppler shift is introduced which may vary from pulse to pulse, changing the Doppler centroid and Doppler rate. The echo from the ground will possess a

certain Doppler bandwidth proportional to the antenna beamwidth for each pulse, whereas the target has a narrow bandwidth for each pulse although its mean Doppler frequency varies through time (i.e. is non-stationary) [6].

One of the most important applications of TF analysis is estimating a signal's instantaneous Doppler frequency, particularly in the presence of white noise, since it allows exploitation of the different frequency behaviours between signal and noise [5]. Although the target has an extended Doppler bandwidth due to radar-target motion during the synthetic aperture, its instantaneous bandwidth is much smaller, such that a point target has zero instantaneous bandwidth [5]. Conversely, white noise has a large instantaneous bandwidth, and therefore a TF transform will concentrate signal energy along the target's instantaneous frequency, while dispersing noise amongst many frequencies.

In order to focus a target (i.e. perform azimuth compression) to obtain high azimuthal resolutions, one requires accurate knowledge of the relative motion between the radar and the target [7]. However, in some applications, this relative motion is not known to a sufficient accuracy (such as in airborne systems with poor inertial sensors) or the information is not available (such as when the target is moving). In these cases, one can estimate the motion-induced phase shift directly by integrating the instantaneous frequency estimated within the TF domain over time. This phase shift can then be used in a matched filter to achieve a focused image of the target (see Chapter 7).

Another advantage of TF analysis is that one can determine the instantaneous frequency without making any assumptions regarding its modulation through time. Conventional autofocusing techniques compensate only linear and quadratic phase shifts, whereas the TF approach allows estimation and compensation regardless of the phase structure [5]. While the conventional techniques may be sufficient to focus a target moving with constant velocity (possessing a nearly parabolic range-history), an accelerating target with non-zero along-track acceleration or time-varying across-

track acceleration will have a significant cubic term in its range-history (see equation 2.11), and will benefit from TF focusing methods.

2.4.3 Time-frequency transformations

The initial stage in any TF analysis is mapping the one-dimensional time series of data into the two-dimensional time-frequency domain. Many time-frequency distributions (or transforms) have been developed, each with their own advantages and drawbacks. Typically, TF transforms are separated into two categories: linear and quadratic [2]. Linear transforms are computationally efficient, but suffer from poor time-frequency resolution. Quadratic transforms, on the other hand, have improved resolution, but require increased computational power and introduce undesirable cross-terms if the input signal has multiple components. The general properties of linear and quadratic TF representations are further reviewed in subsequent sections.

Before taking the TF transform it is assumed that the radar signal data has been compressed in range but not azimuth. As well, to avoid issues accompanying multi-component signals and to maximize the signal-to-clutter ratio, clutter cancellation should be performed prior to taking the time-frequency transform. The problem of filtering radar data to cancel clutter returns has been extensively treated in the literature (e.g. [4, 26, 35, 49, 50, 94]). For dual-channel SAR-GMTI data, DPCA as described in section 2.3.2 is commonly used for clutter cancellation. Reliable detection, focusing, and parameter estimation in the TF domain requires the preliminary cancellation of the background clutter [4].

Linear TF transforms

Short-time Fourier transform (STFT) One of the simplest and most widely used methods of analyzing signals in the TF domain is the STFT [5, 85]. Essentially, the STFT breaks up a signal into small time segments, and applies the Fourier transform to each piece in order to determine the frequencies present in each segment [85]. To mathematically introduce time-dependency into the Fourier transform, a short

time analysis window $h(\tau - t)$ centred at time t may be added [85]:

$$\mathrm{STFT}_s(t, f) = \frac{1}{2\pi} \int_{-\infty}^{\infty} \exp(-j2\pi f\tau) s(\tau) h(\tau - t) d\tau, \tag{2.29}$$

where f is the frequency, and $s(\tau)$ is the input signal. Multiplication by the relatively short window $h(\tau - t)$ suppresses the signal outside a neighbourhood close to the analyzed time $t = \tau$, creating a local spectrum of the signal [2].

The problem is that the STFT demands a trade-off between time and frequency resolutions [2]; a high time resolution requires a short window $h(t)$, but high frequency resolution requires a narrow bandwidth filter (i.e. a long window $h(t)$). This constraint is known as the Heisenberg-Gabor inequality. Time resolution is fundamentally determined by the duration of the window function (denoted as Δt), and frequency resolution is determined by the bandwidth of the same window, lower-bounded by the reciprocal of the window duration (denoted B where $B = 1/\Delta t$). Thus, the time-bandwidth product (a measure of the joint TF resolution) is always greater than or equal to one (i.e. $\Delta t B \geq 1$) [2].

Additional linear TF transforms Additional linear TF transforms have been developed including the discrete or continuous wavelet transform [2], the S-transform [85], and the so-called 'adaptive' time-frequency transform [15].

Instead of employing a single analysis window $h(t)$ as in the STFT, these algorithms adapt the window function to the frequency of interest. Short windows are used at high frequencies (increasing the time resolution although degrading the frequency resolution) while long windows are used at low frequencies (increasing the frequency resolution while decreasing the time resolution). Like the STFT, these linear algorithms offer a compromise between time and frequency resolutions. Additional details regarding these transforms are available in [2, 15, 85].

Quadratic TF transforms

The linear transforms previously discussed decompose a signal into elementary components well-localized in time and frequency. Another approach to TF transforms

involves distributing the signal energy over the two variables of time and frequency [2]. The energy of a signal s (denoted E_s) can be computed by integrating the square of the signal or its Fourier transform [2]:

$$E_s = \int_{-\infty}^{\infty} |s(t)|^2 dt = \int_{-\infty}^{\infty} |S(f)|^2 df. \tag{2.30}$$

Since the energy E_s is a quadratic function of the signal, the TF energy distributions will also be quadratic representations of the signal. The goal is find a joint TF energy density $\rho_s(t, f)$ such that

$$E_s = \int_{-\infty}^{\infty} \int_{-\infty}^{\infty} \rho_s(t, f) dt \; df, \tag{2.31}$$

and

$$|S(f)|^2 = \int_{-\infty}^{\infty} \rho_s(t, f) dt \tag{2.32}$$

$$|s(t)|^2 = \int_{-\infty}^{\infty} \rho_s(t, f) df, \tag{2.33}$$

where energy densities fulfilling the equalities in equations 2.32 and 2.33 are said to satisfy the marginal conditions [2]. Cohen has described a general class of quadratic TF distributions for two input signals $s_1(t)$ and $s_2(t)$ by [67]:

$$C_{s_1 s_2}(t, f) = \int_{-\infty}^{\infty} \int_{-\infty}^{\infty} \int_{-\infty}^{\infty} \left[\exp(-j2\pi\nu t - j2\pi f\tau + j2\pi\nu u) g(\nu, \tau) \right. \tag{2.34}$$
$$\left. s_1\left(u + \frac{\tau}{2}\right) s_2^*\left(u - \frac{\tau}{2}\right) \right] du \; d\nu \; d\tau,$$

where C is the signal after transformation, and $g(\tau, \nu)$ is a two-dimensional kernel function. Certain choices of the kernel function will preserve the desired energy density properties, and all distributions in Cohen's class possess time and frequency covariance. This guarantees that shifts in time and frequency of the signal will result in shifts of the same amount in the TF plane [2]. Several of the most common quadratic transforms (also called bilinear or non-linear transforms) are described in subsequent sections.

Wigner-Ville distribution The Wigner-Ville distribution (WVD) is one member of the Cohen class which is a simple yet powerful tool to analyze the Doppler history of SAR signals [67]. Wigner originally developed the distribution for use in quantum mechanics in 1932, and it was introduced for signal analysis by Ville sixteen years later [85]. To obtain the Wigner-Ville distribution at a particular time, we add up pieces made from the product of the signal at a past time multiplied by the signal at a future time [85]. The continuous WVD of a signal is derived by using the all-pass kernel $g(\nu, \tau) = 1$ in equation 2.34 for $s_1(t) = s_2(t) = s(t)$ [67]:

$$\mathrm{WVD}_s(t, f) = \int_{-\infty}^{\infty} s\left(t + \frac{\tau}{2}\right) s^*\left(t - \frac{\tau}{2}\right) \exp(-j2\pi f\tau) d\tau. \tag{2.35}$$

The WVD can be regarded as the TF distribution offering the best resolution in the form of delta-pulses along the instantaneous frequency of a signal [61, 67]. Additionally, the lack of smoothing maximally conserves the information content of the signal [67]. The WVD is always real-valued, preserves time and frequency shifts, and satisfies the marginal properties from equations 2.32 and 2.33. A more thorough description of the properties of the WVD is offered in [2, 6, 67, 85].

One disadvantage is that problems arise in using the WVD for signals consisting of multiple components. Since it is a non-linear transformation, the WVD signal is not simply the sum of the WVD of each part. For instance, given a signal composed of two parts s_1 and s_2 such that

$$s = s_1 + s_2, \tag{2.36}$$

the spectrum of s is the sum of the Fourier transforms of each component:

$$S = S_1 + S_2. \tag{2.37}$$

However, the energy density (which is related to the WVD of the signal) is not the

sum of the energy densities of each part [85]:

$$\begin{aligned} |S|^2 &= |S_1 + S_2|^2 \\ &= |S_1|^2 + |S_2|^2 + 2\Re\{S_1^* S_2\} \\ &\neq |S_1|^2 + |S_2|^2, \end{aligned} \tag{2.38}$$

where the $\Re\{\cdot\}$ operation retains the real component of its argument.

The non-linearity of the WVD emphasizes the need to remove all clutter contributions to the signal prior to computing the TF transform. If clutter is not removed, even if the signal occupies a bandwidth well-separated from the clutter, the WVD cross-terms may obscure the target signal [6].

If the clutter is removed but the processed signal data contains multiple moving targets, cross-terms between these signals will still be present in the WVD. Generally, detection and tracking of the instantaneous frequency for multiple targets is completed by combining the WVD with the Hough transform [5, 15, 61]. The Hough transform is typically used for detecting straight lines in noisy imagery, although it may also be used to find higher-order polynomials (such as parabolas) [10] traced out by accelerating targets in the time-frequency domain.

Discrete WVD The SAR signals to be analyzed are generally discrete, and thus it is useful to examine the discretized version of the WVD. Re-writing the continuous WVD from equation 2.35 as

$$\mathrm{WVD}_s(t, f) = 2 \int_{-\infty}^{\infty} s\left(t + \tau\right) s^*\left(t - \tau\right) \exp(-j4\pi f\tau) d\tau, \tag{2.39}$$

and assuming $s(t)$ is sampled every Δt seconds, we obtain the discrete-time Wigner-Ville distribution:

$$\mathrm{WVD}_s(n\Delta t, f) = 2\Delta t \sum_{k=-\infty}^{\infty} s\left((n+k)\Delta t\right) s^*\left((n-k)\Delta t\right) \exp(-j4\pi f k), \tag{2.40}$$

where n and k are integers [2, 85]. The discrete WVD is periodic in frequency with period $1/(2\Delta t)$, whereas the Fourier transform of a Nyquist-sampled signal has a

period twice that amount at $1/\Delta t$. Thus, the discrete WVD may be affected by spectral aliasing [2]. However, an important advantage of the WVD is that it allows the recovery of a target's instantaneous frequency history even in the case of undersampling. Barbarossa explains that "the TF representation prevents superposition of spectrum replicas created by undersampling because, even if the replicas occupy the same bandwidth, they occur at different times" [5]. Ambiguities may still exist in the target frequency history due to undersampling, but the undersampling will not cause overlapping signal spectra in the TF domain.

Pseudo Wigner-Ville Distribution When computing the WVD at a certain time, the Wigner-Ville distribution weighs all signal values in the past and future equally. In practice, we may not be able to integrate from minus to plus infinity if we do not have knowledge of the quantity $s(t+\tau/2)s^*(t-\tau/2)$ for all possible τ [2]. As well, in determining the TF distribution for a time t, we may wish to emphasize the properties near the time of interest [85].

In these cases, a windowing function may be introduced into the WVD equation leading to a new distribution termed the 'pseudo WVD' or PWVD. The PWVD is defined as:

$$PWVD_s(t,f) = \int_{-\infty}^{\infty} h(\tau) s\left(t+\frac{\tau}{2}\right) s^*\left(t-\frac{\tau}{2}\right) \exp(-j2\pi f\tau) d\tau, \tag{2.41}$$

where $h(\tau)$ is a window function peaked around $\tau = 0$. This windowing operation is equivalent to smoothing in frequency, which can improve the estimation accuracy of the instantaneous frequency (IF) in the presence of noise [5]. The PWVD partially suppresses cross-terms from multi-component signals including interference terms between the target signal and noise. However, as a consequence of the windowing operation many of the properties of the WVD are lost such as fulfillment of the marginal conditions, and frequency resolution is also slightly degraded.

Additional quadratic TF distributions Beginning with the Wigner-Ville distribution, numerous quadratic TF transforms have been developed in an attempt to

improve the time-frequency resolution over that achievable with the STFT [52]. In addition to the pseudo WVD, the Choi-Williams and Cone kernel transforms have been proposed to attenuate interference effects and cross-terms in signals [2, 67]. However, like the PWVD, these techniques cause some loss in TF resolution and increase the computational cost compared with the WVD. Other variations on the WVD include the polynomial WVD [8] and the rotational WVD [14]. Each technique has its respective advantages and drawbacks, and the choice of a particular transform will depend on the requirements of each signal processing application.

Among the many time-frequency representations available, the PWVD was chosen to transform one-dimensional time series SAR-GMTI data into the two-dimensional time-frequency space due to the PWVD's high time-frequency resolution, and its ability to suppress cross-terms. Further analysis on the use of the PWVD for detecting accelerating targets and obtaining a focused response are given in Chapter 7.

Chapter 3

Detection

The first step in any SAR-GMTI processing system is the detection of moving targets, afterwhich focusing and motion parameter estimation may be carried out. As discussed in section 2.3.2, the DPCA technique is a widely-used method of clutter cancellation, enabling users to separate stationary clutter from targets of interest.

The objective of this chapter is to describe the impact of target acceleration on the DPCA signal of a dual-channel SAR system, and to determine its consequences on target detection. Firstly, the mathematical expression for the DPCA response from a moving point target is derived. The expected influence of acceleration as well as the other motion parameters on the DPCA signal are predicted by inspection.

Next, an airborne radar-target scenario is simulated to determine the impact of each motion parameter on the DPCA response, and to investigate the consequence of a zero-acceleration assumption on the ability to detect moving targets. Lastly, the DPCA algorithm is applied to experimental data to detect moving targets, and comparisons are made to the theoretical and simulated results.

3.1 Theory

Detection is carried out using the DPCA technique because of its widespread use in GMTI processing, its algorithmic simplicity, and because it is the optimal linear filter for detecting a target in homogeneous clutter [43]. Further details on the DPCA method are given in section 2.3.1. DPCA may be performed on data that have been fully compressed (i.e. in range and azimuth dimensions) or data that have been range compressed but are uncompressed in azimuth [79].

Each domain (azimuth compressed and azimuth uncompressed) allows for target

detection over a different range of across-track velocities v_{y0}. For large v_{y0}, sidelobe suppression during azimuth compression suppresses the target signal, giving an advantage to using the range compressed domain. However, for low v_{y0} and targets with low RCS, azimuth compression facilitates detection by concentrating the energy spread over the entire synthetic aperture into a few pixels [79].

Although explained further in Chapter 4, azimuth compression requires a reference filter matched to the target phase history in order to obtain a sharply focused image. When targets are travelling with significantly non-zero velocity and/or acceleration, the target Doppler frequencies are so mismatched to the standard processing filter that they are not imaged at all [37]. Iterative procedures using multiple processing filters are possible, but this requires detection and parameter estimation to be done simultaneously. Working with range compressed data allows a separation of these two steps.

To avoid iteration, to enable separation of the detection and estimation stages, and to observe how the DPCA response changes over the course of a synthetic aperture, the DPCA signal is examined in the range compressed domain only.

3.1.1 DPCA mathematical representation

The DPCA response for an accelerating point target is computed below. We begin from the range compressed responses of the fore and aft channels (represented as $s_1(t)$ and $s_2(t)$, respectively) given by equations 2.24 and 2.25. The one-way range to the fore antenna from the target is given by $R_1(t)$ in equation 2.22, and the difference in the two-way ranges to the fore and aft apertures is given by the residual term $g(t)$ in equation 2.23.

The DPCA response, as a function of time and vehicle dynamics, is then given by

the difference between the two channels:

$$\begin{aligned}
\text{DPCA}(t) &= A(t)e^{-2jkR_1(t)} - A(t)e^{-jk[2R_1(t)+g(t)]} \\
&= A(t)e^{-2jkR_1(t)}\left(1 - e^{-jkg(t)}\right) \\
&= A(t)e^{-2jkR_1(t)}e^{-jkg(t)/2}\left(e^{jkg(t)/2} - e^{-jkg(t)/2}\right) \\
&= A(t)e^{-2jkR_1(t)}e^{-jkg(t)/2}2j\sin\left(\frac{kg(t)}{2}\right),
\end{aligned} \tag{3.1}$$

where it has been assumed that the fore and aft antennas have identical amplitude such that the combined target reflectivity and gain is $A(t)$ for each channel. For detection purposes, it is the magnitude of equation 3.1 that is of greatest interest:

$$\begin{aligned}
|\text{DPCA}(t)| &= 2|A(t)|\left|\sin\left[\frac{kg(t)}{2}\right]\right| \\
&= 2|A(t)|\Bigg|\sin\Bigg[\frac{k}{2}\Bigg(\frac{y_0 v_{y0}}{R_0}\frac{d}{v_a} \\
&\quad + \frac{1}{R_0}\left[(v_{x0}-v_a)^2 + v_{y0}^2\left(1 - \frac{y_0^2}{R_0^2}\right) + y_0 a_{y0}\right]\left(\frac{d}{v_a}t + \frac{d^2}{4v_a^2}\right) \\
&\quad + d\frac{(v_{x0}-v_a)\left(t + \frac{d}{2v_a}\right)}{R_0}\Bigg)\Bigg]\Bigg|,
\end{aligned} \tag{3.2}$$

where the third term of $g(t)$ from equation 2.23 has been dropped due its minimal contributions in relation to the other terms. Detection using DPCA is performed by thresholding the magnitude signal from equation 3.2. All pixels with DPCA magnitudes equal to or above the threshold are potential moving targets, whereas all pixels below are assumed to be clutter. The threshold is a subjective value and may be chosen based on experience with the particular data set of interest, or based on a constant false alarm rate (CFAR), in which case an accurate model of the target and clutter probability density functions is required to choose the appropriate threshold [32].

3.1.2 Analysis of the DPCA expression

The expected influence of the target motion parameters on the DPCA magnitude may be examined using equation 3.2. Assuming that the target amplitude is relatively constant over the course of the synthetic aperture, the DPCA magnitude is determined by the $g(t)$ function, which is the difference in the two-way path length to the fore and registered aft apertures.

In the argument of equation 3.2 the first term (proportional to v_{y0}) is dominant. The second and third terms are of similar magnitudes (whose absolute values depend primarily on the quantity $(v_{x0} - v_a)$) but the terms have opposite signs. This is true for $t > -d/(4v_a)$ and $t < -d/(2va)$ since $(v_{x0} - v_a)^2$ (from the second term) is always positive, and $(v_{x0} - v_a)$ (from the third term) is always negative for targets of interest (i.e. targets with speeds lower than the aircraft velocity). The second and third terms nearly cancel each other out, such that for $v_{x0} = v_{y0} = 5$ m/s and $a_{y0} = 0$, the absolute value of the first term of $g(t)$ is close to thirty times larger than the maximum sum of the second and third terms for typical airborne scenarios, and nearly 400 times larger than the sum for the RADARSAT-2 spaceborne scenario. Also note that the first term in $g(t)$ is a function of only the across-track velocity v_{y0}, and is not dependent upon time; this suggests that the DPCA magnitude will not be significantly affected by target acceleration and will be relatively constant over the course of the synthetic aperture.

As discussed above, the dominant term in the sine argument from equation 3.2 is the first term of $g(t)$, given by $ky_0v_{y0}d/(2R_0v_a)$. The DPCA magnitude is thus maximized when this term takes on a value of $(2n+1)\frac{\pi}{2}$, where n can be any integer $(n = 0, \pm1, \pm2, \ldots)$. These DPCA magnitude maxima occur for:

$$v_{y0} = \frac{(2n+1)\lambda R_0 v_a}{2y_0 d} \qquad \text{where } n = 0, \pm1, \pm2, \ldots \quad . \tag{3.3}$$

For a pass collected using parameters typical of Environment Canada's CV 580 SAR (with parameters shown in Table 3.1), the first maxima (n = 0,-1) occur at v_{y0} =

± 10.2 m/s. A target imaged at the same incidence angle using RADARSAT-2 (where $\lambda = 0.0565$ m, $R_0 \approx 104$ km, $v_a = 7500$ m/s, and $d = 7.5$ m) has maxima at ± 43.9 m/s.

Similarly, the DPCA magnitude goes to zero when the sine argument takes on a value of $n\pi$, where n can be any integer ($n = 0, \pm 1, \pm 2, \ldots$). These DPCA magnitude minima occur for:

$$v_{y0} = \frac{n\lambda R_0 v_a}{y_0 d} \qquad \text{where } n = 0, \pm 1, \pm 2, \ldots \quad . \tag{3.4}$$

For data collected using the CV 580 SAR in the same radar-target geometry, the first non-zero minima ($n = \pm 1$) occur at $v_{y0} = \pm 20.3$ m/s. The first non-zero minima for such a target viewed from the RADARSAT-2 sensor occur at ± 87.9 m/s. If it is assumed that the antenna gain patterns, spherical propagation loss, target reflectivity, and all other factors influencing signal amplitude have been removed from the input fore and aft data (and thus that $A(t) = 1$), then the DPCA magnitudes will vary from 0 to 2, depending on the across-track velocity of the target. At the minima values, the DPCA magnitude will be zero and thus these represent 'blind velocities' at which targets cannot be detected. Thus, even if a target possesses non-zero along-track velocity and/or any acceleration components, if its broadside velocity v_{y0} is close to zero or to a blind velocity, detection may be difficult.

3.2 Simulations

To investigate how DPCA magnitude is influenced by target velocities and accelerations, a MATLAB program was created to simulate airborne DPCA signal returns. Range compressed fore and aft signals free from noise, clutter contamination, and antenna gain patterns were generated for a radar-target geometry similar to that encountered using the CV 580 SAR sensor. A list of radar parameters and airborne geometry parameters used in the simulation is provided in Table 3.1:

To minimize numerical errors, equation 2.9 was used to compute $R_{\text{fore}}^{2-\text{way}}(t)$, and

Table 3.1: Radar and geometry parameters for airborne SAR simulations.

Parameter	Value
Pulse repetition frequency (f_{PRF})	642.5 Hz
Wavelength (λ)	0.0565 m
Range at broadside (R_0)	10 km
Incidence angle to target (θ_{inc})	40°
Aircraft velocity (v_a)	125 m/s
-3 dB antenna beamwidth (β)	3°
Physical antenna separation distance (d)	0.54 m
Synthetic aperture time (T)	4.2 s

equations 2.15 and 2.19 were used to determine $R^{2-\mathrm{way}}_{\text{aft reg.}}(t)$, which make use of the far-field approximation only. Tests were conducted varying v_{x0}, v_{y0}, a_{x0}, a_{y0}, and $\dot{a}_{y0}$ independently and examining the DPCA magnitude over time.

3.2.1 DPCA magnitude with v_{y0}

To begin, a target was simulated with non-zero across-track velocity v_{y0} varied from -25 to 25 m/s in steps of 0.25 m/s, with all other motion parameters set to zero in order to isolate the effects of v_{y0} on the DPCA magnitude. Figure 3.1 (a) shows the sinusoidal variation of the range compressed DPCA magnitude as a function of across-track velocity v_{y0} and time as predicted by equation 3.2. The magnitude is constant for all times over the course of the synthetic aperture, and a two-dimensional cross-section is shown in Figure 3.1 (b).

As predicted by equation 3.4, the DPCA magnitude goes to zero at $v_{y0} = 0$ and $v_{y0} = \pm 20.3$ m/s, and reaches a maximum at ± 10.2 m/s (as anticipated from equations 3.3 and 3.4). Note the sharp notch filter about zero-velocity, such that targets travelling with even slight across-track velocities will possess a non-zero DPCA magnitude.

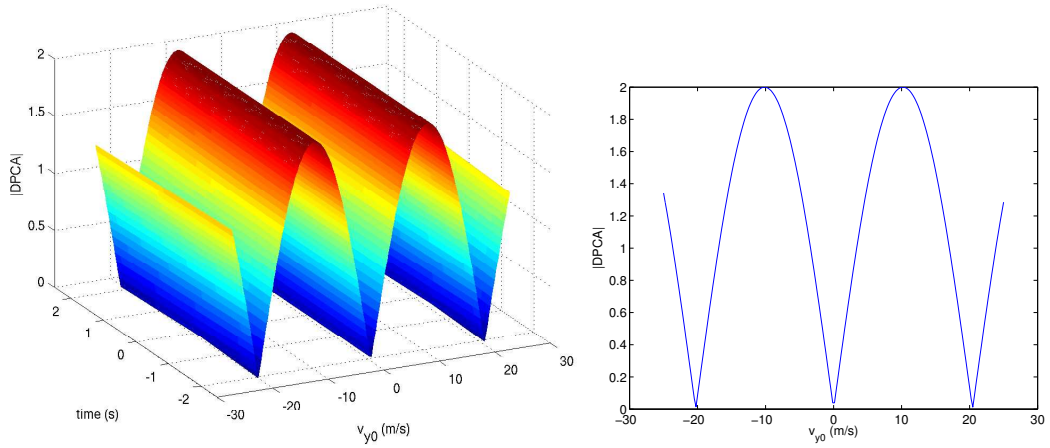

(a) Variation of DPCA magnitude through time where the magnitudes are examined over the course of one synthetic aperture and time t=0 corresponds to broadside time.

(b) A two-dimensional cross-section of figure (a).

Figure 3.1: Range compressed DPCA magnitude for a simulated target with constant velocity v_{y0} varied from -25 to 25 m/s and $v_{x0} = 0$. For a particular v_{y0} the magnitude is constant for all times over the synthetic aperture. Note the sinusoidal variation with v_{y0} as predicted by equation 3.2, the null at $v_{y0} = 0$ m/s, and the blind velocities at approximately ± 20 m/s.

3.2.2 DPCA magnitude with v_{x0}

Simulations were performed varying along-track velocity v_{x0} from -25 to 25 m/s in steps of 0.25 m/s. Again, v_{y0} was set to zero in order to isolate the effects of v_{x0} on the DPCA magnitude. Figure 3.2 shows the variation in DPCA magnitude as a function of along-track velocity v_{x0} and time from broadside. In this case, the

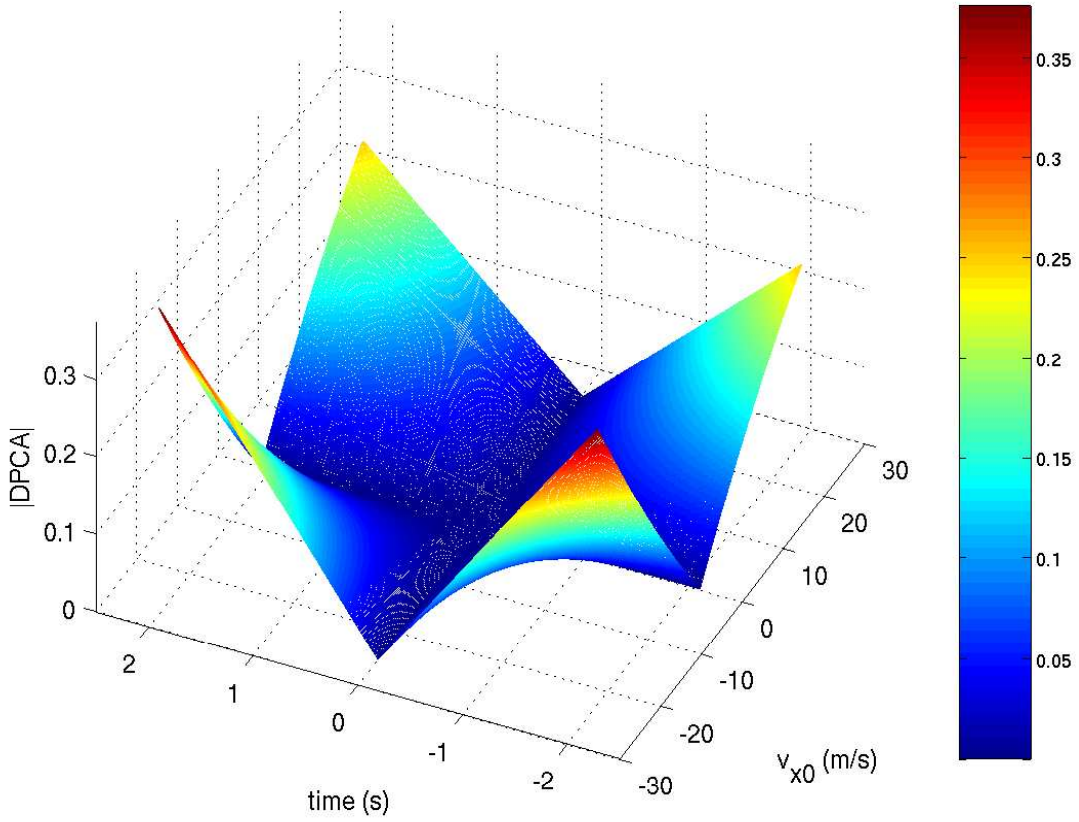

Figure 3.2: Range compressed DPCA magnitude through time for a simulated target with constant velocity v_{x0} varied from -25 to 25 m/s and $v_{y0} = 0$. Magnitudes are examined over the course of one synthetic aperture where time t=0 corresponds to broadside time. Note the low DPCA magnitude for even high along-track velocities as well as the time-varying nature of the magnitude as predicted by equation 3.2.

dynamic range in the magnitude is smaller than when varying v_{y0} (such that DPCA magnitude is much more sensitive when a target has a v_{y0} velocity component than

only a v_{x0} component, even if the along-track velocity is relatively large). Also, note that the DPCA magnitude varies with time from broadside for a constant non-zero v_{x0} as predicted by the second and third terms in the sine argument of equation 3.2.

In many situations targets will be travelling with both along- and across-track velocity components. Figure 3.3 displays the DPCA magnitude for a simulated target with v_{y0} varied from -25 m/s to 25 m/s, but with constant v_{x0} = -25 m/s for all trials. This value of v_{x0} was chosen since it gave the largest variation in DPCA magnitude

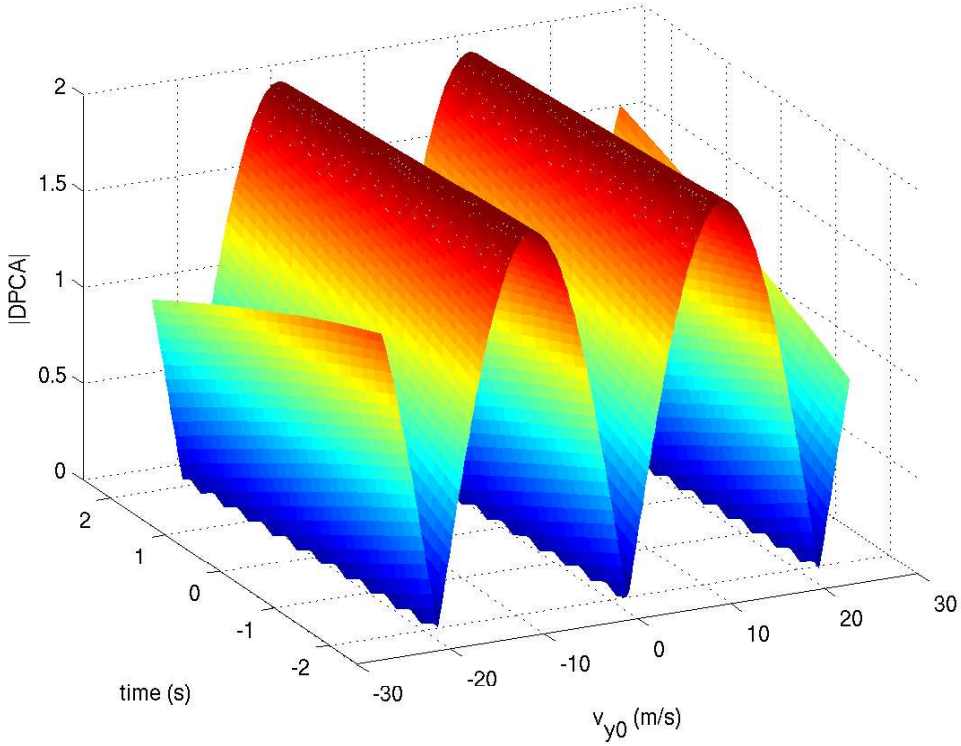

Figure 3.3: Range compressed DPCA magnitude through time for a simulated target with constant velocity $v_{x0} = -25$ m/s and v_{y0} varied from -25 to 25 m/s. Magnitudes are examined over the course of one synthetic aperture where time t=0 corresponds to broadside time. Note the similarities to Figure 3.1 (a) indicating that DPCA magnitude is dictated primarily by v_{y0} even in the presence of high along-track velocities v_{x0}.

for the $v_{y0} = 0$ case (see Figure 3.2). However, as expected, the DPCA magnitude is

determined primarily by the across-track velocity v_{y0}, with some small modulations introduced by v_{x0}. As predicted by equation 3.2, this modulation creates a sloping DPCA magnitude over time which is most easily visible at the furthest ends of Figure 3.3 for $v_{y0} = \pm 25$ m/s. One two-dimensional cross-section of Figure 3.3 at $v_{y0} = 1$ m/s is shown in Figure 3.4. Note that the v_{x0} velocity has driven the DPCA magnitude to zero at one point in the observation interval. However, for across-track velocities with an absolute value greater than 1.2 m/s, the DPCA magnitude is completely non-zero over the synthetic aperture (in this specific scenario).

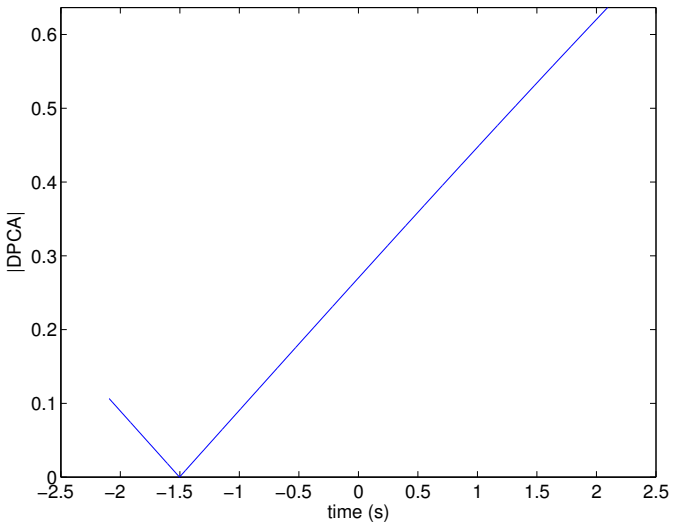

Figure 3.4: Range compressed DPCA magnitude through time for a simulated target with constant velocities $v_{x0} = -25$ m/s and $v_{y0} = 1$ m/s. Magnitudes are examined over the course of one synthetic aperture where time t=0 corresponds to broadside time. Note the changing magnitude over time, and zero magnitude at 1.5 seconds before broadside.

3.2.3 DPCA magnitude with a_{y0}

The introduction of across-track acceleration a_{y0} has a similar effect upon DPCA magnitude as non-zero along-track velocity v_{x0}. Figure 3.5 displays the DPCA magnitude for a simulated target with constant a_{y0} varied from -1 m/s^2 to 1 m/s^2. Again,

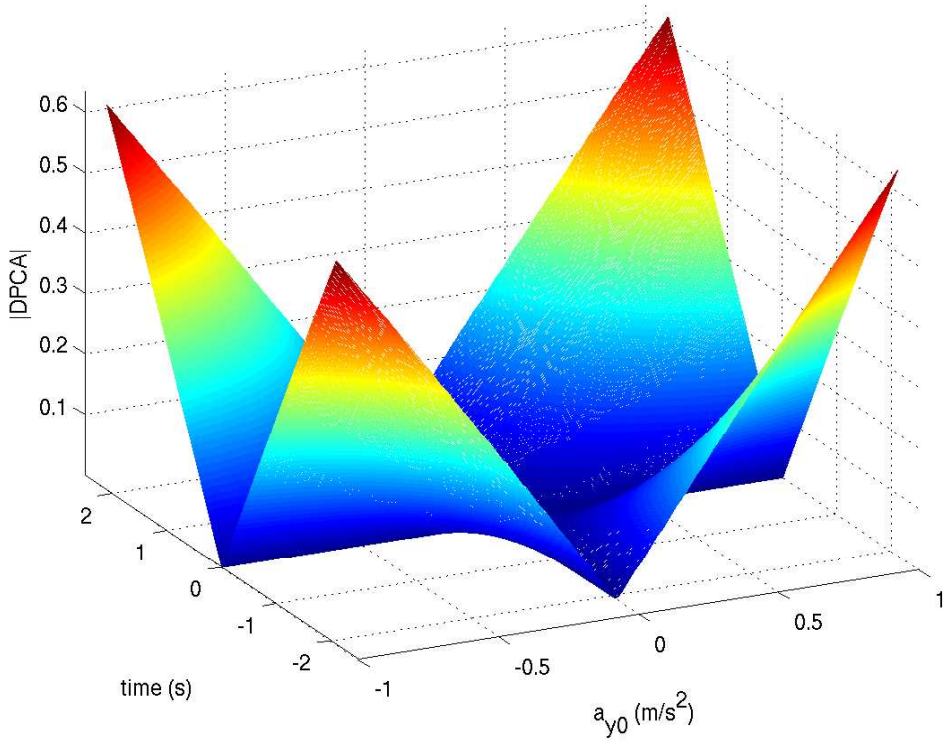

Figure 3.5: Range compressed DPCA magnitude through time for a simulated target with constant across-track acceleration a_{y0} varied from -1 to 1 m/s^2, and with $v_{y0} = v_{x0} = 0$. Magnitudes are examined over the course of one synthetic aperture where time t=0 corresponds to broadside time. Note the low DPCA magnitude for even high across-track accelerations as well as the time-varying nature of the magnitude as predicted by equation 3.2.

the magnitudes are time-varying as predicted by the second term in the sine function of equation 3.2. The DPCA magnitude at relatively high accelerations (e.g. 1 m/s^2) rivals that of the DPCA magnitude for large along-track velocities (e.g. $\pm$ 25 m/s). to put these values in context, an acceleration of 1 m/s^2 is equivalent to adding 3.6 km/h to one's velocity over the course of one second.

Depending on the direction of acceleration (i.e. in the positive or negative across-track direction) and its magnitude, the v_{x0} and a_{y0} influences may nearly cancel each other out to give a DPCA magnitude of close to zero, or they may add constructively to increase the effective DPCA magnitude. This behaviour is due to the fact that they both appear in the same term in equation 3.2.

As before, when across-track acceleration a_{y0} is added to a non-zero broadside across-track velocity v_{y0}, the DPCA magnitude is dominated by the v_{y0} term, although the magnitude displays a slope (either positive or negative depending on the signs of a_{y0} and v_{y0}) over the observation interval.

3.2.4 DPCA magnitude with along-track acceleration a_{x0}

Along-track acceleration a_{x0} has a nearly negligible effect on DPCA magnitudes. Figure 3.6 displays the DPCA magnitude for a simulated target with a_{x0} varied from -1 m/s^2 to 1 m/s^2. Note the extremely small DPCA magnitude along the z-axis when compared to Figures 3.2 and 3.5. Equation 3.2 does not contain the a_{x0} variable because only second order terms of the Taylor expansion were included in its derivation. However, to compute the DPCA target signature in each simulation, equation 2.15 was used, which does include along-track acceleration a_{x0} and whose only approximation is the far-field approximation (which contributes a two-way range error of only 1.5×10^{-5} metres to the estimate of $R_{\text{aft}}^{2-\text{way}}(t)$). The low DPCA magnitudes due to a_{x0} confirm that the third-order term in the Taylor expansion of the range equation is not significant in this case, and thus equation 3.2 is an acceptable approximation of the closed form expression for DPCA magnitude.

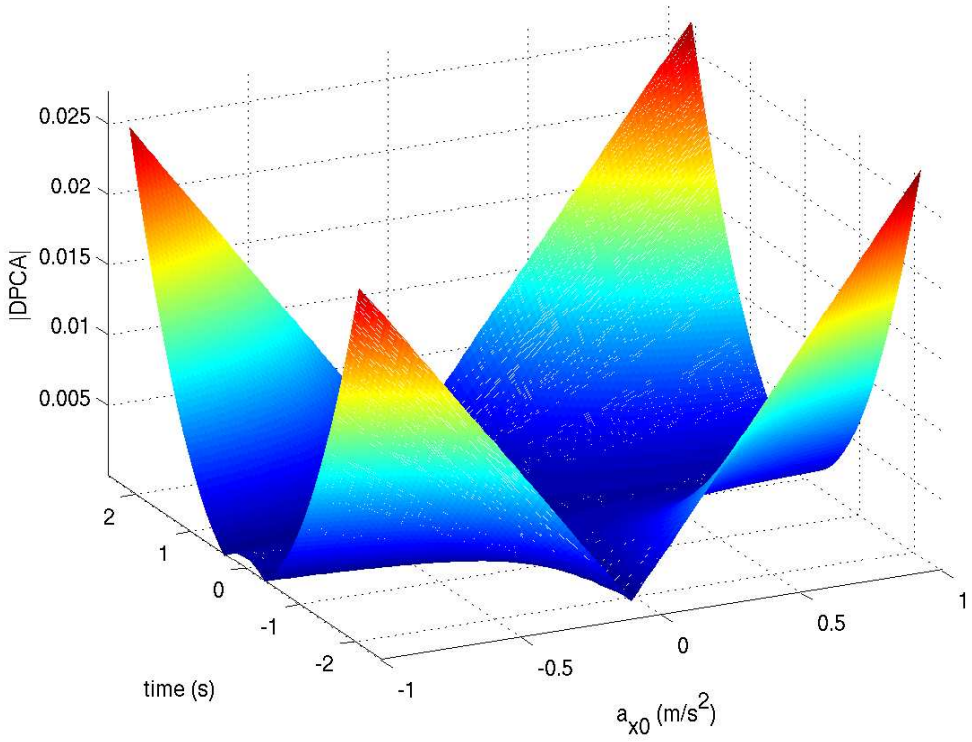

Figure 3.6: Range compressed DPCA magnitude through time for a simulated target with constant along-track acceleration a_{x0} varied from -1 to 1 m/s^2, and with $v_{y0} = v_{x0} = 0$. Magnitudes are examined over the course of one synthetic aperture where time t=0 corresponds to broadside time. Note the extremely low DPCA magnitude for even high along-track accelerations.

3.2.5 DPCA magnitude with $\dot{a}_{y0}$

Similar to along-track acceleration, time-varying across-track acceleration with non-zero $\dot{a}_{y0}$ has minimal impact upon the DPCA magnitude. The effects of time-varying accelerations changing from -0.1 to 0.1 m/s^3 over the course of one synthetic aperture has effects on the DPCA magnitude of the same order as the range of a_{x0} tested. These DPCA magnitude variations for changing $\dot{a}_{y0}$ while all other motion parameters are set to zero are shown in Figure 3.7.

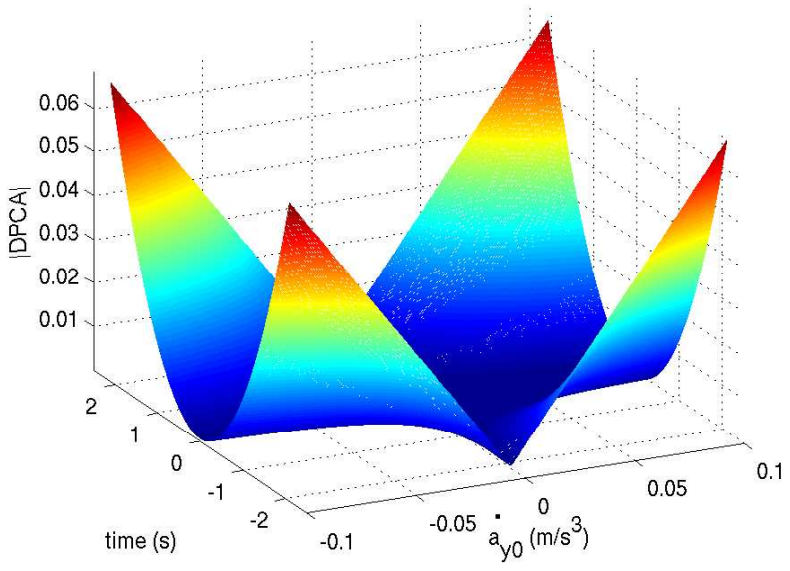

Figure 3.7: Range compressed DPCA magnitude through time for a simulated target with time-varying across-track acceleration with rate of change $\dot{a}_{y0}$ varied from -0.1 to 0.1 m/s^3 and with $[v_{x0}\ v_{y0}\ a_{x0}\ a_{y0}]^T = \vec{0}$. Magnitudes are examined over the course of one synthetic aperture where time t=0 corresponds to broadside time. Note the extremely low DPCA magnitude for even high rates of acceleration change.

3.2.6 DPCA magnitude for spaceborne geometries

In addition to airborne simulations, a spaceborne scenario using parameters projected for the RADARSAT-2 sensor was simulated. The simulation was simplistic and did

not take into account earth curvature, earth rotation, atmospheric propagation effects, antenna gain, clutter, or noise. However, a general idea about how velocity and acceleration might affect DPCA magnitudes for a spaceborne geometry may be determined using the simulation.

A list of radar and geometry parameters for the upcoming Canadian RADARSAT-2 SAR is provided in Table 3.2.

Table 3.2: Radar and geometry parameters for RADARSAT-2 simulations [18].

Parameter	**Value**
Pulse repetition frequency (f_{PRF})	1300-3800 Hz
Wavelength (λ)	0.0555 m
Altitude (H)	800 km
Incidence angle to target (θ_{inc})	40°
Range at broadside (R_0)	1044 km
Platform velocity (v_a)	7500 m/s
-3 dB antenna beamwidth (β)	0.21 - 0.63°
Physical antenna separation distance (d)	7.5 m

Note that both the azimuth beamwidth and the PRF are programmable by the operator. In the spaceborne simulations, a PRF of 2000 Hz and a beamwidth of 0.4° were chosen to give a synthetic aperture time of approximately one second, with the rest of the radar parameters set to the values given in Table 3.2.

Figure 3.8 displays the DPCA magnitude for a simulated target observed in a spaceborne geometry with v_{y0} varied from -25 m/s to 25 m/s and all other motion parameters set to zero. Although an entire period of the DPCA magnitude is not visible for the range of simulated velocities, the sinusoidal variations in the magnitude and the null at zero-velocity as predicted by equation 3.2 are still visible. One advantage of the spaceborne scenario is that there are no DPCA blind speeds at the target velocities of interest.

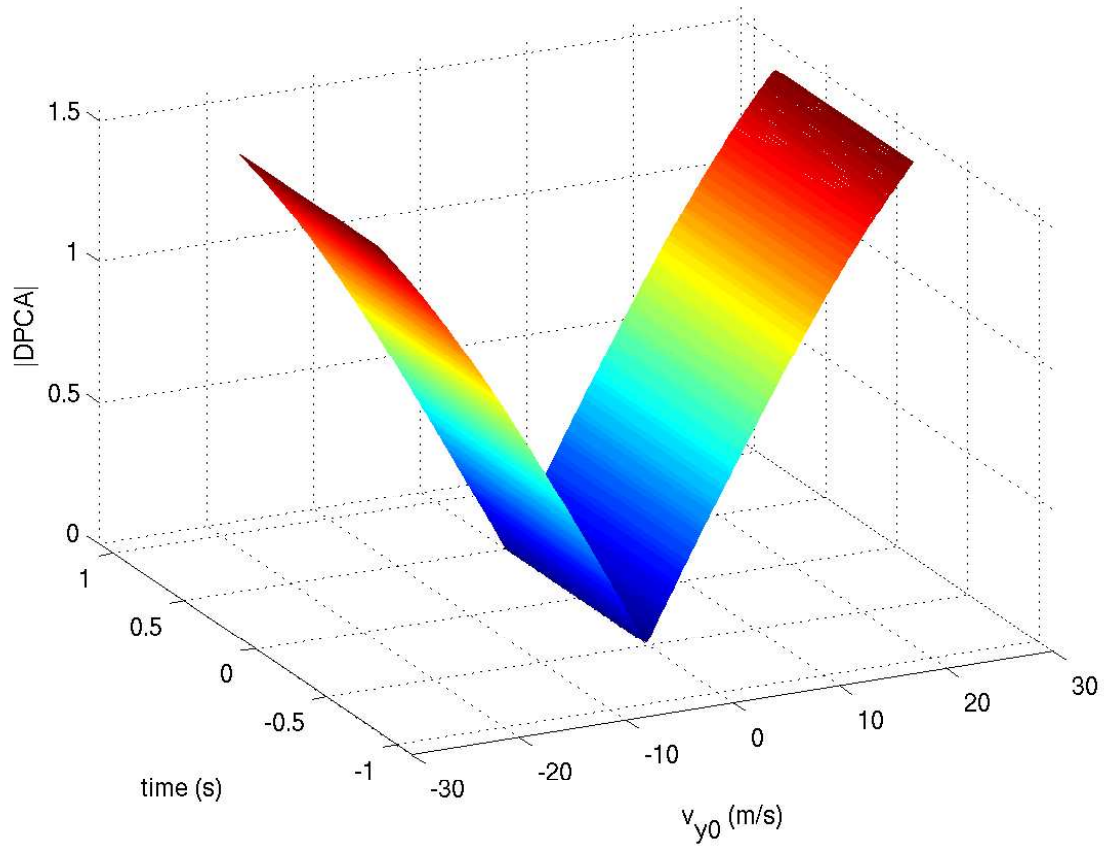

Figure 3.8: Range compressed DPCA magnitude through time for a simulated target observed in a spaceborne geometry with across-track velocity v_{y0} varied from -25 to 25 m/s. Magnitudes are examined over the course of one synthetic aperture where time t=0 corresponds to broadside time. Note the similarities to Figure 3.1, including the sinusoidal variation with v_{y0} as predicted by equation 3.2, and the null at $v_{y0} = 0$ m/s.

Targets with non-zero across-track acceleration a_{y0} were also simulated for the spaceborne case. Figure 3.9 displays the DPCA magnitude for a simulated target with constant a_{y0} varied from -1 m/s^2 to 1 m/s^2. In the spaceborne case the geometry

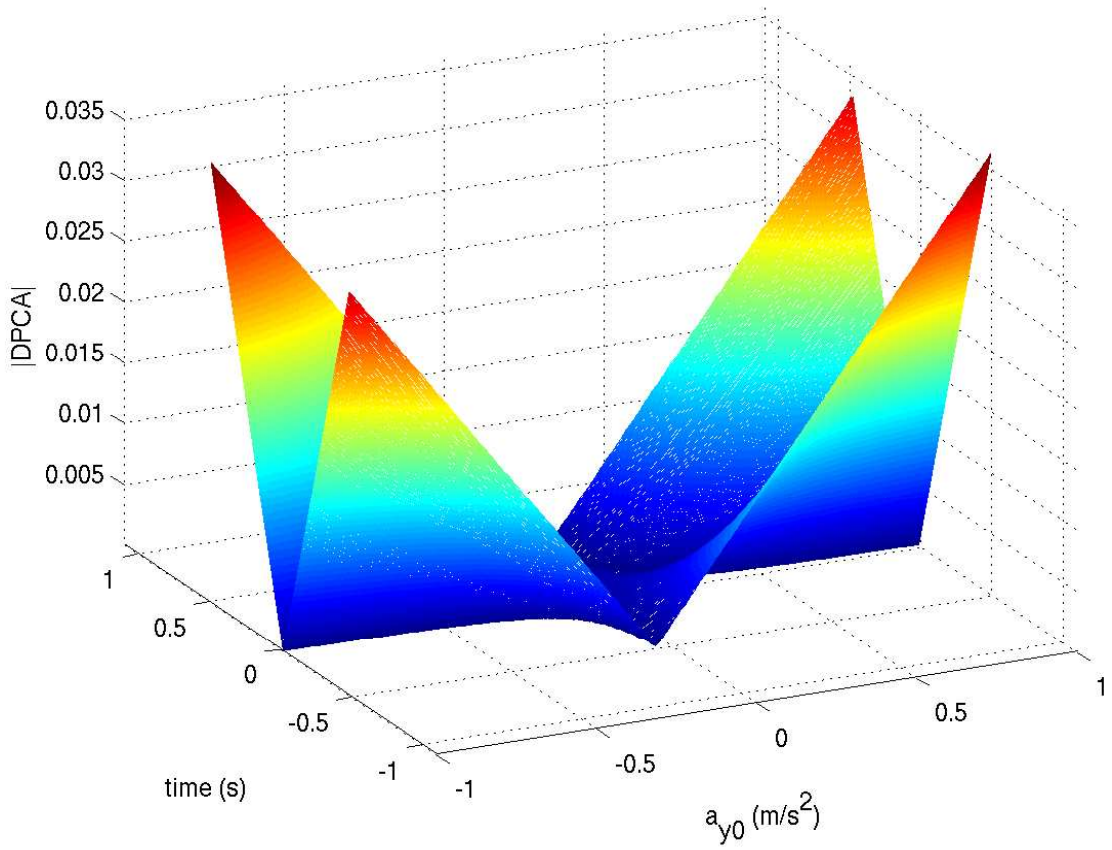

Figure 3.9: Range compressed DPCA magnitude through time for a simulated target observed in a spaceborne geometry with constant across-track acceleration a_{y0} varied from -1 to 1 m/s^2, and with $v_{y0} = v_{x0} = 0$. Magnitudes are examined over the course of one synthetic aperture where time t=0 corresponds to broadside time. Note the low DPCA magnitudes compared to the airborne case of Figure 3.5.

is such that v_{x0} and a_{y0} have even less of an influence on the DPCA magnitude than in the airborne scenario. For instance, comparisons between Figures 3.5 and 3.9 reveal peak DPCA magnitudes twenty times lower in the spaceborne case than in the

airborne scenario. This is due to differences in the d/v_a factor multiplying v_{x0} and a_{y0} in equation 3.2, which is approximately four times smaller in the spaceborne scenario. Additionally, the synthetic aperture time is approximately four times shorter in the spacebased case, which further decreases the peak DPCA magnitudes.

3.2.7 Analysis of DPCA magnitude simulations on target detection

As discussed in previous sections, DPCA magnitudes may be used in combination with a decision rule or threshold to separate pixels containing moving targets from clutter. Following the initial target detection, the target may be tracked through azimuth for the duration of the synthetic aperture to extract the track for further processing including focusing and parameter estimation.

Detection and tracking of targets with non-zero across-track velocity v_{y0} is relatively straightforward as long as targets are not travelling at a blind velocity. The notch in the sine function about zero-velocity in Figure 3.1 is quite sharp, such that targets travelling with even small across-track velocities will have non-zero DPCA magnitudes that will remain constant across the observation interval. However, in the presence of residual clutter and high noise levels, the DPCA magnitude threshold for detection must be raised significantly above zero, and thus the detection of slow-moving targets or targets moving close to the blind velocities remains challenging [41].

The time-varying nature of the DPCA range compressed magnitudes as observed in the simulations has implications on the effectiveness of target detection and tracking through azimuth. Non-zero DPCA magnitudes are observed in Figure 3.2, such that given sufficiently low noise and significant clutter suppression, one can detect targets in the range compressed data moving completely in the along-track direction. However, the time-varying nature of the magnitudes across the observation interval may make it difficult to track a target through azimuth which is travelling only with a v_{x0} component. The peaks in the DPCA magnitude signal occur well away from

broadside, and tracking the target over the entire observation interval is not possible as the DPCA signal magnitude fades to zero as the time approaches broadside. Additionally, because the peak responses from targets moving along-track occur at the far edges of the beam, their DPCA magnitudes may be suppressed due to the antenna gain pattern, making the targets even more difficult to discern from the background residual clutter.

These same observations apply to a target moving with across-track acceleration a_{y0} and across-track velocity $v_{y0} = 0$ at broadside. However, although the scenario of targets moving completely along-track may be quite common, a target with zero across-track broadside velocity and non-zero across-track acceleration is somewhat of a pathological case. It is difficult to conceive of a plausible situation in which this would occur, although the simulations with zero v_{y0} were useful in isolating the influence of a_{y0} on DPCA magnitude.

In the presence of non-zero v_{y0} and large a_{y0} or v_{x0}, it is likely that a target will be detected using the DPCA magnitude, but it may be difficult to extract the entire target track. The sloping DPCA magnitude presents a problem at across-track broadside velocities v_{y0} very close to the the blind velocities (within 1.2 m/s of the blind velocities for the simulated airborne scenario). In these cases, the slope introduces a null in the DPCA magnitude, which will create a break in the extracted target track. If the DPCA detection threshold is sufficiently low however, the gap in the extracted track will be small and may be bridged using a moving average filter to connect track segments. This type of approach was used in tracking targets in experimental data, as will be described in section 3.3.1.

Even large values of along-track acceleration a_{x0} and across-track acceleration rates $\dot{a}_{y0}$ did not have an noticeable impact on DPCA magnitudes, and thus would not hamper detection as long as an across-track v_{y0} component is present. Simulations of the RADARSAT-2 spaceborne scenario revealed relatively small modulations introduced by v_{x0}, a_{x0}, a_{y0}, and $\dot{a}_{y0}$ on the DPCA magnitude when compared to the

airborne case. This suggests that time-varying DPCA magnitudes will be even less of a concern for spaceborne GMTI sensors.

In summary, theory and simulations have shown that the addition of target acceleration will not severely deteriorate target detection using DPCA; it is expected that most targets will be detected and tracked for the entire observation interval if they possess an across-track velocity component away from the blind velocities.

3.3 Experimental results

Having described the theory and conducted simulations of detection by DPCA, it was desired to examine target detection using experimental data. Dual-channel SAR data were collected during an experiment conducted at Canadian Forces Base (CFB) Petawawa with the Environment Canada CV 580 C-Band SAR in November of 2000. Three control targets were used in the experiment, each of which was equipped with a trihedral corner reflector and a GPS (Global Positioning System) receiver. The corner reflector increases target reflectivity (RCS) such that the target is more visible in the radar imagery, and the GPS data allows precise determination of the target position and velocities at all times. Two targets (dubbed 'Juliet' and 'Delta') were rail cars moving along a rail track, and the third target (called 'Convoy') was a vehicle driving along a gravel road. All targets attempted to maintain constant speed during the synthetic aperture of the radar. Eight passes were flown from four different aspect angles with a total of twenty-two control target tracks to analyze. Further descriptions and images of the experimental set up are given in Appendix A and [49]. Appendix A also outlines the pre-processing performed on the data.

3.3.1 Detection and tracking algorithm

A detection and tracking algorithm in the range compressed domain using the DPCA technique for clutter suppression was employed to extract and store the track of each target. The algorithm was developed by Christoph Gierull [36], although slight

modifications were made by this author to ease input and calculation of the required parameters, and to set algorithmic thresholds appropriate for the data set.

The program (designed for CV 580 SAR data) accepts range compressed fore and aft data chips as input as well as a number of input parameters including aircraft velocity (v_a), near range to the first pixel of the data chips, aircraft altitude, and f_{PRF}/v_a ratio. The algorithm assumes that internal clutter motion is insignificant, and that the range pixel is large enough (or the target size is small enough) such that the energy of each target is concentrated in a single range cell at each azimuthal time. Whereas many detection techniques are applied in the azimuth compressed domain, this algorithm works with only range compressed data, which is not biased against high-velocity targets for detection, and allows a separation of the detection and estimation stages as described in section 2.3.2. The algorithm is described below, with images from one pass of the Delta target given to illustrate the detection process.

The algorithm begins with the computation of several magnitude maps. Firstly, the average magnitude of both channels is determined as

$$\overline{|s(t)|} = \frac{|s_1(t)| + |s_2(t)|}{2}, \tag{3.5}$$

where $\overline{s}$ denotes the mean value of s. Next, the DPCA magnitude is computed as $|DPCA| = |s_1(t) - s_2(t)|$. Both magnitude maps are then convolved with a one-dimensional moving average (i.e. lowpass) filter in azimuth to smooth the data (thereby decreasing noise), and then each pixel is normalized by dividing it by the mean magnitude value. The smoothed DPCA magnitude image may also be referred to as the *nLooks* DPCA map, where *nLooks* represents the length of the lowpass filter. An example of the DPCA magnitude image before and after smoothing is shown in the first two columns of Figure 3.10 for one pass of the Delta target.

Next a two-step power detector is applied to the convolved and normalized magnitude maps. Potential target pixels must meet the following criteria:

$$10\log_{10}|\mathrm{DPCA}| > 2 \text{ dB} \qquad \text{AND} \qquad 10\log_{10}\frac{\overline{|s(t)|}}{|\mathrm{DPCA}|} < -2 \text{ dB}, \tag{3.6}$$

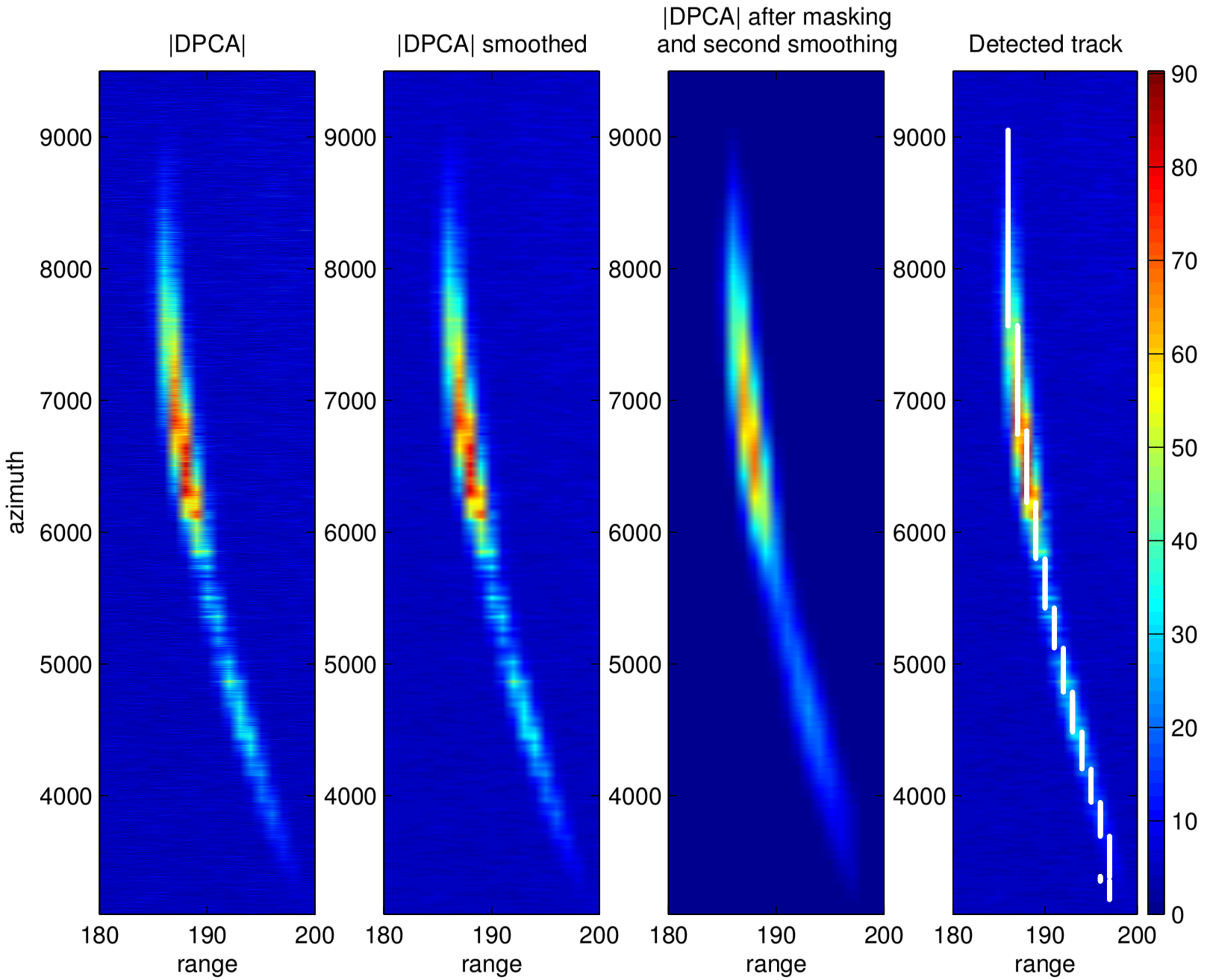

Figure 3.10: Four stages of the target detection and tracking process operating in the range compressed domain. From left: DPCA magnitude image, DPCA image smoothed with a 20 pixel moving average filter, thresholded DPCA map heavily smoothed with a 750 pixel moving average filter (to bridge gaps in the track), final detected track after clustering overlaid on smoothed DPCA image.

where the two thresholds (2 dB and -2 dB) may be changed if the user so desires. The first condition ensures that the target has a significant non-zero DPCA magnitude. The second condition examines the ratio of power before and after the application of DPCA. This is done to eliminate bright, stationary scatterers (clutter discretes such as buildings) whose signals have been significantly suppressed by DPCA, even though the DPCA magnitudes remain relatively large compared to other clutter. This approach was also suggested by White et al. [92].

The next step is to further smooth the detected pixels in order to bridge any gaps in the track using a second (and much longer) moving average filter. The first threshold from equation 3.6 is then reapplied, and a binary detection map is created by assigning pixels as moving or not. The third column in Figure 3.10 demonstrates the thresholded, heavily smoothed target DPCA image. The binary detection map is then applied as a mask onto the *nLooks* DPCA map to extract only the pixels of interest for tracking.

For each pulse (i.e. each range line), the local maxima in the masked DPCA image are stored. This reduces a target track spread out across multiple range cells (perhaps due to sidelobes) to a target track only a single range cell thick.

The next step is to identify separate target tracks in the binary detection image (i.e. to cluster all detections into a finite number of tracks). A target track is permitted to jump from one range cell to a neighbouring range cell, but is not allowed to have any gaps in azimuth, since the long moving average filter should have bridged any azimuthal gaps.

The tracking algorithm works by systematically stepping through all azimuthal slow times and all range lines in two nested loops. When the first detection is reached, a new cluster is created if a second detection is found in the next azimuth slow time and in a nearby range cell. Clusters are grown by comparing each detection with detections at the previous azimuth time. If a cluster already exists in a nearby range cell, the new pixel is added to the cluster. If a 'detected' pixel cannot find a nearby

detection in the past azimuth time, a new cluster is created. Finally, any target tracks consisting of too few pixels are considered false alarms and are removed. Ideally, one should be able to track a target through the entire synthetic aperture time, which is on the order of 2700 pixels for the CV 580 SAR azimuthal pixel spacing, beamwidth, and ranges.

The program requires several thresholds to be set including the size of the various moving average filters, the power detector thresholds, the minimum number of consecutive detections in azimuth (slow time) required to be considered a genuine target track, and the maximum jump in range bins permitted when clustering target pixels into a single track (generally set to one pixel). Some of these thresholds are data specific, and they were set using educated guessing and trial and error. In practice they will be calculated as CFAR thresholds, although this lies beyond the scope of this thesis.

Once set, all thresholds were kept constant for processing the eight passes of the Petawawa 2000 data, except the maximum jump in range bins, which had to be relaxed to two pixels to ensure the continuity of two detected tracks. In these instances target segments were clustered separately due to range jumps in the maximum magnitude of the DPCA target track of more than one pixel.

3.3.2 Analysis and results of experimental detections

The detection and tracking algorithm described in section 3.3.1 was applied to data patches containing each of the twenty-two control targets. From the GPS data and aircraft headings, it was known that all targets had non-zero across-track velocity components, and thus it was expected from the theory and simulation results (see section 3.2.7) that all targets would be detected in the DPCA magnitude imagery.

As expected, all twenty-two targets were detected and successfully tracked through azimuth despite the presence of along-track velocity or any type of acceleration components. It was mentioned earlier that the controlled movers attempted to maintain

a constant velocity during data collection. However, miscommunication between the aircraft and the control vehicles sometimes resulted in them being imaged during times of non-constant velocity and even during non-constant acceleration.

Unfortunately, it is difficult to verify the true acceleration of the control targets over time since GPS data were only collected at a data rate of 0.5 Hz, and thus updates are available only every two seconds. A target is illuminated by the -3 dB beamwidth of the antenna for approximately 4 seconds in the CV 580 geometry ($t_{\text{aperture}} \simeq R_0\beta/v_a$ where range to the target R_0 can be approximated as 10 km, the -3 dB beamwidth β as three degrees, and the aircraft velocity v_a as 125 m/s). However, when targets are mounted with a corner reflector, the available synthetic aperture time may significantly increase due to the extremely strong sidelobe responses that are not completely suppressed by the fading antenna gain pattern. For instance, the Delta target from one pass was tracked for 8.9 seconds through azimuth time.

Even with this extended illumination time however, accurately capturing the acceleration time-history over the course of the target observation period is not possible due to the low sampling rate of the GPS measurements. However, one can get a rough idea of whether the target was maintaining a constant velocity or not by examining the GPS velocity measurements over time. Technical specifications [58] cite RMS (root mean square) accuracies of 0.03 m/s in velocities computed from differentially processed GPS data such as that available for the experimental data set, and therefore small changes in target velocity over the synthetic aperture should be visible.

The GPS velocities of the controlled movers during one pass are shown in Figure 3.11 in the vicinity of broadside time t=0 (where the GPS times were loosely synchronized to the radar azimuth times, although there may be errors of several seconds). Observe the acceleration and deceleration occurring in each case, although the speeds have not been separated into along- and across-track components. The presence of acceleration is not surprising since the Delta and Juliet targets were on relatively short tracks, and thus required significant acceleration to bring them up to the de-

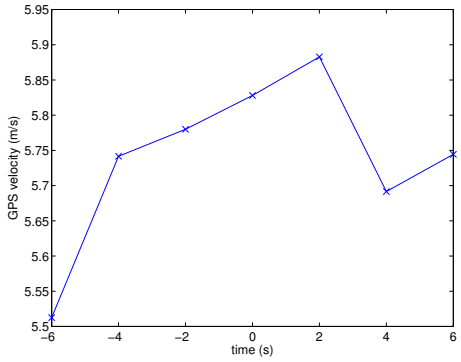

(a) GPS velocities for Juliet.

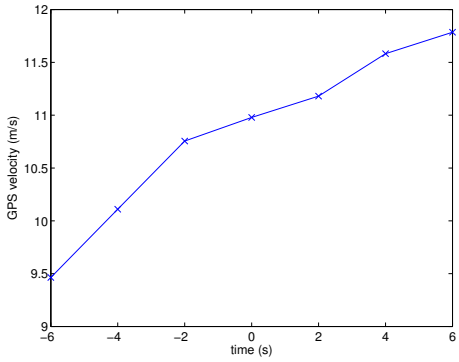

(b) GPS velocities for Delta.

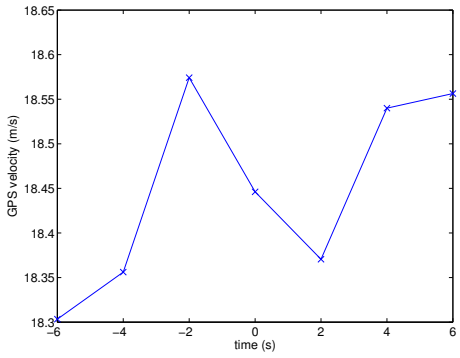

(c) GPS velocities for Convoy.

Figure 3.11: Variation of target velocity (obtained from GPS) through time in the vicinity of broadside time t=0 for a single pass.

sired test speeds, and then significant deceleration to slow them down before the end of the track. The convoy was travelling on a longer road, but the road surface was uneven gravel, and the speeds were subject to human-errors such as small changes in pressure on the gas pedal. In addition, it was very difficult to time the trials exactly such that the airborne system was imaging the targets only when they were travelling at constant velocities.

As mentioned earlier, all targets were tracked through azimuth despite the presence of along-track velocity and/or along-track and across-track accelerations. However, the slight sloping of the DPCA magnitude over time due to v_{x0} and/or a_{y0} (as observed in simulations from section 3.2) is not observable in the experimental data. This may be due to the presence of the antenna gain pattern, noise, the effects of complex scattering mechanisms off the vehicles, and incomplete tracking of the target through all azimuth bins. The DPCA magnitude through time for one pass of the Juliet target is given in Figure 3.12 (a), where the parabolic antenna gain pattern dominates the magnitude response, masking the influence of any time-varying DPCA components due to motion parameters. Even after detrending using a higher-order polynomial to remove the effects of antenna gain, the DPCA magnitude remains noisy and target flickering is clearly visible in Figure 3.12 (b).

Summarizing, the three control targets were detected and tracked in every pass of the dual-channel experimental SAR data when using the DPCA technique for clutter suppression. All targets were detected despite the presence of along-track velocity and along- and across-track acceleration components. Each target had a non-zero across-track velocity not equal to a blind velocity which increased the DPCA magnitude above the noise floor such that the targets could be detected. The experimental results are thus in agreement with the theoretical and simulated results from previous sections. Having described the detection process, the extracted target tracks may be passed onto the focusing and parameter estimation stages, which are examined next.

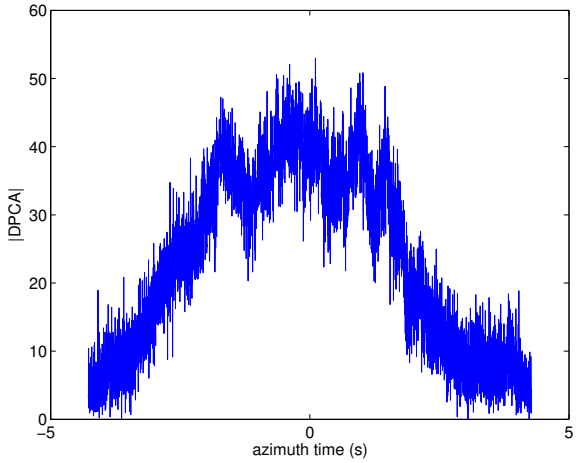

(a) DPCA magnitude including antenna gain pattern.

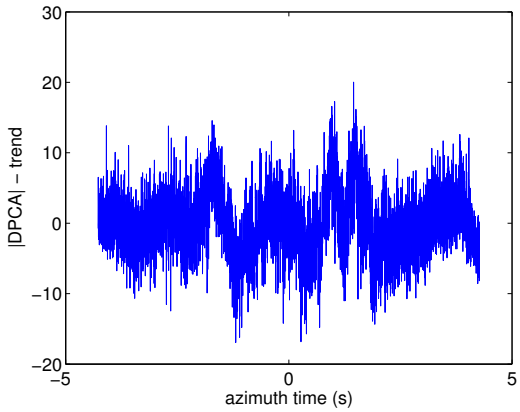

(b) DPCA magnitude with antenna gain pattern removed using polynomial detrending.

Figure 3.12: Range compressed DPCA magnitude through time for one pass of the Juliet target, where time t=0 corresponds to broadside time. The antenna gain pattern dominates the return signal on the top, masking any time-varying effects due to motion parameters. After polynomial detrending (bottom), the DPCA response is somewhat noisy and shows evidence of target flickering.

Chapter 4

Focusing

To reconstruct a range compressed moving target signal into a focused target image, azimuth compression of each receiver channel is required. Focusing (also known as azimuth compression) was briefly discussed in section 2.1. Details on focusing theory and its application to simulated and experimental data are presented here.

The objective of this chapter is to describe the impact of acceleration on the focused response from a point target in the fore and aft channels, and the consequences of a zero-acceleration assumption. Focusing is discussed prior to motion parameter estimation, since the estimation algorithms discussed in subsequent chapters implement azimuth compression in their solution. Airborne geometries are assumed for the majority of the theoretical and simulated cases, although the application of the results to spaceborne scenarios are described for certain computations. Theory and simulations are combined since it was not possible to derive a closed form expression for the azimuth compressed response when there are higher-order terms in the phase history of the target signal, although we can observe the response in simulations.

4.1 Theory and simulations

Azimuth compression is achieved by constructing a reference filter with a phase history matched to that of the received signal, and then cross-correlating this reference with the target signal [29]. This operation is called 'matched filtering'. Thus, for the i^{th} (either fore or aft) channel,

$$I_i(t) = \frac{1}{T} \int_{-\infty}^{\infty} s_i(t+\tau)\; r_i^*(\tau)\; d\tau, \tag{4.1}$$

where $I_i(t)$ is the focused signal for the i^{th} channel, $s_i(t)$ is the received target signal (after range compression), $r_i(t)$ is the reference signal, and * denotes complex conju-

gation. Duration T is the maximum usable synthetic aperture time, often taken as the -3 dB azimuthal beamwidth. A division by T is inserted into equation 4.1 such that the focused signal is unitless.

Gierull and Livingstone note that the quality and focus of an image is constrained by noise and noise-like processes, by knowledge of the relative motion between the radar and the target, and by the fidelity of the processor in applying the matched filter [35]. The noise-like processes may include additive thermal noise of the radar and multiplicative noise (such as oscillator phase noise) caused by real hardware and sampling limitations. Further details on the SAR image formation process and algorithms for focusing stationary targets are provided in [9, 13, 29, 73, 87].

The azimuth compressed signal after matched filtering is derived in subsequent sections for both stationary and moving targets. The impact of a mismatch between the reference and target phase histories due to uncompensated target motion is also examined.

Matched filtering requires knowledge of the two-way ranges to the fore and aft apertures. Assuming an airborne radar-target geometry identical to that described in section 2.3.1, the two-way ranges $R_{\text{fore}}^{2-\text{way}}(t)$ and $R_{\text{aft reg.}}^{2-\text{way}}(t)$ (after channel registration) were derived using a third-order Taylor series expansion of the range equation, and are given by equations 2.17 and 2.21, respectively.

4.1.1 Focusing a stationary target

If a target is stationary (i.e. the target position has no time dependence), then the target in both channels may be focused using a stationary world matched filter (SWMF):

$$r_{\text{SWMF}}(t) = \exp\left(-2jk\left[\frac{v_a^2}{2R_0}t^2\right]\right)\text{rect}\left(\frac{t}{T}\right), \tag{4.2}$$

where $r_{\text{SWMF}}(t)$ represents the reference signal whose range history is derived by setting all target velocities and accelerations to zero in equation 2.22, and removing the first R_0 term (which will simply add a constant phase term). The target signal $s(t)$

from equation 2.12 for both channels is equivalent to $r_{\mathrm{SWMF}}(t)$ except that $s(t)$ contains a magnitude factor $A(t)$ and a constant phase term $\exp(-2jkR_0)$. Performing the cross-correlation in equation 4.1 and assuming that the antenna gain is removed such that the magnitude is no longer a function of time and is identical in both channels (i.e. $A_i(t) = A$), then the focused stationary target image (for both the fore and aft channels for a target with broadside position described in section 2.3.1) is given by:

$$I(t) = \frac{A\,(T - |t|)}{T}\ \exp\left(-2jkR_0\right)\ \mathrm{sinc}\left(\frac{kv_a^2(T - |t|)}{R_0}\ t\right)\ \mathrm{rect}\left(\frac{t}{2T}\right), \tag{4.3}$$

where $\mathrm{sinc}(x) = \sin x/x$.

The maximum of $I(t)$ occurs when the argument of the sinc function is zero, and thus the peak response of the focused target appears at broadside time t=0 which coincides with the true position of the scatterer. The first zeroes of $I(t)$ occur when the argument of the sinc function is $\pm\pi$. Solving equation 4.3, this occurs at

$$t = \frac{\pm T \mp \sqrt{T^2 - \frac{2\lambda R_0}{v_a^2}}}{2}. \tag{4.4}$$

For radar parameters and an airborne geometry typical of Environment Canada's CV 580 SAR (see parameters listed in Table 3.1), this translates to nulls at $\pm$0.54 m or a -3 dB width of 0.47 m. This is much finer than the achievable azimuth resolution of the CV 580 system (approximately 0.85 m [46]) since the real system has noise, system losses, and significant energy loss of the target signal due to the antenna gain patterns and weighting functions used for sidelobe suppression.

4.1.2 Focusing a moving target with a SWMF

The SAR imaging of moving targets and the target response when processed using conventional SAR-imaging techniques was first treated by Raney [62]. He found that the response from a moving target is highly dependent upon the target dynamics, such that the image becomes smeared in range and shifted in azimuth due to across-track velocity, and smeared in azimuth due to along-track velocity and across-track

acceleration. Since that time, numerous papers (e.g. [17, 20, 35, 41, 67, 80, 90, 93]) have examined the influence of target motion upon the processed SAR response both theoretically and experimentally. A summary of these effects and their causes is given below by the theoretical development of the SWMF response to a moving target signal. Oftentimes, target responses from badly mismatched reference signals may not be discernible in the SAR image due to the presence of clutter, increasing the difficulty of detection and subsequent parameter estimation. However, in this treatment, simulations are carried out without any added clutter or noise.

If the stationary world reference signal from equation 4.2 is used to focus the range compressed signal $s_1(t)$ received by the fore antenna of an accelerating target, the phase history is not matched. Let the target signal be modelled as $s_1(t) = A\exp(-jkR_{\text{fore}}^{2-\text{way}}(t))\text{rect}(\tau/T)$, where $R_{\text{fore}}^{2-\text{way}}(t)$ is given in equation 2.17. Then, the azimuth compressed image is given by the following:

$$\begin{aligned} I_1(t) &= \frac{A}{T}\int_{-\infty}^{\infty} \exp\left(-2jk\left[R_0 + \frac{y_0 v_{y0}}{R_0}(t+\tau)\right.\right. \\ &+ \left.\left.\frac{1}{2R_0}\left((v_{x0}-v_a)^2 + v_{y0}^2\left(1-\frac{y_0^2}{R_0^2}\right) + y_0 a_{y0}\right)(t+\tau)^2 + O((t+\tau)^3)\right]\right) \\ &\cdot \exp\left(+2jk\left[\frac{v_a^2}{2R_0}\tau^2\right]\right)\cdot \text{rect}\left(\frac{t+\tau}{T}\right)\text{rect}\left(\frac{\tau}{T}\right)d\tau, \end{aligned} \tag{4.5}$$

where $O(t^3)$ represents all terms of third-order and above. Pulling all terms not a function of τ out of the integration we have:

$$\begin{aligned} I_1(t) &= \frac{A}{T}\exp\left(-2jk\left[R_0 + \frac{y_0 v_{y0}}{R_0}t\right.\right. \\ &\left.\left. + \frac{1}{2R_0}\left((v_{x0}-v_a)^2 + v_{y0}^2\Big(1-\frac{y_0^2}{R_0^2}\Big) + y_0 a_{y0}\Big)t^2 + O(t^3)\right]\right) \\ &\cdot \int_{-\infty}^{\infty}\exp\left(-2jk\left[\frac{y_0 v_{y0}}{R_0}\tau + \frac{1}{2R_0}\left((v_{x0}-v_a)^2 + v_{y0}^2\left(1-\frac{y_0^2}{R_0^2}\right) + y_0 a_{y0}\right)(2t\tau+\tau^2)\right.\right. \\ &+ \left.\left. O(t^2\tau + t\tau^2 + \tau^3)\right]\right)\exp\left(+2jk\left[\frac{v_a^2}{2R_0}\tau^2\right]\right)\text{rect}\left(\frac{t+\tau}{T}\right)\text{rect}\left(\frac{\tau}{T}\right)d\tau. \end{aligned} \tag{4.6}$$

The above equation cannot be solved analytically because there is no closed form expression for the definite integral of $\exp(\tau^2)$ and $\exp(\tau^3)$ with respect to τ. However,

this integration may be performed numerically using a software program such as MATLAB; since sampled radar signals are discrete rather than continuous with time in any case, this representation is justified. A simulator initialized with radar and geometry parameters similar to those encountered using the CV 580 airborne system (see Table 3.1) was created within MATLAB to determine the influence of various target motion parameters on focusing. Each velocity and acceleration component is treated separately in order to isolate the effects of each parameter on target focusing.

The response from a stationary point target is given as a reference in the top portion of Figure 4.1. The response is not an ideal sinc function due to the fact that the sampling times (determined by the PRF) are not coincident with the zeros of the sinc function. As mentioned in section 4.1.1, the -3 dB width of the peak magnitude response is 0.47 m. This peak is centred about azimuth position x=0 metres corresponding to a broadside time of t=0 seconds. Using results from MATLAB simulations, the properties of moving target signals processed using a stationary world matched filter are examined below.

Focusing with across-track velocity v_{y0}

When a target is given a non-zero across-track velocity component, the peak magnitude decreases in the azimuth compressed signal and its azimuth location shifts with respect to the stationary case, although its -3 dB width increases only slightly. For constant velocity, let $v_x = v_{x0}$ and $v_y = v_{y0}$ for the entire observation period. The effects of v_y on focusing are evident in the middle frame of Figure 4.1, which shows the magnitude response from a simulated non-accelerating point target with $v_x = 0$ and $v_y = 1$ m/s.

These effects are perhaps most easily understood in the time-frequency domain (see section 2.4 for an introduction to time-frequency analysis). A stationary world matched filter and moving target signal are depicted in the time-frequency domain in Figure 4.2. Azimuth compression consists of convolving the reference (SWMF) signal with the target signal, with the maximum response occurring when there is the

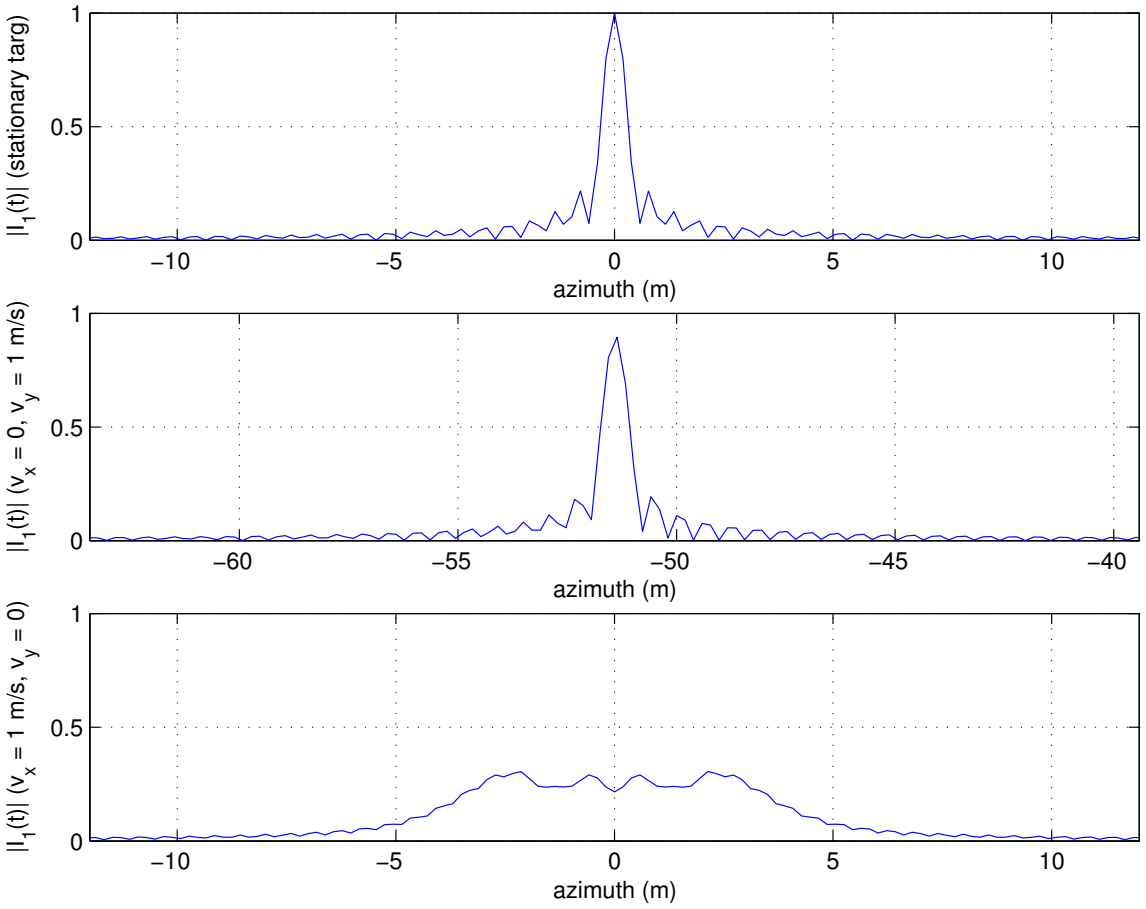

Figure 4.1: Magnitude response (after azimuth compression) of simulated non-accelerating point targets focused using a stationary world matched filter versus azimuthal distance. The stationary target response is given as a reference, and an azimuth of 0 metres is broadside. Top: stationary target. Middle: target with across-track velocity ($v_y = 1$ m/s, $v_x = 0$). Bottom: target with along-track velocity ($v_y = 0$, $v_x = 1$ m/s). Note the azimuthal shift due to v_y and the azimuthal smearing due to v_x.

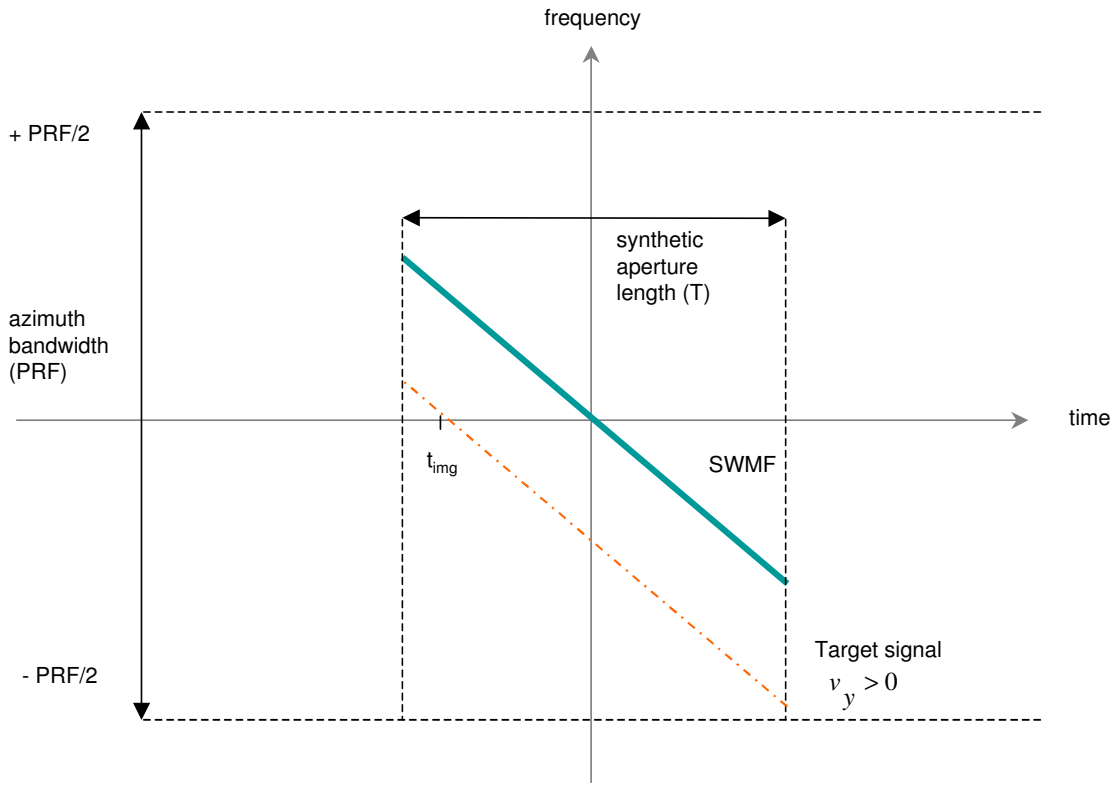

Figure 4.2: Example time-frequency representation of a stationary world matched filter (SWMF in solid blue) and a target moving in the across-track direction with $v_y > 0$ m/s (in dotted red). During azimuth compression the SWMF (of length T seconds) is convolved with the the target signal, giving a focused peak at a time $t_{\text{img}} < 0$.

greatest overlap between the two signals. If one imagines the reference filter being dragged along the time-axis, and that the product of the reference and target signals is summed at each time instance, the azimuth time of greatest overlap occurs at a value less than zero. This is also the azimuth time at which the target is focused, which is significantly offset from broadside for even small across-track velocities. The offset for $v_y = 1$ m/s is 0.4 s, translating to -51 m off-broadside, as shown in the middle frame of Figure 4.1. This azimuthal shift may be computed theoretically by determining the time at which the Doppler is zero (see equation 4.7), or by computing the peak location of an approximation of equation 4.6, which has a closed form solution for the compressed target response (see section 4.1.3).

The peak magnitude response decreases with increasing target across-track velocity magnitudes. Again, this can be visualized in the time-frequency domain where the target signal is offset along the frequency axis from the reference signal because of a different Doppler centroid value. During azimuth compression, the SWMF is dragged across the time-axis. Even at maximal overlap the two signals do not completely coincide, and thus some target energy is not captured.

Due to a finite azimuth bandwidth (equal to the PRF), parts of the target energy may be aliased such that the TF history wraps to fall within a frequency range of $\pm$PRF/2 (see Figure 4.3). The point at which the TF history wraps is dependent upon the target motion parameters (both along- and across-track velocities and accelerations, which determine the Doppler rate and Doppler centroid) as well as the radar parameters (including azimuthal beamwidth and PRF, which determine the synthetic aperture length and the total available bandwidth). In the case of wrapping, a secondary peak may appear at another azimuth time (other than t_{img}), which may create ghosting and lead to ambiguities if its magnitude rivals that of the first peak. These issues are discussed further in Appendix B.1.

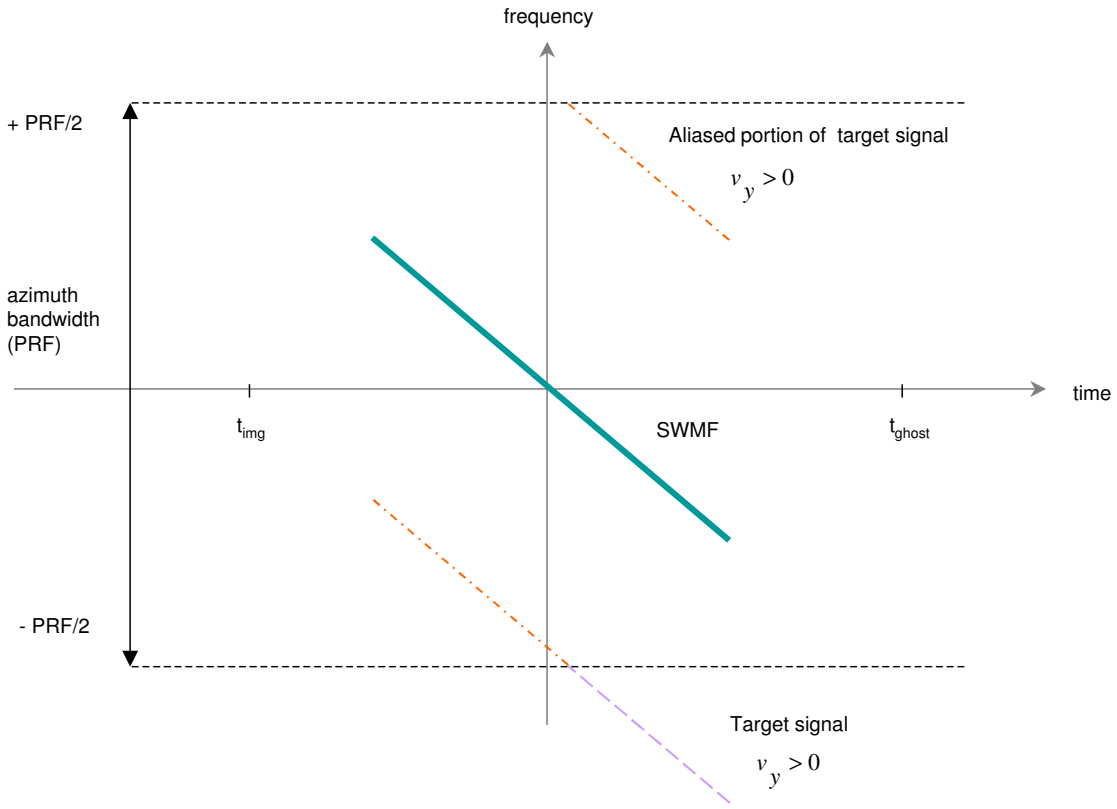

Figure 4.3: Example time-frequency representation of a stationary world matched filter (SWMF in solid blue) and a target moving in the across-track direction with sufficient $v_y > 0$ m/s such that the Doppler frequency wraps across the $\pm$PRF/2 boundary. While the true target TF representation continues past -PRF/2 with the dotted purple line, the spectrum is aliased to +PRF/2, such that the TF signal appears as the dotted red lines. During azimuth compression the SWMF is convolved with the the target signal, giving focused peaks at times t_{img} and t_{ghost}.

Focusing with along-track velocity v_{x0}

When a target possesses a non-zero along-track velocity component, its azimuth compressed response is characterized by a severe decrease in peak power and by a smearing in azimuth due to azimuthal displacement during the synthetic aperture time. These effects are illustrated in the bottom frame of Figure 4.1 for a simulated non-accelerating target with $v_x = 1$ m/s and $v_y = 0$. The decrease in peak power may again be illustrated in the time-frequency domain (see Figure 4.4). The SWMF has

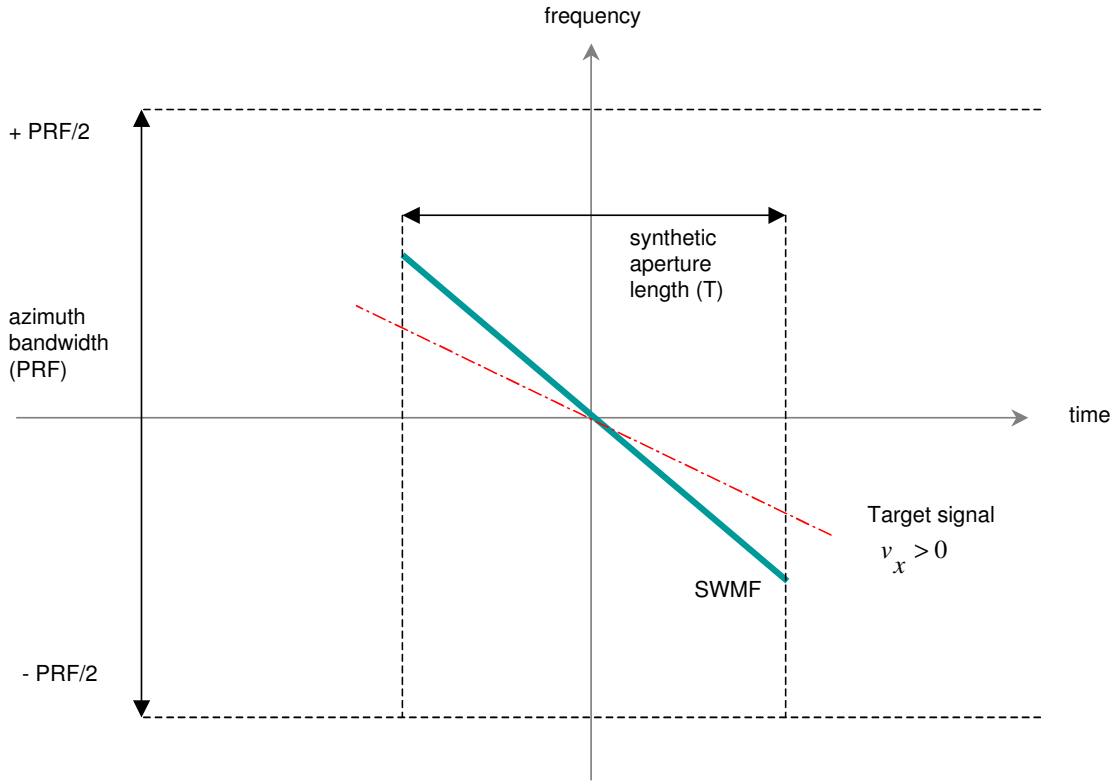

Figure 4.4: Example time-frequency representation of a stationary world matched filter (SWMF in solid blue of length T seconds) and a target moving in the across-track direction with $v_x > 0$ m/s (in dotted red). During azimuth compression the SWMF and target signals are convolved, giving a low power and smeared peak which spreads across multiple times in the vicinity of t=0.

a different slope (i.e. Doppler rate) than the moving target's TF representation. As

the reference filter slides across the time-axis, the two signals never line up, and thus the target energy is never completely captured at any one time. In fact, very little energy is captured at each time instance, although *some* overlap is achieved for a relatively long period of time, which creates the azimuthal smearing. Conservation of target energy is maintained, since although focus errors reduce the peak magnitude, the impulse response of the target is spread in azimuth, giving the same total power.

The -3 dB width of the point target response is proportional to the azimuth displacement of the target over the observation interval (i.e. the synthetic aperture time multiplied by the along-track velocity v_x). For a synthetic aperture time of 4.2 seconds and an along-track velocity of 1 m/s, the target moves 4.2 metres during the observation period. As expected, the response when focused using a SWMF (see bottom frame of Figure 4.1) extends approximately twice this distance (to $\pm$4.2 m) due to the convolution operation. A small change in the bandwidth of the target signal also occurs with a non-zero along-track velocity, although its effects on azimuth compression are not apparent when focusing with a mismatched filter. This phenomenon is further examined in section 4.1.3.

Focusing with constant across-track acceleration a_{y0}

If a SWMF is used to focus a target with constant across-track acceleration, defocusing and an azimuthal shift in the peak response may be present in the compressed image. In the event of constant acceleration, $\dot{a}_{y0} = 0$ and $\dot{a}_{x0} = 0$, such that $a_y = a_{y0}$ and $a_x = a_{x0}$ over the entire observation period. Similar to the presence of v_{x0}, the introduction of a constant a_y also smears the target in azimuth. If an along-track velocity v_{x0} accompanies an across-track acceleration a_y, values of the same sign will counteract some of the spreading, although values of opposite signs will smear the response even further (which can be predicted from the size of the quadratic term in equation 2.22). The effects of a constant across-track acceleration of 0.1 m/s^2 on focusing (with v_{y0}, v_{x0} and a_x set to zero) are shown in Figure 4.5. Unless otherwise stated, a target with a given acceleration is assumed to have $v_{x0} = v_{y0} = 0$.

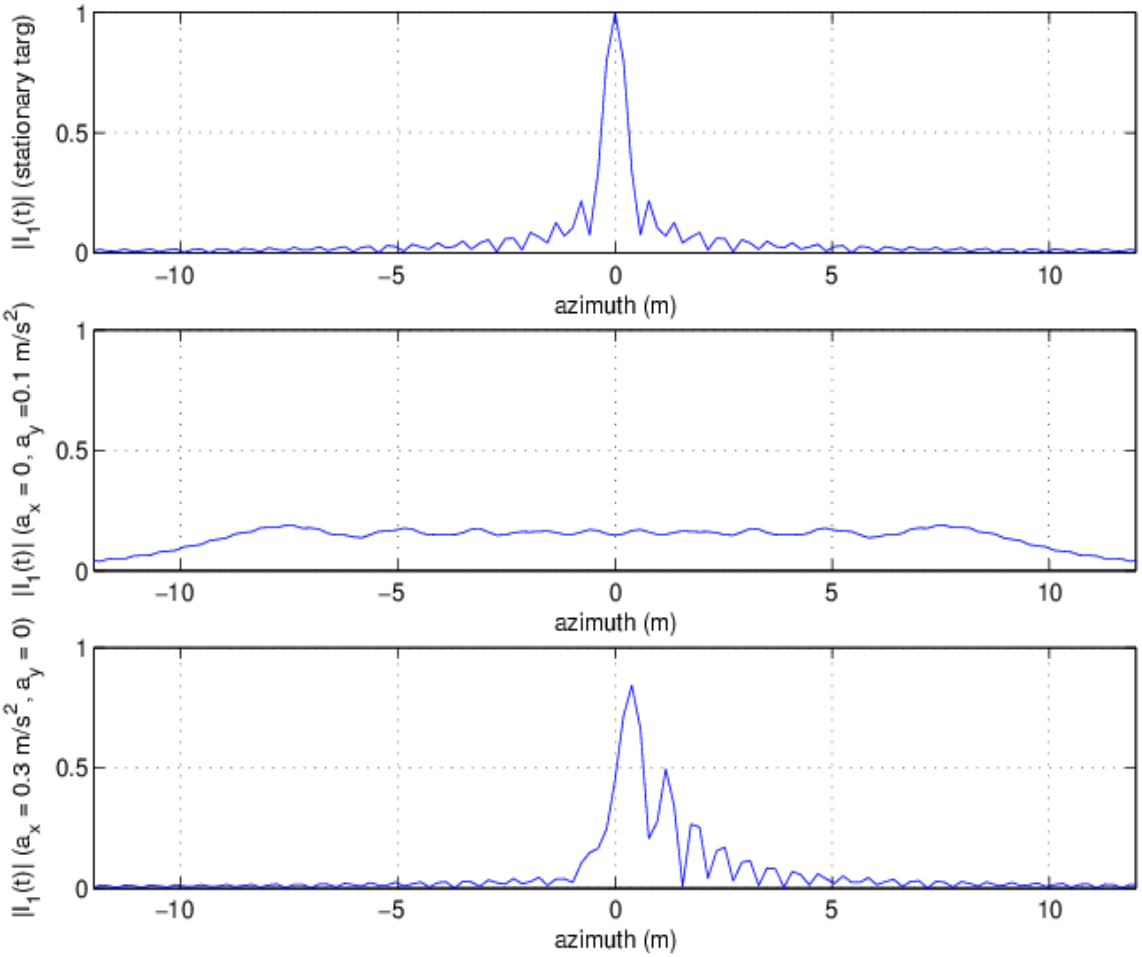

Figure 4.5: Magnitude response (after azimuth compression) of simulated point targets with constant acceleration focused using a stationary world matched filter versus azimuthal distance. The stationary target response is given as a reference, and an azimuth of 0 metres is broadside. Top: stationary target. Middle: target with constant across-track acceleration ($a_y = 0.1$ m/s^2, $a_x = 0$) and zero velocity at broadside. Bottom: target with constant along-track acceleration ($a_y = 0$, $a_x = 0.3$ m/s^2) and zero velocity at broadside. Note the azimuthal smearing due to a_y and the asymmetric sidelobes due to a_x.

The decrease in power and the smeared response due to across-track acceleration is similar to the effects of an uncompensated along-track velocity (see Figure 4.1), since both variables (v_{x0} and a_y) are present in the quadratic term of the Taylor expansion of the range equation (see equation 2.22). Carrara [12] describes similar effects on the SAR system impulse response from quadratic phase errors caused by inaccuracies in the velocity and acceleration measurements of radar platform motion. Although in Carrara's case the targets being imaged were stationary, uncompensated motion (whether from the target or the radar platform) will have similar degradations upon the focused target response.

In the presence of non-zero v_{y0}, a_y can cause a significant azimuthal displacement of the peak response for even small accelerations (e.g. when $v_{y0} = 5$ m/s, $v_{x0} = 0$, an additional shift of ten metres will be introduced for $a_y = 0.1$ m/s^2 than when compared with the constant velocity scenario). If the cubic term in equation 2.22 is neglected, the target will appear at an offset of t_{img} seconds from broadside, approximated as the time at which the range derivative $R'_{\text{fore}}^{\,2-\text{way}}(t) = 0$ (i.e. Doppler is zero):

$$t_{\text{img}} = \frac{-y_0 v_{y0}}{(v_{x0} - v_a)^2 + v_{y0}^2 \left(1 - \frac{y_0^2}{R_0^2}\right) + y_0 \, a_{y0}}, \tag{4.7}$$

where t_{img} is clearly a function of a_{y0}. Although azimuth focusing is sensitive to uncompensated cubic terms in the range equation (see ensuing sections describing the effects of a_x and $\dot{a}_{y0}$ on focusing), the azimuthal shift is insensitive to these terms. The error in t_{img} from neglecting the cubic term is a shift on the order of 1 cm for $v_{y0} = 5$ m/s, $a_y = 0.1$ m/s^2, and all other target motion parameters equal to zero, which is insignificant when compared to the overall shifted distance of tens of metres. Note that the use of the third-order Taylor series expansion in equation 2.22 (as opposed to the square root function of equation 2.9) introduces a 15 cm error in the predicted azimuthal shift, which is an order of magnitude greater than the error from neglecting the cubic term.

Focusing with constant along-track acceleration a_{x0}

The effects of constant along-track acceleration on focusing are subtle at low magnitudes (e.g. $a_x = 0.1$ m/s^2), and thus $a_x = 0.3$ m/s^2 is used for emphasis in the bottom frame of Figure 4.5. Again, to isolate the influence of along-track acceleration, v_{y0}, v_{x0}, and a_y are set to zero. Uncompensated along-track acceleration results in decreased peak power, a slightly wider -3 dB width, and a small azimuthal shift in the position of the focused peak. However, the principal impact of a_x is the creation of asymmetrical peak sidelobes, with raised sidelobes on one side of the peak target response and suppressed sidelobes on the other. These findings are consistent with Carrara's observations that cubic phase errors cause asymmetric sidelobes in the system impulse response [12].

Focusing with time-varying across-track acceleration $a_y(t)$

Continuous across-track acceleration The introduction of time-varying across-track acceleration has additional impact upon the focused SAR response. The -3 dB coherent integration time (synthetic aperture time) is approximately four seconds for the simulated airborne scenario previously described, and variation in target acceleration is plausible over this time period (for instance a vehicle accelerating from rest over the observation period). Such a scenario is illustrated in Figure 4.6, where a stationary target accelerates to an a_y of 0.1 m/s^2 over the course of one synthetic aperture, corresponding to a constant $\dot{a}_{y0}$ of 0.024 m/s^3.

The target response when focused using a SWMF (see Figure 4.7) has asymmetric sidelobes due to the uncompensated cubic phase term (to which $\dot{a}_{y0}$ contributes in equation 2.22). Note the severe azimuthal smearing and low peak power despite the low target velocities and accelerations involved.

Discontinuous across-track acceleration If $a_y(t)$ is a continuous function, as in the above example, then the range expression from equation 2.9 is valid if higher-order acceleration terms are negligible. However, if $a_y(t)$ is discontinuous, then the

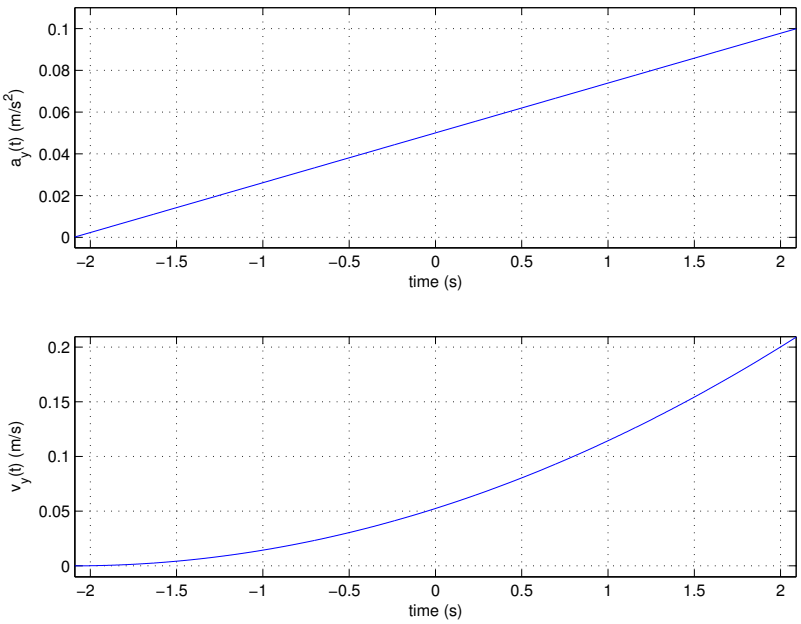

Figure 4.6: Across-track acceleration $a_y(t)$ (with constant $\dot{a}_{y0}$) and corresponding across-track velocity $v_y(t)$ for a point target through time, where t=0 corresponds to broadside. The target's azimuth response upon compression with a SWMF is given in Figure 4.7.

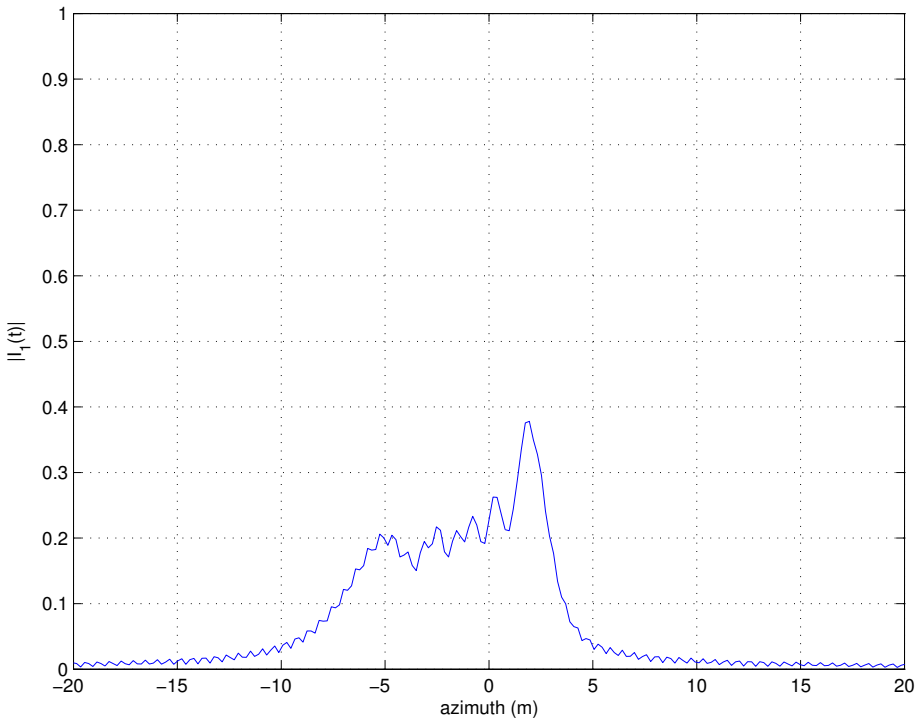

Figure 4.7: Magnitude response (after azimuth compression) of a simulated point target (with constant $\dot{a}_{y0}$ and an $a_y(t)$ given in Figure 4.6) focused using a stationary world matched filter versus azimuthal distance. An azimuth of 0 metres is broadside. Note the low power and severe asymmetric smearing due to $\dot{a}_{y0}$.

expression in equation 2.9 representing the y position of the target ($y = y_0 + v_{y0}t + \frac{1}{2}a_{y0}t^2 + \frac{1}{6}\dot{a}_{y0}t^3$) does not give the correct y away from time t=0. Although in the real world target range histories will be continuous functions, the radar signal data have been sampled at the PRF and are thus discrete. If a target is moving at a constant velocity and then suddenly begins accelerating over a time interval less than the sampling rate, its acceleration and the time-derivative of acceleration will certainly be discontinuous.

To expand any function into an n^{th} order Taylor series, it is required that the function has continuous derivatives of orders one through n [1]. If this condition is not met, then the range equation must instead be represented as a series of functions that are piecewise continuous. An example of such an acceleration time-history is given in the top portion of Figure 4.8, where the target is initially at rest. An acceleration of 0.1 m/s^2 is introduced 0.5 seconds before broadside time, maintained for one second, then dropped back to zero. The range from the target to the fore antenna $R_1(t)$ consists of three continuous functions: $R_{1-1}(t)$, $R_{1-2}(t)$ and $R_{1-3}(t)$, such that fore signal $s_1(t)$ becomes:

$$s_1(t) = A_1(t)\ \exp\left(- jk2\big(R_{1-1}(t) + R_{1-2}(t) + R_{1-3}(t)\big)\right)\ \text{rect}\left(\frac{t}{T}\right), \qquad (4.8)$$

where

$$\begin{aligned} R_{1-1}(t) &\neq 0 \text{ for} \quad -T/2 < t < t_1 \\ R_{1-2}(t) &\neq 0 \text{ for} \quad t_1 \leq t \leq t_2 \\ R_{1-3}(t) &\neq 0 \text{ for} \quad t_2 < t < T/2, \end{aligned}$$

where t_1 is -0.5 seconds and t_2 is 0.5 seconds for this scenario. The focused magnitude response of this target is given in Figure 4.9. The peak response at broadside is significantly lowered compared to the stationary case, and a secondary peak of similar magnitude is created approximately five metres off broadside. Additional smaller peaks are found between the two larger ones, thus smearing the target energy over

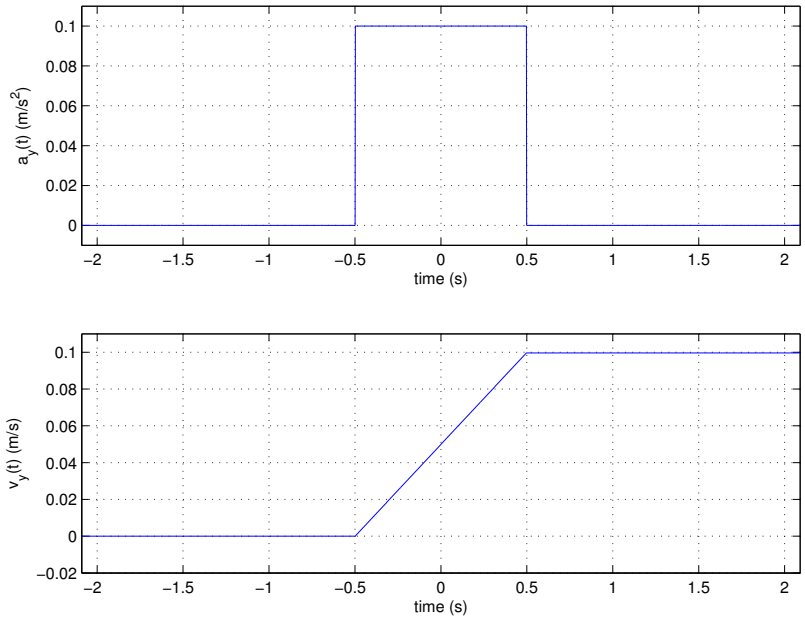

Figure 4.8: Across-track acceleration $a_y(t)$ (a rectangular window centred at broadside) and corresponding across-track velocity $v_y(t)$ for a point target through time whose azimuth response to a SWMF is given in Figure 4.9.

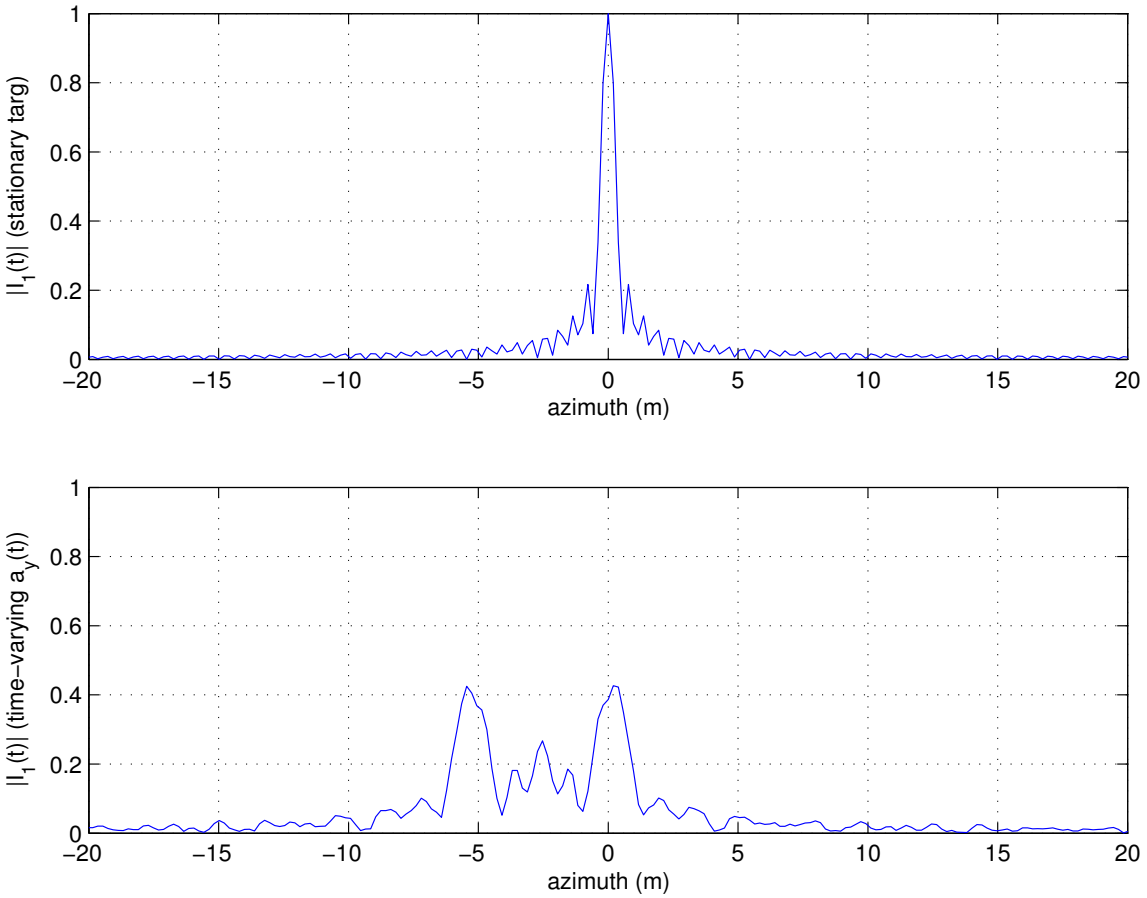

Figure 4.9: Magnitude response (after azimuth compression) of a simulated point target (with time-varying across-track acceleration) focused using a stationary world matched filter versus azimuthal distance. The stationary target response (top) is given as a reference, and an azimuth of 0 metres is broadside. The bottom frame is the response from a target with time-varying across-track acceleration given in Figure 4.8. Note the multiple peaks and reduced peak response due to $a_y(t)$.

many resolution cells. The presence of time-varying across-track acceleration can thus have a severe effect on target focusing.

The focused (azimuth compressed) target responses to additional across-track acceleration scenarios were also tested. The time-varying acceleration effects can be seen more clearly by introducing accelerations which are asymmetric about broadside time. In a second simulation, an across-track acceleration of 0.1 m/s^2 is introduced 0.8 seconds after broadside time, maintained for one second, and then once again dropped to zero. Plots of the time-varying velocity and acceleration, and the focused target track (when applying a SWMF) are shown in Figure 4.10. These may be compared with the response from a stationary target shown in the top portion of Figure 4.9.

In both acceleration scenarios (from Figures 4.9 and 4.10 (b)), smearing of the focused responses, decreased peak power, and increased -3 dB widths of the peak are evident. Spurious responses are introduced to one side of broadside (where the sidelobe location depends on whether the target is accelerating or decelerating, and whether acceleration occurs before or after broadside time). If acceleration is asymmetric about broadside time (as in Figure 4.10), the smearing will appear in one sidelobe and well-removed from the main target response in azimuth. However, when the acceleration is symmetric about broadside time (as in Figure 4.8), the acceleration sidelobes may overlap the mainlobe response. Again, these findings are confirmed by Carrara who found that cubic phase errors (to which time-varying acceleration contributes) may distort the mainlobe and will raise sidelobes on one side of the impulse response [12].

A third across-track acceleration configuration was simulated in which a stationary target experiences a sudden jump in acceleration of 0.1 m/s^2 at broadside time, after which the acceleration remains constant. Although the acceleration occurs at broadside time, it continues for the remainder of the observation period (as opposed to other scenarios in which it is dropped back to zero), and the acceleration side-

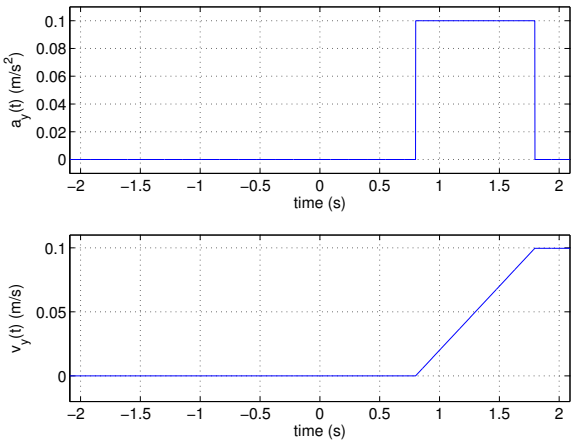

(a) Across-track acceleration $a_y(t)$ (a rectangular window centred at 1.3 s past broadside) and corresponding across-track velocity $v_y(t)$ for a point target through time.

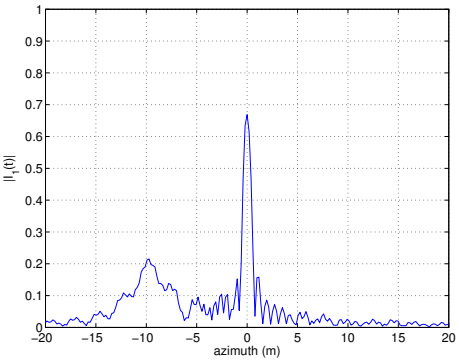

(b) Corresponding magnitude response (after azimuth compression) of a simulated point target (with time-varying across-track acceleration given in the previous figure) focused using a stationary world matched filter versus azimuthal distance.

Figure 4.10: Across-track acceleration $a_y(t)$ (a rectangular window centred at 1.3 s past broadside) for a simulated point target, corresponding across-track velocity $v_y(t)$, and its magnitude response (after azimuth compression) when focused using a SWMF. An azimuth of 0 metres is broadside. Note the large sidelobe and reduced peak response due to $a_y(t)$.

lobes do not interfere with the mainlobe response. The acceleration and velocity time-histories, and the azimuth compressed response for this target are shown in Figures 4.11 and 4.13, respectively. Since the time during which the target experiences

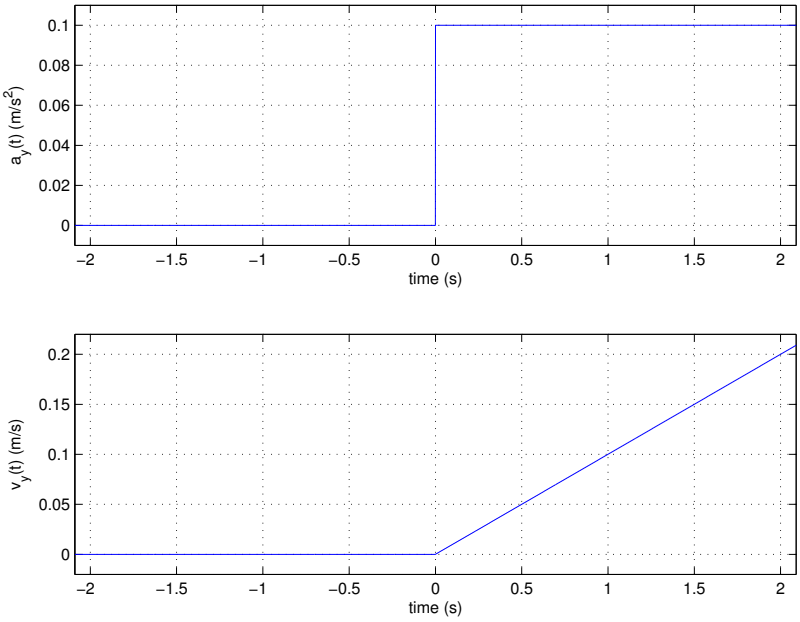

Figure 4.11: Across-track acceleration $a_y(t)$ (a unit step function with height 0.1 m/s^2) and corresponding across-track velocity $v_y(t)$ for a point target through time whose azimuth response to a SWMF is given in Figure 4.13.

acceleration has been greatly extended, this leads to much wider sidelobes prior to broadside time than in the previous scenarios. If the target was decelerating instead of accelerating, the same sidelobes would appear on the opposite side of the peak response (i.e. after t=0 at an azimuth location location greater than 0 m).

A fourth scenario similar to the third simulation was constructed in which the acceleration begins 0.5 seconds before broadside and is then ramped up over 0.5 seconds to 0.1 m/s^2, after which it remains constant for the remainder of the observation period. The ramping is done to avoid sudden changes in acceleration (possibly making the simulation more realistic), although the time-derivative of acceleration is still discontinuous at the times acceleration starts and ends, even with this model. Plots

of the time-varying velocity and acceleration, and the focused target after correlation with the SWMF are shown in Figures 4.12 and 4.13. The focused response from the ramped accelerating target is similar to that from the target with sudden acceleration change, although the acceleration sidelobe in the ramped case has been shifted slightly further from broadside since the acceleration begins earlier in the observation interval.

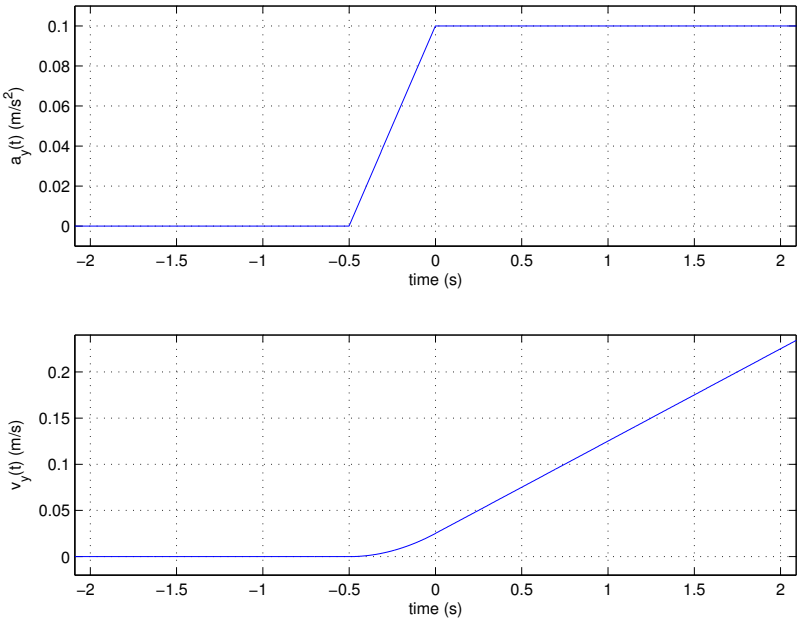

Figure 4.12: Across-track acceleration $a_y(t)$ and corresponding across-track velocity $v_y(t)$ for a point target through time whose azimuth response to a SWMF is given in Figure 4.13. The acceleration has been slowly ramped up over 0.5 seconds to simulate more realistic vehicle situations.

Summarizing, both continuous and discontinuous time-varying across-track acceleration results in asymmetrical sidelobes in the azimuth compressed image after focusing with a SWMF. Even small changes in a_y over the course of the synthetic aperture will create significant sidelobes. Simulations using similar (e.g. 0.1 m/s^2) changes in along-track acceleration a_x had insignificant effects on azimuth focusing, and thus a separate section of results is not presented.

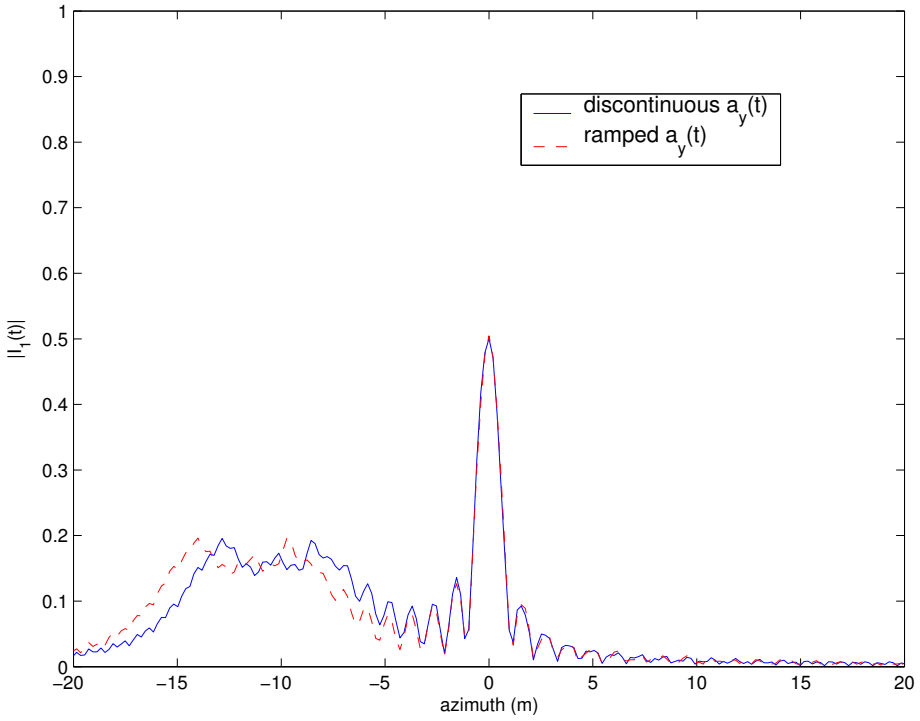

Figure 4.13: Magnitude response (after azimuth compression) of simulated point targets (with time-varying across-track accelerations given in Figures 4.11 and 4.12) focused using a stationary world matched filter versus azimuthal distance. Responses from both discontinuous and ramped accelerations are given, and an azimuth of 0 metres is broadside. Note the similar smeared azimuthal response and reduced peak response due to $a_y(t)$ in both cases.

Focusing in a spaceborne geometry

Having examined the influence of target acceleration on focusing for an airborne scenario, simulations of a spaceborne geometry were conducted. Parameters typical of the RADARSAT-2 sensor (see Table 3.2) were used in the simulations. As in the previous spaceborne simulations, the azimuthal beamwidth was set as 0.4°, although the PRF was increased to its maximum value of 3800 Hz to increase the level of detail visible in the focused response. Again, as described in section 3.2.6, the simulations did not account for earth curvature or rotation effects, but should give an indication of the consequences of uncompensated target motion on focusing for the space-based case.

Uncompensated across-track velocity v_{y0} results in significant shifts off of broadside (as observed for the airborne case) for even small velocities (e.g. a shift of -90 m off broadside is observed for a constant $v_y = 1$ m/s). However, the spaceborne case is less sensitive to along-track velocity v_{x0}. This is due to the fact that the quadratic term $(v_{x0} - v_a)^2/(2R_0)$ from the range equation (equation 2.11) is not heavily influenced by v_{x0} due to the very large v_a component, such that along-track velocities upwards of 5 m/s are required before smearing effects become evident. The magnitude responses of a stationary target and moving targets with constant velocity for the RADARSAT-2 spaceborne geometry are shown in Figure 4.14. The -3 dB azimuth resolution is on the order of 3.6 m for the stationary target (compared to 0.5 m in the airborne scenario) due to the shortened coherent integration time in the space-based case of one second (instead of 4.2 s as in the airborne scenario).

Although along-track velocity and across-track acceleration both appear in the quadratic term of the range equation (equation 2.11), the $y_0 a_{y0}/(2R_0)$ term is of the same order in both the airborne and spaceborne cases, and thus across-track acceleration is expected to have a larger impact on spaceborne target focusing than along-track velocity. Simulations reveal that across-track accelerations on the order of 0.1 m/s^2 or larger are required before smearing is noticeable, where the slightly

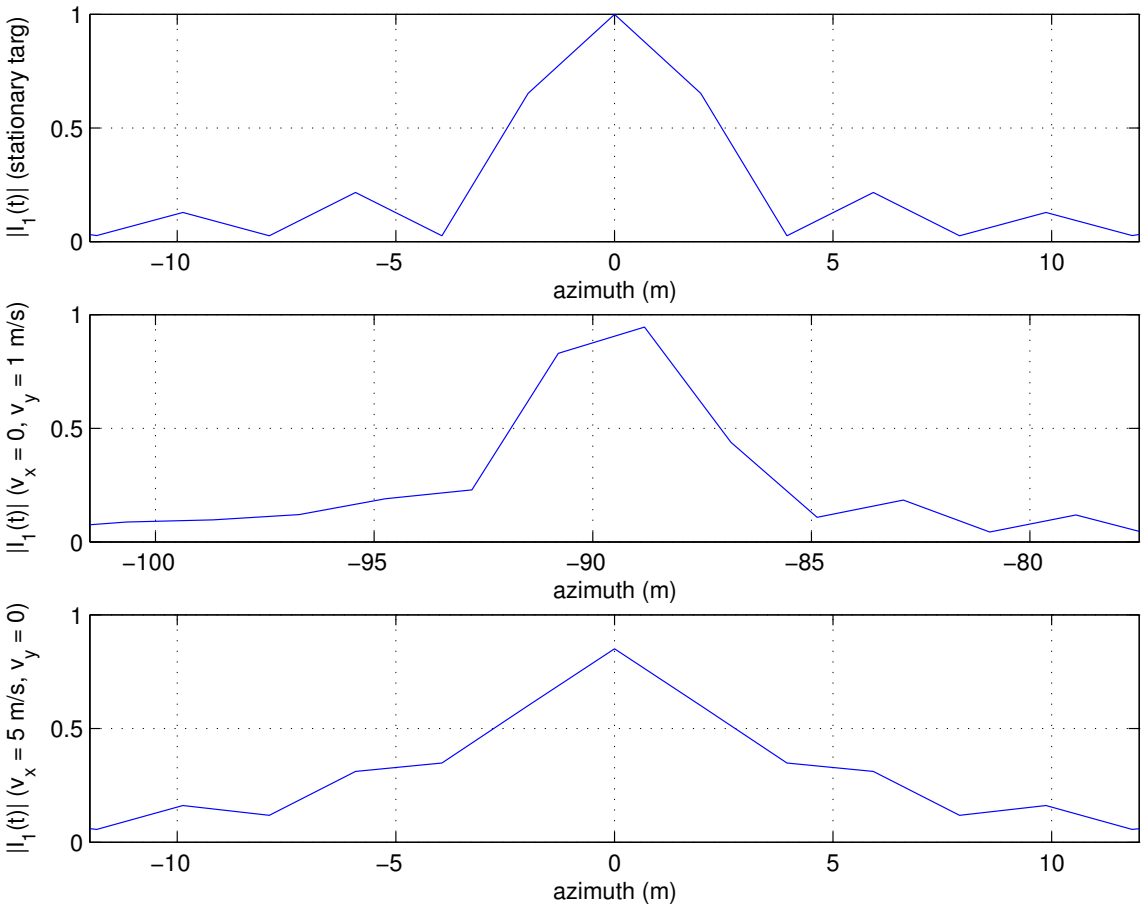

Figure 4.14: Magnitude response (after azimuth compression) of simulated non-accelerating point targets focused using a stationary world matched filter versus azimuthal distance for a spaceborne geometry. The stationary target response is given as a reference, and an azimuth of 0 metres is broadside. Top: stationary target. Middle: target with across-track velocity ($v_y = 1$ m/s, $v_x = 0$). Bottom: target with along-track velocity ($v_y = 0$, $v_x = 5$ m/s). Note the large azimuthal shift due to v_y and the azimuthal smearing due to v_x.

reduced sensitivity to acceleration compared to the airborne case is due to the coarser azimuthal resolution. The middle frame of Figure 4.15 shows the severe smearing resulting from a simulated target with a_y=0.2 m/s^2.

Along-track acceleration appears in the cubic term of equation 2.11 as the factor $a_{x0}(v_{x0}-v_a)/(2R_0)$, which is approximately two times smaller in the spaceborne versus airborne case. Additionally, this factor is multiplied by t^3, which is small for $|t| < 1$, thus reducing the contribution of the third-order term to the range equation due to the shortened observation time in the spaceborne scenario. As a consequence, only extremely large along-track accelerations of 10 m/s^2 or higher (which are unrealistic for the ground vehicles of interest) will have a discernible impact on the focusing of moving targets. The lower frame of Figure 4.15 depicts the magnitude response from a simulated target with a_x = 10 m/s^2, where the small azimuthal shift and raised sidelobes due to an uncompensated cubic term are visible.

Similarly to a_x, time-varying across-track acceleration is not as much of a concern in the spaceborne case due to the shortened synthetic aperture time of one second for the RADARSAT-2 scenario. Again, largely unrealistic acceleration rates of change (e.g. $\dot{a}_{y0} > 5$ m/s^3) were required to influence target focusing.

Consequences of a zero-velocity assumption

This section has revealed the severe effects of uncompensated target motion on the focused magnitude response from a point target for both airborne and spaceborne geometries. When focused using a SWMF, across-track velocity results in a large azimuthal displacement from a scatterer's true position, having ramifications on image interpretation if it is not known whether the object is moving, or if its direction and speed are unknown.

Along-track velocity creates severe spreading of the impulse response, such that targets may be indistinguishable from the background clutter in the azimuth compressed imagery. The airborne scenario has a greater sensitivity to along-track target motion than the RADARSAT-2 spaceborne case, although there will a noticeable im-

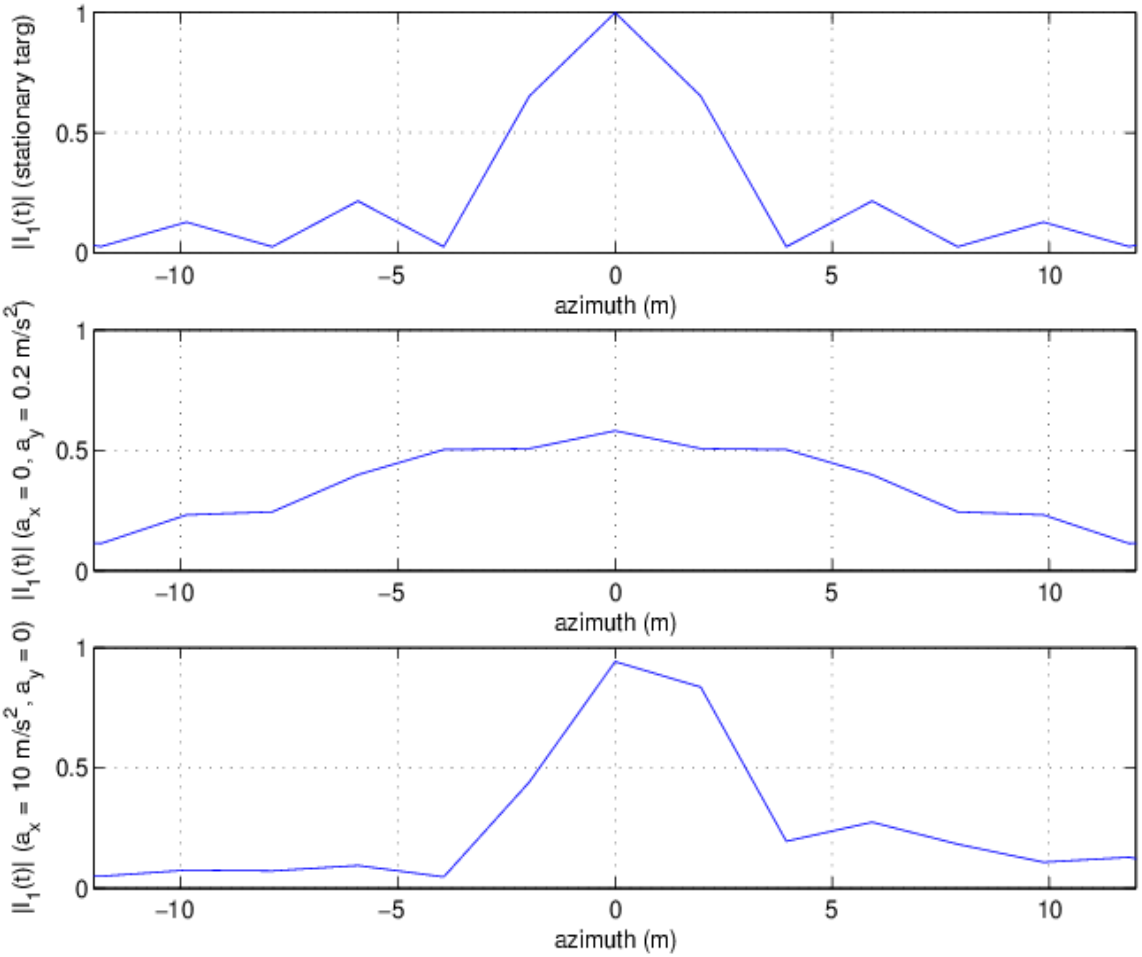

Figure 4.15: Magnitude response (after azimuth compression) of simulated point targets with constant acceleration focused using a stationary world matched filter versus azimuthal distance for a spaceborne geometry. The stationary target response is given as a reference, and an azimuth of 0 metres is broadside. Top: stationary target. Middle: target with constant across-track acceleration ($a_y = 0.2$ m/s^2, $a_x = 0$) and zero velocity at broadside. Bottom: target with constant along-track acceleration ($a_y = 0$, $a_x = 10$ m/s^2) and zero velocity at broadside. Note the azimuthal smearing due to a_y and the asymmetric sidelobes due to a_x.

pact on the compressed imagery using either platform for the range of target velocities of interest.

Across-track acceleration results in a small azimuthal shift (whose magnitude is also dependent upon the broadside across-track velocity v_{y0}) and significant smearing of the target magnitude response. Both the airborne and spaceborne geometries are sensitive to this parameter, and even small accelerations on the order of 0.1 m/s^2 will result in a severely defocused magnitude response. Mismatched reference filters due to uncompensated v_{x0} and a_y may also influence target detection if detection is performed in the azimuth compressed domain, since the signal-to-clutter (SCR) ratio may be lowered to below 0 dB as the target energy is spread across multiple azimuth cells.

Along-track acceleration and time-varying across-track acceleration will create asymmetric raised sidelobes which may be mistaken as additional targets in the focused image. For velocities typical of ground vehicles, these terms pose a potential problem in the airborne scenario only, since the cubic term of the range equation (in which these motion parameters appear) is much smaller in the space-based case.

4.1.3 Focusing a moving target with a matched reference filter

The previous section described the effects on focused imagery when applying a SWMF to a moving target. In those cases, the correlation could not be performed analytically due to exponential quadratic and cubic terms, and azimuth compression was performed numerically. However, if these exponential quadratic and cubic terms were removed by the reference filter, the integration could be completed in closed form. The following sections investigate the form of the focused target response when a perfectly matched filter is used and when one matched to the quadratic (but not linear) term is used. Finally, estimation of the target motion parameters (essential in defining a properly matched reference filter) is briefly discussed.

Note that if a range compressed signal matrix is focused using a filter matched

to the motion of one target, it results in all other signals being mismatched (i.e. defocused) in the processed image. Since there are a variety of motions affecting the different scatterers in a scene, they cannot all be optimally processed simultaneously [64]. The signal strength of a target refocused under a perfectly matched filter is expected to increase due to the coherent integration gain. Meanwhile, stationary targets such as discrete clutter will be blurred in the output of a moving target filter [41]. Thus, the moving target filter suppresses clutter magnitudes and leads to increased signal-to-clutter ratios (SCRs), which may be a significant advantage in detection and parameter estimation.

Perfectly matched moving target filter

Although no closed form expression may be derived when correlating a moving target with a SWMF, one may consider the response of the fore channel data to a filter $r_{1\ matched}(t)$ which is matched to the correct v_{x0}, v_{y0}, a_{y0}, a_{x0} and $\dot{a}_{y0}$:

$$\begin{aligned} r_{1\ matched}(t) &= \exp\left(-2jk(R_1(t) - R_0) \right) \text{rect}\left(\frac{t}{T}\right) \qquad (4.9) \\ &= \exp\left(-2jk\left\{ \frac{y_0 v_{y0}}{R_0} t + \frac{1}{2R_0}\left[(v_{x0} - v_a)^2 + v_{y0}^2\left(1 - \frac{y_0^2}{R_0^2}\right) + y_0 a_{y0} \right] t^2 \right.\right. \\ &+ \left.\left. \frac{1}{2R_0}\left[v_{y0} a_{y0}\left(1 - \frac{y_0^2}{R_0^2}\right) + a_{x0}(v_{x0} - v_a) + \frac{y_0\ \dot{a}_{y0}}{3} \right] t^3 \right\} \right) \text{rect}\left(\frac{t}{T}\right). \end{aligned}$$

If the matched filter in equation 4.9 is correlated with the signal $s_1(t)$ given in equation 2.12, there is one residual quadratic term $\int \exp(Ct\tau^2)\ d\tau$ (where C is a constant coefficient) that must be integrated. This term exists for non-zero a_{x0} and $\dot{a}_{y0}$, and results in azimuthal smearing in the compressed SAR response such that it cannot be neglected. Thus, even a perfectly matched filter will not focus the target into a well-defined sinc function if there are significant third-order terms in the Taylor expansion of the range equation.

However, one may consider the scenario in which a_{x0} and $\dot{a}_{y0}$ are zero, such that the third-order term of the Taylor series expansion of the range equation is neglegibly

small. The correlation integral is then a linear function of τ and may be integrated in closed form. Performing the cross-correlation from equation 4.1 and assuming that the antenna gain is removed such that the signal amplitude is no longer a function of time, then the focused moving target image for the fore channel is given by:

$$\begin{aligned} I_1(t) &= \frac{A_1\ (T-|t|)}{T}\ \exp\left(-jk2R_1(t)\right)\ \exp\left(jk\alpha t^2\right) \qquad (4.10)\\ &\cdot\ \ \mathrm{sinc}\left(k(T-|t|)\ \alpha t\right)\ \mathrm{rect}\left(\frac{t}{2T}\right), \end{aligned}$$

$$\text{where} \qquad \alpha = \frac{1}{R_0}\left[(v_{x0}-v_a)^2 + v_{y0}^2\left(1-\frac{y_0^2}{R_0^2}\right) + y_0 a_{y0}\right]. \qquad (4.11)$$

The maximum of $I_1(t)$ occurs when the argument of the sinc function is zero, and thus the peak response of the focused target appears at broadside time t=0 which coincides with the true broadside position of the scatterer. The first zero crossings of $I_1(t)$ occur when the argument of the sinc function is $\pm\pi$, i.e. at:

$$t = \frac{\pm T \mp \sqrt{T^2 - \frac{2\lambda}{\alpha}}}{2}. \qquad (4.12)$$

Assuming typical airborne geometries, the -3 dB width of the sinc function in equation 4.10 is heavily dependent upon the parameters v_{x0} and a_{y0}, and to a much lesser extent on v_{y0}. In section 4.1.1 it was found that a stationary target processed with a SWMF had a -3 dB width of 0.47 metres. Variations in v_{x0}, a_{y0} and v_{y0} (see the quadratic coefficient in equation 2.11) influence the Doppler rate of change between the target and the radar platform, resulting in a broadening or narrowing of the impulse response. If the target is travelling in the opposite direction to the radar platform (with negative v_{x0}), the Doppler rate increases and the available azimuth bandwidth will also increase, thus improving azimuth resolution. Conversely, a target travelling parallel to the radar (with positive v_{x0}) will have a lower Doppler bandwidth and thus a slightly poorer along-track resolution. If the target is accelerating in the positive y (across-track) direction (i.e. away from from the radar with $a_{y0} > 0$), again the increased Doppler bandwidth will give finer azimuth resolution, with the opposite

occurring for target deceleration. The corresponding impulse response functions of a focused target for several test scenarios varying v_{x0} and a_{y0} are shown in Figure 4.16. Along-track velocities of ± 30 m/s worsen/improve the -3 dB width by a factor

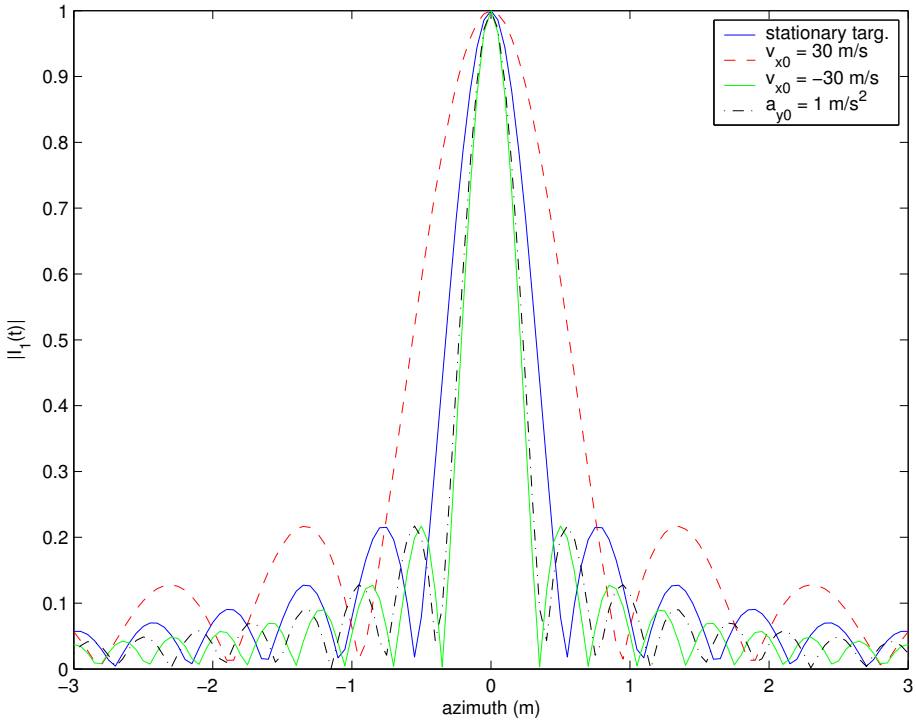

Figure 4.16: Impulse responses of simulated point targets focused using perfectly matched filters. An azimuth of 0 metres is broadside. The -3 dB width of the stationary target response is 0.47 m, 0.82 m for $v_{x0} = 30$ m/s, 0.26 m for $v_{x0} = -30$ m/s and 0.30 m for $a_{y0} = 1$ m/s^2.

of approximately 1.7, and across-track accelerations of ± 1 m/s^2 improve/worsen the -3 dB width by a factor of 1.6.

These results are expected based on the azimuthal slow-time resolution predicted in equation 4.12; positive v_{x0} and negative a_{y0} will decrease the value of the square root term from T (and thus coarsen the resolution) whereas negative v_{x0} and positive a_{y0} will have the reverse effect (improving resolution by allowing the square root term to approach T). Since v_{y0}^2 (from α in equation 4.11) is expected to be much smaller

than $y_0 a_{y0}$ and v_a^2, its effect on resolution is minor compared with that of a_{y0} and v_{x0}.

Aft Channel We may compute the closed form focused response from the aft signal data if we again use the matched filter from equation 4.9, retaining the linear and quadratic terms and assuming a_{x0} and $\dot{a}_{y0}$ are zero such that the cubic term may be dropped. The reference filter is matched perfectly to the target dynamics, and upon correlation of signal $s_2(t)$ with $r_{1\ \mathrm{matched}}(t)$, the following compressed image is obtained:

$$I_2(t) = \frac{A_2\ (T-|t|)}{T}\ \exp\Bigg(-jk[2R_1(t)+g(t)]\Bigg)\ \exp\Bigg(jk[\alpha t+\beta]t\Bigg) \tag{4.13}$$
$$\cdot\ \mathrm{sinc}\Bigg(k(T-|t|)(\alpha t+\beta)\Bigg)\ \mathrm{rect}\left(\frac{t}{2T}\right)$$

where

$$\beta = \frac{\alpha}{2}\frac{d}{v_a} + \frac{d}{2R_0}(v_{x0}-v_a) \tag{4.14}$$

$$g(t) = \frac{y_0 v_{y0}}{R_0}\frac{d}{v_a} + \alpha\left(\frac{d}{v_a}t + \frac{d^2}{4v_a^2}\right) + \frac{d(v_{x0}-v_a)}{R_0}\left(t+\frac{d}{2v_a}\right), \tag{4.15}$$

and α is given in equation 4.11.

The sinc function in the focused aft channel data is similar to that from the fore channel (see equation 4.10). Despite the added β term in the sinc argument, the peak response of the aft channel is shifted only a few centimetres from that of the fore channel and is thus much less than one resolution cell for typical airborne scenarios (e.g. for $v_x = 30$ m/s, the shift is 9 cm whereas one azimuth resolution cell is over 80 cm in length, although the azimuth pixel spacing is only 19 cm for the CV 580 system). The shift of the sinc peaks when using RADARSAT-2 parameters is four orders of magnitude smaller than in the airborne case. These small shifts will impact the magnitude if the signals are combined (e.g. by computing the DPCA or ATI signal), although the most significant difference between the fore and aft focused signals arises in the extra phase terms. Along-track interferometry (see Chapter 6) makes use of this phase difference for parameter estimation.

Moving target filter matched to the quadratic term

Oftentimes, the across-track velocity v_{y0} of the target is unknown prior to azimuth compression and thus cannot be included in the reference filter. However, even without compensation of target v_{y0}, the target response may be derived in closed form. Assuming that the quadratic term in the signal data is known (where the quadratic coefficient may be estimated using a bank of matched filters, see Chapter 5), and that a_{x0} and $\dot{a}_{y0}$ are zero, the only uncompensated term in the target signal is the linear term containing v_{y0}. The focused response of a target in the fore and aft channels from a reference filter matched to everything but v_{y0} is:

$$I_1(t) = \frac{A_1\ (T-|t|)}{T}\ \exp\left(-jk2R_1(t)\right)\ \exp\left(jk[\frac{y_0 v_{y0}}{R_0}t + \alpha t^2]\right) \tag{4.16}$$
$$\cdot \operatorname{sinc}\left(k(T-|t|)\ \left[\frac{y_0 v_{y0}}{R_0} + \alpha t\right]\right)\ \operatorname{rect}\left(\frac{t}{2T}\right)$$
$$I_2(t) = \frac{A_2\ (T-|t|)}{T}\ \exp\left(-jk[2R_1(t) + g(t)]\right) \tag{4.17}$$
$$\cdot \exp\left(jk[\frac{y_0 v_{y0}}{R_0}t + \alpha t^2 + \beta t]\right)$$
$$\cdot \operatorname{sinc}\left(k(T-|t|)\left[\frac{y_0 v_{y0}}{R_0} + \alpha t + \beta\right]\right)\ \operatorname{rect}\left(\frac{t}{2T}\right),$$

where $I_1(t)$ and $I_2(t)$ are the compressed signals from the fore and aft channels, respectively, α is given in equation 4.11, β in equation 4.14, and $g(t)$ in equation 4.15.

The peak response of the fore channel $I_1(t)$ occurs when the argument of the sinc function goes to zero at time $t = t_{\text{img}}$ from equation 4.7. The focused imaging time is determined primarily by the across-track velocity v_{y0} (assuming y_0, v_a, and R_0 are fixed). This shift in the focused peak away from broadside is the azimuthal shift caused by across-track motion described in section 4.1.2 and well-documented in the literature (e.g. [17, 20, 35, 41, 62, 80, 90, 93]). As before, the aft channel response $I_2(t)$ is centred at essentially the same location as that of the fore channel.

A reference filter matched to the quadratic range term thus enables one to obtain a focused image of the target - albeit at a shifted location from broadside - for non-

zero v_{y0}. Note that there is no smearing of the impulse response due to a reference filter unmatched in across-track velocity. However, the finite azimuth bandwidth of the signal will compromise this focusing, such that a reference filter completely unmatched in v_{y0} may still pose some problems. These issues are further described in Appendix B.1.

Parameter Estimation

A major difficultly in achieving a focused moving target is determining the correct target velocities and accelerations with which to construct the reference filter. The literature describing parameter estimation is quite extensive on determining across-track velocity v_y and slightly less so in determining along-track velocity v_x. No techniques are available with which to estimate accelerations since the problem becomes underdetermined with a greater number of unknowns than equations when only two SAR channels of data are available. In most instances, it is assumed that the targets are moving at a constant velocity, whether or not this is actually the case. A summary of parameter estimation methods used in GMTI was presented in section 2.3.2.

Rather than estimate the target motion parameters themselves, one can compress the signal data with a bank of reference filters initialized with various quadratic and/or linear coefficients. The compressed image from the filter returning the highest magnitude when correlated with the target signal is then retained for subsequent analysis. It may be assumed that this method was applied to initialize the reference filters described in section 4.1.3.

4.2 Experimental Results

After examining the theoretical response of accelerating targets to various matched filters, azimuth compression was carried out on experimental data from the CV 580 airborne system. A description of the data set and its preprocessing is described in Appendix A. It is assumed that the moving targets have already been detected and

have had their tracks extracted through azimuth time as described in section 3.3. It is verified that stationary point targets can be successfully focused before turning our attention to the results of using a SWMF and filters matched to various motion parameters to compress moving targets in azimuth.

4.2.1 Focusing a stationary target

To ensure that the focusing algorithm being applied is correct, the responses from stationary corner reflectors in experimental data were examined. A correct focusing algorithm is critical in examining the effectiveness of matched filtering the moving target track data.

The time domain correlation operation from equation 4.1 is more efficiently implemented in the Fourier domain, where the convolution becomes a multiplication. The Fourier transform of the signal data and the time-reversed complex conjugate of the reference signal are taken using two FFTs. The FFTs are then multiplied together, and the inverse FFT is performed to transform the data back into the time domain. A weighting function (such as a cosine-shaped Hanning window) is applied to the reference function to reduce the sidelobes of the point spread function. When focusing stationary targets, the length of the reference function was set as the length of the -3 dB width at the range bin of interest. For focusing moving targets, the reference function length was chosen to be the length of the detected target track.

Stationary corner reflectors are a reasonable approximation of a point target which may be used to verify the compression algorithm. Unfortunately, in the Petawawa 2000 data all corner reflectors at the designated calibration site were set mere metres from the ARCs (Active Radar Calibrators). Consequently, in the imagery one cannot distinguish the two responses. This was not a problem in a second data set collected in the Ottawa area in 2001 with the same airborne system. Focusing the calibration site data, it was found that the corner reflectors' responses were two-dimensional sinc functions, with -3 dB widths of approximately 0.95 metres in azimuth and 5.6 metres

in range. These values are very close to the resolution limits of the system (quoted as 0.85 metres in azimuth and 5.7 metres in range [46]), and thus the compression algorithm is functioning as expected. Figure 4.17 displays one example of a focused stationary corner reflector from the Ottawa 2001 data set. Note the high peak power and narrow mainlobe of the focused image.

4.2.2 Focusing a moving target with a SWMF

From section 4.1, we expect that moving targets focused using a SWMF may suffer from azimuthal displacement, a loss of peak power, smearing of the impulse response, and asymmetric sidelobes, where the particular image degradations will depend upon their motion parameters.

In order to isolate the target signal and suppress clutter, the DPCA signal was computed for each target track by subtracting the two channels. As described in section 4.1.3, the azimuth compressed fore and aft signals are nearly coincident sinc functions with a phase difference which is a function of the target motion parameters. If compressed using a filter matched to at least the quadratic coefficient, the DPCA signal is a sinc-like response with high peak power and low sidelobes, and is free from clutter interference (although mathematically it is not an exact sinc).

The aircraft headings and target GPS data indicate that each controlled mover had both along-track and across-track motion components. Because each target has non-zero along-track velocity v_{x0} (and possibly non-zero a_y) every target was smeared upon azimuth compression with a SWMF. The focused image after DPCA for one pass of the Convoy target is given in Figure 4.18. The wide mainlobe and low peak power indicate non-zero v_{x0} and/or a_{y0}, and the asymmetric sidelobes point to possible a_{x0} and/or $\dot{a}_{y0}$ acceleration components. Time-frequency analysis is used to obtain a focused image of this target in section 7.3.4.

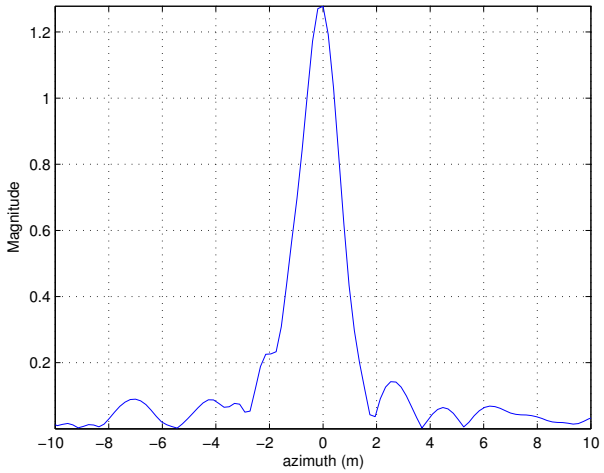

(a) Magnitude response of corner reflector.

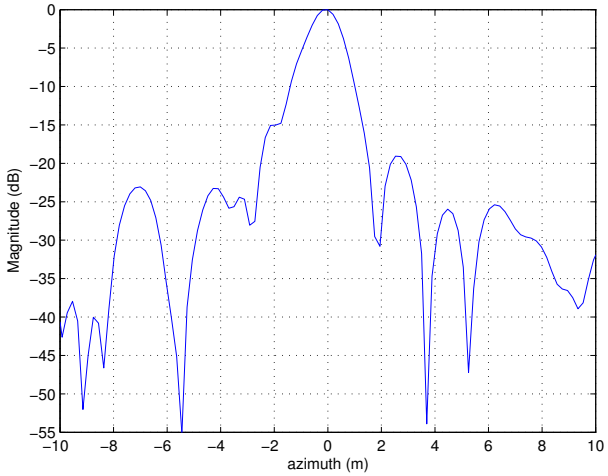

(b) Magnitude response of corner reflector in decibels, normalized to 0 dB.

Figure 4.17: Magnitude response after azimuth compression of a stationary corner reflector from the Ottawa 2001 data set. Note the narrow mainlobe and high peak power. The -3 dB width is approximately 1.1 m.

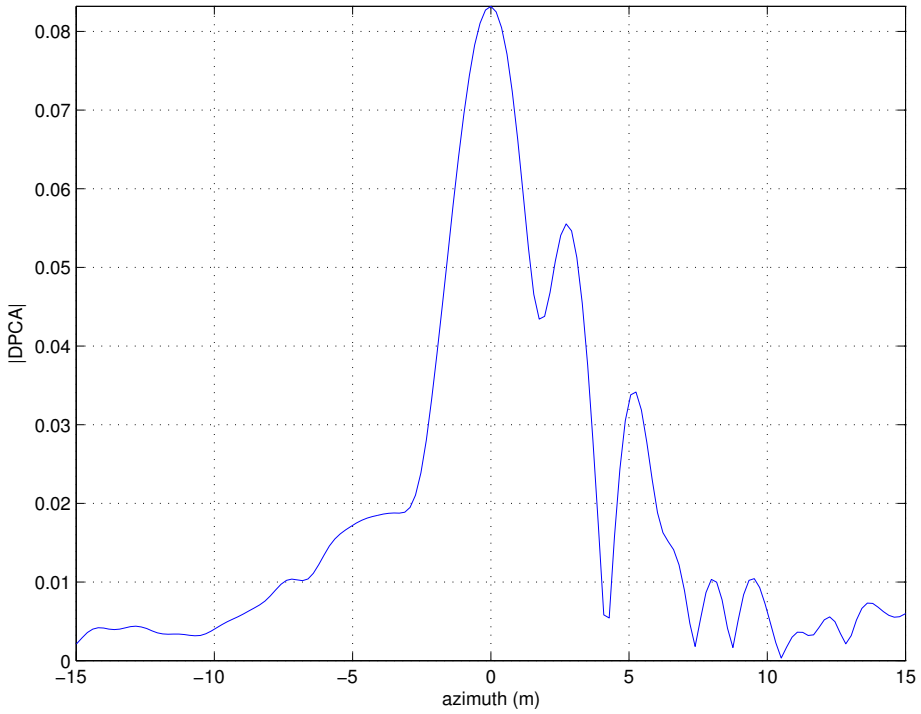

Figure 4.18: Magnitude response (after clutter suppression using DPCA) for a moving target (l1p9 Convoy) focused using a SWMF. Note the low peak power, wide mainlobe, and asymmetric sidelobes which indicate possible acceleration components.

4.2.3 Focusing a moving target with a matched reference filter

Next it was attempted to focus each moving target using a reference filter matched to the quadratic and linear components of the received signal. As described in section 4.1.3, the creation of a matched reference filter requires knowledge of the motion parameter vector. Using a bank of matched filters (which is described more thoroughly in Chapter 5) the quadratic coefficient of the fore channel signal $s_1(t)$ is approximated. Using the ATI phase (described in detail in Chapter 6), the across-track velocity v_{y0} is estimated and used to initialize the linear coefficient of the reference filter. The third-order coefficient is assumed to be negligible, which is a reasonable assumption if there is no acceleration.

However, even after matched filtering with these estimated parameters, most targets remain unfocused, some showing virtually no improvement at all in focusing. Two examples of targets focused using a SWMF and a matched filter initialized with the best estimates of the linear and quadratic signal coefficients are shown in Figures 4.19 and 4.20. A filter matched to the moving target's phase history is abbreviated as MTMF (moving target matched filter). Note that an azimuth of 0 m is arbitrarily set at the location of each peak response such that the width of the mainlobe can be read directly off each graph. In actuality, the position of the focused target will shift significantly in azimuth upon compensation of the linear (v_{y0}) term, as was described in section 4.1. Figure 4.19 shows significant improvement in focusing with the use of a MTMF over a SWMF, such that the mainlobe has narrowed, and there is a higher peak power, although there are still significant sidelobes. The target depicted in Figure 4.20 shows no improvement in focusing with the use of a MTMF, perhaps indicating the presence of a significant uncompensated cubic term or indicating that there is an error in the quadratic coefficient used in the matched filter. Both azimuth compressed targets focused using a MTMF are not ideal sinc functions, and thus there is some uncompensated platform-target motion. The residual sidelobes from both target images are typical of the entire data set. A different method is

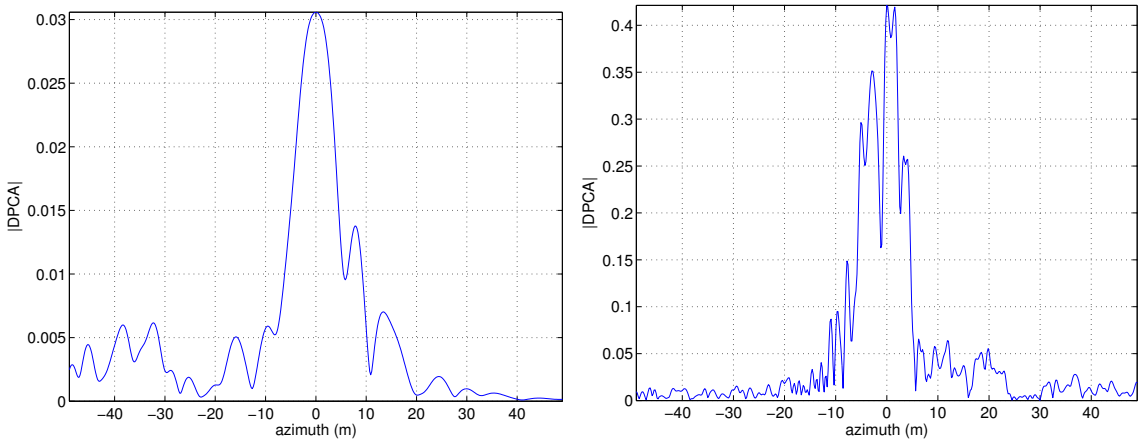

(a) Focused image using a stationary world matched filter (SWMF).

(b) Focused image using a moving target matched filter (MTMF).

Figure 4.19: DPCA magnitude after azimuth compression of one pass of the Convoy target using a stationary world matched filter and a moving target matched filter. Note the change in scale of the y-axes between the two plots. The MTMF is initialized with estimates of the linear and quadratic signal coefficients, although all cubic and higher-order coefficients remain uncompensated. Note the large increase in peak power and narrower mainlobe when filtering with a MTMF, although the response is still not an ideal sinc function, indicating the presence of uncompensated platform-target motion such as an uncompensated cubic term.

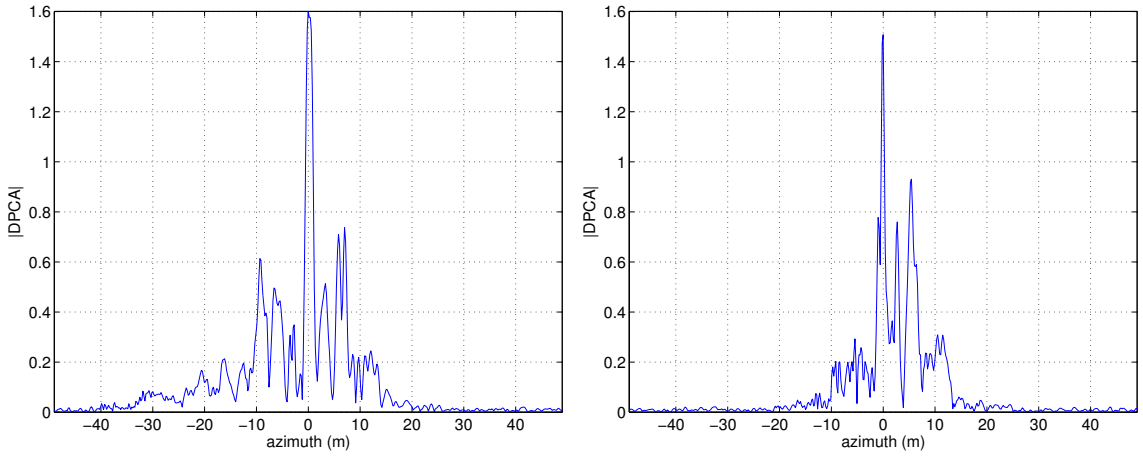

(a) Focused image using a stationary world matched filter (SWMF).

(b) Focused image using a moving target matched filter (MTMF).

Figure 4.20: DPCA magnitude after azimuth compression of one pass of the Juliet target using a SWMF and a MTMF. The MTMF is initialized with estimates of the linear and quadratic signal coefficients, although all cubic and higher-order coefficients remain uncompensated. There is little improvement in focusing between the SWMF and MTMF. Both possess significant sidelobes indicative of uncompensated radar-target motion.

thus required to obtain a focused image of the moving targets. This issue is further examined using time-frequency analysis in Chapter 7.

Having derived the azimuth compressed fore and aft channel expressions in this chapter, we can examine the effects of acceleration on banks of matched filters (for estimation of v_{x0}) and on ATI phase (for estimation of v_{y0}) in the next two chapters.

Chapter 5

Estimation of along-track velocity v_{x0}

After detection of a moving target, it is often desirable to determine its velocity in the along- and across-track directions. This information is useful for monitoring ground vehicles, repositioning them to their true azimuth broadside location on the image, and extrapolating a target's future position.

The objective of this chapter is to describe the impact of acceleration on estimating the along-track velocity v_{x0}, and the repercussions of a zero-acceleration assumption. The effects of acceleration on along- and across-track velocity estimation are very different, which is why the treatment of each velocity component is given in separate chapters.

Along-track velocity estimation is accomplished using a bank of matched filters to focus the target data, and then searching for the filter giving the maximum magnitude response. This algorithm is described, followed by an analysis of the effect of each motion parameter (velocities and accelerations) on the resulting v_{x0} estimate. Simulations of the filter-bank responses to stationary, constant velocity, and accelerating targets are carried out for both airborne and spaceborne geometries. As in the previous chapter, theory and simulations are combined due to difficulties in analytically maximizing the cross-correlation expression involved in azimuth compression. Finally, the matched filter-bank algorithm is applied to experimental data to estimate the along-track velocity of each target. These velocity estimates are compared to GPS velocities, and the similarities and discrepancies between the values are discussed.

5.1 Theory and Simulations

One method of estimating along-track velocity is to apply a bank of reference filters to the target signal to determine which filter best focuses the data [36, 80]. The filters are generally initialized with various v_{x0} velocities and $[v_{y0}\ a_{x0}\ a_{y0}\ \dot{a}_{y0}]^T = \vec{0}$, thus changing the quadratic term of reference filter's range equation (see equation 2.11). The filter returning the highest magnitude when correlated with the target signal corresponds to the filter giving the best focus and thus the best match to the combined quadratic and higher-order terms in the target's range history. In other words we are searching for the value of v_{x0} (where our estimate is denoted $\hat{v}_{x0}$) which maximizes the magnitude of the azimuth compressed response. This velocity can be found by taking the partial derivatives of the azimuth compressed magnitude from equation 4.1 with respect to $\hat{v}_{x0}$ and time t, setting the equation to zero, and solving for $\hat{v}_{x0}$ and t:

$$0 = \frac{d}{d\hat{v}_{x0}\ dt}\left|\frac{1}{T}\ \int_{-\infty}^{\infty} s(t+\tau)\ r^*(\tau)\ d\tau\right|, \tag{5.1}$$

where the reference filter $r(t)$ for best focus is given by:

$$r(t) = \exp\left(-2jk\left[\frac{(\hat{v}_{x0}-v_a)^2}{2R_0}t^2\right]\right)\text{rect}\left(\frac{t}{T}\right). \tag{5.2}$$

However, as will be shown in section 5.1.1, equation 5.1 cannot be solved in closed form, and a numerical solution over a two-dimensional search space is required to determine $\hat{v}_{x0}$. The effect of each motion component on the estimation of along-track velocity is examined below.

5.1.1 Estimating v_{x0} for a target with only along-track velocity

The simplest scenario is one in which it is desired to estimate along-track velocity v_{x0} when the target is only moving in the along-track direction with constant velocity. In this case, the range compressed signal from the fore channel $s_1(t)$ is modelled by:

$$s_1(t) = A\exp\left(-2jk\left[R_0 + \frac{1}{2R_0}(v_{x0}-v_a)^2t^2\right]\right)\text{rect}\left(\frac{t}{T}\right) \tag{5.3}$$

Substituting equations 5.2 and 5.3 into the maximization from equation 5.1 we have the following:

$$\begin{aligned} 0 &= \frac{d}{d\hat{v}_{x0}\ dt}\left|\frac{1}{T}\ \int_{-\infty}^{\infty} A\exp\left(-2jk\left[R_0+\frac{1}{2R_0}(v_{x0}-v_a)^2(t+\tau)^2\right]\right)\right. \\ &\quad \left.\cdot\exp\left(2jk\left[\frac{(\hat{v}_{x0}-v_a)^2}{2R_0}\tau^2\right]\right)\ \text{rect}\left(\frac{t+\tau}{T}\right)\text{rect}\left(\frac{\tau}{T}\right)\ d\tau\right|. \end{aligned} \tag{5.4}$$

Terms not a function of τ may be pulled out of the integration and the exponential terms may be regrouped as:

$$\begin{aligned} 0 &= \frac{d}{d\hat{v}_{x0}dt}\left|\frac{A}{T}\exp\left(-2jk\left[R_0+\frac{1}{2R_0}(v_{x0}-v_a)^2t^2\right]\right)\right. \\ &\quad \cdot\int_{-\infty}^{\infty}\exp\left(-2jk\left[\frac{(v_{x0}-v_a)^2}{2R_0}(2t\tau)+\frac{1}{2R_0}\left[(v_{x0}-v_a)^2-(\hat{v}_{x0}-v_a)^2\right]\tau^2\right]\right) \\ &\quad \left.\cdot\ \text{rect}\left(\frac{t+\tau}{T}\right)\text{rect}\left(\frac{\tau}{T}\right)\ d\tau\right|. \end{aligned} \tag{5.5}$$

Analytically equation 5.5 cannot be solved in closed form because of the integration of the exponential quadratic term τ^2. Instead, a two-dimensional search over the synthetic aperture time $-T/2 \leq t \leq T/2$ s and over the along-track velocity range of interest (e.g. $-30 \leq v_{x0} \leq 30$ m/s) is required to determine the parameters returning the maximum magnitude in the azimuth compressed response. This search can be performed using a simple algorithm to create a bank of reference filters initialized with various v_{x0} values. The signal data is convolved with each reference filter in turn, and the output is saved to a matrix, which is then scanned to find the location of the maximum magnitude value. Oftentimes, the DPCA signal is compressed using the filter-bank rather than only the fore or aft channel in order to avoid obtaining maxima due to clutter from discrete targets.

Along-track velocity was estimated using this filter-bank and search method for simulated signal data of a point target travelling in the along-track direction. The DPCA signal was not used since it is zero for $v_{y0} = 0$, as was described in Chapter 3, and here we wish to observe the effects of a v_{x0} velocity component only. From

equation 5.5, it is seen that if $\hat{v}_{x0} = v_{x0}$, then the quadratic τ^2 term in the integration disappears and the azimuth compressed signal will be the modulated sinc function given in equation 4.10. This sinc function has high peak power (there is no azimuthal smearing), and it is thus expected that this reference filter will give the largest magnitude response in the compressed imagery at broadside time $t = 0$.

Simulations were used to verify the unbiasedness of the $\hat{v}_{x0}$ estimate for a target moving only with constant v_{x0} and all other motion parameters set to zero. An airborne geometry typical of the CV 580 system (with radar and geometry parameters given in Table 3.1) was simulated. A point target was given an along-track velocity v_{x0} of 10 m/s, with all other velocity components set to zero. A filter-bank of 300 reference filters was created with azimuth velocities ranging from -30 to 30 m/s. Along-track velocities were evenly spaced along this interval every 0.2 m/s. Figure 5.1 shows an enlarged image of the resulting 'filter-bank map' after azimuth compression with each reference filter. Each row of the filter-bank map corresponds to the output after compression using one reference filter. There is a clear peak at a $v_{x0} = 10$ m/s (the true target velocity) and time $t = 0$ (the true broadside position of the target), and thus the estimate is unbiased.

5.1.2 Estimating v_{x0} in the presence of v_{y0}

Next, the estimation of v_{x0} using the filter-bank method is investigated in the presence of non-zero across-track velocity v_{y0}. Again, the analytical expression maximizing the magnitude response cannot be solved in closed form. However, we can use observations from section 4.1.3 to predict the output of the matched filter-bank method for non-zero v_{x0} and v_{y0}. When compressing a signal with a reference filter matched to the quadratic component of the target signal but not the linear component (as in section 4.1.3), it was found that the focused response is still a sinc function although it is shifted in azimuth to a position related to the across-track velocity v_{y0}. Thus, we expect that a target with non-zero v_{y0} will give a well-focused peak in the filter-bank

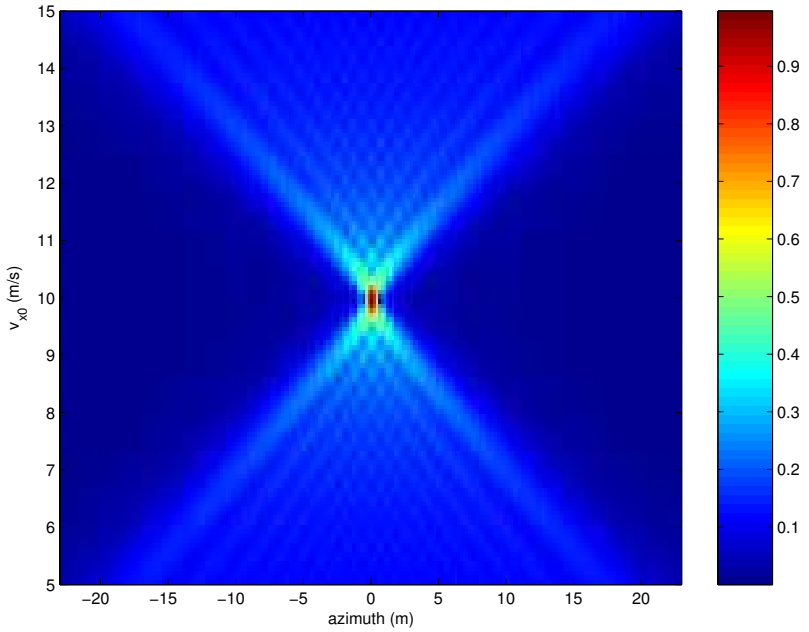

Figure 5.1: Magnitude responses of a simulated point target with constant $v_{x0} = 10$ m/s (and all other motion parameters set to zero) after compression with a bank of reference filters initialized with various v_{x0} velocities. An azimuth of 0 m is broadside. Note that $\hat{v}_{x0}$ (estimated from the location of peak power) matches the true target velocity of 10 m/s.

map, although it will be shifted away from broadside.

One problem with the proposed matched filter-bank algorithm is that it assumes the quadratic coefficient in the range equation is due solely to contributions from along-track target-platform motion (i.e. from v_{x0} and v_a). However, as seen in equation 2.11, the second-order component of the range equation also contains a $v_{y0}^2(1-y_0^2/R_0^2)$ term which will bias the estimation of v_{x0}, especially in the presence of large v_{y0} velocities. This bias can be determined by equating the assumed quadratic coefficient (from the reference filter of equation 5.2) with the true quadratic coefficient (from equation 2.11):

$$\frac{1}{2R_0}\left[(\hat{v}_{x0}-v_a)^2\right] = \frac{1}{2R_0}\left[(v_{x0}-v_a)^2 + v_{y0}^2\left(1-\frac{y_0^2}{R_0^2}\right)\right]. \tag{5.6}$$

Solving for $\hat{v}_{x0}$:

$$\hat{v}_{x0} = v_a - \sqrt{(v_{x0}-v_a)^2 + v_{y0}^2\left(1-\frac{y_0^2}{R_0^2}\right)}, \tag{5.7}$$

where it has been assumed that $|v_{x0}| \ll |v_a|$ such that only one solution is retained. The bias in the velocity estimate is $(\hat{v}_{x0} - v_{x0})$.

According to equation 5.7, the largest biases in $\hat{v}_{x0}$ will occur for large positive v_{x0} and large v_{y0} of either sign. For example, for a moving point target with $v_{x0} = v_{y0} = 30$ m/s and zero acceleration, equation 5.7 predicts a bias of 2.7 m/s for the CV 580 airborne scenario. A target travelling completely in the across-track direction (i.e. $v_{x0} = 0$) with large $v_{y0} = 30$ m/s will create a bias of 2.1 m/s in the estimate of v_{x0} (from equation 5.7). The output filter-bank map for this situation from a simulated point target after DPCA is shown in Figure 5.2. As expected there is an azimuthal shift in the location of the peak response away from broadside due to the presence of across-track velocity v_{y0}. The azimuthal shift is not 1.5 km (as predicted by the t_{img} of equation 4.7 multiplied by v_a) due to the finite synthetic aperture footprint; the focused response must fall within the synthetic aperture such that the response wraps around to give the -88 m displacement observed in Figure 5.2. As predicted by equation 5.7, the $\hat{v}_{x0}$ estimated from the filter-bank approach is biased by 2.1 m/s

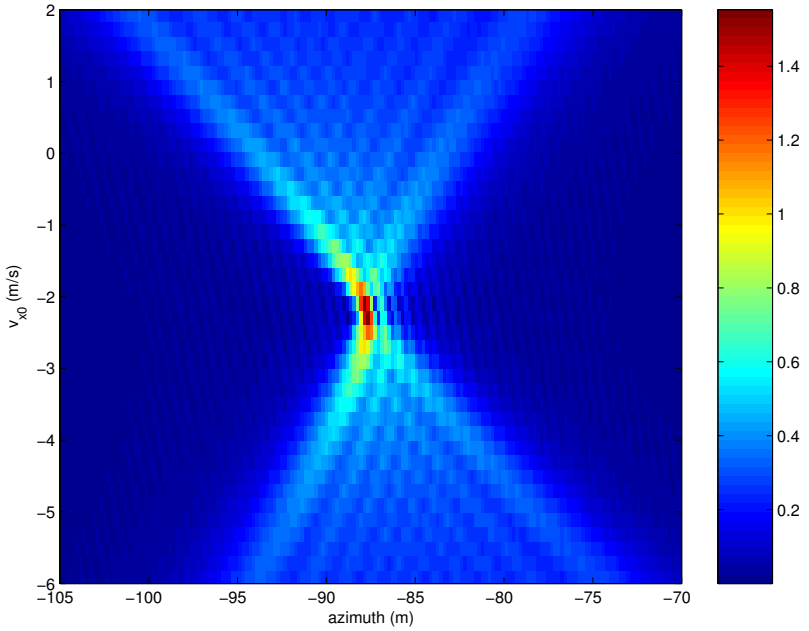

Figure 5.2: DPCA magnitude responses of a simulated point target with $v_{y0} = 30$ m/s (and all other motion parameters set to zero) after compression with a bank of reference filters initialized with various v_{x0} velocities. An azimuth of 0 m is broadside. Note that $\hat{v}_{x0}$ (estimated from the location of peak power) is biased by 2.1 m/s, since the true along-track velocity is zero.

(since the true along-track velocity is zero). This bias is due to ignoring the v_{y0}^2 term in the second-order coefficient of the range equation.

However, biases due to non-zero v_{y0} are not overly severe, and there are methods of compensating for such errors. Large biases upwards of 2 m/s are only observed for very large across-track velocities, whereas smaller v_{y0} do have a significant effect. For instance, an across-track velocity of 10 m/s introduces biases on the order of only 0.2 m/s into the estimation of $\hat{v}_{x0}$. As well, a more accurate estimate of $\hat{v}_{x0}$ can be found if estimation is performed in an iterative fashion. For example, one can estimate v_{x0} using the filter-bank approach, and use this value to compress the signal. The across-track velocity v_{y0} can then be estimated from the focused signal using along-track interferometric phase (see Chapter 6), and then $\hat{v}_{y0}$ can be used to derive a revised $\hat{v}_{x0}$. This process can be repeated to converge upon the true along-track velocity. It should be noted that these computations have assumed perfect knowledge of the aircraft along-track velocity v_a and incidence angle to the target $\theta_{\text{inc}} = \sin^{-1}(y_0/R_0)$, which may not always be the case for experimental data.

5.1.3 Estimating v_{x0} in the presence of a_{y0}

When a target possesses an across-track acceleration component, estimation of v_{x0} becomes challenging. Both a_{y0} and v_{x0} determine the value of the second-order coefficient of the range equation (equation 2.11), and their effects are difficult to separate. As discussed in section 4.1.2, uncompensated v_{x0} and a_{y0} both cause severe defocusing of the target in the azimuth compressed response. If it is assumed that a target has constant velocity when it is actually accelerating, this acceleration will be mistaken for along-track velocity and there may be a sizeable bias in the estimate of $\hat{v}_{x0}$.

The magnitude of the bias can be examined by again equating the assumed quadratic coefficient (from the reference filter of equation 5.2) with the true quadratic coefficient (from equation 2.11):

$$\frac{1}{2R_0}\left[(\hat{v}_{x0} - v_a)^2\right] = \frac{1}{2R_0}\left[(v_{x0} - v_a)^2 + v_{y0}^2\left(1 - \frac{y_0^2}{R_0^2}\right) + y_0 a_{y0}\right]. \tag{5.8}$$

Solving for $\hat{v}_{x0}$ we obtain:

$$\hat{v}_{x0} = v_a - \sqrt{(v_{x0} - v_a)^2 + v_{y0}^2 \left(1 - \frac{y_0^2}{R_0^2}\right) + y_0 a_{y0}}, \tag{5.9}$$

where the bias is again $(\hat{v}_{x0} - v_{x0})$.

Assuming $v_{y0} = 0$ in order to isolate the effects of a_{y0}, and assuming an airborne geometry typical of the CV 580 system, equation 5.9 predicts a bias of -23.5 m/s for an acceleration of $a_{y0} = 1$ m/s^2 and $v_{x0} = 0$. Even a slight acceleration of $a_{y0} = 0.1$ m/s^2 introduces a bias of -2.5 m/s, as shown in the filter-bank map of Figure 5.3. The DPCA response is not shown because it is negligible when $v_{y0} = 0$, as in this scenario.

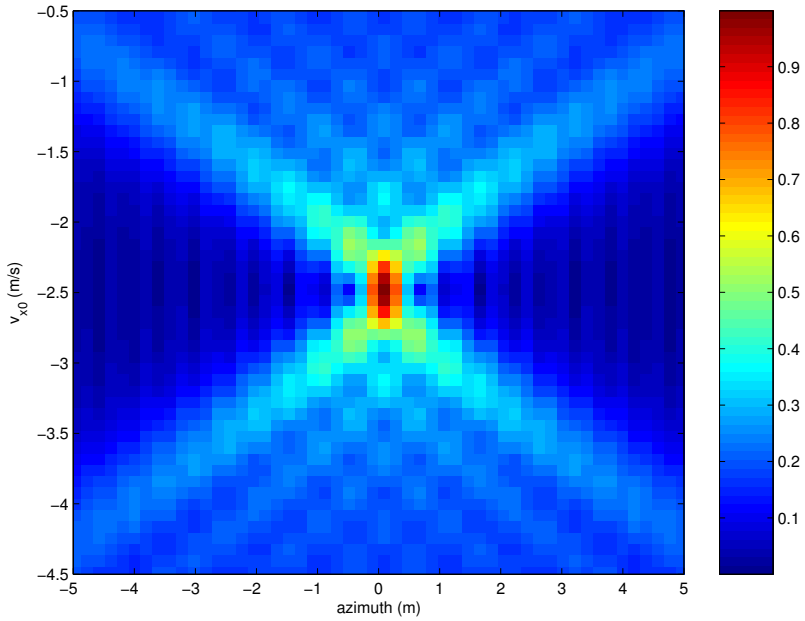

Figure 5.3: Magnitude responses of a simulated point target with $a_{y0} = 0.1$ m/s^2 (and all other motion parameters set to zero) after compression with a bank of reference filters initialized with various v_{x0}. An azimuth of 0 m is broadside. Note that $\hat{v}_{x0}$ (estimated from the location of peak power) is biased by -2.5 m/s, since the true along-track velocity is zero.

Across-track acceleration can thus introduce significant biases when estimating $\hat{v}_{x0}$ if it assumed that targets travel at a constant velocity. However, even if one

acknowledges the possibility of across-track acceleration, a_{y0} will be indistinguishable from v_{x0}; they are both contained in the quadratic coefficient of the range equation and they cannot be estimated independently in the absence of *a priori* data (such as from inertial systems onboard the target) or additional SAR channels.

Across-track acceleration combined with non-zero across-track velocity (as is generally the case in realistic moving target scenarios) introduces a small cubic component into the target range history according to equation 2.11. From the range equation it is theoretically possible to solve for a_{y0} (assuming $a_{x0} = \dot{a}_{y0} = 0$) by implementing a three-dimensional match filter-bank algorithm to determine the third-order coefficient. However, for the range of target velocities and accelerations of interest, the contribution of a_{y0} to this component is virtually negligible; it is a_{x0} and $\dot{a}_{y0}$ which are dominant in determining the cubic component.

5.1.4 Estimating v_{x0} in the presence of a_{x0}

In the presence of an along-track acceleration component, the target signal has a significant cubic term as predicted in the range equation (see equation 2.11). When the filter-bank method is applied to the data, it is attempted to match a quadratic reference filter to a cubic signal. As described in section 4.1.2, this results in an uncompensated third-order component whose impacts on the azimuth compressed response include:

- a smearing of the target energy across multiple v_{x0} velocities in the filter-bank and multiple cells in azimuth, which severely decreases peak power
- the creation of two v_{x0} peaks (instead of one) (where, for instance, the peaks are shifted from zero in the stationary case to ± 0.3 m/s for an $a_{x0} = 0.5$ m/s^2 and all other motion parameters set to zero)
- a slight shift in the azimuth focused position (the two peaks focus at an azimuth 0.4 m away from broadside for an $a_{x0} = 0.5$ m/s^2 and all other motion

parameters set to zero)

Some of these effects may be seen in a comparison between the filter-bank magnitude image of a stationary target, and a target with $a_{x0} = 0.5$ m/s^2 (with all other motion paramters set to zero) in Figure 5.4. The most striking effect is the decrease

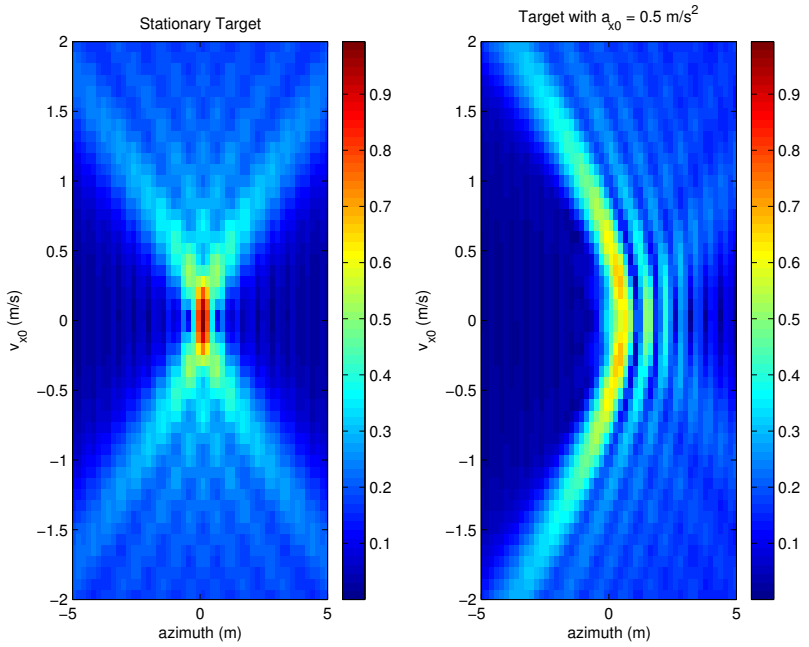

Figure 5.4: Magnitude responses of a simulated point target with $a_{x0} = 0.5$ m/s^2 (and all other motion parameters set to zero) after compression with a bank of reference filters initialized with varying v_{x0}. An azimuth of 0 m is broadside. Note the smearing of target energy across multiple v_{x0} velocities in the accelerating case, and the small bias in estimated $\hat{v}_{x0}$ on the order of 0.3 m/s.

in peak power of the target responses (evident from the common color bars between the accelerating and stationary cases); the full target energy is never captured by one v_{x0} filter since none of the reference filters represents the true phase history of the target through time. This uncompensated cubic term creates asymmetric sidelobes (visible in Figure 5.4 as fringes extending in the positive azimuth direction) as was observed in section 4.1.2. Also apparent in Figure 5.4 is the smearing of target energy across multiple v_{x0} filters. This effect is perhaps most easily examined in the

time-frequency domain (which was introduced in section 2.4). As mentioned in section 2.4.2, time-frequency analysis is useful for examining a target's instantaneous Doppler frequency, which may be found by taking the derivative of the target phase history and dividing by 2π to obtain units of Hz. Recall that the target phase history is given by the argument of the exponential term in equations 2.24 and 2.25 for the fore and aft channels, respectively, yielding a quadratic expression for instantaneous frequency. However, if there is no target acceleration, frequency varies linearly with time and reduces to the following equation:

$$f(t) = \frac{-2}{\lambda}\left[\frac{y_0 v_{y0}}{R_0} + \frac{1}{2R_0}\left[(v_{x0} - v_a)^2 + v_{y0}^2\left(1 - \frac{y_0^2}{R_0^2}\right)\right]t\right], \tag{5.10}$$

where $f(t)$ represents the instantaneous frequency.

The time-frequency history for a non-accelerating target can thus be represented by a line, whose slope is determined principally by v_{x0} and whose y-intercept is determined by v_{y0}. The line has finite start and end points determined by the synthetic aperture length. Matched filtering correlates this time-frequency line with a reference signal. This reference is generally chosen as another line; a stationary world matched filter (SWMF) is a line with a y-intercept of zero, and a slope of $-v_a^2/(\lambda R_0)$.

When attempting to focus a target, a bank of matched filters is initialized with various v_{x0} velocities (i.e. lines of various slopes in the TF domain). The filter returning the highest magnitude when correlated with the target signal corresponds to the chosen estimate of v_{x0}. However, for a target with non-zero a_{x0}, the time-frequency history is a quadratic function (as opposed to a linear one), and thus there is no one best v_{x0} filter (or TF line) to capture the entire target energy. An exaggerated diagram of this effect is illustrated in Figure 5.5.

In reality the time-frequency history will appear only slightly non-linear since the quadratic TF coefficient is much smaller than the linear coefficient. However, the effect is significant enough to impact the matched filtering process. In Figure 5.4, two peaks are observed in the filter-bank of the accelerating target. This could be due to two lines of different slopes (as pictured in Figure 5.5) giving relatively large

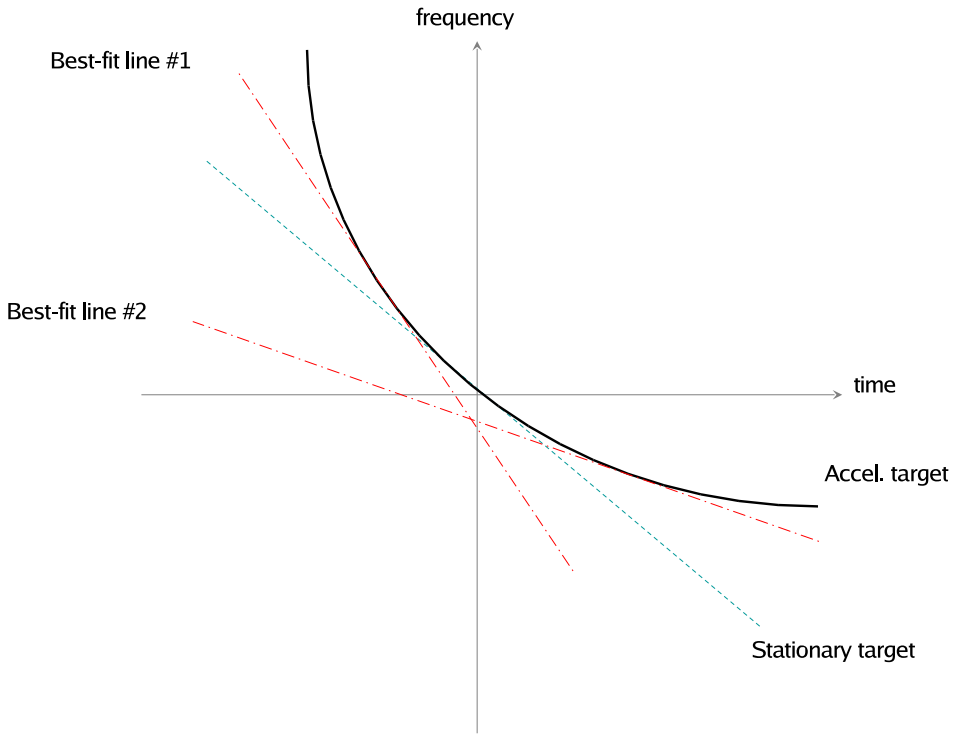

Figure 5.5: Example time-frequency history for a target accelerating in the along-track direction (solid black line). The nonlinear component of the TF history has been greatly exaggerated for demonstration purposes. For reference, the time-frequency history for a stationary target is provided (dashed blue line). The two best-fit lines which capture the most target energy (and hence might give two peaks in the filter-bank magnitude map as in Figure 5.4) are shown in red.

magnitude responses compared to the other matched filters. If these lines do not have y-intercepts of 0, then the target will not be focused exactly at broadside (i.e. at $t = 0$, or an azimuth $x = 0$). It can be seen in Figure 5.4 that the peaks are slightly offset from broadside position by approximately 0.4 metres, although this shift is negligible when compared to the shift induced by an uncompensated across-track velocity component.

Uncompensated a_{x0} will introduce small biases into the estimation of v_{x0} velocity (on the order of 1 m/s for $a_{x0} = 1$ m/s^2). However the most severe effect is a decrease in peak power which may make it difficult to find the location of peak power and thus to estimate v_{x0}, especially in the presence of residual clutter and noise.

5.1.5 Estimating v_{x0} in the presence of $\dot{a}_{y0}$

Since both a_{x0} and $\dot{a}_{y0}$ appear in the cubic coefficient of the range equation (see equation 2.11), it is expected that the effects of time-varying across-track acceleration on v_{x0} estimation would be very similar to the impact of along-track acceleration a_{x0}. This was confirmed in simulations of the CV 580 airborne geometry. Figure 5.6 displays the filter-bank magnitude map for a point target with $\dot{a}_{y0} = 0.04$ m/s^3 and all other motion parameters set to zero. There is a bias in the estimate of v_{x0} which is on the order of 0.6 m/s for the simulated scenario. Again, perhaps the most problematic effect is the decrease in peak power and severe smearing, which makes it difficult to identify the true peaks in the filter-bank magnitude map for noisy signal data. This in turn can lead to errors in the estimated along-track velocity.

5.1.6 Estimating v_{x0} in a spaceborne geometry

In addition to airborne geometries, estimation of along-track velocity was conducted for a simulated spaceborne RADARSAT-2 scenario (see parameters in Table 3.2) for targets possessing various motion components. The influences of target motion on v_{x0} estimation as observed in the airborne scenarios are very similar to the spaceborne

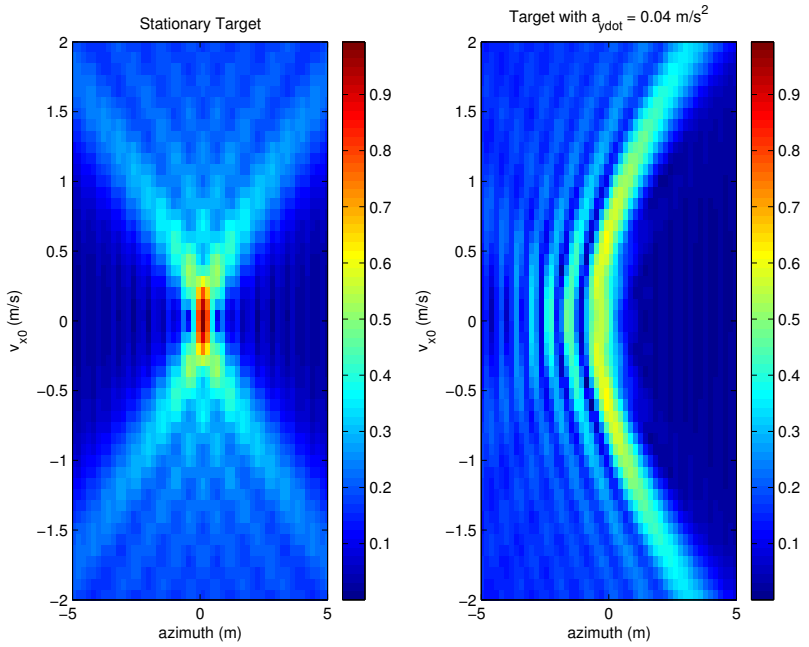

Figure 5.6: Magnitude responses of a simulated point target with $\dot{a}_{y0} = 0.04$ m/s^3 (and all other motion parameters set to zero) after compression with a bank of reference filters initialized with various v_{x0} velocities. An azimuth of 0 m is broadside. Note the similarities to uncompensated along-track acceleration a_{x0} in Figure 5.4, including a small bias in the estimate of v_{x0} on the order of 0.6 m/s .

case, although the sensitivity of the estimation to various motion parameters may change due to differences in the scale of the radar-target geometry.

In the presence of an along-track velocity component only, as in the airborne case, there is no bias in estimating v_{x0}. However, due to the large platform velocity (i.e. large v_a), the sensitivity of the quadratic term to small changes in v_{x0} decreases, and thus the precise location of the peak response is more difficult to determine in the space-based case, which will decrease the accuracy with which one may estimate $\hat{v}_{x0}$. Figure 5.7 is the filter-bank magnitude for a target with $v_{x0} = 10$ m/s and all other motion parameters set to zero observed in a spaceborne radar-target geometry. Although well-localized in azimuth, note the large peak power for v_{x0} velocities in the vicinity of the true $v_{x0} = 10$ m/s value.

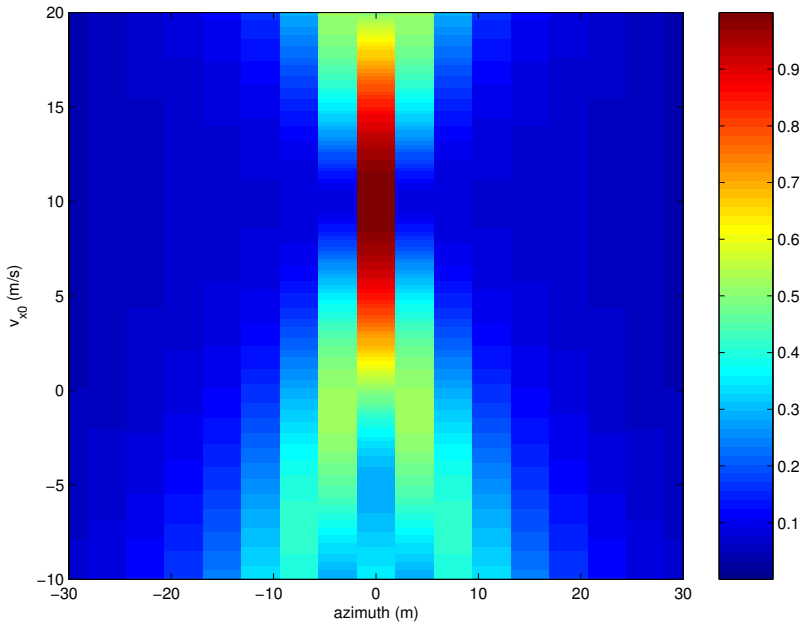

Figure 5.7: Magnitude responses of a simulated point target for a spaceborne geometry with $v_{x0} = 10$ m/s (and all other motion parameters set to zero) after compression with a bank of reference filters initialized with various v_{x0} velocities. An azimuth of 0 m is broadside. Note that $\hat{v}_{x0}$ matches the true target velocity of 10 m/s, although the location of peak power is not as well defined as it is in the airborne case.

In the spaceborne case, targets with large across-track velocities on the order of 30 m/s have no discernible effect on the estimation of v_{x0}. In this geometry, the $v_{y0}^2(1-y_0^2/R_0^2)$ term in the second-order component of the range equation is sufficiently small compared to the value of $(v_{x0}-v_a)^2$ (also in the quadratic component) that the bias in v_{x0} is negligible; no iteration or two-step process is required (as was suggested for the airborne case in section 5.1.2) for an accurate estimate of $\hat{v}_{x0}$.

However, the spaceborne case is even more sensitive to biases in $\hat{v}_{x0}$ caused by across-track accelerations than the airborne situation. For instance, an across-acceleration of $a_{y0} = 0.1$ m/s^2 introduces a bias of -4.5 m/s in $\hat{v}_{x0}$ for the spaceborne case compared to a bias of -2.5 m/s in the airborne scenario. Along-track acceleration and time-varying across-track acceleration on the other hand, do not noticeably affect v_{x0} estimation. There are no apparent asymmetric sidelobes and no discernible decrease in peak power in the filter-bank magnitude map for $|a_{x0}| \leq 1$ m/s^2 and $|\dot{a}_{y0}| \leq 0.1$m/s^3, and a bias of only 0.1 m/s was observed in $\hat{v}_{x0}$ for an $a_{x0} = 1$ m/s^2.

5.2 Experimental Results

To test along-track velocity estimation in experimental data, the filter-bank method was applied to each of the twenty-two target tracks extracted from the Petawawa 2000 data. Appendix A includes a description of this data set, and section 3.3 details how the targets were detected and their tracks extracted. A filter-bank of 2000 matched filters with along-track velocities ranging from -30 to 30 m/s (spaced every 0.03 m/s) were used to focus the data. A more sophisticated algorithm may be used to iterate this operation using progressively denser (i.e. narrowly-spaced) filter-banks in a smaller velocity range to converge upon the peak response, although only a simple filter-bank was applied in this instance.

The range compressed fore and aft target tracks were subtracted and then convolved with each matched filter to compute the azimuth compressed DPCA signals. DPCA was used to suppress clutter, thus preventing any clutter from discrete targets

(e.g. buildings) from biasing the v_{x0} estimation. All targets had non-zero across-track velocity v_{y0} not equal to a blind velocity, and thus all targets had non-zero DPCA magnitude. The location of the peak power response in the DPCA filter-bank map was used to find the filter most closely matched to the true along-track velocity v_{x0}.

The along-track velocities estimated using the filter-bank method for each target and their velocities as measured using GPS are presented in Appendix A.3. The procedure to convert GPS velocity into along- and across-track velocity components, and the expected accuracy in the GPS measurements (approximately 0.5 m/s) are also detailed in Appendix A.3. Taking the absolute value of the differences between the GPS velocities and the estimated target velocities, a mean error of 2.9 m/s was found in $\hat{v}_{x0}$ as estimated from the SAR data with a standard deviation of 2.6 m/s. A number of targets had significant biases in their along-track velocity estimates when compared to the GPS values, with a maximum bias of 9.3 m/s. These large biases may indicate the presence of possible along- and across-track acceleration components.

An example of a biased v_{x0} estimation from one pass of the Convoy target is shown in Figure 5.8. There is a clear peak response in the filter-bank magnitude map at a v_{x0} of 11.5 m/s. However, the GPS velocity is only 5.7 m/s, pointing to a likely acceleration bias due to a_{y0} as described in section 5.1.3.

In addition to biases in v_{x0}, the smearing effects and asymmetric sidelobes characteristic of an uncompensated cubic term are also visible in the experimental data. This suggests that one can predict the existence of a cubic term by examining the filter-bank magnitude map for the characteristic smearing patterns described in sections 5.1.4 and 5.1.5. Figure 5.9 shows the filter-bank map from one pass of the Juliet target in which along-track acceleration a_{x0} and/or time-varying across-track acceleration $\dot{a}_{y0}$ may be causing the smearing and sidelobe effects as were observed in simulations. There may also be higher-order target motion components, improper motion compensation of the platform velocity, incorrect estimates of v_a, y_0/R_0 and other parameters, or residual clutter, which may be having additional impact upon

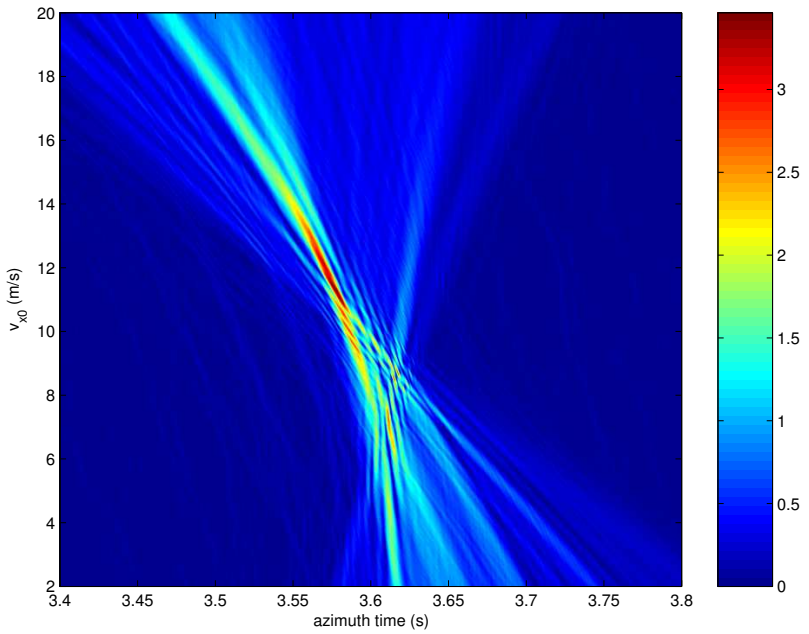

Figure 5.8: DPCA filter-bank magnitude map from one pass of the Convoy target (line 1, pass 5). The peak response occurs at v_{x0}=11.5 m/s, whereas the GPS velocity is 5.7 m/s, indicating a severe bias in the $\hat{v}_{x0}$ estimate which may be due to the presence of across-track acceleration a_{y0}.

the filter-bank map.

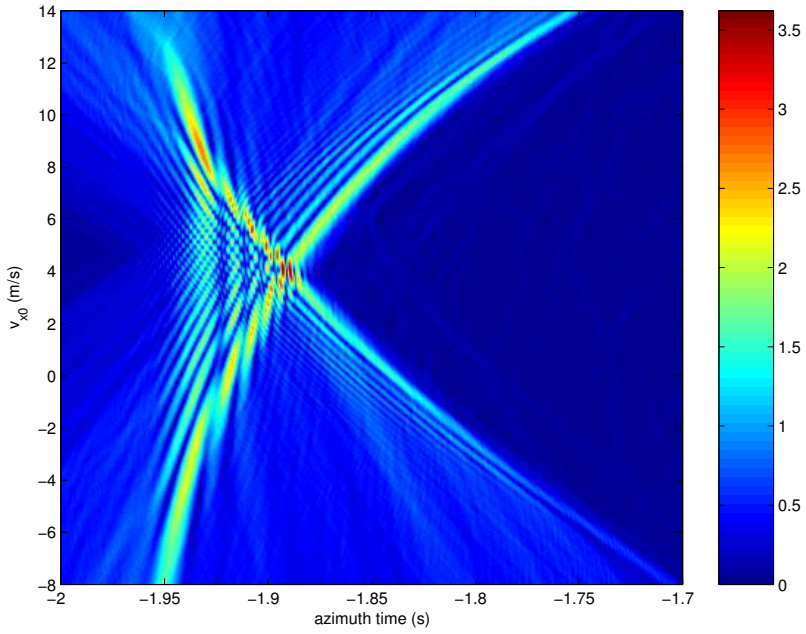

Figure 5.9: DPCA filter-bank magnitude map from one pass of the Juliet target (line 2, pass 2). In addition to a bias in the $\hat{v}_{x0}$ estimate, this target displays asymmetric sidelobes to the left-hand side of the peak response and smearing of the target energy characteristic of an uncompensated cubic component in the focusing operation.

As well, oftentimes, the target energy in the filter-bank magnitude maps is smeared across multiple v_{x0} velocities, making it difficult to determine if the correct peak is being selected by the algorithm. Figure 5.10 displays the filter-bank map for one pass of Juliet whose peak response is in excellent agreement with the GPS data (within 0.24 m/s). However, despite the accuracy of the estimate, one can see extensive smearing on the right-hand side, again suggesting an uncompensated cubic term. Again, higher-order motion components as well as incomplete clutter suppression may be causing some of the smearing and local maxima effects visible elsewhere in the image.

Unfortunately, as described in section 3.3.2, it is difficult to determine the target's true acceleration since GPS data were only collected every two seconds. Extremely

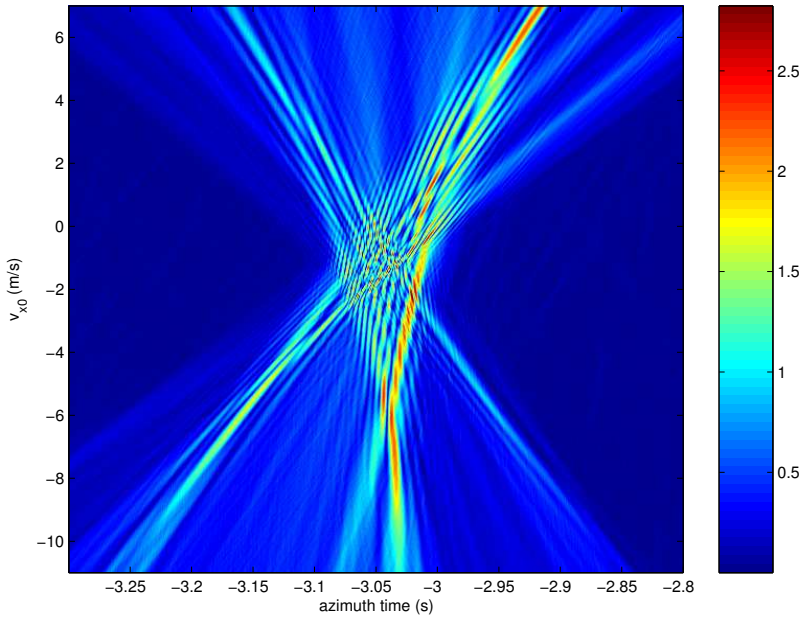

Figure 5.10: DPCA filter-bank magnitude map from one pass of the Juliet target (line 3, pass 3). Although there is no discernible bias in the $\hat{v}_{x0}$ estimate, this target displays a smearing of the target energy on the right-hand side characteristic of an uncompensated cubic component.

accurate estimates of acceleration would be needed in any case, since simulations have shown that one must be concerned with even slight accelerations on the order of 0.1 m/s^2 or less. Future experimental trials could equip controlled movers with high-accuracy GPS systems functioning at a higher sampling rate and inertial systems with gyroscopes in order to determine a target's acceleration time-history.

Summarizing, acceleration (both along- and across-track components) may have a severe effect on estimation of along-track velocity. This was demonstrated using theory, simulations, and experimental data. Across-track acceleration a_{y0} severely biases the v_{x0} estimate if it is assumed that targets are travelling at a constant velocity. If acceleration is acknolwedged as an additional unknown, then there are insufficient degrees of freedom to solve for all parameters. This issue is further addressed in Chapter 7. Along-track acceleration a_{x0} and time-varying across-track acceleration $\dot{a}_{y0}$ also effect v_{x0} estimation by smearing the target energy across multiple cells in the filter-bank map and introducing a slight bias in the location of the peak response. Having described the effects of acceleration on along-track velocity estimation, we examine its influence on estimating the *across-track* velocity component in the next chapter.

Chapter 6

Estimation of across-track velocity v_{y0}

Across-track velocity is a fundamental parameter of interest for GMTI applications. This chapter examines the estimation of across-track velocity using along-track interferometric (ATI) phase, and the impact of acceleration upon this phase. As in previous chapters, the theory of ATI is reviewed, followed by v_{y0} estimation using simulated point targets with various motion components, and ending with examples from experimental data. The across-track velocities of controlled movers from the experimental data are estimated using the ATI phase and are compared with GPS velocities.

6.1 Theory

The along-track interferometric phase computed from two channels of SAR data may be used to determine the across-track velocity of a target. The history of ATI was outlined in section 2.3.2 and the basic ATI equation was given in equation 2.27, in which the fore channel is multiplied by the complex conjugate of the registered aft channel. The phase is then the argument of the ATI signal, where in the noise-free case a stationary target should theoretically have zero phase (since fore and registered aft channels are identical) and a moving target will possess an ATI phase related to its motion components. The ATI method was chosen to estimate across-track velocity because of its sensitivity to v_{y0} compared to other techniques (such as those described in the latter portions of section 2.3.2). However, ATI phase suffers from a number of ambiguities which must be resolved prior to velocity estimation. These are outlined in Appendix B.1.

Along-track interferometric phase is generally computed in the azimuth com-

pressed domain for improved signal-to-clutter ratios (see Appendix B.2 for further explanation). Using the expressions derived for the azimuth compressed signal returns from the fore and aft channels (equations 4.16 and 4.17 from section 4.1.3), where the reference filter has been matched to the quadratic term of the range equation only, we can determine a closed form expression for the ATI signal. Applying equation 2.27 (the ATI equation), and assuming that along-track acceleration a_{x0} and across-track acceleration rate $\dot{a}_{y0}$ are zero, we have:

$$\begin{aligned} ATI(t) &= I_1(t)\ I_2^*(t) \\ &= \frac{A_1\ (T-|t|)}{T}\ \mathrm{sinc}\left(k(T-|t|)\ \left[\frac{y_0 v_{y0}}{R_0}+\alpha t\right]\right) \\ &\cdot\ \ \frac{A_2\ (T-|t|)}{T}\ \mathrm{sinc}\left(k(T-|t|)\left[\frac{y_0 v_{y0}}{R_0}+\alpha t+\beta\right]\right)\ \exp\left(jk[g(t)-\beta t]\right). \end{aligned} \tag{6.1}$$

Substituting equations 4.14 and 4.15 for β and $g(t)$, respectively, and dropping the negligible d^2/v_a^2 term, the ATI phase is given as:

$$\angle ATI(t) = \frac{k y_0 d v_{y0}}{R_0 v_a} + \frac{kd}{2R_0}\ t\left[(v_{x0}-v_a)+\frac{\left[(v_{x0}-v_a)^2+v_{y0}^2\left(1-\frac{y_0^2}{R_0^2}\right)+y_0 a_{y0}\right]}{v_a}\right]. \tag{6.2}$$

Evaluated at its focused location $t = t_{\mathrm{img}}$ from equation 4.7, the ATI phase becomes:

$$\angle ATI(t_{\mathrm{img}}) = \frac{k d y_0 v_{y0}}{2R_0}\ \left(\frac{1}{v_a}-\frac{(v_{x0}-v_a)}{(v_{x0}-v_a)^2+v_{y0}^2\left(1-\frac{y_0^2}{R_0^2}\right)+y_0 a_{y0}}\right). \tag{6.3}$$

Note that equation 6.3 is the ATI phase only for a target focused using a reference filter matched in the quadratic term. If the reference filter contains a non-zero v_{y0} (and thus a non-zero linear coefficient), then the image focusing time t_{img} will change, and the ATI phase may be computed using equation 6.2.

6.2 Simulations

Equations 6.2 and 6.3 are verified using simulations for various v_{x0}, v_{y0} and a_{y0}. The SAR signals are determined using equation 2.9 to compute the fore channel range

history, and equations 2.15 and 2.19 to compute the aft channel range history, which make use of the far-field approximation only. Additional simulations using non-zero along-track acceleration a_{x0} and across-track acceleration rate $\dot{a}_{y0}$ are also conducted. The influence of these parameters on the ATI phase and on the estimation of across-track velocity is described below. The estimated across-track velocity is denoted $\hat{v}_{y0}$.

6.2.1 Variation in ATI with v_{y0}

ATI phase is extremely sensitive to across-track target velocity v_{y0} since it appears in the numerator of equation 6.3. This sensitivity may be exploited to derive precise estimates of the across-track velocity component. However, for $v_{y0} = 0$ m/s or the blind-velocities discussed in Appendix B.1 (corresponding to across-track target displacements a multiple of $\lambda/2$), the ATI phase vanishes and no information for parameter estimation can be extracted from the ATI phase alone. Polar plots of the ATI signal at time $t = t_{\text{img}}$ for a target with unambiguous across-track speeds varying from -2.5 to 10 m/s (and all other motion parameters set to zero) are given in Figure 6.1. Since the ATI magnitude is determined by the multiplication of two relatively narrow sinc functions (see equation 6.1), the focused image location can be determined after ATI as the point at which the ATI magnitude is maximum. This technique may be made more robust using a keyhole filter (as described in Appendix B.2) to remove interfering clutter with strong amplitudes yet small phases lying close to the positive real axis.

In the plots of Figure 6.1, one can see distinctly non-zero ATI phase for even small across-track velocities (e.g. a v_{y0} of 2.5 m/s gives an ATI phase of approximately 44°). As well, note that a target with negative across-track velocity has the same ATI phase as a target with positive v_{y0} of the same magnitude, except that the phase has opposite sign. A stationary target has zero ATI phase but has maximum magnitude, since the reference and target signal functions have complete spectral overlap. As across-track velocity increases, the spectral overlap decreases, reducing

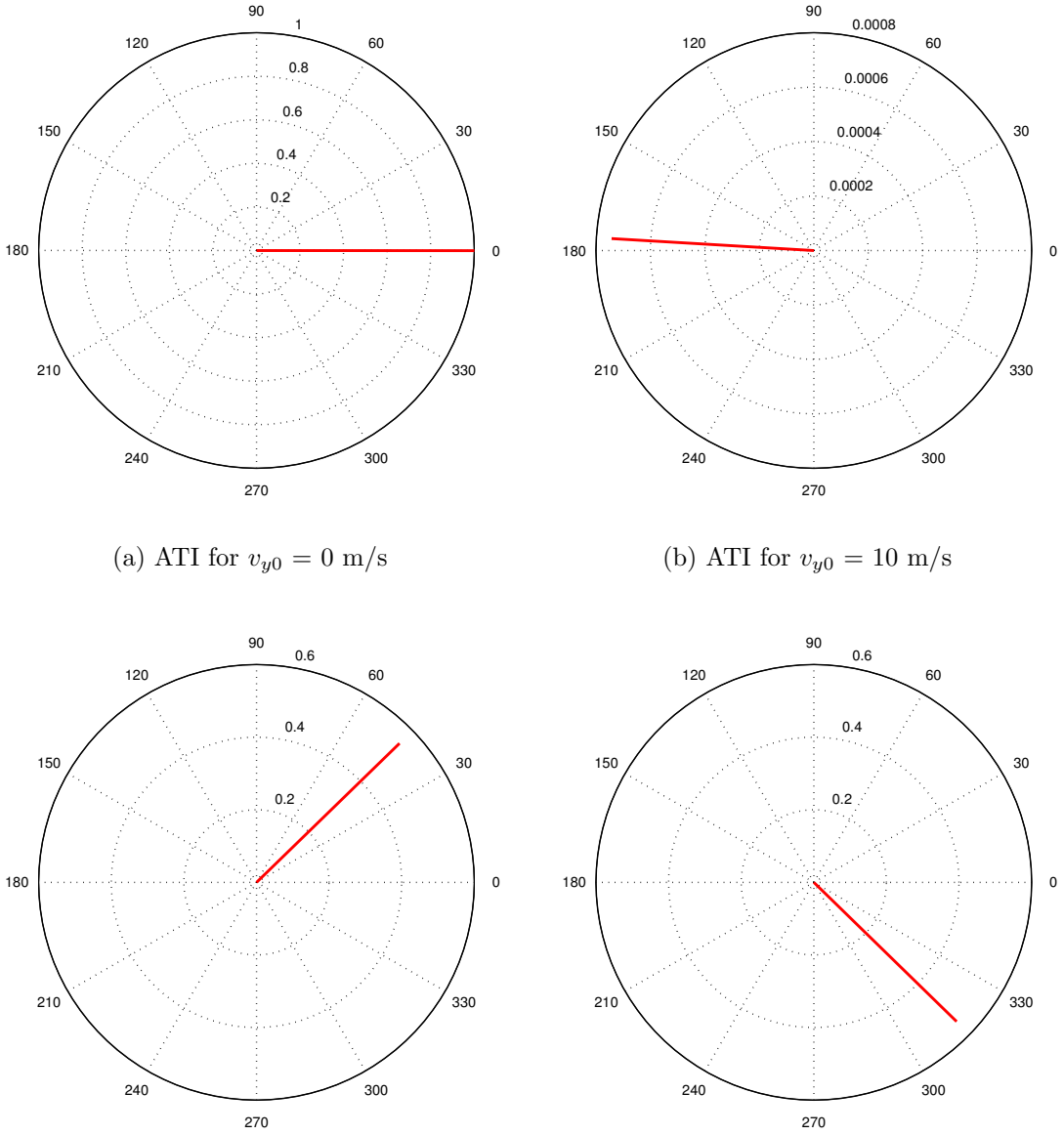

(a) ATI for $v_{y0} = 0$ m/s

(b) ATI for $v_{y0} = 10$ m/s

(c) ATI for $v_{y0} = 2.5$ m/s

(d) ATI for $v_{y0} = -2.5$ m/s

Figure 6.1: ATI signal for varying across-track velocities v_{y0} (with zero acceleration). Phase is given in degrees as an angle measured from the positive real axis, and magnitude as a distance from the origin. Note the sensitivity of the phase to non-zero v_{y0} and the variation in ATI magnitudes for non-zero v_{y0}.

the magnitude of the output ATI signal as described in Appendix B.1.

The theoretical ATI phases (from equation 6.3) and simulated phases agree extremely well. Differences on the order of 0.1° are observed due to the use of the Taylor expansion of the range equation to only the second-order in the theoretical expression, the application of the far-field approximation, and numerical rounding errors. This error corresponds to a negligible bias of 0.005 m/s in the across-track velocity (where v_{y0} is computed from equation 6.3, assuming that $v_{x0} = 0$ and that the denominator term $[(v_{x0} - v_a)^2 + v_{y0}^2(1 - y_0^2/R_0^2) + y_0 a_{y0}]$ is known from a matched filter-bank, as was assumed for the azimuth compression integration). For comparison, a phase error of 17.7° is required to cause an error of 1 m/s in the $\hat{v}_{y0}$ estimate for the airborne scenario under consideration.

Oftentimes, the ATI phase is approximated by the following expression (e.g. [11, 49, 53, 59]):

$$\angle ATI(t_{\text{img}}) \simeq \frac{k d y_0 v_{y0}}{R_0 v_a}, \tag{6.4}$$

such that an estimate of v_{y0} can be computed directly given the interferometric phase, and the estimate is not dependent upon along-track velocity v_{x0} nor across-track acceleration a_{y0}. For $[v_{x0}\ a_{x0}\ a_{y0}\ \dot{a}_{y0}] = \vec{0}$, errors of up to 0.3° in ATI phase (computed using equation 6.4, corresponding to a bias of 0.02 m/s in $\hat{v}_{y0}$) were found when varying v_{y0} between -10 and 10 m/s. Note that if a reference filter perfectly matched to the linear and quadratic range equation terms is applied during azimuth compression, the target is imaged at broadside time (i.e. $t_{\text{img}} = 0$), and equation 6.2 reduces exactly to equation 6.4. However, generally v_{y0} is not known *a priori*, and the objective is to estimate it using the ATI phase.

As discussed in Appendix B.1, if v_{y0} shifts the target's Doppler centroid such that there is no spectral overlap of the target signal with the reference filter, there will be no target peak and the ATI phase cannot be found. As well, in the presence of moderate v_{x0} and a_{y0}, equation 6.4 will begin to degrade if the target data are focused using a filter mismatched to the linear coefficient.

6.2.2 Variation in ATI with v_{x0}

As can be seen from equation 6.3, v_{x0} will influence the ATI phase. The amount it will shift the ATI phase is dependent both upon the value of v_{x0} and the across-track velocity v_{y0}. Examining the theoretical expression for the ATI phase in equation 6.3, the bias caused by ignoring the v_{x0} dependence increases indefinitely with increasing v_{x0} and v_{y0}. However, this equation does not take into account wrapping of the spectrum due to a finite azimuth bandwidth. The focused image location t_{img} used to derive equation 6.3 can only fall between $-T$ and T (twice the original signal length due to the convolution operation), and thus the error in ATI phase due to ignoring the v_{x0} component will not increase indefinitely.

Examining the differences between the *simulated* ATI phase and that determined from equation 6.4 for only those target signals with some spectral overlap with the reference signal, it was found that the maximum bias for $-30 \leq v_{x0} \leq 30$ m/s and $-30 \leq v_{y0} \leq 30$ m/s (scanned in steps of 1 m/s) is 21.7 degrees or 1.2 m/s occurring at $v_{x0} = -30$ m/s and $v_{y0} = \pm 16$ m/s . Figure 6.2 shows some biases between the v_{y0}-only ATI phase computation and its actual value for a target with $v_{x0} = -30$ m/s. These values were computed by taking the simulated ATI phase at its maximum amplitude, and differencing it from the ATI phase computed from equation 6.4.

If a reference filter closely matched in v_{y0} (within one m/s) is used to focus the target data (in addition to being matched in the quadratic term), variation in the ATI phase with v_{x0} will bias the $\hat{v}_{y0}$ estimate by a maximum of 0.16 m/s, which may or may not be a concern depending on the required accuracy of the application. When a reference filter perfectly matched to v_{y0} is applied in compression, the bias in $\hat{v}_{y0}$ is negligible (for any v_{x0}), and is due only to use of the far-field approximation and the Taylor series expansion of the range equation.

In the above examples it has been assumed that the quadratic term in the reference filter has been matched to the quadratic coefficient of the target range history such that comparisons to the theoretical expression could be made. If this quadratic

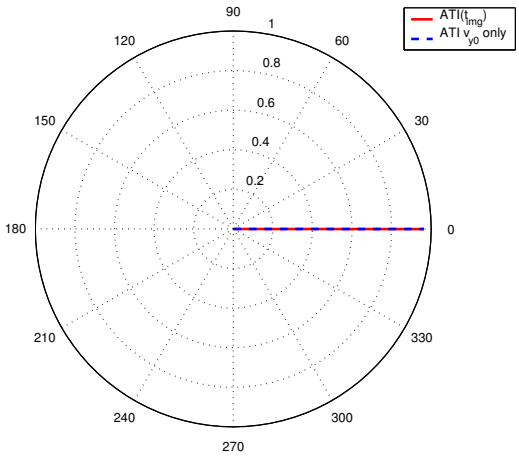

(a) ATI for $v_{x0} = -30$ m/s, $v_{y0} = 0$ m/s

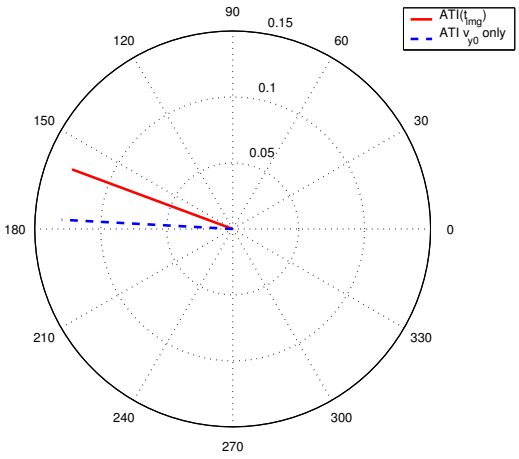

(b) ATI for $v_{x0} = -30$ m/s, $v_{y0} = 10$ m/s

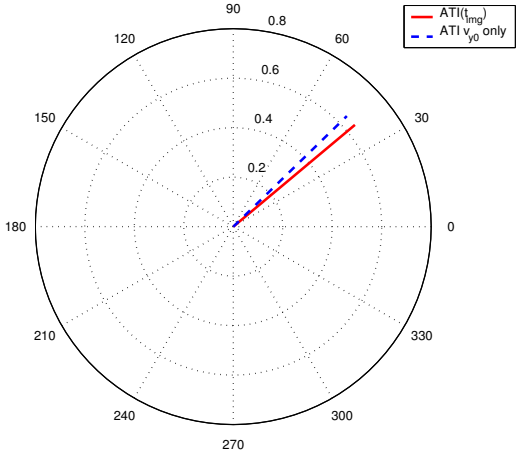

(c) ATI for $v_{x0} = -30$ m/s, $v_{y0} = 2.5$ m/s

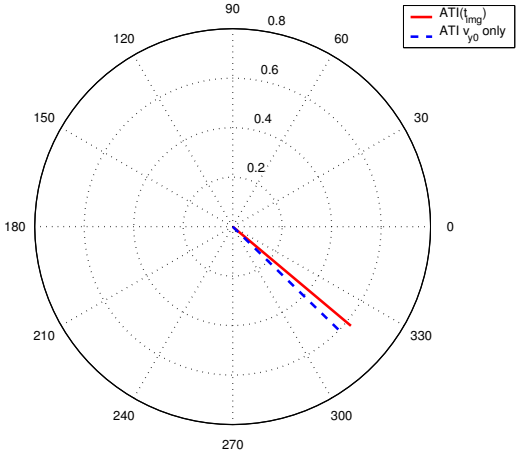

(d) ATI for $v_{x0} = -30$ m/s, $v_{y0} = -2.5$ m/s

Figure 6.2: ATI signal for varying across-track velocities v_{y0} (with zero acceleration) and constant $v_{x0} = -30$ m/s (in solid red) compared with the expected ATI phase when the v_{x0} dependence is neglected (in dotted blue). Phase is given in degrees as an angle measured from the positive real axis, and magnitude as a distance from the origin.

term is unmatched then the target will be defocused in both the fore and aft channels, decreasing the SCR such that the ATI phase will be subject to increased clutter contamination as described in section B.2. In addition, the smearing of the target response (as described in section 4.1.2) due to an unmatched quadratic term creates peaks away from broadside time, such that the peak ATI magnitude is not at broadside when $v_{y0} = 0$, and the ATI phase at this peak magnitude will give an incorrect estimate of v_{y0}. This is illustrated in Figure 6.3, where Figure 6.3(a) shows the coincident fore and aft responses for a point target with $v_{x0} = 10$ m/s, $v_{y0} = 0$, compressed using a SWMF, and Figure 6.3(b) shows the target's ATI phase (for all times, not just t_{img}). The peak magnitudes occur away from broadside with an ATI phase of $\pm 5.7°$, biasing the computation of $\hat{v}_{y0}$ by 0.3 m/s.

6.2.3 Variation in ATI with a_{y0}

Similar to v_{x0}, non-zero a_{y0} will effect the ATI phase (see the denominator of the second term in equation 6.3). Because a_{y0} is multiplied by y_0, even small accelerations such as 0.1 m/s^2 will have a noticeable impact upon the phase. For example, for $v_{x0} = 0$ m/s, $v_{y0} = 10$ m/s and $a_{y0} = 0.1$ m/s^2, the ATI phase shifts 3.8 degrees, creating an error of 0.2 m/s if equation 6.4 is used to compute $\hat{v}_{y0}$. This shift may be lessened or increased in the presence of an along-track velocity depending the signs of the motion parameters as described in section 4.1.2; v_{x0} and a_{y0} of the same sign will reduce the overall shift, whereas values of opposite signs will increase the shift in ATI phase. When more severe accelerations (but still plausible) of ± 1 m/s^2 are introduced, shifts of up to 36.6° (or biases of 2.1 m/s in $\hat{v}_{y0}$) are present. Combined with shifts resulting from v_{x0} velocity, neglecting the contributions of a_{y0} to the ATI phase can give erroneous estimates of $\hat{v}_{y0}$. Examples of the effect of a_{y0} on ATI phase are shown in Figure 6.4.

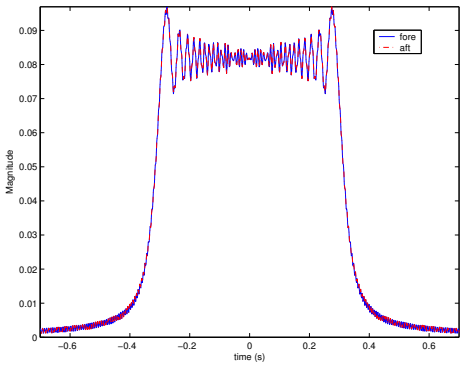

(a) Fore and aft target responses (with nearly perfect overlap) compressed using a stationary reference filter.

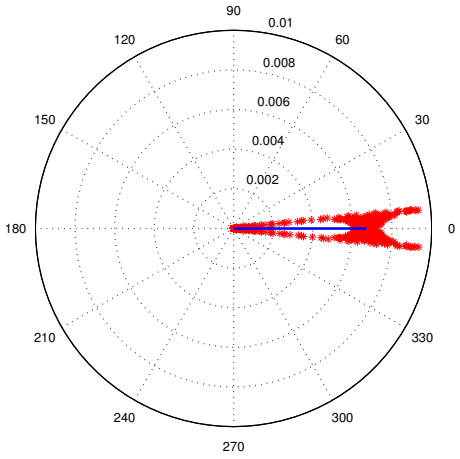

(b) ATI signal of the target (in red) with ATI signal at broadside time given in blue.

Figure 6.3: Compressed target response from a SWMF and ATI signal for a point target with $v_{x0} = 10$ m/s and all other motion parameters equal to zero. Phase is given in degrees as an angle measured from the positive real axis, and magnitude as a distance from the origin. Note the spread in the ATI phase and note that the maximum channel responses and ATI magnitudes occur at times other than broadside time $t = 0$.

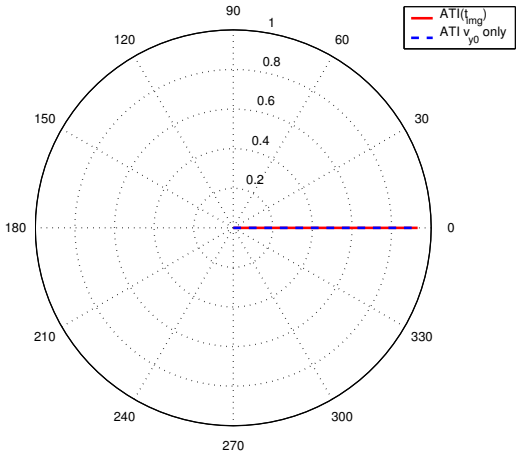

(a) ATI for $a_{y0} = 1$ m/s^2, $v_{y0} = 0$ m/s

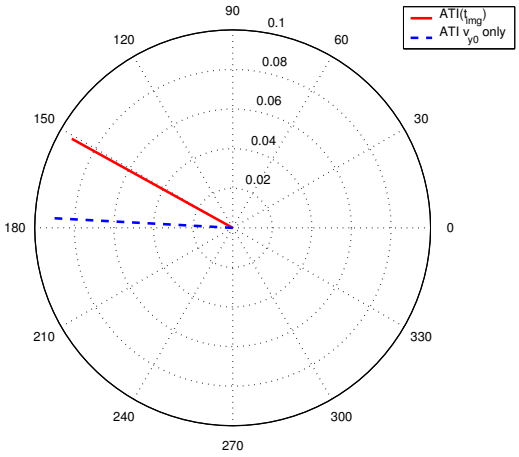

(b) ATI for $a_{y0} = 1$ m/s^2, $v_{y0} = 10$ m/s

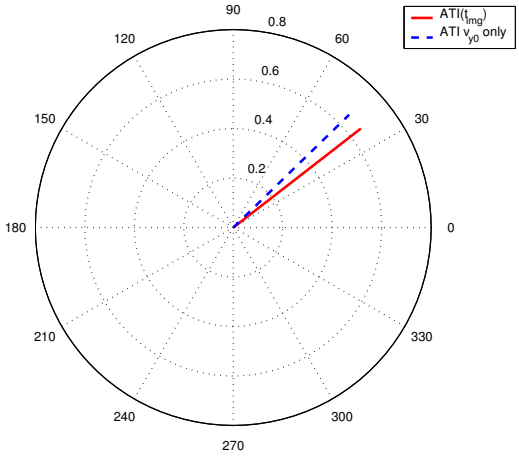

(c) ATI for $a_{y0} = 1$ m/s^2, $v_{y0} = 2.5$ m/s

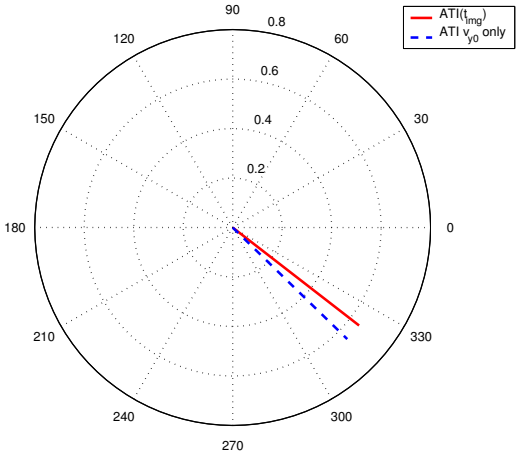

(d) ATI for $a_{y0} = 1$ m/s^2, $v_{y0} = -2.5$ m/s

Figure 6.4: ATI signal for varying across-track broadside velocities v_{y0} and constant across-track acceleration $a_{y0} = 1$ m/s^2 (in solid red) compared with the expected ATI phase when the a_{y0} dependence is neglected (in dotted blue). Phase is given in degrees as an angle measured from the positive real axis, and magnitude as a distance from the origin.

6.2.4 Variation in ATI with a_{x0} and $\dot{a}_{y0}$

Analytically, the ATI phase of a target with non-zero a_{x0} and/or $\dot{a}_{y0}$ components cannot be computed in closed form. However, we may examine the errors in using equation 6.4 to estimate $\hat{v}_{y0}$ in the presence of along-track acceleration and/or time-varying across-track acceleration using simulations.

Compared to v_{x0} and a_{y0}, a_{x0} and $\dot{a}_{y0}$ have a relatively small impact on ATI phase. For a_{x0} varied from -1 to 1 m/s^2 (scanned in steps of 0.1 m/s^2), and v_{y0} varied from -30 to 30 m/s (scanned in steps of 1 m/s), the maximum deviation from equation 6.4 was 2.4°, translating to a bias in $\hat{v}_{y0}$ of 0.14 m/s. Similarly, varying $\dot{a}_{y0}$ over ± 0.1 m/s^3 gave a maximum deviation of 4.6° or a bias of 0.26 m/s in $\hat{v}_{y0}$. Thus, for the parameter ranges examined, the effects of a_{x0} and $\dot{a}_{y0}$ on ATI phase are nearly an order of magnitude lower than the influence of v_{x0} and a_{y0}.

6.2.5 Variation in ATI phase for spaceborne scenarios

The previous sections have presented simulations of the ATI signal based exclusively on the CV 580 system parameters. The CV 580 airborne system has a comparatively large azimuth oversampling factor ($\simeq 2.8$) compared to certain configurations of the proposed RADARSAT-2 system. The main RADARSAT-2 parameters influencing ATI phase computations are given in Table 3.2, where both the azimuthal beamwidth and the PRF are programmable by the operator.

If the azimuth beamwidth is chosen as 0.4° and the PRF as 2000 Hz (mid-range values), and if we are observing a target with an incidence angle of 40° from the satellite, the azimuth oversampling factor will be only 1.1, such that nearly complete spectral overlap is present between the reference filter and target signal for any target motion. In this case, the azimuth compression will capture nearly all the target energy into one peak (due to the large amount of overlap) and the ATI phase will depend only upon v_{y0}. One disadvantage of the lower overlap factor is that there is little data uncontaminated by clutter, whereas with a large PRF and a small beamwidth, all

signal data with Doppler frequencies outside of the clutter limits and within $\pm f_{\mathrm{PRF}}/2$ are free from main-beam clutter (although some sidelobe clutter may remain).

If the azimuth beamwidth is reduced to its minimum of 0.21° and the PRF is increased to its maximum of 3800 Hz, the oversampling factor becomes 3.9, and thus complete loss of spectral overlap is possible, giving erroneous ATI phase and $\hat{v}_{y0}$ estimates. However, for the ground moving target velocities in which we are interested ($-30 \leq v_{x0} \leq 30$ m/s and $-30 \leq v_{y0} \leq 30$ m/s), the maximum bias is only 0.33° (or 0.07 m/s). Similarly, a_{y0} varied in between ± 1 m/s^2 introduces a maximum bias of 0.83° in the ATI phase from equation 6.4 (or 0.13 m/s in $\hat{v}_{y0}$). These biases are very small compared to the expected standard deviation of the ATI phase in the spaceborne case of 3.2 m/s (derived in section B.2). Because the spaceborne platform moves with along-track velocity several hundred times faster than the vehicular velocities being observed, even high target v_{x0} does not significantly change the Doppler rate (or slope of the target signal in the TF domain) and its contribution to the ATI phase in equation 6.3 is small. The denominator of equation 6.3 contains an a_{y0} term, but again its contribution is small compared to v_a^2. As well, even high v_{y0} does not significantly shift the Doppler centroid with respect to the total bandwidth, such that the $\pm f_{\mathrm{PRF}}/2$ wrapping will not occur for velocities of interest (at this reduced azimuth beamwidth and high PRF), and significant spectral overlap will always occur for velocities of interest. Thus, one need not be concerned with the influence of v_{x0}, small accelerations ($|a_{x0}, a_{y0}| \leq 1$ m/s^2), or small across-track acceleration rates ($|\dot{a}_{y0}| \leq 0.1$ m/s^3) on the ATI phase in the RADARSAT-2 scenario.

6.2.6 ATI simulation summary

Along-track interferometric phase has been presented as one metric for estimating the across-track velocity of a target. However, because ATI uses phase measurements, this method is subject to ambiguities in its estimates due to directional-ambiguities from π wraps of the ATI phase and due to sampling limitations in azimuth. The relation

between ATI phase and the target motion parameters for non-zero v_{y0}, v_{x0}, and a_{y0} was derived for a target compressed with a reference filter matched to the quadratic term. If processed using a reference filter perfectly matched to the target phase history (both to linear and quadratic terms), the ATI phase reduces to a dependency on v_{y0} only.

This suggests that to converge upon the correct v_{y0}, the ATI phase should first be computed using a bank of reference filters initialized with the quadratic coefficient giving maximal magnitude response (for the highest SCR) and initialized with widely-spaced v_{y0} velocities (to ensure that some spectral overlap between the target signal and reference filter is obtained). With an initial approximation of across-track velocity obtained by solving equation 6.4 for v_{y0}, the target is re-compressed using the estimated $\hat{v}_{y0}$ in the reference filter. After several iterations, this process should converge upon the correct $\hat{v}_{y0}$ if the ambiguities have been resolved (either using the target range walk, sub-beam partitioning methods, or *a priori* knowledge of the approximate target motion). Using this method, even significant v_{x0} or accelerations will not bias the $\hat{v}_{y0}$ estimated using the ATI phase.

Alternatively, an ATI phase dependent only upon the v_{y0} motion parameter can also be derived by extending the length of the reference filter past the -3 dB synthetic aperture length. If this reference filter is matched to the quadratic coefficient of the target range history, and if it is sufficiently extended in time, there will be complete spectral overlap between the target signal and the reference filter, and the ATI phase may be reduced to equation 6.4. However, in the presence of clutter, extending the reference filter introduces additional clutter contamination into the phase estimate, and thus despite the added computational cost of carrying out multiple correlations, the algorithm suggested in the previous paragraph is preferred for estimating $\hat{v}_{y0}$.

Determining the ATI phase from a space-based radar geometry was also considered. For the velocities and accelerations experienced by realistic ground-based vehicles, equation 6.4 may be used directly to estimate $\hat{v}_{y0}$, without the need for a

bank of matched filters.

6.3 Experimental Results

Across-track velocity was estimated for each control target extracted from the Petawawa 2000 data using along-track interferometric phase. Appendix A includes a description of this data set, and section 3.3 details how the targets were detected and their tracks extracted. A description of the $\hat{v}_{y0}$ estimation algorithm is provided below, followed by a comparison of the across-track velocity estimates from ATI to GPS velocities.

6.3.1 Across-track velocity estimation algorithm

This section outlines the algorithm used to estimate $\hat{v}_{y0}$ for the experimental data set. Firstly, an estimate of along-track velocity $\hat{v}_{x0}$ is obtained using the filter-bank method from Chapter 5. The target track is then azimuth compressed using this $\hat{v}_{x0}$ in the reference filter to obtain focused responses for the fore and aft channels. By processing the data with a filter matched to the signal's quadratic component, the target is no longer smeared in the azimuth direction and the signal-to-clutter ratio is improved.

The ATI signal is computed by multiplying the focused fore data with the complex conjugate of the focused aft data. The ATI signal is then smoothed using a one-dimensional moving average filter to reduce noisy peaks, and local maxima in the ATI magnitude are stored. To avoid clutter contamination, each of these maxima (which have been normalized to fall between 0 and 1) is weighted by the absolute value of their phase (which varies from $-\pi$ to π, with the highest weight given to those points furthest away from the zero-phase clutter region). The maximum after weighting should give the best estimate of the ATI phase of the target, and we should be relatively confident that it has not focused on a clutter peak. The phase is then unwrapped to fall between 0 and 2π, and its phase shift is translated into an across-

track velocity $\hat{v}_{y0\ \mathrm{ATIphs}}$ using an inversion of equation 6.4:

$$\hat{v}_{y0\ \mathrm{ATIphs}} = \angle\mathrm{ATI}(t_{\mathrm{img}})\frac{R_0 v_a}{k d y_0}. \tag{6.5}$$

A second although less accurate estimate of $\hat{v}_{y0}$ is then determined in order to resolve the π-wrap ambiguity in the ATI phase (see Appendix B.1.1 for a description of this ambiguity). The range trajectory of the extracted target track provides a range history over time, although the resolution is only as good as the range pixel spacing (4 metres in slant range for the CV 580 system). Fitting a parabola (i.e. second-order polynomial) to this range history, the first-order coefficient (see equation 2.11) is $v_{y0}y_0/R_0$, which - given known incidence angle θ_{inc} (where $\sin\theta_{\mathrm{inc}} = y_0/R_0$) - can be used to solve for v_{y0}. This estimate of across-track velocity is denoted $\hat{v}_{y0\ \mathrm{parabola}}$, and it should have the correct sign and a magnitude in the general vicinity of the true v_{y0}.

Note that only a small portion of the target's range-history function will be visible due to the limited synthetic aperture time during which the target is in the radar beam. If the target is moving very slowly across-track, then the parabolic range history will be relatively flat and the estimate of $\hat{v}_{y0\ \mathrm{parabola}}$ will be very poor. However, if the target is moving fast across-track, it will cross many range cells during the observation period, and one will be able to more robustly fit a range-history parabola to the data and estimate target parameters.

To resolve the ambiguity in the ATI phase, the target is classified as a slow, medium, or fast mover. To determine the mover category, $\hat{v}_{y0\ \mathrm{parabola}}$ is compared to velocity $v_{y0\ \theta=\pi}$, which is the across-track velocity corresponding to an ATI phase of π rads.

If:

$|\hat{v}_{y0\ \mathrm{parabola}}| < |v_{y0\ \theta=\pi}|$

Then it is a slow mover whose velocity is determined by re-computing $\hat{v}_{y0\ \mathrm{ATIphs}}$ in equation 6.5 after wrapping the phase back to a range of $-\pi$ to π to get the

correct sign.

$|\hat{v}_{y0\ \text{parabola}}| > |v_{y0\ \theta=\pi}|$ AND $|\hat{v}_{y0\ \text{parabola}}| < 2|v_{y0\ \theta=\pi}|$

The target has medium speed whose direction (i.e. sign) is determined by $\hat{v}_{y0\ \text{parabola}}$. Its velocity is given by $\hat{v}_{y0\ \text{ATIphs}}$ if moving in the positive y-direction, or $(2\pi - \hat{v}_{y0\ \text{ATIphs}})$ if moving in the negative y-direction.

$|\hat{v}_{y0\ \text{parabola}}| > 2|v_{y0\ \theta=\pi}|$

This is a fast mover which will travel through multiple range cells (if range resolution is reasonably good) over the observation time. Thus, the parabolic coefficients will likely represent the correct trajectory, and we may take the across-track velocity to simply be $\hat{v}_{y0\ \text{parabola}}$.

6.3.2 Analysis of estimated velocities

The algorithm described above in section 6.3.1 was applied to each control target in the Petawawa 2000 experimental data set to estimate across-track velocities. The across-track velocities for each pass determined using ATI phase and their velocities as measured using GPS are presented in Appendix A.3. Further examination of the accuracy of the GPS measurements (estimated at worst-case to be 0.5 m/s), possible timing synchronization errors between the radar imagery and GPS, and the method used to convert GPS speed and heading into an across-track velocity component are also described in Appendix A.3. Given the level of agreement between $\hat{v}_{y0}$ GPS and SAR estimates for many of the targets (e.g. four had differences of less than 0.05 m/s), GPS accuracies are likely much higher than 0.5 m/s.

The mean of the absolute value of the differences between ATI and GPS $\hat{v}_{y0}$ estimates was 0.9 m/s, with a standard deviation of 1.5 m/s. The mean falls well within the standard deviation, and thus no overall bias in the measurements is suspected. There are three outliers (see l1p5, l1p9 and l3p3 Convoy passes) which have significantly worse accuracies than the rest of the $\hat{v}_{y0}$ estimates. These errors could be

due to a poor estimate of $\hat{v}_{y0\ \mathrm{parabola}}$, asymmetric target tracks (i.e. not centred about broadside time, which is examined in [36]), or contamination of the ATI phase by other moving vehicles in the convoy.

The standard deviation of 1.5 m/s is slightly higher than that predicted in section B.2 for an airborne scenario. However, the theoretical estimation took only phase decorrelation due to additive noise into account. Time decorrelation, speckle and internal clutter motion, and imperfect channel balancing may also contribute to ATI phase variations affecting $\hat{v}_{y0}$ estimation.

Polar plots of ATI signals after azimuth compression for several of the controlled movers are shown in Figure 6.5. Figure 6.5(a) shows a well-defined phase for one pass of the Juliet target. The $\hat{v}_{y0}$ estimate for this target is within 0.03 m/s of the GPS velocity. However, a clean ATI signature does not necessarily guarantee an accurate estimate of $\hat{v}_{y0}$; Figure 6.5(b) displays the ATI signal for l1p9 Convoy with a sharply defined phase, whose $\hat{v}_{y0}$ is 6.2 m/s off from the GPS estimate. Not all targets have well-defined phases. The l2p6 Convoy target (with an error of 0.25 m/s in its velocity compared to the GPS) in Figure 6.5(c) shows significant variation in the ATI phase across the synthetic aperture, likely due to clutter contamination or contamination from other nearby moving vehicles. However, recall that the ATI phase used for velocity estimation is only at the peak response of the azimuth compressed ATI signal, which will have the maximum signal-to-clutter ratio. Bright stationary clutter is also visible in Figure 6.5(c) as the cluster of points near the positive real axis with zero ATI phase.

In summary, the results of across-track velocity estimation in experimental data are in general agreement with the conclusions from the ATI theory and simulations examined in sections 6.1 and 6.2. As expected, the presence of target acceleration does not introduce significant biases into the $\hat{v}_{y0}$ estimation from along-track interferometric phase. The mean of the absolute errors was only 0.9 m/s, which is more than a threefold improvement over the mean error in $\hat{v}_{x0}$ for the same targets exam-

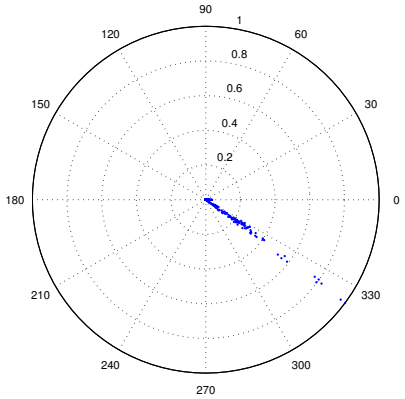

(a) ATI for l3p3 Juliet.

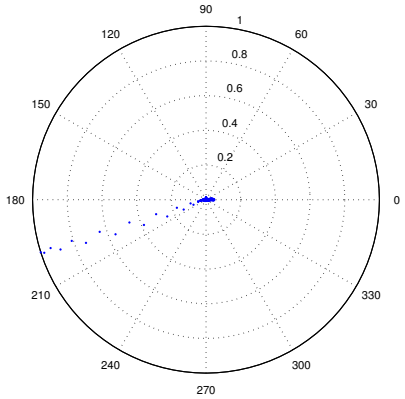

(b) ATI for l1p9 Convoy.

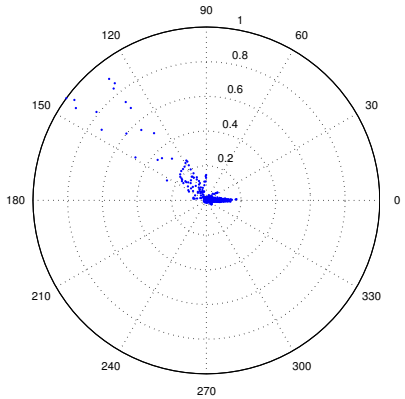

(c) ATI for l2p6 Convoy.

Figure 6.5: ATI signal (with normalized magnitude) for various experimental target tracks. Phase is given in degrees as an angle measured from the positive real axis, and magnitude as a distance from the origin. Note the well-defined phases in (a) and (b), although this does not indicate the accuracy of the ATI phase estimate (target in (a) had an error of only 0.03 m/s compared to the GPS velocity whereas the target in (b) had an error of 6.2 m/s). Oftentimes the ATI phase is somewhat variable across the compressed synthetic aperture as in (c), which suffers from what is likely clutter contamination. However, its peak response has a high SCR giving an error of only 0.25 m/s compared to the GPS.

ined in Chapter 5. A simple algorithm was used to estimate $\hat{v}_{y0}$ that did not extend the reference filter length or apply a bank of reference filters initialized with various v_{y0} velocities as was suggested in section 6.2.6. It is fortunate that some amount of spectral overlap between the target and reference signals was present for each pass, and thus the filter-bank method was not required for this data set.

Chapter 7

Acceleration detection and focusing improvements

Previous chapters have described the effects of target acceleration on detection, focusing, and velocity estimation. It was found that acceleration has only minor effects on detection, but can have detrimental effects on focusing moving target signals and can significantly bias the estimation of along-track velocity v_{x0} if a constant target velocity is assumed. It would be desirable to find a method of focusing targets irrespective of their motion components and to avoid biased velocity estimates. Even if one cannot solve for acceleration, being able to detect its presence would provide a warning to users of the data that along-track velocity estimates may be erroneous.

As previously discussed in Chapter 5, it is difficult to separate across-track acceleration a_{y0} and along-track velocity v_{x0} components in the second-order term of the range equation, and thus it is difficult to detect across-track acceleration. However, some possibilities lie in detecting the dominant motion components in the third-order term of the range equation (along-track acceleration a_{x0} and time-varying across-track acceleration $\dot{a}_{y0}$). A third-order polynomial may be fit to the range history, after which hypothesis testing may be used to determine if the target signature possesses a significant cubic component.

An alternative to polynomial fitting in the range domain is performing the same operation in the time-frequency domain. The advantages of the TF domain (including the reduction of white noise) were described in section 2.4.2. The TF domain also enables an estimation of the instantaneous frequency of the target track, which is useful in reconstructing the target phase history for use in a matched filter.

The objective of this chapter is to explore the possibilities that certain acceleration components(a_{x0} and $\dot{a}_{y0}$) may be detected in target signals, and that accelerating targets can be focused using time-frequency analysis. The theory of detecting and

focusing targets in the TF domain is described, followed by verification of these algorithms and evaluation of their sensitivity to target motion through simulations. These algorithms are then applied to the Petawawa 2000 data to detect and focus accelerating targets in experimental data.

7.1 Theory

The rationale for studying signals in the time-frequency (TF) domain, as well as various methods of transforming the signal data into the TF domain were outlined in section 2.4. Recall that the Pseudo Wigner-Ville distribution (PWVD) was identified as the preferred mapping transform for this application. Estimation of the instantaneous frequency of the target is critical to both target focusing and acceleration detection in the TF domain. An algorithm for extracting the time-frequency history of a target after applying the PWVD is discussed. Using this frequency history, one can attempt to detect the presence of certain target accelerations and to estimate the phase history, with which a focused target image may be obtained.

7.1.1 Tracking the instantaneous frequency

Time-frequency analysis provides a useful tool with which to estimate the instantaneous Doppler frequency shift induced by relative radar-target motion [5]. The signal received by the radar experiences a phase shift $\varphi(t)$ proportional to the variation in range due to radar and target motion. The instantaneous frequency (IF or $f(t)$) is then defined as the first derivative of this phase function with respect to time divided by 2π [12, 67]:

$$f(t) = \frac{-1}{2\pi}\frac{d\varphi(t)}{dt}, \tag{7.1}$$

where the negative sign is introduced such that positive frequencies represent Doppler components moving towards the radar, and negative frequencies represent Doppler components moving away from the radar [52]. We would like to estimate the IF

history of accelerating targets, such that the phase function $\varphi(t)$ can be determined through integration of equation 7.1 for use in focusing and acceleration detection algorithms.

Having transformed a target signal into the time-frequency domain using the PWVD, the next step is to extract the TF history (i.e. the IF). An automated algorithm was developed based on the tracking scheme used by Gierull in his target detection program (see [36, 75]). It is assumed that we are tracking point targets such that the instantaneous bandwidth of the IF is only one pixel wide (see section 2.4.2).

The frequency detection algorithm begins by applying a power detector to the DPCA TF magnitude image. All pixels with a DPCA magnitude several dB larger than the mean (across the entire two-dimensional TF domain) are passed to a tracking stage. At each azimuth time (or pulse) the pixel with the maximum DPCA magnitude is added to the frequency track. This reduces a target track spread out across multiple frequency bins at any one time to a target track a single cell wide in frequency.

In order to create a smoothly varying TF history, one must resolve the frequency ambiguities to remove wraps at $\pm f_{\mathrm{PRF}}/2$. These jumps are present due to undersampling of the signal in azimuth, and the fact that after application of the PWVD the signal has a period twice that of the original signal spectrum (see section 2.4.3), such that the PWVD bandwidth is reduced to half the PRF. The tracking algorithm searches for frequency jumps on the order of $\pm f_{\mathrm{PRF}}/2$ and removes these jumps by shifting the signal up or down in frequency to create a smoothly varying time-frequency history. Finally, the entire frequency track is shifted by a multiple of $\pm f_{\mathrm{PRF}}/2$ such that the Doppler centroid agrees with the ATI (along-track interferometry) estimate of across-track velocity (see Chapter 6 for details on the ATI algorithm used).

This method of estimating the instantaneous frequency makes no assumptions regarding the form of the phase function, and can thus be used for accelerating target signals as well as linear frequency-modulated signals (such as echoes from targets

travelling at constant velocities). However, it is assumed that there is a rough estimate of the Doppler centroid available with which to centre the extracted TF track in frequency. Instead of using the ATI phase, this ambiguity may also be resolved by sub-beam partitioning [49], or with knowledge of the target's range walk from data in the range compressed domain. If the ambiguity is offset from its true value by $\pm f_{\mathrm{PRF}}/2$, then the error becomes obvious upon focusing; there will be a lack of spectral overlap between the reference and true target signal, and will therefore not focus to an optimal peak (see Appendix B.1.3 for a discussion of spectral overlap and section 7.1.3 for a description of focusing from the TF domain). However, if the ambiguity is in error by $\pm f_{\mathrm{PRF}}$, then it will be possible to obtain a focused target with an incorrect Doppler centroid.

7.1.2 Detecting acceleration using TF analysis

As previously mentioned, some possibilities lie in using TF analysis to detect accelerating targets. The IF of targets with constant velocity are well-approximated by a linear TF history (see equation 5.10). In these instances, the cubic coefficient in the range equation from equation 2.11 is zero, and when the time derivative of the range is taken (where range rate is directly proportional to frequency), there is a linear dependency of frequency on time. However, in the presence of along- and across-track accelerations, the TF history will have a quadratic or higher-order dependence on time.

Upon closer examination of the third-order component of equation 2.11, it is seen that a_{x0}, $\dot{a}_{y0}$, and v_{x0} dominate its value. The contribution from $v_{y0}a_{y0}\left(1-\frac{y_0^2}{R_0^2}\right)$ is much smaller compared to the second two terms, and thus even in the presence of constant across-track acceleration a_{y0}, the TF history will remain nearly linear. However, in the presence of non-zero along-track acceleration a_{x0} and time-varying acceleration $\dot{a}_{y0}$, the cubic term of the range equation may be significant enough to induce a distinctly non-linear TF history.

Polynomial fits to the instantaneous frequency provide a method of detecting a_{x0} and $\dot{a}_{y0}$. One may fit a quadratic (i.e. parabola) to the IF of a target and determine whether or not there is a significant second-order term. However, it is difficult to theoretically determine the threshold at which the quadratic coefficient is 'significant'; this depends on the SCR, CNR, and probability density function of the clutter, plus a small second-order coefficient is expected in any case (terms smaller than $1/R_0^2$ were dropped in Taylor series expansion of equation 2.11, but are actually still present). The acceleration detection threshold will also be constrained by the acceptable probability of false alarms. The statistical modelling required for significance testing is beyond the scope of this research, although it represents a potential area for further study.

A similar approach to acceleration detection could be used in the one-dimensional (1-D) time domain without any transformation into time-frequency space. In this case, a cubic polynomial may be fit to the extracted DPCA phase history of the target, and a threshold may be used to determine whether or not there is a significant third-order component. However, due to the wide bandwidth of noise in the TF domain (section 2.4.2), it is expected that time-frequency analysis may provide some advantage over the 1-D time domain for detecting accelerating targets, particularly at low SCRs.

In order to compare acceleration detection in the 1-D time and 2-D time-frequency domains, the IF may be integrated over time to estimate the target phase history $\varphi(t)$. A third-order polynomial may then be fit to each phase history, and the mean and variance in each estimate of the cubic coefficient examined. Section 7.2.2 describes the results of simulations of acceleration detection, including comparisons using phase histories derived in each domain.

7.1.3 Focusing using TF Analysis

The objective of this section is to find a method of generating SAR images of moving vehicles that does not require knowledge of the vehicle's motion parameters. Focusing a moving target is possible if the phase modulation induced on the signal by the radar-target relative motion can be determined [5]. Provided that the target signal is sufficiently strong in the DPCA image such that the instantaneous frequency may be reliably estimated, the IF may be used to compute this phase modulation [5].

Barbarossa was one of the first researchers to propose a scheme for detecting and focusing moving targets based on joint TF analysis [5]. He put forward one technique in which the instantaneous phase is used in a matched filter to obtain a focused image [5, 7], where the instantaneous phase $\varphi(t)$ is evaluated by integrating the estimated frequency track through time. The integration of a discrete TF track is given by:

$$\varphi(t) = \frac{1}{f_{\mathrm{PRF}}} \sum_{t'=-T/2}^{t} f(t') \qquad |t| \leq \frac{T}{2}, \tag{7.2}$$

where T is the synthetic aperture length in units of time, and $f(t)$ is the target IF at sampled times $t = n/f_{\mathrm{PRF}}$ for integer n. Apart from an unimportant constant term, the resulting phase from equation 7.2 is a replica of the target phase history.

The reference signal is then $\exp(j\varphi(t))$; the time-reverse complex conjugate of this reference is convolved with the target signal to focus a moving target [29]. Rieck [67] has demonstrated the use of this technique to focus a moving vessel using multi-channel SAR data. The advantage of this method is that it does not require any assumptions regarding the type of phase modulation on the signal (e.g. quadratic, cubic, etc.) [5], and thus it may be used to focus accelerating targets or targets with even higher-order motion components. This method may also be used to focus moving targets distributed over multiple resolution cells if a rigid body assumption may be used such that the entire target possesses the same motion.

7.2 Simulations

Simulations were conducted to verify the IF tracking, acceleration detection, and focusing algorithms described in section 7.1. An airborne geometry with radar parameters typical of the CV 580 system (see values in Table 3.1) is assumed.

7.2.1 Tracking the instantaneous frequency

To verify the ability of the tracking algorithm from section 7.1.1 to extract the instantaneous frequency of a target through time, simulations were performed using various target motion parameters and various SCRs. An example of the TF history prior to correction of $\pm f_{\mathrm{PRF}}/2$ frequency jumps for a simulated target with $v_{x0} = 10$ m/s and $v_{y0} = 15$ m/s (zero acceleration) and an SCR of 0 dB is shown in Figure 7.1. An enlarged portion of Figure 7.1 is shown in Figure 7.2, where the detected

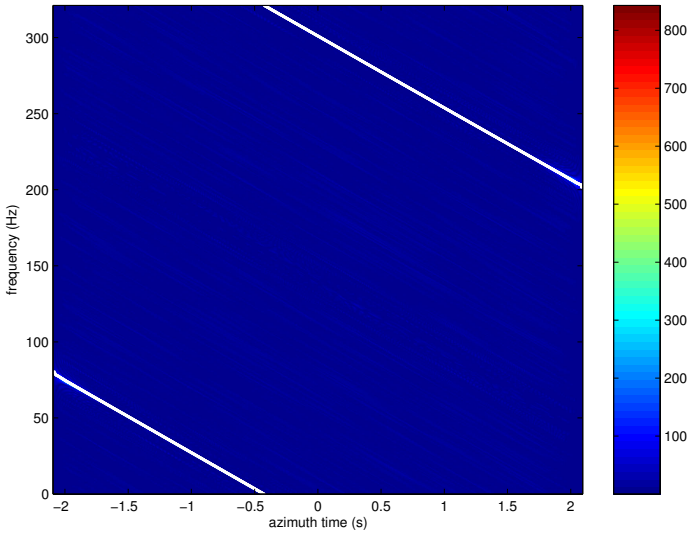

Figure 7.1: Instantaneous frequency of a simulated target with constant velocity ($v_{x0} = 10$ m/s, $v_{y0} = 15$ m/s, SCR = 0 dB) tracked through azimuthal slow-time (in white), and overlaid on DPCA magnitude transformed into the TF domain using the PWVD.

frequency for each azimuth time is shown in white, clearly following the peak DPCA

magnitude in the TF domain. Correlated complex Gaussian clutter was simulated

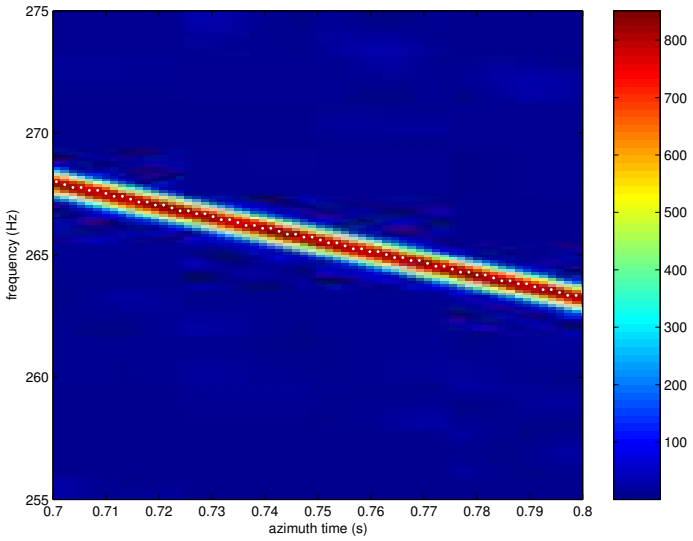

Figure 7.2: Enlarged portion of Figure 7.1. Instantaneous frequency of a simulated target with constant velocity (v_{x0} = 10 m/s, v_{y0} = 15 m/s, SCR = 0 dB) tracked through azimuthal slow-time (in white). The IF track is overlaid on the DPCA magnitude image transformed into the TF domain using the PWVD. Note that the IF tracking algorithm follows the peak DPCA magnitude response.

with a coherence (represented by ρ) of 0.95, which is a relatively conservative value for land clutter observed from typical airborne platforms [35]. Additional information on coherence is available in Appendix B.2.

The tracking algorithm works well for reasonable SCRs. At SCRs below -15 dB however, the tracking algorithm breaks down as bright noise spikes in the TF domain, diverting the tracker off of the true IF. Recall that an SCR of 0 dB means that clutter and target signal components are equally bright, i.e. have equal reflectivity in the range compressed domain, and thus an SCR of -15 dB is very low, below the anticipated SCRs for ground moving vehicles [46].

Tracking the IF in a spaceborne geometry

The time-frequency tracking algorithm may also be applied to simulations of a spaceborne scenario. Radar/geometry parameters typical of the RADARSAT-2 scenario (see Table 3.2) were used with a PRF of 2000 Hz and an azimuthal beamwidth of 0.4°. The increased distance to the scatterers and the radiation-resistant hardware used in space decreases the clutter-to-noise ratio by approximately 5 to 10 dB [46]. This increase in noise makes tracking of the IF within the 2-D TF DPCA magnitude image more difficult, particularly for low across-track velocities v_{y0} which result in low DPCA magnitudes. Although IF tracking is successful for a simulated target with $v_{y0} = 15$ m/s (as simulated above), noise spikes in the TF domain begin to pose a problem for $v_{y0} < 5$ m/s in the space-based case. An example of the instantaneous frequency (before correction for $\pm f_{PRF}/2$ jumps) for a target with $v_{y0} = 3$ m/s and all other motion parameters set to zero is shown in Figure 7.3. Note the errors in the extracted target time-frequency history, which should follow a smooth line. However, the majority of these errors could be removed with some type of filtering to ignore isolated IF points, giving a more robust TF track.

7.2.2 Detecting acceleration using TF analysis

Having established the effectiveness of the IF tracking algorithm, the acceleration detection techniques suggested in section 7.1.2 are now evaluated. Simulations were performed with non-zero a_{x0} and $\dot{a}_{y0}$ to examine the magnitude of the third-order coefficient for an accelerating target. The objective was to determine whether or not this cubic component in the range equation is discernible such that the acceleration may be detected, even if the target is embedded in strong background clutter.

An approximation of the third-order component can be computed by fitting a cubic polynomial to the target's DPCA phase directly. However, as previously mentioned, the wide bandwidth of noise in the TF domain is expected to prove advantageous over the 1-D time domain for detecting accelerating targets at low SCRs.

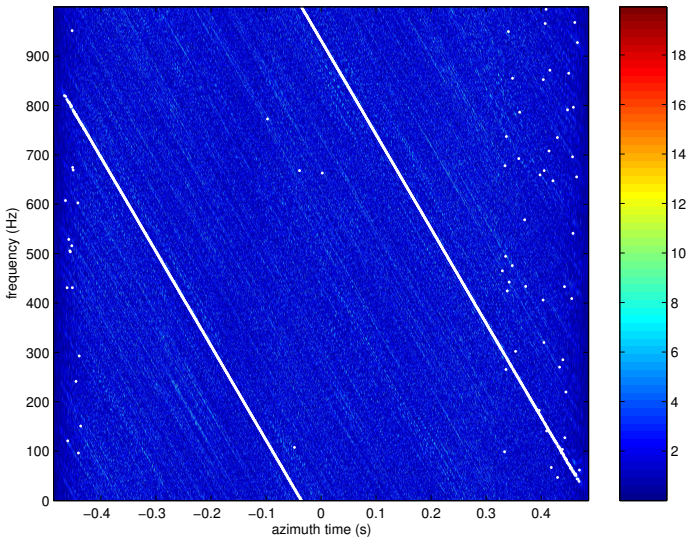

Figure 7.3: Instantaneous frequency of a simulated target in a spaceborne geometry with slow constant velocity ($v_{y0} = 3$ m/s and SCR $= 0$ dB) tracked through azimuthal slow-time (in white). The IF track is overlaid on the DPCA magnitude image transformed into the TF domain using the PWVD. Low coherence and low DPCA magnitudes introduce errors in the extracted IF track.

In order to perform a fair comparison between the TF and 1-D time domains, it was ensured that no *a priori* information was introduced into either technique. For this reason, the thresholding operation used to filter TF pixels before the IF estimation stage (see section 7.1.1) was removed for these simulations, although this may degrade the IF tracking operation by capturing bright noise spikes.

Monte Carlo simulations

Monte Carlo simulations were conducted for accelerating and non-accelerating point targets at a variety of SCRs. The Monte Carlo method solves a problem by generating a large number of trial runs, and then observes the fraction obeying some property or properties. This technique is useful in obtaining a numerical solution to problems too complicated to solve analytically [88].

A constant velocity target with $v_{y0} = 1$ m/s and $v_{x0} = 10$ m/s was simulated in addition to an accelerating target with $v_{y0} = 1$ m/s, $v_{x0} = 10$ m/s, and $a_{x0} = 0.5$ m/s^2. A non-zero v_{y0} was chosen such that the DPCA magnitude signal was non-zero over the course of the observation interval (see Chapter 3). The SCR was varied from -10 to 30 dB in steps of 2 dB. Two hundred realizations of each target at each SCR were created in order to generate a statistically significant sample.

An airborne scenario was assumed with radar and geometry parameters given by Table 3.1. Correlated complex Gaussian clutter was simulated with a coherence (ρ) of 0.95. Assuming that the only factor contributing to decorrelation of the data is additive noise, then coherence is related to the clutter-to-noise ratio (CNR) by:

$$\rho = \frac{1}{1 + \frac{1}{CNR}}, \tag{7.3}$$

such that $\rho = 0.95$ corresponds to a CNR of 25.6 dB. Note that CNRs for the spaceborne RADARSAT-2 scenario are projected to be to be 5 to 10 dB lower than the airborne scenario, resulting in coherences on the order of 0.94 [46], although lower coherences due to image misregistration and other factors are possible.

For each realization, the DPCA target phase was unwrapped to generate the time-

dependent phase function $\varphi(t)$. A third-order polynomial was fit to $\varphi(t)$, and the coefficients recorded. Some issues were encountered in unwrapping the DPCA phase for high velocity targets at the given sampling frequency. If the target travels more than $\lambda/4$ between sampling intervals in the slant-range direction (i.e. more than π rads in a polar plot), then the unwrapping algorithm does not know in which direction to unwrap. Additional unwrapping difficulties may occur if the target bandwidth over the synthetic aperture exceeds the PRF. See Appendix B.1 for further discussion on the velocity/acceleration bounds at which these problems occurs. However, neither of the simulated targets described above had slant-range displacements exceeding $\lambda/4$ nor a bandwidth exceeding the PRF, and thus these sampling issues did not affect the Monte Carlo simulation results.

Having estimated the third-order coefficient in the time domain, each simulated target track was transformed into the TF domain using the PWVD. The IF was extracted using the same method as described in section 7.1.1, except for the omission of the thresholding operation as mentioned in section 7.2.2. The IF was then integrated over time to estimate the phase history $\varphi(t)$. A third-order polynomial was fit to the phase output from equation 7.2, and the coefficients were retained for further analysis.

Cramer-Rao lower bound

For comparison purposes, the Cramer-Rao lower bound (CRLB) of the third-order coefficient was estimated for each target at each SCR. The Cramer-Rao inequality provides a lower bound on the variance of an unbiased estimator [40, 44]:

$$\langle(\hat{\theta}-\theta)^2\rangle \geq \frac{1}{\left\langle\left[\frac{d}{d\theta}\ln p(\mathbf{x};\theta)\right]^2\right\rangle}, \tag{7.4}$$

where $\langle\cdot\rangle$ is the expectation operator, θ is the true value of the parameter, $\hat{\theta}$ is its estimate, $p(x;\theta)$ is the probability density function of variable x dependent on parameter θ, and the right-hand side of the equation is the minimum achievable variance. Ristic and Boashash [69] have derived the CRLBs of a signal with constant

amplitude and polynomial phase measured in additive noise. The signal model is given by:

$$s(n\Delta) = A\exp\left(j\sum_{i=0}^{p} b_i(n\Delta)^i\right) + w(n\Delta) \qquad n = -\frac{N}{2}, -\frac{(N-1)}{2}, \ldots, \frac{N}{2} \tag{7.5}$$

where s is the signal, A is the signal amplitude, N is the number of samples in the signal, Δ is the sampling interval (i.e. $\Delta = 1/f_{\mathrm{PRF}}$), p is the polynomial order of the phase, and $w(n\Delta)$ is stationary complex Gaussian white noise with zero mean and variance σ_w^2.

Assuming that the DPCA target phase may be represented as a third-order polynomial ($p = 3$):

$$\angle\mathrm{DPCA} = b_0 + b_1(n\Delta) + b_2(n\Delta)^2 + b_3(n\Delta)^3, \tag{7.6}$$

the variance of the third-order coefficient has a minimum possible value of [69]:

$$\mathrm{CRLB}\{b_3\} = \frac{1400\sigma_w^2}{N^7A^2\Delta^6}. \tag{7.7}$$

The third-order polynomial of equation 7.6 may represent the phase of both the constant velocity and accelerating targets. Note that although the third-order coefficient is zero in the approximated Taylor expansion of the range equation for a target moving at constant velocity (equation 2.11), small terms on the order of $1/R_0^2$ were dropped from the expression, and thus a small third-order term does exist.

The variance of the white noise σ_w^2 may be computed by examining the expected value and variance of the clutter difference after DPCA. Let $\vec{c}_1 = [c_0 \ \ldots \ c_N]^T$ represent the clutter contribution from the fore channel, and $\vec{c}_2$ the contribution from the aft channel, where ^{T} represents the transpose operation. Each $\vec{c}_i$ is a vector with zero mean and variance σ_{ci}^2 for $i = 1, 2$. Assume that each SAR channel is independent, but has common clutter power $\sigma_{c1}^2 = \sigma_{c2}^2 = \sigma_c^2$. Then, the expected value of the clutter difference is:

$$\langle\vec{c}_1 - \vec{c}_2\rangle = \langle\vec{c_1}\rangle - \langle\vec{c_2}\rangle = 0, \tag{7.8}$$

and the variance is:

$$\begin{aligned}\mathrm{var}[\vec{c}_1 - \vec{c}_2] &= \langle (\vec{c}_1 - \vec{c}_2)^*(\vec{c}_1 - \vec{c}_2)\rangle \\ &= \langle \vec{c}_1^{\,*}\vec{c}_1\rangle - \langle \vec{c}_1^{\,*}\vec{c}_2\rangle - \langle \vec{c}_2^{\,*}\vec{c}_1\rangle + \langle \vec{c}_2^{\,*}\vec{c}_2\rangle \\ &= \sigma_c^2 - \sigma_c^2\rho\exp(j\theta) - \sigma_c^2\rho\exp(-j\theta) + \sigma_c^2 \\ &= 2\sigma_c^2 - 2\rho\cos\theta\sigma_c^2.\end{aligned}$$

For stationary terrain the along-track interferometric phase $\theta = 0$, and thus:

$$\mathrm{var}[\vec{c}_1 - \vec{c}_2] = 2\sigma_c^2(1-\rho), \tag{7.9}$$

where ρ is the scene coherence. Substituting equation 7.9 into equation 7.7, and replacing A/σ_c by the SCR, we find:

$$\mathrm{CRLB}\{b_3\} = \frac{2800(1-\rho)f_{\mathrm{PRF}}^6}{N^7\mathrm{SCR}^2}. \tag{7.10}$$

Analysis of simulations

Figures 7.4 and 7.5 display the absolute mean error and inverse variance of the third-order coefficient from 200 realizations of a constant velocity target at various signal-to-clutter ratios. A decibel scale is used in order to emphasize the differences between polynomial fitting to the DPCA phase directly, and fitting to the phase output from integration of the IF. Due to the decibel scale, absolute values of the mean error are taken to avoid taking the logarithm of a negative number.

Similarly, Figures 7.6 and 7.7 illustrate the mean error and inverse variance of the third-order coefficient from 200 realizations of an accelerating target (v_{x0} = 10 m/s, v_{y0} = 1 m/s, a_{x0} = 0.5 m/s^2) at various signal-to-clutter ratios. The plots from the accelerating and non-accelerating targets are very similar; both display the same trends as a function of SCR with regards to mean error and variance of the third-order coefficients. Neither the polynomial fit directly to the DPCA phase nor the polynomial fit to the output from IF integration have coefficient variances

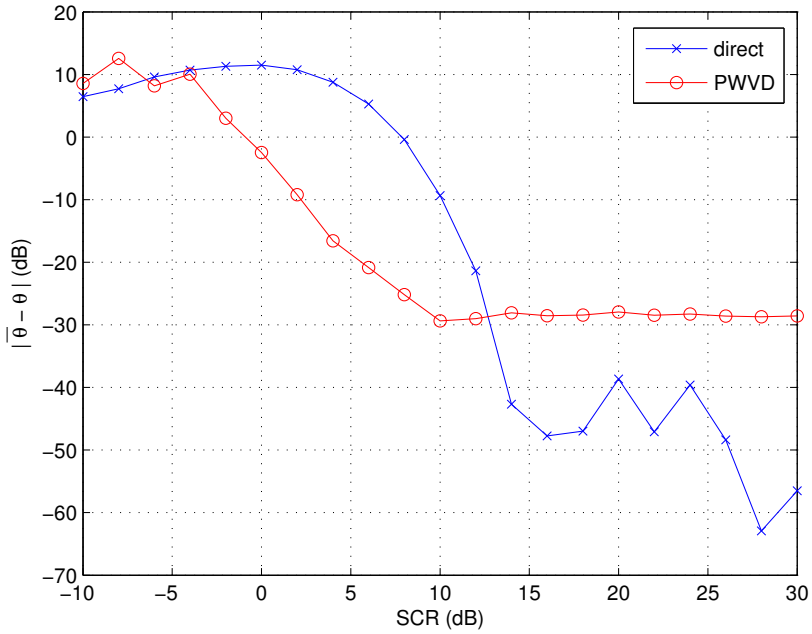

Figure 7.4: Absolute error in the mean value of the cubic coefficient (of a polynomial fit to the DPCA phase) for a simulated target moving with constant along-track velocity $v_{x0} = 10$ m/s and across-track velocity $v_{y0} = 1$ m/s, graphed as a function of SCR. 'Direct' represents a polynomial fit to the DPCA phase directly, while 'PWVD' uses integration of the IF estimated from the PWVD for polynomial fitting. Means are generated from 200 realizations of the target at each SCR. Note the decibel scale on both axes.

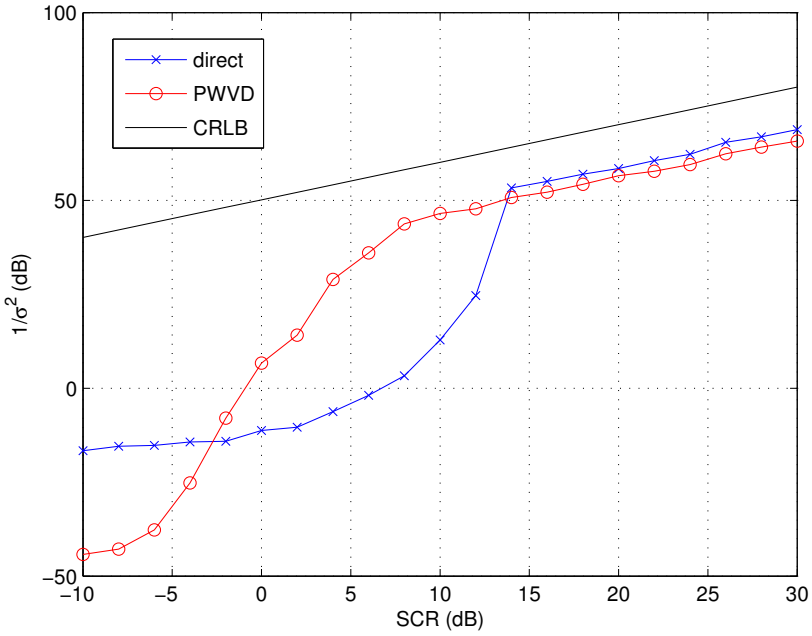

Figure 7.5: Inverse variance of the cubic coefficient (of a polynomial fit to the DPCA phase) for a simulated target moving with constant along-track velocity $v_{x0} = 10$ m/s and across-track velocity $v_{y0} = 1$ m/s, graphed as a function of SCR. 'Direct' represents a polynomial fit to the DPCA phase directly, while 'PWVD' uses integration of the IF estimated from the PWVD for polynomial fitting. Variances are generated from 200 realizations of the target at each SCR. The Cramer-Rao lower bound is in black for reference. Note the decibel scale on both axes; the figure format was modelled on figures from [68].

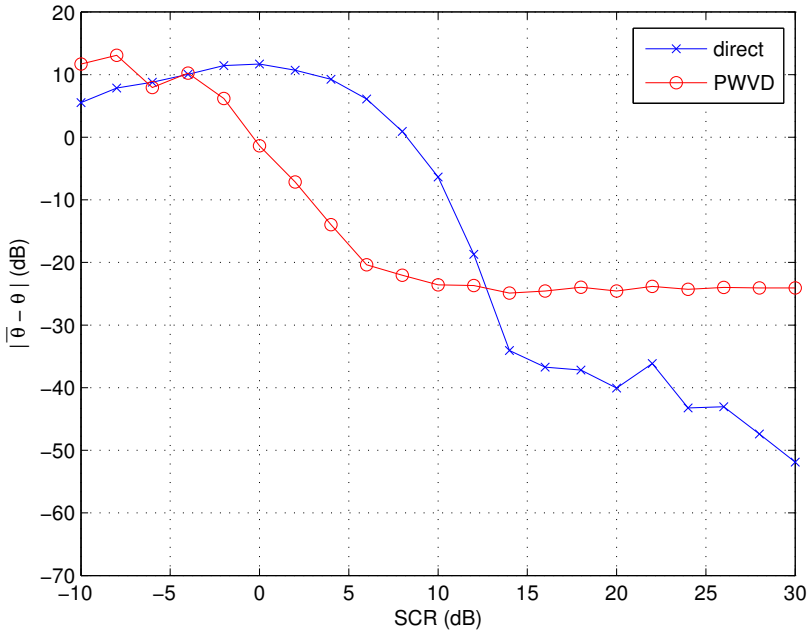

Figure 7.6: Absolute error in the mean value of the cubic coefficient (of a polynomial fit to the DPCA phase) for a simulated accelerating target moving with $v_{x0} = 10$ m/s, $v_{y0} = 1$ m/s and $a_{x0} = 0.5$ m/s^2, graphed as a function of SCR. 'Direct' represents a polynomial fit to the DPCA phase directly, while 'PWVD' uses integration of the IF estimated from the PWVD for polynomial fitting. Means are generated from 200 realizations of the target at each SCR. Note the decibel scale on both axes.

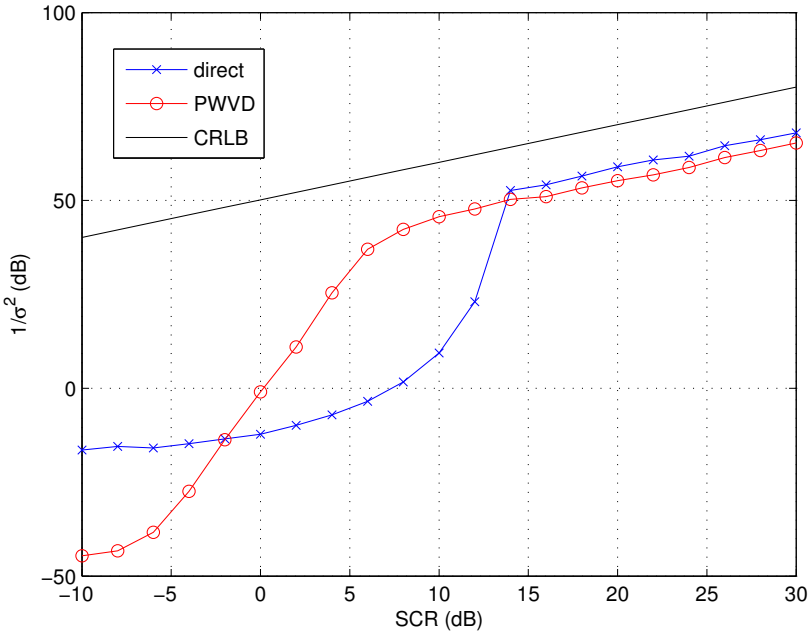

Figure 7.7: Inverse variance of the cubic coefficient (of a polynomial fit to the DPCA phase) for a simulated accelerating target moving with $v_{x0} = 10$ m/s, $v_{y0} = 1$ m/s and $a_{x0} = 0.5$ m/s^2, graphed as a function of SCR. Variances are generated from 200 realizations of the target at each SCR. 'Direct' represents a polynomial fit to the DPCA phase directly, while 'PWVD' uses integration of the IF estimated from the PWVD for polynomial fitting. The Cramer-Rao lower bound is in black for reference. Note the decibel scale on both axes; the figure format was modelled on figures from [68].

approaching the Cramer-Rao lower bound, and thus neither are statistically efficient estimators. Further analysis on the statistical properties of each technique was beyond the scope of this research.

At very low signal-to-clutter ratios (approximately less than -2 dB), the phase output from the IF integration has both a higher bias in the mean third-order coefficient and higher variance than integrating the phase directly, although both methods yield relatively poor results. Improved results may be obtained using the TF method by reintroducing the power detector threshold in the IF tracking operation, although this makes comparisons between the direct and PWVD fitting methods inappropriate. Such low SCRs may be present in range compressed data collected over urban areas. However, as SCR increases to within the 0 to 10 dB range, there is a clear advantage to using time-frequency analysis, with lower mean errors and lower variances in the cubic coefficient than when using the direct phase fitting technique. These improvements are significant given the decibel scale of the plots.

The gains when using the IF to estimate phase can be attributed to reduced contribution from the clutter noise to the tracked target signal. As discussed in section 2.4.2, the instantaneous bandwidth of a target in the TF domain is extremely small at any one time, while the bandwidth of the noise is much larger. After taking the PWVD, the target energy is concentrated along one arc, whereas the noise is spread or diluted over the 2-D time-frequency space, and therefore has less influence on the target signal. A comparison between the phase function $\varphi(t)$ of the unwrapped DPCA phase, and $\varphi(t)$ computed from the output of IF integration for a constant velocity target with an SCR of 0 dB, is shown in Figure 7.8. Note the close agreement between the phase determined using TF analysis and the true DPCA phase of the target signal (uncorrupted by clutter or noise).

Signal-to-clutter ratios between 0 and 10 dB are expected to be common in realistic scenes of moving vehicles observed from airborne and spaceborne platforms. Vehicles moving along a highway in the experimental data (Appendix A.1) were detected with

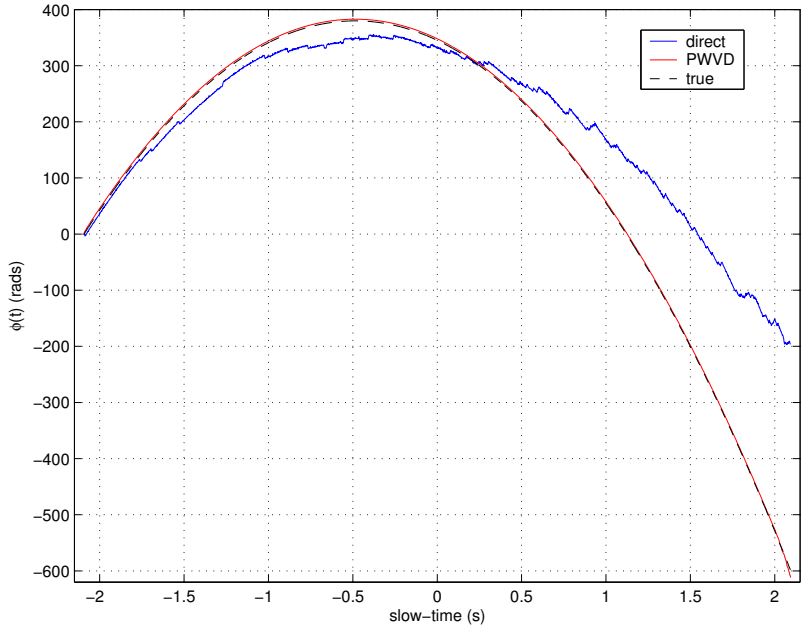

Figure 7.8: Unwrapped DPCA phase through azimuthal slow-time for a target with an SCR of 0 dB moving with constant velocity ($v_{x0} = 10$ m/s, $v_{y0} = 1$ m/s). Phases are shown prior to polynomial fitting for the direct case (blue) and after transformation by the PWVD and integration of the IF (red). The true DPCA phase of the target signal (no added clutter or noise) is given in black.

SCRs of between 0.6 to 10.8 dB. Note that the SCR for each vehicle was estimated from the maximum intensity in the range compressed domain. Thirty-four sample targets were extracted, which had a mean SCR of 6.4 dB.

As the SCR continues to increase upwards of 10 dB, the target signal sufficiently overpowers the noise such that direct polynomial fitting to the DPCA phase is the preferred method of estimating the third-order coefficient to obtain small errors in the mean and small variances. Whereas the direct method continues to converge upon the true coefficient value with increasing SCR (where a difference of $-\infty$ in the logarithmic scale represents zero error in the mean), the TF technique appears to be a biased estimator of the cubic coefficient (see Figures 7.4 and 7.6). Transformation into the TF domain is accompanied by some inevitable loss in resolution, and the tracking operation introduces some quantization noise in determining the IF, thus limiting the achieveable accuracy and precision in determining the third-order coefficient.

The third-order coefficient for the non-accelerating target phase had a true value of 0.0094, whereas the cubic coefficient for the accelerating target was 18.3 dB greater (or approximately 68 times greater) at 0.64. Thus, at high SCRs, accelerating targets with non-zero a_{x0} or $\dot{a}_{y0}$ should be discernible from targets moving with constant velocity.

Although beyond the scope of this work, one could assume certain probability density functions for the target and clutter signals (e.g. Gaussian target and K-distributed clutter) in order to determine a constant false alarm rate threshold to be used for acceleration detection. Targets whose third-order coefficients after polynomial fitting to the phase exceed this threshold could then be flagged as accelerating targets with a known level of confidence.

To summarize, for targets with very low SCRs TF analysis is poor at detecting acceleration (worse than fitting a polynomial to the DPCA phase itself), for low SCRs from 0 to 10 dB TF analysis has lower variance than using the direct phase, and for high SCRs the direct phase is best. TF analysis is thus promising for the detection

of accelerating targets with medium to low SCRs although more research is needed.

Detecting acceleration in a spaceborne geometry

Theoretically the acceleration detection method used to identify significant third-order coefficients in the airborne scenario may be applied to the space-based case. However, as previously mentioned, CNRs in the spaceborne situation are expected to be up to 10 dB lower than in the airborne scenario, decreasing the scene coherence to approximately 0.94. This increased noise reduces the ability to track the IF and accurately model the instantaneous DPCA phase, leading to errors in estimates of the third-order coefficient and difficulties in discerning whether or not there exists a significant third-order term. As discussed in section 4.1.2, only extremely large cubic terms create mismatches in the reference and target signals to defocus target responses, and thus one may not be concerned with detecting the effects of a_{x0} and $\dot{a}_{y0}$ in the spaceborne scenario in any case.

7.2.3 Focusing using TF Analysis

As described in section 7.1.3, instantaneous phase (estimated from IF integration) may be used to compress moving point target signals. Simulations of various target motion parameters and SCRs were conducted to test this method of focusing. In each instance, focused images of the targets were obtained in the azimuthal dimension, where a focused point target appears as a narrow sinc function. Simulations concentrated on an SCR range from 0 to 10 dB, typical of real vehicle targets observed from an airborne platform. The focused image of a simulated target embedded in clutter with an SCR of 0 dB, and moving target parameters $[v_{x0}\ v_{y0}\ a_{x0}\ a_{y0}\ \dot{a}_{y0}]^T = [10\text{ m/s} \quad 1\text{ m/s} \quad 0.1\text{ m/s}^2 \quad 0.1\text{ m/s}^2 \quad 0.01\text{ m/s}^3]^T$ is shown in Figure 7.9. An airborne scenario was assumed with radar/geometry parameters typical of those encountered using the CV 580 system, and the clutter was given a coherence of 0.95. The -3 dB width of the focused response is approximately 1.0 m. The theoretical -3 dB limit for focusing a stationary target with this system is

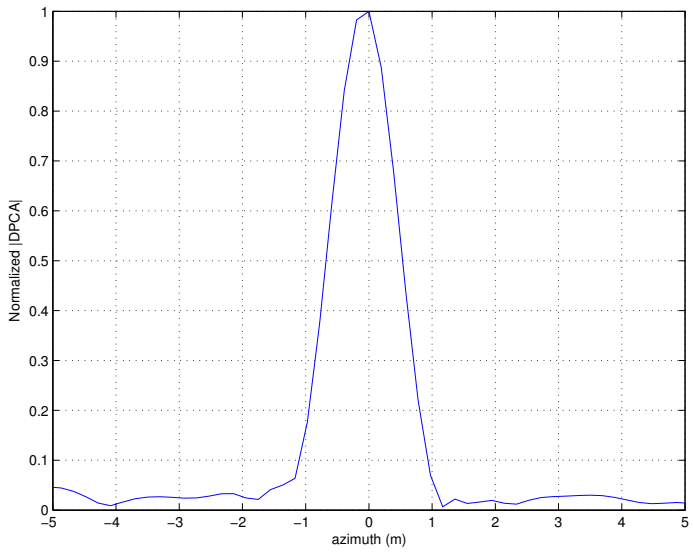

Figure 7.9: Normalized DPCA magnitude of a simulated accelerating target with parameters $[v_{x0}\ v_{y0}\ a_{x0}\ a_{y0}\ \dot{a}_{y0}]^T = [10\text{ m/s} \quad 1\text{ m/s} \quad 0.1\text{ m/s}^2 \quad 0.1\text{ m/s}^2 \quad 0.01\text{ m/s}^3]^T$ focused using instantaneous phase from IF integration. An SCR of 0 dB and a clutter coherence of 0.95 were modelled. Note the narrow sinc response with a -3 dB width of approximately 1.0 m.

0.47 m. Transformations into the TF domain and decorrelation of the clutter due to additive noise create a slight loss in resolution. As well, changes in the chirp rate of the received echo due to target motion may impact the azimuthal resolution of the system by increasing or decreasing the available target bandwidth (see section 4.1.3).

For comparison, the same simulated moving target was focused using conventional SAR azimuth processing (i.e. a reference filter assuming zero velocity and acceleration), and the compressed image is shown in Figure 7.10. Note the severe degradation in resolution (with a -3 dB width of 16 m) and the decrease in peak power (where the DPCA magnitude was normalized by the same factor as that in Figure 7.9).

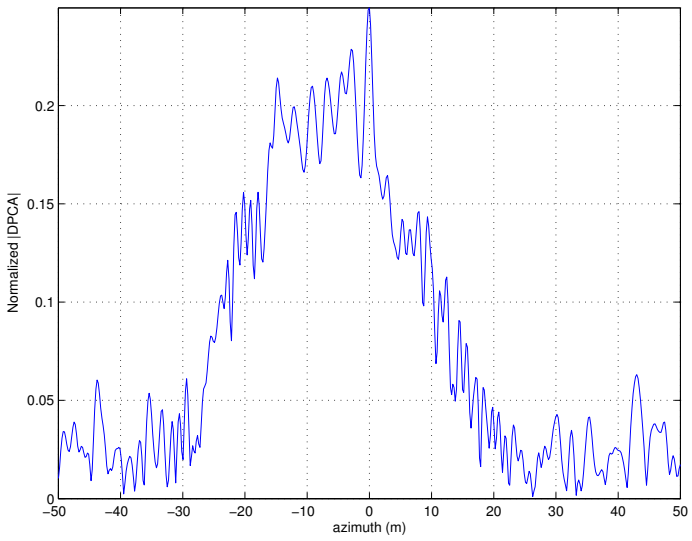

Figure 7.10: Normalized DPCA magnitude of a simulated accelerating target with parameters $[v_{x0}\ v_{y0}\ a_{x0}\ a_{y0}\ \dot{a}_{y0}]^T = [10\text{ m/s} \quad 1\text{ m/s} \quad 0.1\text{ m/s}^2 \quad 0.1\text{ m/s}^2 \quad 0.01\text{ m/s}^3]^T$ focused using conventional SAR processing (i.e. assuming a stationary target). An SCR of 0 dB and a clutter coherence of 0.95 were modelled. Note the broad and smeared response with a -3 dB width of approximately 16 m. DPCA magnitudes were normalized by the same factor as in Figure 7.9 for comparison purposes.

Focusing in a spaceborne geometry

Theoretically, this method of focusing may also be used to focus targets in the spaceborne case. However, as discussed in the latter portion of section 7.2.2, the decreased

clutter-to-noise ratios in the space-based scenario decreases scene coherence such that may be difficult to track the IF through azimuthal time due to large noise spikes in the 2-D TF domain. For the simulated target from section 7.9 with $[v_{x0}\ v_{y0}\ a_{x0}\ a_{y0}\ \dot{a}_{y0}]^T = [10\text{ m/s}\quad 1\text{ m/s}\quad 0.1\text{ m/s}^2\quad 0.1\text{ m/s}^2\quad 0.01\text{ m/s}^3]^T$ and an SCR of 0 dB, the time-frequency history of the target could not be successfully tracked for a spaceborne geometry and noise level. The problem is that v_{y0} is only 1 m/s, and thus the DPCA magnitude is very low. Unless the CNR and SCR of the target under consideration are unusually large, focusing using the IF track will be successful in the RADARSAT-2 spaceborne case only for targets with at least moderate across-track velocities (e.g. $v_{y0} > 5$ m/s).

7.3 Experimental Results

Experimental data were examined in the TF domain with the goal of detecting and focusing accelerating targets. The data were collected during an experiment conducted at Canadian Forces Base (CFB) Petawawa with the CV 580 C-Band SAR. The experimental set-up and further results are described in Appendix A. A detection and tracking algorithm in the range compressed domain using the DPCA technique for clutter suppression was employed to extract and store the signal history of each target (see section 3.3).

7.3.1 TF transform

After clutter suppression, the PWVD was applied to each control target to transform the data into the time-frequency domain. The PWVD was chosen due to its high TF resolution compared to linear methods, and its ability to attenuate cross-terms between the signal and noise components. When the standard WVD algorithm was applied to the experimental data, the noise terms made tracking of the instantaneous frequency through time much more difficult than compared with the PWVD.

Time-frequency operations were performed using a freely-available toolbox of

MATLAB functions developed by Auger et al. at the CNRS (Centre National de la Recherche Scientifique) in France and at Rice University [2]. Because the target tracks were extracted individually prior to taking the TF transform, we expect to see only one target in each TF image. An example of the magnitude of the DPCA signal from a vehicle target in the TF domain is shown in Figure 7.11. The next section continues by extracting the frequency history for each target from the two-dimensional TF image.

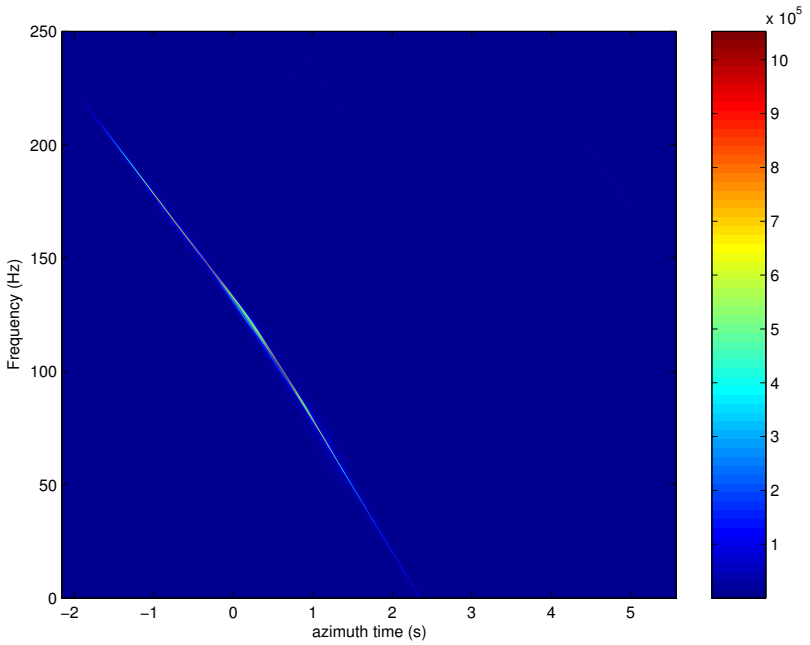

Figure 7.11: DPCA magnitude of a target track (l1p9 Convoy) in the time-frequency domain after application of the PWVD.

7.3.2 Tracking the instantaneous frequency

The IF tracking algorithm for point targets described in section 7.1.1 was applied to each of the controlled movers. The corner reflectors and vehicles being tracked in the experimental data are reasonable approximations of point targets, such that one should be able to reduce the IF to a single resolution cell for each azimuth time.

As an example of the TF history of a target from experimental data, the final IF track for the target from Figure 7.11 is shown in Figure 7.12 after application of the IF extraction algorithm. Note that the TF track does not appear perfectly linear; this IF behaviour will be further examined in sections 7.3.3 and 7.3.4.

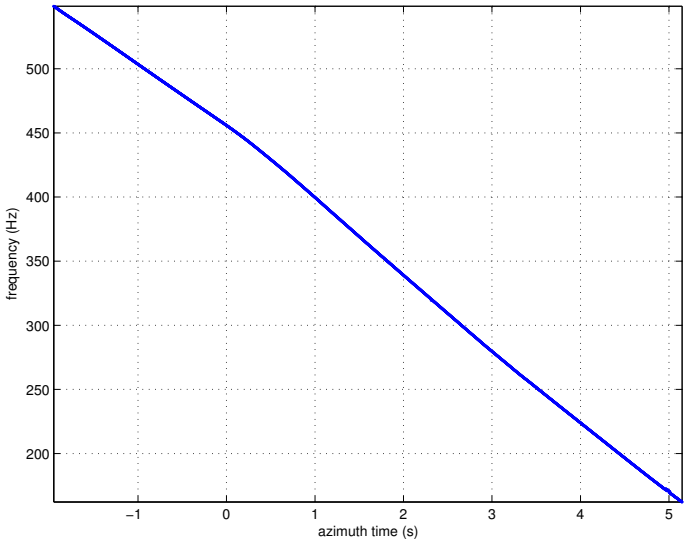

Figure 7.12: Instantaneous frequency of a vehicle target (l1p9 Convoy) through azimuth time. This frequency history was extracted from the TF image of Figure 7.11 and corrected for $\pm f_{PRF}/2$ wraps.

Centring the IF in time

One additional step was performed on the experimental data in order to correctly centre the target track about the time-axis. A time of $t = 0$ is chosen to be broadside (denoted t_0). If the complete target track for each target is collected (as can be assumed for simulated targets), then one has only to find the mid-point of the target track through time, and assign this as broadside. However, in experimental data the extracted target track may not be symmetrical, and assuming that the mid-point is t_0 may result in an erroneous estimate of broadside time.

In this work, t_0 is determined by cross-correlating the antenna gain pattern with a polynomial fit of the DPCA signal magnitude (where DPCA magnitude is a scaled

version of the gain pattern nearly constant over the course of one synthetic aperture, see Chapter 3). The time of maximal correlation is then determined, which should be approximately equal to broadside time. A polynomial fit to the DPCA magnitudes is used since the received signal amplitudes are noisy; when the DPCA magnitudes are input directly into the correlation algorithm, local peaks rather than the apparent centre of the parabolic forms are selected as broadside. One problem with this technique is that the gently sloping gain pattern (see Figure 7.13) does not provide a sharp correlation peak, and thus some errors in the estimated broadside location are expected. As well, small changes in the DPCA magnitude over the course of the synthetic aperture due to target along-track velocities and along- and across-track accelerations (see Chapter 3) will contribute additional errors to the correlation matching. This technique also assumes that there is no aspect-angle dependence on the signal amplitude. This may be realistic for corner reflectors, although vehicles may display slight changes in their RCS over the azimuthal beamwidth. These errors may give inaccurate estimates of v_{y0} velocity, but they will not significantly affect the detection of acceleration, nor the focusing of moving targets since they will only change the linear component of the IF history.

7.3.3 Detecting acceleration using TF analysis

Polynomial fitting may be applied to the time-frequency tracks of the experimental data in order to determine whether or not targets possess certain acceleration components (specifically a_{x0} and $\dot{a}_{y0}$). Despite efforts to maintain a constant velocity during the field trial, many of the target tracks extracted from the experimental data were non-linear in the TF domain, indicating the presence of acceleration. For example, examining the time-frequency history from an experimental vehicle target in Figure 7.12, it appears as if the IF is a combination of several linear segments. Further insight into the target motion may be revealed using polynomial fits to the frequency history and analysis of the residuals between these fits and the extracted IF.

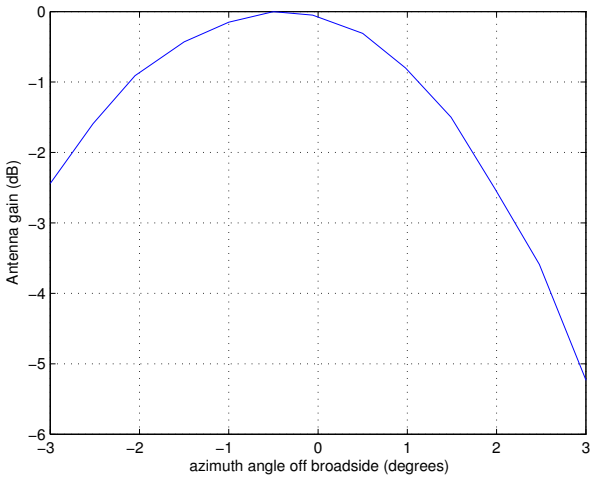

Figure 7.13: Antenna gain pattern of the receiving fore antenna for the CV 580 system. Note the parabolic shape which does not provide a sharp correlation peak at broadside.

Polynomials of various orders were fit to the time-frequency tracks of experimental targets. The majority of target TF tracks had significant second-order components in their polynomial fits, which suggests the presence of target acceleration. To compare the results from the experimental data to those from the simulated targets in section 7.2.2, the IF frequency was integrated to determine the phase, and a third-order polynomial was fit to this phase function. Comparisons of the twenty-two target signals to nearby clutter revealed a mean SCR of 10.8 dB, and the mean absolute value of the cubic coefficient was 1.17. Note that the SCR for each target track was estimated from the maximum intensity in the range compressed domain. Recall that each target was equipped with a corner reflector, which is why the SCR is higher than for typical road vehicles. Note the large mean third-order coefficient in the experimental data, which is nearly twice the value of the cubic coefficient from the simulated target with $a_{x0} = 0.5$ m/s^2 at a similar SCR, suggesting the presence of significant target acceleration.

Differences between the target TF history and polynomial fits to this history for

the sample vehicle from Figure 7.12 are shown in Figure 7.14. A suitable model for

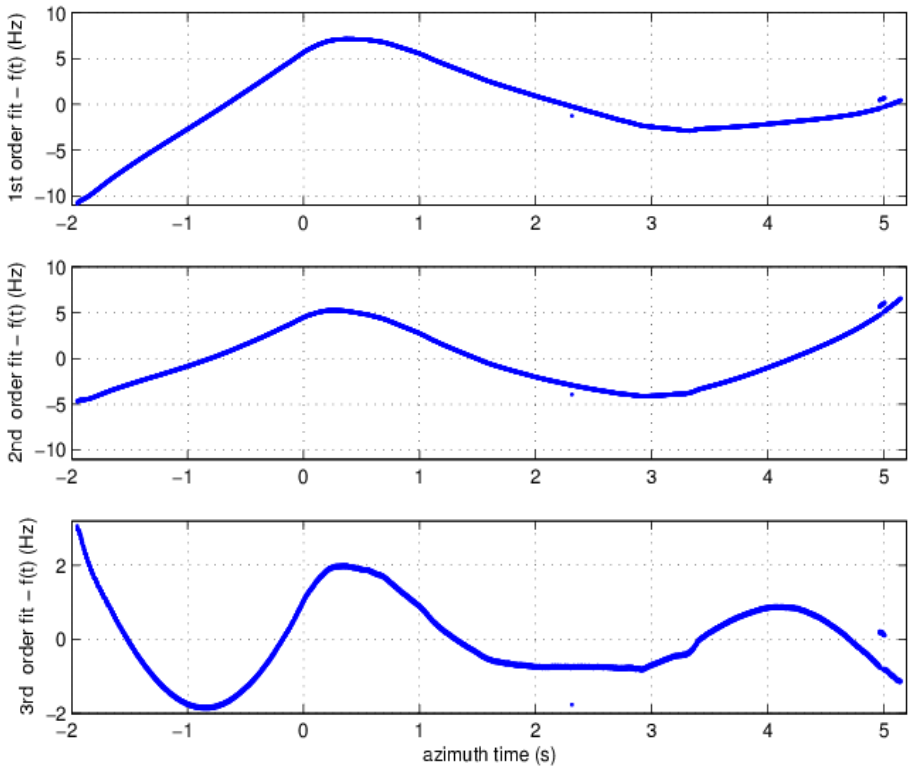

Figure 7.14: Differences between a target's TF track $f(t)$ and its linear fit over time (top), its quadratic fit over time (middle), and its cubic fit over time (bottom). The target is l1p9 Convoy. Note the change in scale of the y-axis in the bottom frame. The trends in the residuals indicate the existence of higher-order uncompensated phase terms in the data.

the target TF history would show residuals randomly distributed about zero. A linear fit (assuming a target with constant velocity and/or constant v_{x0} and constant a_{y0}) is a clearly a poor model of the IF based on the large residuals displayed in the top frame of Figure 7.14. However, even after compensation of a_{x0} and $\dot{a}_{y0}$ with a second-order TF fit (see middle frame of Figure 7.14) there exist trends in the residuals, indicating the presence of higher-order terms in the TF track. A cubic fit to the TF history somewhat reduces the magnitude of the residuals (see bottom frame noting the scale change in the y-axis), but deterministic (possibly sinusoidal) trends still

persist, revealing a complex (higher-order) TF history for this target.

There are several possible sources for these higher-order variations in the IF track. Carrara suggests that the primary causes of phase variations (which lead to time-varying Doppler frequency shifts) are due to uncompensated target and sensor motion, and approximations in the image formation algorithm [12]. Improvements in the motion compensation procedures and channel balancing algorithms used to process the airborne experimental data are in the process of being implemented at the time of writing. Additional time-variations in the TF track may result from target vibration and rotation, fluctuation of the rotation centre, inaccuracy in tracking the phase (or frequency) history, and other variations in the system and the environment [16].

7.3.4 Focusing using TF Analysis

Focusing using instantaneous phase as described in section 7.1.3 was attempted for the experimental data. For each target track, the instantaneous phase was computed and a matched filter of the form $\exp(j\varphi(t))$ was constructed for azimuth compression. The reference filter was then convolved with the target signal to focus each moving target.

To further emphasize the non-linearity and higher-order behaviour of the TF history of experimental targets, several matched filters were constructed based on various orders of polynomial fits to the IF. Each polynomial fit was then integrated through time to obtain an estimate of the instantaneous phase for use in matched filtering. Figure 7.15 shows the focusing achieved for the vehicle target from Figures 7.12 and 7.14 using three different filters. In the first case (top frame) a reference filter based on a linear fit to the time-frequency history (which assumes no along-track acceleration nor time-varying across-track acceleration) was used. The extended sidelobes to one side of the peak response suggest the presence of uncompensated cubic terms in the target phase function [12]. In the second case (middle frame) a reference filter based on a third-order polynomial fit was used (which accounts for acceleration terms

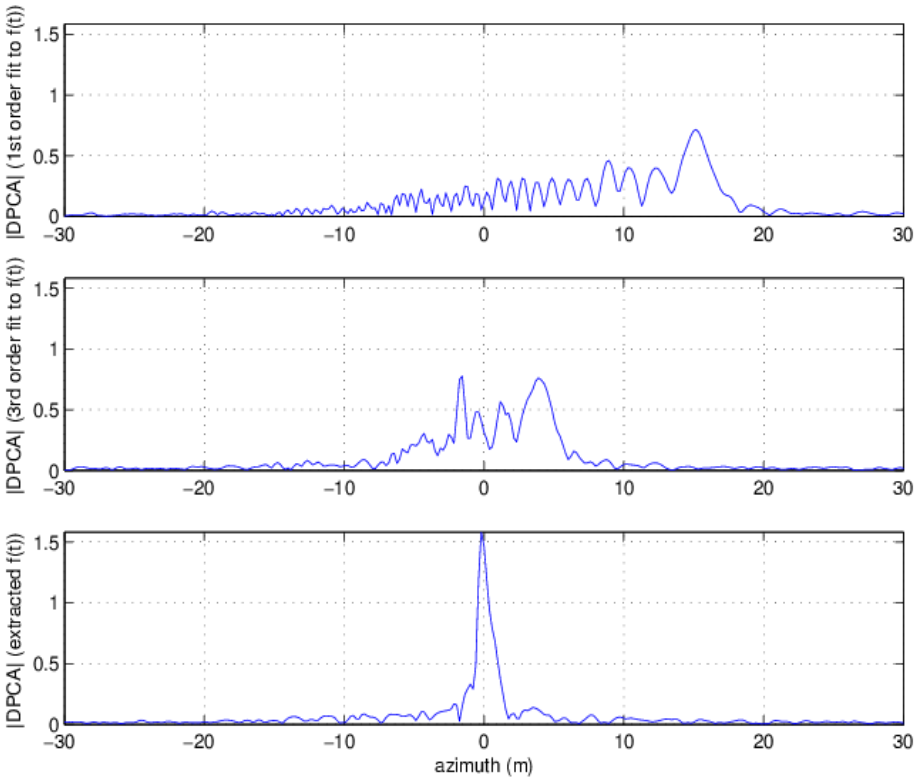

Figure 7.15: DPCA magnitudes of a vehicle target (l1p9 Convoy) focused using matched filters derived from various TF histories. Top: focused from a linear (first-order) fit to frequency history $f(t)$. Middle: focused from a third-order polynomial fit to $f(t)$. Bottom: focused from IF track $f(t)$ as extracted from the PWVD distribution. Note the superior focusing achieved using the extracted time-frequency track as opposed to a polynomial fit of the IF.

up to $\ddot{a}_{y0}$ and $\dot{a}_{x0}$). In the final case (bottom portion of Figure 7.15), the extracted time-frequency track itself (no polynomial fit) was summed to determine the phase history. The -3 dB width of the azimuth response when focused using the IF track itself is 0.7 m, which is on the order of the expected azimuth resolution of the CV 580 system (quoted as approximately 0.8 m [46] when system noise, system losses, and energy loss due to the antenna gain patterns are taken into account).

Differences between the third-order TF track and the extracted TF target track could be caused by target manoeuvring, rotation, vibration and higher-order acceleration terms as well as uncompensated sensor motion. Thus, although target focusing is improved using a third-order polynomial fit over a linear one, even higher-order acceleration terms are present, and the best resolution is achieved using the extracted TF target track itself.

The experimental data have shown that azimuth focusing is extremely sensitive to residual phase deviations from the reference filter. Focusing using the instantaneous phase offers marked improvements over focusing using stationary world matched filters or filters initialized with $\hat{v}_{x0}$ and $\hat{v}_{y0}$ estimated from Chapters 5 and 6. For instance, note the sharpened focus of the l1p9 Convoy target in the bottom frame of Figure 7.15 compared to the response from the SWMF in Figure 4.18. Substantial improvements in focusing are also obtained using the instantaneous phase instead of a reference filter initialized with $\hat{v}_{x0}$ and $\hat{v}_{y0}$, whose azimuth compressed response is shown in Figure 7.16.

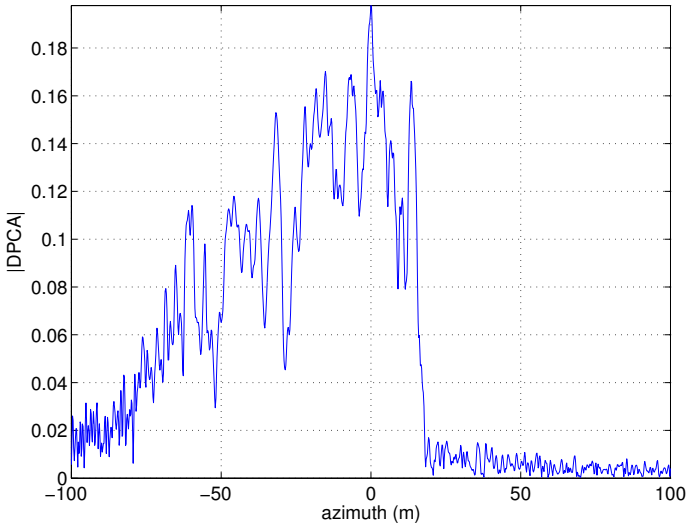

Figure 7.16: DPCA magnitude of a vehicle target (l1p9 Convoy) focused using a reference filter initialized with $\hat{v}_{x0}$ and $\hat{v}_{y0}$ computed from a matched filter-bank and from the ATI phase, respectively. Note the severely smeared response and decreased peak power compared to focusing using the instantaneous phase in the bottom frame of Figure 7.15

.

Chapter 8

Conclusions and extensions

8.1 Conclusions

This research has examined the influence of acceleration on detection, focusing, and velocity estimation of targets in dual-channel SAR-GMTI data. Although conventional GMTI analysis assumes that targets travel with constant velocity, both constant and time-varying accelerations have detrimental effects on target focusing and velocity estimation if left uncompensated.

Detection

It was shown that detection of moving targets using the displaced phase centre antenna (DPCA) technique is not significantly affected by acceleration. Targets moving with non-zero across-track velocity several metres per second away from the blind velocities have non-zero DPCA magnitudes which may be used to detect and track the targets through azimuth time.

Focusing

However, acceleration has considerable impact upon focusing. The significant loss of peak power, azimuthal shift, and azimuthal smearing caused by acceleration were demonstrated. Across-track acceleration uncompensated in the reference filter during azimuth compression severely smears the target response. This effect is identical to the consequence of an uncompensated along-track velocity upon focusing. However, the smearing due to across-track acceleration can be eliminated using a filter-bank to determine the quadratic coefficient of the reference filter giving the highest magnitude response. The primary effect of along-track acceleration and time-varying across-track

acceleration is the creation of asymmetric sidelobes to one side of the peak response, which may be mistakenly identified as secondary targets in the azimuth compressed imagery. These asymmetric sidelobes may also mask weak targets located close by.

Velocity Estimation

The effects of acceleration on velocity estimation were explored using a bank of matched filters and along-track interferometric (ATI) phase to estimate the along- and across-track components, respectively. Estimation of along-track velocity is severely biased in the presence of even slight across-track acceleration (e.g. less than 0.1 m/s^2) under a constant velocity assumption. However, even if one acknowledges the possibility of acceleration, there are insufficient degrees of freedom to solve for all unknowns with dual-channel SAR data, and thus across-track acceleration and along-track velocity cannot be separated. Along-track acceleration and time-varying across-track acceleration smear the filter-bank response, making identification of the appropriate filter and corresponding along-track velocity more difficult.

The effects of acceleration on across-track velocity estimated using the ATI phase were shown to be minimal as long as there is spectral overlap between the target signal and reference filter. The best estimates of across-track velocity are derived in the presence of complete spectral overlap, such that a bank of matched filters or an iteration scheme is recommended for increased accuracies in velocity estimation.

Spaceborne geometries

The impacts of acceleration on GMTI data were primarily considered from an airborne geometry due to the availability of experimental data from the CV 580 airborne platform. However, spaceborne geometries were also examined since the RADARSAT-2 sensor (which will operate in GMTI mode part of the time) is to be launched in the near future. Due to changes in geometry for the spaceborne case, resulting in a shorter synthetic aperture time, the effects of acceleration are not as severe as in

the airborne scenario. Many of the effects on focusing and velocity estimation of an uncompensated third-order component in the range history (due to along-track acceleration and time-varying across-track acceleration) are negligible in the spaceborne case. However, across-track acceleration will introduce an even larger bias into the estimate of along-track velocity if a constant velocity is assumed in the space-based scenario.

Detection of acceleration and focusing improvements

In addition to determining the effects of acceleration, it was attempted to detect the presence of target acceleration and to obtain a focused azimuth response irrespective of the motion parameters. Acceleration detection and focusing methods were suggested making use of the instantaneous frequency (IF), which may be estimated after transformation of the data into the two-dimensional time-frequency domain. Polynomial fits to the IF allow the identification of along-track acceleration and time-varying across-track acceleration by the targets' non-linear time-frequency histories. Equivalently, integration of the IF gives instantaneous phase, to which a third-order polynomial may be fit and the coefficients examined for a significant cubic component to indicate acceleration. Due to the suppression of white noise in the TF domain, the use of the IF for acceleration detection in regions with medium to low signal-to-clutter ratios (between 0 and 10 dB) was shown to be superior to fitting a polynomial to the target phase directly.

Integration of the IF allows the target phase history to be reconstructed through time. This phase history may then used in the reference filter during azimuth compression to obtain a focused image of the target. Targets in simulated and experimental data possessing acceleration components were presented, and were focused using the instantaneous phase method. These acceleration detection and focusing algorithms may also be applied in the spaceborne case for moderate across-track velocities (e.g. greater than 5 m/s) such that the DPCA magnitudes are sufficiently

large to track the IF.

8.2 Extensions

Additional work on the detection and compensation of acceleration is required before these detection and focusing methods may be applied operationally. Robust statistical models must be developed for the phase and amplitude of the DPCA clutter signal, such that the appropriate detection threshold may be chosen for a given false alarm rate [35, 78]. Further investigation into reliable methods of phase unwrapping are required for application of the instantaneous phase focusing algorithm, such that it may be applied to targets whose displacements exceed the directional ambiguity over one synthetic aperture.

Even more than detecting acceleration, it would be desirable to estimate the complete velocity and acceleration vector of a moving target. The use of additional *a priori* information such as a database of road networks may help resolve some of the ambiguities associated with the estimation of target motion parameters. As well, the use of additional channels of SAR data (beyond the dual-channel scenarios examined) would provide further degrees of freedom with which to solve for the motion parameters. The next generation of SAR systems will be equipped with phased array antennas, allowing increased flexibility and multi-mode operations including splitting the radar beam into multiple channels [27, 28].

To extend this research on the effects of acceleration, increasingly realistic simulations incorporating inhomogeneous clutter, antenna gain patterns, and fluctuating radar cross sections could be considered. Collecting GPS data at a higher sampling rate, or equipping controlled movers with accelerometers or inertial sensors would provide further insight into the range of acceleration values of interest for ground vehicles and acceleration's effects on experimental SAR data.

It also would be useful to examine the theoretical effects of acceleration on incomplete target tracks not centred about broadside, and the effects of acceleration in the

presence of incorrect estimates of other parameters, situations commonly encountered in experimental data. One of the most active topics in SAR research today is bistatic SAR in which the transmitter and receiver are at different locations, sometimes widely separated, such as an airborne system transmitting and ground antennas receiving [66]. Investigations of the effects of target acceleration on SAR data collected in bistatic geometries would be beneficial to a more thorough understanding of bistatic GMTI.

Perhaps the most important extension of this and other GMTI work is the development of error models to estimate the confidence in detection and parameter estimates. Such a model would require the SCR, CNR, clutter and texture characteristics, system parameters, and noise levels to obtain the correct error bounds. Attaching a level of uncertainty to each detection and estimate is required before GMTI may find widespread use in military and civilian applications.

References

[1] Adams, R. A. (1995). *Calculus: A complete course*. Addison-Wesley Publishers Limited, third edition.

[2] Auger, F., Flandrin, P., Gonçalvès, P., and Lemoine, O. (1996). *Time-Frequency Toolbox: Tutorial*. Centre National de la Recherche Scientifique (CNRS), France and Rice University, USA.

[3] Bamler, R. and Just, D. (1993). Phase statistics and decorrelation in SAR interferograms. *Proceedings of the IEEE International Geoscience and Remote Sensing Symposium (IGARSS)*, 3:980–984.

[4] Barbarossa, S. (1992). Detection and imaging of moving objects with synthetic aperture radar. Part 1. Optimal detection and parameter estimation theory. *IEE Proceedings F Radar and Signal Processing*, 139(1):79–88.

[5] Barbarossa, S. and Farina, A. (1992). Detection and imaging of moving objects with synthetic aperture radar. Part 2: Joint time-frequency analysis by Wigner-Ville distribution. *IEE Proceedings F Radar and Signal Processing*, 139(1):89–97.

[6] Barbarossa, S. and Farina, A. (1994). Space-time-frequency processing of synthetic aperture radar signals. *IEEE Transactions on Aerospace and Electronic Systems*, 30(2):341–358.

[7] Barbarossa, S. and Scaglione, A. (1998). Autofocusing of SAR images based on the product high-order ambiguity function. *Proceedings of the IEE Radar, Sonar and Navigation*, 145(5):269–273.

[8] Barkat, B. (2001). Instantaneous frequency estimation of nonlinear frequency-modulated signals in the presence of multiplicative and additive noise. *IEEE Transactions on Signal Processing*, 49(10):2214–2222.

[9] Blackledge, J. M. (1989). *Quantitative Coherent Imaging Theory, Methods and Some Applications*. Academic Press.

[10] Bock, R. K. (1998). The data analysis briefbook: Hough transform. Available from: http://rkb.home.cern.ch/rkb/AN16pp/node122.html [Accessed: May 10, 2004].

[11] Breit, H., Eineder, M., Holzner, J., Runge, H., and Bamler, R. (2003). Synthetic aperture imaging radar and moving targets. In *Proceedings of the IEEE International Geoscience and Remote Sensing Symposium IGARSS*, volume 2, pages 1187–1189, Toulouse, France.

[12] Carrara, W. G., Goodman, R. S., and Majewski, R. M. (1995). *Spotlight Synthetic Aperture Radar Signal Processing Algorithms*. Artech House Inc.

[13] Cenzo, A. (1981). Synthetic aperture radar and digital processing: An introduction. Technical report N81-18266, Jet Propulsion Laboratory, Pasadena, California, USA.

[14] Chen, V. (2002). Detection of ground moving targets in clutter with rotational Wigner-Radon transforms. In *Proceedings of the European Synthetic Aperture Radar conference (EUSAR)*, pages 229–232, Cologne, Germany.

[15] Chen, V. (2004). Time-frequency analysis for radar imaging, target detection, and feature extraction. IEEE Radar Conference Workshop 3.2.

[16] Chen, V. and Ling, H. (1999). Joint time-frequency analysis for radar signal and image processing. *IEEE Signal Processing Magazine*, 16(2):81–93.

[17] Chen, V., Lipps, R., and Bottoms, M. (2001). Radar imaging of ground moving targets. In *Proceedings of the IEEE Radar Conference*, pages 426–431, Atlanta, Georgia.

[18] Chiu, S. (2002). SAR along-track interferometry with application to RADARSAT-2 ground moving target indication. In *SPIE International Symposium on Remote Sensing*, volume 4885, pages 246–255.

[19] Chiu, S. and Sikaneta, I. (2004). Applying fractional Fourier transform to two-aperture SAR-GMTI. In *Proceedings of the European SAR conference (EUSAR)*, Ulm, Germany.

[20] Choi, H. (1998). *Signal Processing Issues in Synthetic Aperture Radar and Computer Tomography*. PhD thesis, University of Illinois.

[21] Coe, D. and White, R. (1995). Moving target detection in SAR imagery: experimental results. In *Proceedings of the IEEE International Radar Conference*, pages 644–649, Washington DC.

[22] Coe, D. J. and White, R. G. (1996). Experimental moving target detection results from a three-beam airborne SAR. *AEÜ International Journal of Electronic Communication*, 50(2):157–164.

[23] Curry, G. (1996). A low-cost space-based radar system concept. *IEEE Aerospace and Electronic Systems Magazine*, 11(9):21–24.

[24] Ender, J. (1996). Detection and Estimation of Moving Target Signals by Multi-Channel SAR. *AEÜ International Journal of Electronic Communication*, 50(2):150–156.

[25] Ender, J. (1998). Experimental results achieved with the airborne multi-channel SAR system AER-II. In *Proceedings of European Synthetic Aperture Radar Conference (EUSAR)*, pages 687–690, Friedrichshafen, Germany.

[26] Ender, J. (1999). Subspace transformation techniques applied to multi-channel SAR/MTI. In *Proceedings of IGARSS Session BB2*, Hamburg, Germany.

[27] Ender, J., Berens, P., Brenner, A., Rössing, L., and Skupin, U. (2002). Multichannel SAR/MTI system development at FGAN: from AER to PAMIR. In *IEEE International Geoscience and Remote Sensing Symposium (IGARSS)*, volume 3, pages 1697–1701, Toronto, Canada.

[28] Ender, J. and Brenner, A. (2003). PAMIR - a wideband phased array SAR/MTI system. *IEE Proceedings on Radar, Sonar and Navigation*, 150(2):165–172.

[29] Franceschetti, G. and Lanari, R. (1999). *Synthetic Aperture Radar Processing*. CRC Press.

[30] Franceschetti, G., Migliaccio, M., and Riccio, D. (1995). The SAR simulation: an overview. In *Proceedings of the IEEE International Geoscience and Remote Sensing Symposium (IGARSS)*, volume 3, pages 2283–2285.

[31] Gallop, L. (2003). Personal Communication, October.

[32] Gierull, C. H. (2001). Statistics of SAR interferograms with application to moving target detection. Technical report TR 2001-045, Defence Research and Development Canada - Ottawa.

[33] Gierull, C. H. (2002). Moving target detection with along-track SAR interferometry - a theoretical analysis. Technical report TR 2002-084, Defence Research and Development Canada - Ottawa.

[34] Gierull, C. H. (2003). Digital channel balancing of along-track interferometric SAR data. technical memorandum TM 2003-024, Defence Research and Development Canada - Ottawa.

[35] Gierull, C. H. and Livingstone, C. (2004). SAR-GMTI concept for RADARSAT-2. In Klemm, R., editor, *The Applications of Space-Time Processing*. IEE Press, Stevenage, UK.

[36] Gierull, C. H. and Sikaneta, I. (2004). Ground moving target parameter estimation for two-channel SAR. In *Proceedings of the European Synthetic Aperture Radar conference (EUSAR)*, Ulm, Germany.

[37] Gierull, C. H. and Sikaneta, I. C. (2003). Raw data based two-aperture SAR ground moving target indication. In *Proceedings of IGARSS*.

[38] Goldstein, R. and Zebker, H. (1987). Interferometric radar measurements of ocean surface currents. *Nature*, 328(20):707–709.

[39] Goodman, N. A. (2002). *SAR and MTI Processing of Sparse Satellite Clusters*. Doctor of philosophy, Department of Electrical Engineering and Computer Science, University of Kansas.

[40] Helstrom, C. W. (1968). *Statistical Theory of Signal Detection*. Pergamon Press Inc.

[41] Jao, J. K. (2001). SAR image processing for moving target focusing. In *Proceedings of the IEEE Radar Conference*, pages 58–63, Atlanta, Georgia.

[42] Kirscht, M. (1996). Detection and imaging or arbitrarily moving targets with single-channel SAR. *IEE Proceedings - Radar, Sonar and Navigation*, 150(1):7–11.

[43] Klemm, R. (1998). *Space-Time Adaptive Processing: principles and applications*. The Institution of Electrical Engineers, London.

[44] Kullback, S. (1968). *Information theory and statistics*. Dover Publications Inc., New York, N.Y.

[45] Legg, J. A., Bolton, A. G., and Gray, D. A. (1996). SAR moving target detection using a nonuniform pri. In *EUSAR Proceedings*, pages 432–426, Königswinter, Germany.

[46] Livingstone, C. (2003a). Personal Communication, October.

[47] Livingstone, C. (2003b). Multi-look solution to the GMTI ambiguity problem: A proposed algorithm. Defence Research and Development Canada - Ottawa internal webnote.

[48] Livingstone, C. and Sikaneta, I. (2004). Focusing moving targets/terrain imaged with moving-target matched filters: A tutorial. Technical report TM-2004-160, Defence Research and Development Canada - Ottawa.

[49] Livingstone, C., Sikaneta, I., Gierull, C., Chiu, S., Beaudoin, A., Campbell, J., Beaudoin, J., Gong, S., and Knight, T. (2002). An airborne synthetic aperture radar (SAR) experiment to support RADARSAT-2 ground moving target indication (GMTI). *Canadian Journal of Remote Sensing*, 28(6):794–813.

[50] Lombardo, P. (1996). DPCA processing for SAR moving targets detection in the presence of internal clutter motion and velocity mismatch. In *SPIE Proceedings*, volume 2958, pages 50–61, Taormina, Italy.

[51] MacDonald Dettwiler and Associates Ltd (2004). RADARSAT-2 A New Era in Remote Sensing. Available from: http://www.mda.ca/radarsat-2/ [Accessed: June 20, 2004].

[52] Marple, S.L., J. (1998). Time-frequency signal analysis: issues and alternative methods. In *Proceedings of the IEEE-SP International Symposium on Time-Frequency and Time-Scale Analysis*, pages 329–332, Pittsburgh, Pennsylvania.

[53] Moccia, A. and Rufino, G. (2001). Spaceborne along-track SAR interferometry: performance analysis and mission scenarios. *IEEE Transactions on Aerospace and Electronic Systems*, 37(1):199–213.

[54] Moreira, J. R. and Keydel, W. (1995). A new MTI-SAR approach using the reflectivity displacement method. *IEEE Transactions on Geoscience and Remote Sensing*, 33(5):1238–1244.

[55] Murray, D., Coe, D., and White, R. (1997). Experimental MTI with spaceborne geometries. *IEE Colloquium on Radar Interferometry*, 153(3):1–6.

[56] Nathanson, F. E., Reilly, J. P., and Cohen, M. N. (1999). *Radar Design Principles Signal Processing and the Environment*. Scitech Publishing Inc., Mendham, New Jersey, second edition.

[57] Nohara, T. J., Premji, A.-N., and Weber, P. T. (1999). Final report: Simulator - space based radar, volume I: Requirements, design and user guide. Technical Report DND9802, Sicom Systems Ltd., Ottawa, ON.

[58] NovAtel Inc. (2001). *OEM4 Firmware Version 1.00 User Manual - Volume 1 Installation and Operation*. NovAtel Inc. pg. 75.

[59] Pascazio, V., Schirinzi, G., and Farina, A. (2001). Moving target detection by along-track interferometry. In *IEEE Geoscience and Remote Sensing Symposium (IGARSS)*, volume 7, pages 3024–3026, Sydney, Australia.

[60] Pettersson, M. (2001). Extraction of moving ground targets by a bistatic ultra-wideband SAR. *Proceedings of the IEE Radar, Sonar and Navigation*, 148(1):35–49.

[61] Ran, T., Xianjun, P., Xinghao, Z., and Yue, W. (2002). Detection and estimation of moving targets based on fractional Fourier transform. In *Proceedings of the 6th International Conference on Signal Processing*, volume 1, pages 102–105, Beijing, China.

[62] Raney, R. K. (1971). Synthetic aperture imaging radar and moving targets. *IEEE Transactions on Aerospace and Electronic Systems*, 7(3):499–505.

[63] Raney, R. K. (1982). Processing synthetic aperture radar data. *International Journal of Remote Sensing*, 3(3):243–257.

[64] Raney, R. K. (1985). Theory and measure of certain image norms in SAR. *International Journal of Remote Sensing*, 23(3):343–348.

[65] Raney, R. K. (1991). Considerations for SAR image quantification unique to orbital systems. *IEEE Transactions on Geoscience and Remote Sensing*, 29(5):754–760.

[66] Raney, R. K. (1992). Special SAR Techniques and Applications. In *AGARD Conference on Fundamentals and Special Problems of Synthetic Aperture Radar*, pages 10–15, Neuilly Sur Seine, France.

[67] Rieck, W. (1997). Time-frequency distribution of multichannel SAR-data for autofocusing of moving targets. In *Radar Conf. Publ. No. 449*, pages 224–228.

[68] Rieck, W. (1998). *Zeit-Frequenz-Signal-Analyse für Radaranwendungen mit synthetischer Apertur (SAR).* PhD thesis, Rheinisch-Westfälische Technische Hochschule Aachen, Shaker Verlag.

[69] Ristic, B. and Boashash, B. (1998). Comments on "The Cramer-Rao lower bounds for signals with constant amplitude and polynomial phase". *IEEE Transactions on Signal Processing*, 46(6):1708–1709.

[70] Rodriguez, E. and Martin, J. (1992). Theory and design of interferometric synthetic aperture radars. *IEE Proceedings on Radar and Signal Processing*, 139(2):149–159.

[71] Romeiser, R. and Hirsch, O. (2001). Possibilities and limitations of current measurements by airborne and spaceborne along-track interferometric SAR. In *Proceedings of the International IEEE Geoscience and Remote Sensing Symposium*, volume 1, pages 575–577, Sydney, Australia.

[72] Rosen, P., Hensley, S., Joughin, I., Li, F., Madsen, S., Rodriguez, E., and Goldstein, R. (2000). Synthetic aperture radar interferometry. *Proceedings of the International IEEE*, 88(3):333–382.

[73] Schreier, G., editor (1993). *SAR geocoding: data and systems.* Wichmann.

[74] Sedwick, R., Hacker, T., and Marais, K. (2000). Performance analysis for an interferometric space-based GMTI radar system. In *Proceedings of the IEEE International Radar Conference*, pages 689–694, Alexandria, Virginia.

[75] Sharma, J. (2003). Summary of C.H. Gierull's target detection and parameter estimation algorithm. Defence Research and Development Canada - Ottawa internal webnote.

[76] Shrader, W. W. and Gregers-Hansen, V. (1990). MTI radar. In Skolnik, M. I., editor, *Radar Handbook*, pages 15.1 – 15.69. McGraw-Hill Inc.

[77] Sikaneta, I. (2003). Airborne SAR processor. Defence Research and Development Canada - Ottawa internal webnote.

[78] Sikaneta, I. and Chouinard, J.-Y. (2004). Eigen-decomposition of the multi-channel covariance matrix with applications to SAR-GMTI. *Signal Processing*, 84(9):1501–1535.

[79] Sikaneta, I. and Gierull, C. H. (2004). Ground moving target detection for along-track interferometric SAR data. In *Proceedings of the IEEE Aerospace Conference*, Big Sky, Montana, USA.

[80] Soumekh, M. (1997). Moving target detection in foliage using along track monopulse synthetic aperture radar imaging. *IEEE Transactions on Image Processing*, 6(8):1148–1163.

[81] Soumekh, M. (1999). *Synthetic Aperture Radar Signal Processing with MATLAB algorithms*. Wiley Interscience, New York.

[82] Soumekh, M. and Himed, B. (2002). Moving target detection and imaging using an X-band along-track monopulse SAR. *IEEE Transactions on Aerospace and Electronic Systems*, 38(1):315–333.

[83] Sparr, T. and Krane, B. (2003). Time-frequency analysis of vibrating targets in airborne SAR systems. *IEE Proceedings on Radar, Sonar and Navigation*, 150(3):173–175.

[84] Staudaher, F. M. (1990). Airborne mti. In Skolnik, M. I., editor, *Radar Handbook*, pages 16.1 – 16.29. McGraw-Hill Inc.

[85] Thayaparan, T. (2000). Linear and quadratic time-frequency representations. technical memorandum DREO-TM-2000-080, Defence Research and Development Canada - Ottawa.

[86] Thompson, A. and Livingstone, C. (2000). Moving target performance for RADARSAT-2. In *Proceedings of the IEEE International Geoscience and Remote Sensing Symposium (IGARSS)*, volume 6, pages 2599–2601, Honolulu, Hawaii.

[87] Visentin, R. L. (1988). A digital signal processing view of strip-mapping synthetic aperture radar. Master's thesis, University of Illinois, Urbana, Illinois.

[88] Weisstein, E. W. (1999). Monte carlo method from mathworld - a wolfram web resource. Available from: http://mathworld.wolfram.com/MonteCarloMethod.html [Accessed: May 17, 2004].

[89] Werness, S., Carrara, W., Joyce, L., and Franczak, D. (1990a). Moving target imaging algorithm for SAR data. *IEEE Transactions on Aerospace and Electronic Systems*, 26(1):57–67.

[90] Werness, S. A., Stuff, M. A., and Fienup, J. R. (1990b). Two-dimensional imaging of moving targetes in SAR data. In *Proceedings of the 24th Asilomar Conference on Signals, Systems and Computing, paper MP5*, pages 16–22, Monterrey, California.

[91] Werninghaus, R. (2004). DLR web portal: TerraSAR-X - a new approach for science and economy. MacDonald Dettwiler and Associates Ltd., Available from: http://www.dlr.de/dlr/raumfahrt/rf-management/erdbeobachtung/terrasar-x [Accessed: June 20, 2004].

[92] White, R. and Coe, D. (1997). Detection limits for sideways looking MTI radars. In *Conference Publ. No. 449*, pages 434–438.

[93] Yadin, E. (1995). Evaluation of noise and clutter induced relocation errors in SAR MTI. In *Record of the IEEE International Radar Conference*, pages 650–655, Alexandria, Virginia.

[94] Yadin, E. (1996). A performance evaluation model for a two port interferometer SAR-MTI. In *Proceedings of the 1996 IEEE National Radar Conference*, pages 261–266, Ann Arbor, Michigan.

Appendix A

Experimental data

Data were collected during an experiment conducted at Canadian Forces Base (CFB) Petawawa with the Environment Canada CV 580 C-Band SAR in November of 2000. The experimental set up and data processing are described below.

A.1 Experimental set up

The CV 580 system was equipped with two antennas separated in the along-track direction. Dual-channel SAR data were collected in HH (horizontal) polarization for eight passes. The aircraft flew in a square twice such that there were four perpendicular flight lines and two passes at each aspect angle. A list of radar parameters and airborne geometry parameters of the Petawawa 2000 data collection is provided in Table A.1:

Table A.1: Radar and geometry parameters for CV 580 Petawawa data collection in November 2000.

Parameter	**Value**
Carrier frequency (C-band)	5.30 GHz
Wavelength (λ)	0.0565 m
Incidence angle to control targets (θ_{inc})	38 - 57°
-3 dB antenna beamwidth (β)	3°
Physical antenna separation distance (d)	0.54 m
f_{PRF}/v_a ratio	5.14 m^{-1}
Pixel spacing (range) (depends on θ_{inc})	5.1 - 7.1 m
Pixel spacing (azimuth)	0.19 m

Three controlled movers were involved in the data campaign. Control targets were

equipped with GPS receivers collecting carrier-phase data (for precise position and velocity information) and a trihedral corner reflector was mounted to each target. A stationary GPS receiver (also recording carrier-phase information) was located on site to provide a reference for differential GPS post-processing. Vehicle velocities ranged between 2.5 and 18.1 m/s (i.e. between 9 and 65 km/h). The vehicles were travelling in a low-clutter environment of primarily grassy fields and shrubs, such that target to clutter contrasts were generally high. The corner reflectors' bearings and elevation angles were adjusted for each pass, such that each corner was oriented towards the expected broadside position of the radar to increase RCS and visibility in the SAR imagery.

Two of the controlled moving targets (denoted as 'Delta' and 'Juliet') consisted of a corner reflector and a GPS system mounted on a cart that moved on a rail track. These transporters were remotely controlled, engine-powered carts guided by the rail system which were programmed to move at predetermined speeds. Figures A.1 and A.2 show the system that was used on both Juliet (a 700 metre track) and Delta (a 650 metre track).

A four-vehicle convoy was also deployed travelling at a relatively constant speed along a straight segment of Veritable Road (a rough gravel road crossing the military base). The four vehicles used are shown in Figure A.3. Although the entire convoy was travelling at approximately the same speed, the latter three targets (labelled two through four in the figure) were not used in the analysis because they were not equipped with GPS receivers, and thus there is no reliable 'truth' information regarding their positions and velocities over time. The pick-up truck labelled as vehicle number one in Figure A.3 is hereafter referred to as 'Convoy'. A photo mosaic of the Petawawa site used in the experiment is shown in Figure A.4, with the target tracks of the controlled movers shown in red. Vehicles on the Trans-Canada Highway (also visible in Figure A.4) were available as targets of opportunity, although highway targets were not examined here due to a lack of ground truth.

Figure A.1: Delta control target from the Petawawa 2000 data collection (© DRDC Ottawa).

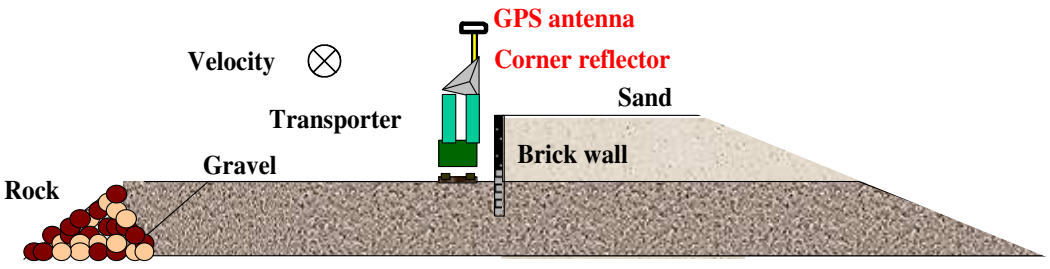

Figure A.2: Sketch of Juliet and Delta moving target rail systems with their surrounding structure and environment (© DRDC Ottawa).

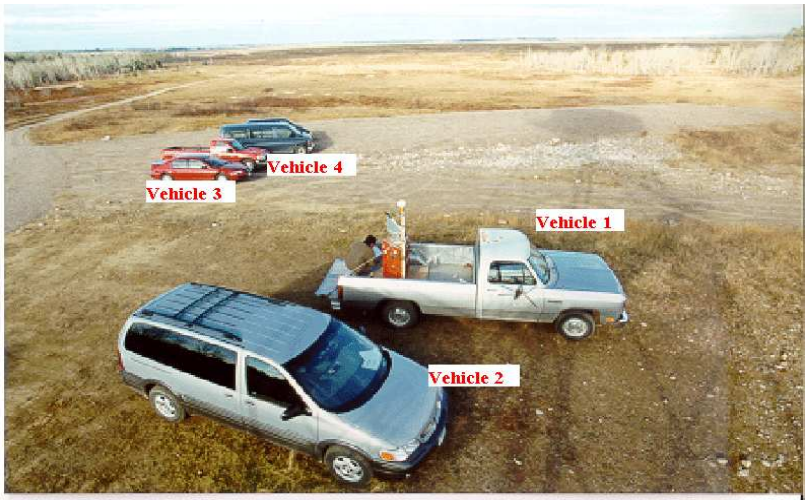

Figure A.3: Four vehicle convoy from the Petawawa 2000 data collection (© DRDC Ottawa).

A.2 Data pre-processing

The data delivered by the CV 580 airborne system are range compressed before being recorded to tape, but are not azimuth compressed. This is subsequently referred to as 'raw data'. The raw data are motion compensated and digitally balanced (in which the amplitude and phase of both channels are matched and registered [34]) using an in-house software package developed by Ishuwa Sikaneta at Defence Research and Development Canada - Ottawa named SARPro (version 0.3.0) [77]. After these pre-processing steps, the data are then passed onto the detection stage.

SARPro begins by performing an IQ balance of each channel separately, in which it is ensured that the real and imaginary portions of the signal have zero mean and similar variance. Next, motion compensation is applied to correct for aircraft platform motion deviating from the prescribed, idealized straight-line path. If motion compensation is not applied, processed images will be defocused and the scatterers' will be shifted from their true positions [72].

Digital balancing (or calibration) is then performed to correct for the unavoidable

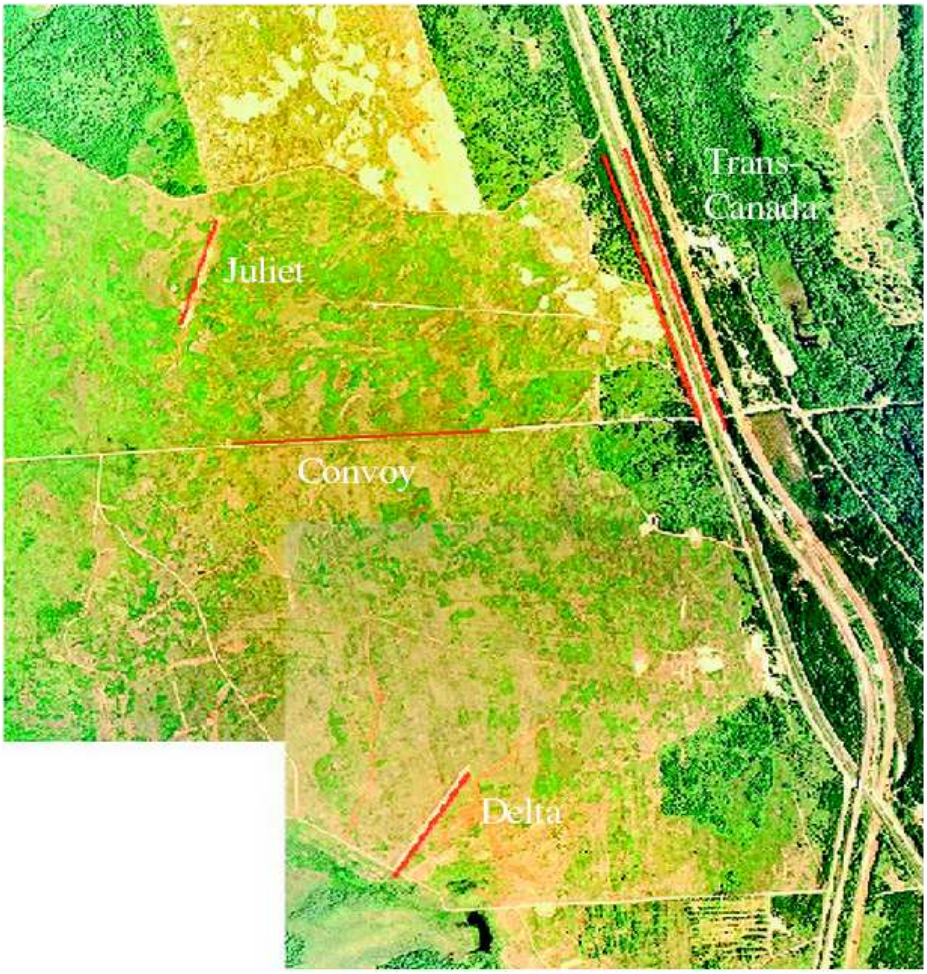

Figure A.4: Aerial photograph mosaic of CFB Petawawa training area, site of the 2000 GMTI experiment. The tracks of the controlled movers Juliet, Delta, and Convoy are shown in red. A portion of the Trans-Canada Highway is also visible on the right-hand side.

channel imperfections and imbalances present in the data. These deficiencies can be due to thermal noise in the channels, non-ideal imbalanced receiver hardware, or different antenna gain patterns. Unmatched fore and aft channel transfer functions result in systematic phase and amplitude terms causing errors in any subtractive method of detection or parameter estimation such as DPCA or ATI (see section 2.3.2) [34, 79].

A routine called 'Digibal' (part of the SARPro package) uses a sophisticated, adaptive two-dimensional calibration technique to simultaneously balance both magnitudes and phases of the fore and aft channels. During the calibration process co-registration is automatically performed to line-up the two channels due to differences in the antenna phase centre locations. The algorithm works by iteratively equalizing the channel transfer functions. Additional details on the channel balancing algorithm are available in [34], and further information on the SARPro software package may be found in [77].

A.3 Motion parameter estimation accuracies

This section includes details on the velocity estimation for each of the twenty-two control target passes. The accuracies in v_{x0} and v_{y0} are broken down separately in Tables A.2 and A.3. Along-track (v_{x0}) velocities are computed using the filter-bank algorithm described in Chapter 5, and across-track (v_{y0}) velocities are computed using along-track interferometric phase, outlined in Chapter 6. Note that line 2, pass 6 (abbreviated l2p6) only had data for the Convoy target since the Juliet and Delta targets were stationary during imaging time due to a miscommunication with the aircraft.

Each velocity is compared to values output from GPS; the GPS data were taken as a best approximation of the true target motion and were used to determine the accuracies of the parameter estimation algorithms. Technical specifications [58] cite RMS (root mean square) accuracies of 0.03 m/s in velocity magnitudes computed

Table A.2: A comparison of along-track velocities (v_{x0}) estimated using the filter-bank method from dual-channel SAR data and GPS. Each of the twenty-two controlled movers in the Petawawa 2000 experiment are examined. The mean of the absolute value of the differences is 2.9 m/s with a standard deviation of 2.6 m/s.

Line & Pass	**Mover Name**	$\hat{v}_{x0}$ **m/s (SAR)**	$\hat{v}_{x0}$ **m/s (GPS)**	$\Delta\hat{v}_{x0}$ **m/s) (SAR - GPS)**
l1p5	Juliet	4.37	4.52	-0.15
	Delta	-1.94	5.99	-7.93
	Convoy	11.45	5.69	5.76
l1p9	Juliet	2.63	2.21	0.42
	Delta	1.46	5.11	-3.65
	Convoy	4.46	4.00	0.46
l2p2	Juliet	4.97	1.57	3.40
	Delta	7.43	7.57	-0.14
	Convoy	17.03	12.55	4.48
l2p6	Convoy	18.77	17.28	1.49
l3p3	Juliet	-2.27	-2.03	-0.24
	Delta	-1.34	-4.81	3.47
	Convoy	-0.53	-4.13	3.60
l3p7	Juliet	-0.29	-4.72	4.43
	Delta	4.73	-4.61	9.34
	Convoy	-4.55	-5.36	0.81
l4p4	Juliet	-3.50	-1.83	-1.67
	Delta	-3.05	-7.52	4.47
	Convoy	-13.70	-12.74	-0.96
l4p8	Juliet	-4.04	-3.61	-0.43
	Delta	-13.07	-9.42	-3.65
	Convoy	-15.41	-17.37	1.96

Table A.3: A comparison of across-track velocities (v_{y0}) estimated using along-track interferometric phase from dual-channel SAR data and GPS. Each of the twenty-two controlled movers in the Petawawa 2000 experiment are examined. The mean of the absolute value of the differences is 0.9 m/s with a standard deviation of 1.5 m/s.

Line & Pass	**Mover Name**	$\hat{v}_{y0}$ **m/s (SAR)**	$\hat{v}_{y0}$ **m/s (GPS)**	$\Delta\hat{v}_{y0}$ **m/s) (SAR - GPS)**
l1p5	Juliet	3.13	3.68	-0.56
	Delta	10.26	9.20	1.07
	Convoy	-20.52	-17.55	-2.98
l1p9	Juliet	1.73	1.92	-0.19
	Delta	8.47	7.73	0.75
	Convoy	-8.67	-12.75	4.08
l2p2	Juliet	-1.51	- 1.94	0.43
	Delta	-4.39	-4.90	0.51
	Convoy	3.43	4.07	-0.64
l2p6	Convoy	5.77	6.02	-0.25
l3p3	Juliet	-1.72	-1.75	0.03
	Delta	-7.37	-7.36	-0.02
	Convoy	6.46	12.64	-6.18
l3p7	Juliet	-3.58	-3.83	0.24
	Delta	-7.32	-7.13	-0.19
	Convoy	16.46	17.17	-0.71
l4p4	Juliet	2.36	2.34	0.02
	Delta	5.15	4.82	0.33
	Convoy	-4.2	-3.92	-0.28
l4p8	Juliet	4.54	4.41	0.13
	Delta	6.50	6.19	0.31
	Convoy	-5.60	-5.63	0.03

from differentially processed GPS data such as that available in this experiment. A summary of the statistical differences between the along- and across-track velocities computed from the SAR data and the GPS velocities is provided in Table A.4.

Table A.4: A comparison of the absolute differences in along- and across-track velocities estimated using SAR data and velocities estimated from GPS. 'Std.Dev.' represents the standard deviation.

	v_{x0} **m/s**	v_{y0} **m/s**
Average | SAR-GPS |	2.9	0.9
Std.Dev.| SAR-GPS |	2.6	1.5

In order to separate each GPS velocity into along- and across-track components, target heading is required. True target heading (with respect to geographic North) was determined by subtracting adjacent GPS position estimates. True target heading was then converted into a heading with respect to the aircraft's line of flight using aircraft heading from the CV 580's GPS system. Simple trigonometry was then used to transform each GPS speed into along- and across-track components for direct comparison with the velocity estimates from the radar data. Table A.5 shows key values in this conversion for each target pass, and the accuracy of the GPS along- and across-track components is further discussed in Appendix A.3.1.

A.3.1 GPS accuracies

Errors in the GPS position estimates will result in GPS velocity and heading inaccuracies. Typically, the greatest GPS errors occur in altitude due to the nature of the satellite geometry (horizontally there are satellites located on almost all sides of the targets such that some errors may cancel, whereas vertically, the satellites are all located above the user such that errors are additive). Users of the CV 580 system report typical RMS horizontal positional errors of between 1 to 3 metres, with vertical

Table A.5: Transforming GPS speed and heading into along-track and across-track velocities (v_{x0} and v_{y0}). Bearing (i.e. heading) is abbreviated as 'brg', speed as 'spd', and 'wrt' represents 'with respect to'.

Line & Pass	**Mover Name**	**GPS spd (m/s)**	**GPS brg (°)**	**aircraft brg (°)**	**brg (°) wrt aircraft**	v_{x0} **(m/s)**	v_{y0} **(m/s)**
l1p5	Juliet	5.83	0.2	321.0	39.2	4.52	3.68
	Delta	10.98	17.9	321.0	56.9	5.99	9.20
	Convoy	18.45	249.0	321.0	288.0	5.69	-17.55
l1p9	Juliet	2.92	2.0	321.0	41.0	2.21	1.92
	Delta	9.26	17.5	321.0	56.5	5.11	7.73
	Convoy	13.37	248.4	321.0	287.4	4.00	-12.75
l2p2	Juliet	2.49	0.0	51.0	309.0	1.57	-1.94
	Delta	9.01	18.1	51.0	327.1	7.57	-4.9
	Convoy	13.19	69.0	51.0	18.0	12.55	4.07
l2p6	Convoy	18.3	70.2	51.0	19.2	17.28	6.02
l3p3	Juliet	2.68	1.7	141.0	220.7	-2.03	-1.75
	Delta	8.79	17.8	141.0	236.8	-4.81	-7.36
	Convoy	13.3	249.1	141.0	108.1	-4.13	12.64
l3p7	Juliet	6.08	0.0	141.0	219.0	-4.72	-3.83
	Delta	8.49	18.1	141.0	237.1	-4.61	-7.13
	Convoy	17.98	248.3	141.0	107.3	-5.36	17.17
l4p4	Juliet	2.97	359.0	231.0	128.0	-1.83	2.34
	Delta	8.93	18.4	231.0	147.4	-7.52	4.82
	Convoy	13.33	68.1	231.0	197.1	-12.74	-3.92
l4p8	Juliet	5.7	0.3	231.0	129.3	-3.61	4.41
	Delta	11.27	17.7	231.0	146.7	-9.42	6.19
	Convoy	18.26	69.0	231.0	198.0	-17.37	-5.63

positions generally 1.5 times worse (as a rule of thumb) to give vertical accuracies of between 1.5 to 4.5 metres [31].

Differencing the mover positions over time gives velocity and heading estimates. However, offsets between the GPS time and the estimated broadside time of the target could result in taking GPS measurements at the incorrect epoch. As well, GPS measurements were collected only every 2 seconds, and the closest measurements to the estimated imaging time were used for velocity estimation. Perhaps interpolating GPS measurements to the nearest second would have provided small improvements in results. If the targets were moving with constant velocity, these timing errors should not affect GPS velocity estimates. However, in the presence of target acceleration, a GPS measurement will have a high accuracy, but for an inappropriate time. Assuming a maximum acceleration of 1 m/s^2 and that timing errors could be incorrect by one epoch (i.e. two seconds), this translates to a worst-case GPS velocity error of 2 m/s for the intended time.

The theoretical accuracy in GPS heading is heavily dependent upon the speed of the moving target being examined. At high velocities (e.g. 18.1 m/s, which was maintained by the Convoy target), a worst-case assumption of 3 metres in horizontal position translates to a heading error of 9.6 degrees using simple trigonometry. At low velocities (e.g. 2.5 m/s, such as several passes for Juliet), the target moves less than the RMS position error between epochs, and thus heading is completely unreliable. However, examining the GPS data, the movers' headings displayed standard deviations on the order of 1.5 degrees. Assuming that there are no biases in the target GPS velocity magnitude and heading estimates, and that the aircraft heading is known exactly, standard deviations in the speed of 0.03 m/s and in the heading of 1.5 degrees gives corresponding worst-case accuracies of 0.5 m/s in v_{x0} and v_{y0} for the velocities and headings observed in the experimental data. This error propagation was carried out by relating speed ($|v|$) and heading (α) to along- and across-track

velocities as follows:

$$v_{x0} = |v| \sin \alpha \tag{A.1}$$

$$v_{y0} = |v| \cos \alpha. \tag{A.2}$$

Partially differentiating equations A.1 and A.2 with respect to each parameter, and squaring, summing, and taking the square root of the result gives the following expressions for standard deviations (σ) in the v_{x0} and v_{y0} velocities from GPS:

$$\sigma_{vx0} = \sqrt{(\sigma_{|v|} \sin \alpha)^2 + (|v| \cos \alpha \sigma_\alpha)^2} \tag{A.3}$$

$$\sigma_{vy0} = \sqrt{(\sigma_{|v|} \cos \alpha)^2 + (|v| \sin \alpha \sigma_\alpha)^2}, \tag{A.4}$$

where σ_α is in units of radians.

Appendix B

ATI ambiguities and performance analysis

This section examines the various ambiguities present in the along-track interferometric phase, and describes possible errors sources within the ATI phase. Coherence is one crucial parameter to determining the level of phase noise in ATI SAR data, and its derivation (assuming the presence of additive noise only) is given in Appendix B.2.1.

B.1 ATI ambiguities

As previously mentioned, the ATI phase is subject to several ambiguities which will effect $\hat{v}_{y0}$ estimation. Each type of ambiguity and its influence on the ATI phase is discussed separately below.

B.1.1 Directional ambiguities

ATI phase can only be measured as a value between 0 and 2π (the fractional wavelength). However, the difference in range to the target between two observations may be several multiples of the radar wavelength, and thus the phase difference may be several multiples of 2π, leading to an ambiguity in the ATI phase. When the difference in the two-way propagation length to the target between observations exceeds $\lambda/2$ (i.e. $|\varphi_1(t) - \varphi_2(t)| \geq \pi$, where $\varphi_1(t)$ and $\varphi_2(t)$ are the fore and aft phase histories), the velocity direction (towards or away from the radar) becomes ambiguous. This occurs for a displacement in slant range greater than or equal to $\lambda/4$ over the time it takes the two apertures to spatially coincide (i.e. $d/(2v_a)$ seconds for the radar-target geometry outlined in section 2.3.1). The minimum ground displacement (D_{ground})

causing an ambiguity is then:

$$D_{ground} = \frac{\lambda}{4}\frac{1}{\sin(\theta_{\text{inc}})}, \tag{B.1}$$

where θ_{inc} is the incidence angle off of vertical from the radar platform to the target. Assuming displacement is only in the across-track direction (although this restriction was lifted in deriving the ATI signal in section 6.1), an ambiguous ATI phase occurs for across-track ground velocities $\geq |v_{\text{ambig}}|$ where

$$v_{\text{ambig}} = \frac{\pm D_{ground}}{(d/2v_a)} = \frac{\pm \lambda v_a}{2d\sin(\theta_{\text{inc}})}. \tag{B.2}$$

With no along-track target motion and no acceleration, ambiguities occur for across-track velocities with magnitudes greater than 10.2 m/s for the airborne case (with an assumed incidence angle of 40° and parameters given in Table 3.1) and for v_{y0} magnitudes greater than 44.0 m/s for the RADARSAT-2 spaceborne case (same incidence angle, with geometry/radar parameters given in Table 3.2). However, these ambiguities can be resolved by sub-beam partitioning [49], or with knowledge of the direction of the target's range walk from data in the range compressed domain. The sub-beam partitioning (or 'multi-look' method) of ambiguity resolution separates each target signal (from both the fore and aft channels) into fore and aft sub-beams. Each sub-beam observes the target at different times. If the Doppler centroids of each sub-beam are sufficiently separated such that the target focuses into separate range bins in each sub-beam upon compression, and if there is sufficient target energy such that the target can be detected in each sub-beam, then this provides a crude estimate of across-track velocity useful in ambiguity resolution [47].

It may be desirable to separate the fore and aft antennae by a short distance d such that the first ambiguous speed exceeds the maximum expected target speed [93]. However, longer antenna separations can be advantageous since they have increased sensitivity to target motion, lowering the minimum detectable velocity, and offering more accurate estimates of across-track velocities if the ambiguities are resolved. There is a limit to the maximum allowable d however, as physical constraints on the

system size prevent the implementation of extremely long interferometric baselines in a single pass.

B.1.2 Blind-speed ambiguities

In addition to target directional ambiguities, blind-speeds result from $n\lambda/2$ displacements of the moving target in slant range over the time between apertures (for any integer n) [47]. Targets with these displacements have an ATI phase a multiple of 2π, which appears as a phase of zero. Such targets are difficult to detect in the raw data domain since their DPCA phase will also be zero (see section 3.1.2), although again, sub-beam partitioning may be used to detect and estimate the parameters of targets moving at blind speeds. Recall from section 3.1.2 that for the CV 580 simulated parameters, the first blind speed occurs at $v_{y0} = 20.3$ m/s, whereas the first blind speed is $v_{y0} = 87.9$ m/s for the same target incidence angle using RADARSAT-2 parameters.

B.1.3 Doppler ambiguities

Additional ambiguities in the ATI phase occur due to the finite azimuth bandwidth of the radar. When the two-way Doppler frequency centroid reaches $\pm f_{\text{PRF}}/2$, one cannot differentiate between targets travelling towards the radar or away. When the target spectrum has Doppler components exceeding $\pm f_{\text{PRF}}/2$, these components are wrapped to the opposite side of the spectrum such that the signal becomes split across the $\pm f_{\text{PRF}}/2$ boundary (see Figure 4.3) [47]. When half or more of the target signal is wrapped, it is not apparent which portion belongs to the true target TF representation, and which portion is wrapped. The Doppler ambiguity occurs for across-track ground velocities $\geq |v_{\text{ambig Dop}}|$ where

$$v_{\text{ambig Dop}} = \frac{\pm\lambda f_{\text{PRF}}}{4\sin(\theta_{\text{inc}})}. \tag{B.3}$$

For signals sampled above twice the Nyquist frequency (where $f_{\text{nyq}} = 2v_a\beta/\lambda$ and β is the -3 dB antenna beamwidth), this ambiguity will always occur at a larger across-

track velocity magnitude than the directional ambiguity discussed above. For the airborne CV 580 case (with a PRF of approximately 642.5 Hz, oversampled above f_{nyq} 2.8 times) $v_{\text{ambig Dop}}$ occurs at $v_{y0} = \pm 14.1$ m/s for an incidence angle of 40°. For the RADARSAT-2 case, the oversampling factor is dependent upon the antenna transmit and receive beamwidths and the PRF (both of which are programmable). This gives flexibility in the oversampling ratio from near-Nyquist sampling (i.e. 1) to nearly 4 (i.e. at a PRF four times the clutter bandwidth), and thus $v_{\text{ambig Dop}}$ may vary from ±28 m/s to ±82 m/s.

However, an additional problem may occur in computing the ATI phase for a target (compressed using a SWMF) when the signal is sampled at more than twice the Nyquist frequency. Target motion may change the Doppler rate and shift the Doppler centroid such that there is no spectral overlap between the target signal and the SWMF, and thus upon compression there is no target peak. The v_{y0} limits within which this occurs is dependent upon the target velocities and accelerations and the incidence angle of observation, and thus varies across the swath and with the target being examined. The instantaneous Doppler frequency of a target signal received by the fore antenna is given as:

$$\begin{aligned} f(t) &= -\frac{d\phi_1(t)}{dt} \cdot \frac{1}{2\pi} \\ &= -2k\frac{dR_1(t)}{dt} \cdot \frac{1}{2\pi} \\ &= -\frac{2}{\lambda}\frac{dR_1(t)}{dt}, \end{aligned} \tag{B.4}$$

where a negative sign is required by the sign convention of positive Doppler frequency, the factor of 2 accounts for the two-way range to the target, the wave number $k = 2\pi/\lambda$ converts units from metres to radians (i.e. range to phase), and the factor of $1/(2\pi)$ converts units from radians/s into Hz.

Differentiating the Taylor expansion of the range equation (equation 2.11) with respect to time we are left with a quadratic expression for instantaneous Doppler

frequency:

$$f(t) = \frac{-2}{\lambda}\left(\frac{y_0 v_{y0}}{R_0} + \frac{1}{R_0}\left[(v_{x0}-v_a)^2 + v_{y0}^2\left(1-\frac{y_0^2}{R_0^2}\right) + y_0 a_{y0}\right]\ t \right. \quad \text{(B.5)}$$
$$\left. + \frac{3}{2R_0}\left[v_{y0}a_{y0}\left(1-\frac{y_0^2}{R_0^2}\right) + a_{x0}(v_{x0}-v_a) + \frac{y_0\ \dot{a}_{y0}}{3}\right]\ t^2\right).$$

Given y_0, R_0 and the target motion parameters $[v_{x0}\ a_{x0}\ a_{y0}\ \dot{a}_{y0}]^T$, one may find v_{y0} such that the Doppler frequency of the target does not overlap the SWMF. The bandwidth of the stationary reference filter is determined by setting all target motion parameters to zero in equation B.5 and evaluating $f(t)$ at the start and end observation times. This gives:

$$f_{\text{sta lims}} = \frac{-2}{\lambda}\frac{v_a^2}{R_0}\left(\pm\frac{T}{2}\right), \quad \text{(B.6)}$$

where $f_{\text{sta lims}}$ are the spectral limits of the SWMF. To find the region of zero spectral overlap, we want to find v_{y0} such that the target Doppler frequency track exceeds the SWMF Doppler limits, and to find v_{y0} such that when wrapped over the $\pm f_{\text{PRF}}/2$ limits, the spectral support of the target does not overlap the trailing/leading edge of the SWMF (see Figure B.1 for an illustration of these boundaries). Setting the left-hand side of equation B.5 to $\pm f_{\text{sta lims}}$ evaluated at $t = \pm T/2$ and solving the quadratic for v_{y0} gives the start of zero overlap. Setting the left-hand side to $f_{\text{PRF}} - \pm f_{\text{sta lims}}$ evaluated at $\mp T/2$ and solving the quadratic gives the end of the zero overlap. Between these limits, a target compressed with a SWMF will show no target peak since there is no spectral overlap.

For the standard CV 580 parameter set with v_{x0} and all accelerations equal to zero, there is no target output for $\pm 10.2 < v_{y0} < \pm 18.0$ m/s. However, increasing the incidence angle by just ten degrees changes these limits to $\pm 8.6 < v_{y0} < \pm 15.1$ m/s. Keeping the original incidence angle but introducing an across-track acceleration of $a_{y0} = -1$ m/s^2 changes these limits to $\pm 8.1 < v_{y0} < \pm 20.1$ m/s. As discussed in section 6.2.6, the ATI phase should be computed by iteration or by using a bank

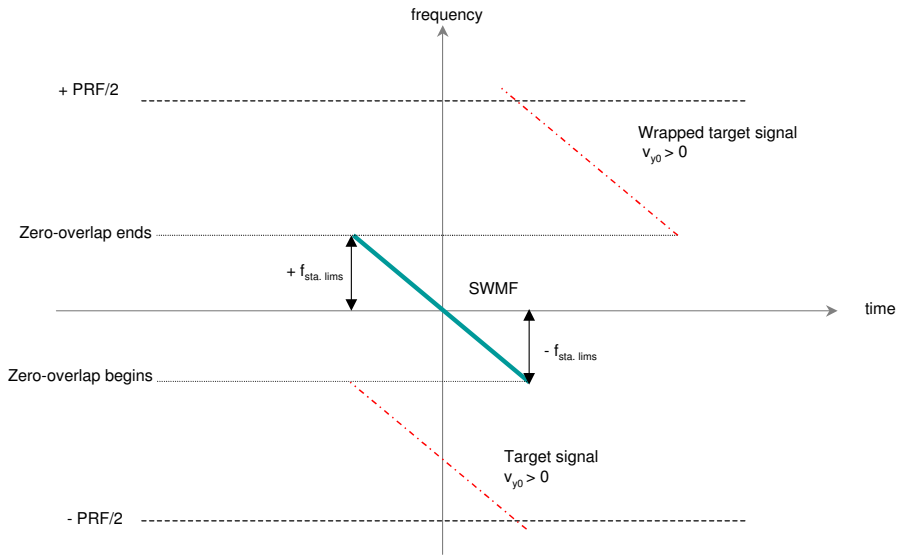

Figure B.1: Example TF representation of a SWMF (in solid blue) and a target moving in the across-track direction with sufficient $v_{y0} > 0$ m/s such that there is zero spectral overlap between the target and reference signals (see dotted red lines). The frequency bounds at which zero spectral overlap begins and ends are delineated for a PRF 2.8 times greater than the clutter bandwidth (simulating the CV 580 system). If v_{y0} increases beyond the end of zero overlap, the aliased signal will wrap back into the spectral boundaries of the reference filter.

of reference filters initialized with various v_{y0} parameters such that some spectral overlap (and thus a target response) will be present for at least one reference filter.

The amount of spectral overlap between the target Doppler bandwidth and the reference filter determines the magnitude of the resulting signal, and thus the magnitude of the ATI phase. When there is no overlap (or very minimal overlap), the magnitude becomes close to zero, approaching levels of the thermal noise and residual clutter, and thus the target phase may not be discernible. At target Dopplers in excess of $\pm f_{\mathrm{PRF}}/2$, the apparent frequencies of the signals become cyclic (due to sampling they are wrapped to be within $\pm f_{\mathrm{PRF}}/2$). At velocity magnitudes above the upper zero-overlap limit, the overlap between the target and reference filter increases until the wrapped Doppler centroid is equal to zero, at which point there is maximal overlap once more with the SWMF. When the target spectrum is split over the $\pm f_{\mathrm{PRF}}/2$ boundary, the two portions of the target track will focus under SAR processing as weak, smeared targets. Unless the target has a strong RCS, spectral segments shorter than 1/4 of the processed bandwidth may not be detectable in the ATI phase [47]. These ambiguities and various other match filtering issues are treated in detail in [48].

B.2 Performance analysis

Ideally, after co-registration the two SAR channels are identical for stationary terrain (i.e. clutter) and examining the interferogram, only moving targets should remain in the differential data [35]. It is generally assumed that the time interval between observations is sufficiently short to avoid the effects of time decorrelation in the scene, and it is assumed that phase differences are due solely to changes in the slant range to targets between epochs [53]. However, in reality, channel decorrelations do exist such that clutter possesses non-zero ATI phase, and the target signal will always be contaminated with clutter power [33]. If the resolution cell is larger than the target size, pixels will contain both clutter and target components. Even if a target occupies

an entire resolution cell (thus masking the clutter beneath it), in the presence of an unmatched v_{y0} in the reference filter, the target is shifted and superimposed on clutter at another azimuthal location. Investigating the probability density function of the SAR interferogram when target signals are superimposed upon clutter echoes, Gierull found that a bias exists in the ATI phase which is dependent upon the SCR of the received signal [33].

This relationship between SCR and ATI phase is the principal reason that ATI phase is generally obtained in the azimuth compressed domain. The SCR is too weak in the range compressed domain to neglect the clutter contamination. However, a reference filter matched to the target's quadratic component of the range equation will increase the SCR by enhancing (focusing) the target signal and smearing the clutter, and thus the complex sum of target and clutter components will be dominated by the strong target signal. For parameter estimation, the ATI phase should be evaluated only at its focused position t_{img} after azimuth compression to reduce these clutter contamination effects.

There are several other potential error sources in the ATI phase although systematic effects are the largest concern. Systematic differential phase between channels will severely bias the ATI phase estimate. This can occur when the transfer functions of the two channels are different and possibly varying across the swath. Unequal phase delays through the two receiver chains, variations in the antenna phase centres with azimuth or incidence angle, and multipath (such as the scattering of radar echoes off the wings, fuselage, or radome in the airborne case or reflections off booms or other structures in the spaceborne scenario) will contribute to errors in the ATI phase [72]. Adaptive channel balancing techniques which match the transfer functions of the two channels may be used to compensate for these systematic low-frequency errors in the data (see [34]).

Phase noise contributes additional uncertainty to the ATI phase and limits one's ability to detect slowly moving targets. System additive noise and speckle/internal

motion from the clutter causes phase decorrelation between the two channels, resulting in a noisy estimate of the interferometric phase of the signal of interest [86]. If we let ρ be the correlation coefficient (also called coherence) between the two signals, and assuming that the only factor contributing to decorrelation is additive thermal noise, then [3, 70]:

$$\rho = \frac{\langle z_1 z_2^* \rangle}{\sqrt{\langle |z_1|^2 \rangle \langle |z_2|^2 \rangle}} = \frac{1}{1 + \frac{1}{CNR}}, \tag{B.7}$$

where z_1 and z_2 are the clutter plus noise signals from the fore and aft apertures respectively, * denotes complex conjugation, $|\,\blacksquare\,|$ denotes absolute value, $\langle\blacksquare\rangle$ denotes expectation, and CNR represents the clutter-to-noise ratio. Equation B.7 is derived in Appendix B.2.1. As the CNR approaches infinity, the coherence goes to unity. For single-pass ATI, coherences are normally quite high (e.g. larger than 0.95) although they may be significantly lower for water surfaces (where ρ less than 0.80 are common) [35]. Assuming that the thermal noise contributing to a non-zero coherence is normally distributed with mean zero and standard deviation σ given by [70]:

$$\sigma = \frac{1}{\sqrt{2}} \frac{\sqrt{1-\rho^2}}{\rho}, \tag{B.8}$$

then the corresponding across-track velocity noise (computed from the phase, assuming no along-track motion or accelerations) is also normally distributed with mean zero and standard deviation σ_{vy} [86]:

$$\sigma_{vy} = \sigma \frac{\lambda}{2\pi} \frac{v_a}{d \sin(\theta_{\text{inc}})}. \tag{B.9}$$

For a coherence of 0.95, equation B.9 gives a standard deviation in v_{y0} of 0.8 m/s for the airborne case and 3.2 m/s for the RADARSAT-2 scenario.

This phase decorrelation also limits the minimum detectable velocity using ATI phase. When plotted on the complex plane, the phase of the ATI signal is the angle measured from the positive real axis, and its magnitude is the distance from the origin. With an ideal 'noise-free' radar and perfectly stationary scatterers, the clutter is completely coherent between channels (i.e. $\rho = 1$) and maps to the real axis [49].

However, partial decorrelation of the channels over the SAR aperture results in ATI phase measurements of stationary scene elements deviating away from the real axis (see Figure B.2). Such decorrelation can result from additive noise in the radar system, phase noise of the radar, and motion of the clutter over the observation period [49]. Note that this mapping of the clutter to the vicinity of the real axis occurs only for land clutter. On sea surfaces, the background clutter will move due to surface waves and currents, and the ATI phase of the background will have a non-zero average angle [78].

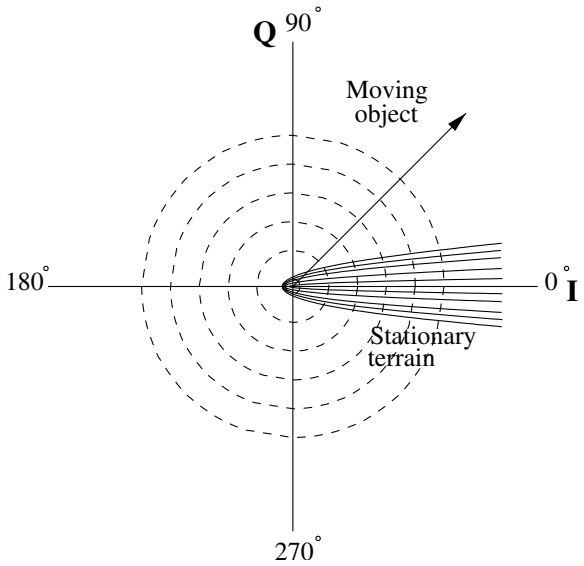

Figure B.2: Illustration of the across-track interferometric (ATI) signal in the complex plane for a moving target with accompanying clutter, where I is the inphase (real) axis and Q the quadrature (imaginary) axis. The moving target has distinctly non-zero phase, whereas (except for thermal noise near the origin) stationary terrain maps into a statistical distribution about the positive real axis. Adapted from [49].

Stationary clutter may be suppressed in the ATI complex image by nulling the magnitudes of all signal components whose phases lie within a given threshold of the real axis[49]. This nulling is accomplished using a so-called 'keyhole' filter, whose threshold may be chosen based on a given constant false alarm rate (CFAR) and

knowledge of the marginal phase distribution [32]. The minimum detectable velocity is limited by the choice of this threshold; moving targets are identified as those data whose phase angles are greater than that defined by the filter threshold. All ATI data (including slow-moving targets) with phases below this threshold are assumed to be stationary clutter and are thus removed.

Other possible sources of error in the ATI phase include atmospheric effects, although these are negligible since both signals propagate through the same portion of the atmosphere nearly simultaneously, such that ionospheric or tropospheric delays are the same in each channel. Errors in the baseline between the two antennas would also contribute to errors in parameter estimation from ATI phase, although in the CV 580 and RADARSAT-2 cases this baseline is very well known; baseline errors pose more of a problem when instead of on a rigid body, antennas are placed on the wings of an aircraft (which oscillate slightly during flight) or on a boom (whose movements may be difficult to control), or when repeat-pass interferometry is performed. The presence of an across-track component in the baseline (such as when the radar pointing angle is not orthogonal to the flight path) will introduce some phase variation due to the topography in addition to phase differences due to target motion.

B.2.1 Coherence

A simplified expression for the correlation coefficient - often called coherence (ρ) - between two interferometric channels of clutter is derived. Let the fore and aft signals at any instant in time be represented by z_1 and z_2, respectively:

$$\begin{aligned} z_1 &= c + n_1 \\ z_2 &= c + n_2, \end{aligned} \tag{B.10}$$

where c is the common clutter component in each channel, and n_1 and n_2 are noise components in each channel. Let the clutter c be a complex random variable with mean 0 and variance σ_c^2, and n_1 and n_2 are also complex random variables, each with

mean 0 and variance σ_n^2. We assume that the clutter and noise are independent, and that n_1 is independent from n_2. Assuming that additive noise n is the only factor contributing to scene decorrelation, the coherence is given by:

$$\rho = \frac{\langle z_1 z_2^* \rangle}{\sqrt{\langle |z_1|^2 \rangle \langle |z_2|^2 \rangle}}, \tag{B.11}$$

where * denotes complex conjugation, $|\,\blacksquare\,|$ denotes absolute value, and $\langle \blacksquare \rangle$ denotes expectation.

Simplifying the numerator:

$$\begin{aligned} \langle z_1 z_2^* \rangle &= \langle (c + n_1)(c + n_2) \rangle \\ &= \langle cc^* + cn_2^* + n_1 c^* + n_1 n_2^* \rangle \\ &= \sigma_c^2. \end{aligned} \tag{B.12}$$

Simplifying each term in the denomentor:

$$\begin{aligned} \langle |z_1|^2 \rangle &= \langle z_1 z_1^* \rangle \\ &= \langle (c + n_1)(c + n_1)^* \rangle \\ &= \langle cc^* + cn_1^* + n_1 c^* + n_1 n_1^* \rangle \\ &= \sigma_c^2 + \sigma_n^2. \end{aligned} \tag{B.13}$$

$$\langle |z_2|^2 \rangle = \sigma_c^2 + \sigma_n^2. \tag{B.14}$$

Plugging in the results from B.12, B.13, and B.14 into B.11, we find the coherence:

$$\rho = \frac{\sigma_c^2}{\sigma_c^2 + \sigma_n^2}. \tag{B.15}$$

Letting σ_c^2/σ_n^2 represent the clutter-to-noise ratio (CNR), the coherence may also be given as:

$$\rho = \frac{1}{1 + \frac{1}{CNR}}, \tag{B.16}$$

which completes the derivation of equation B.7.